https://theses.gla.ac.uk/

Theses Digitisation:

https://www.gla.ac.uk/myglasgow/research/enlighten/theses/digitisation/

This is a digitised version of the original print thesis.

Copyright and moral rights for this work are retained by the author

A copy can be downloaded for personal non-commercial research or study, without prior permission or charge

This work cannot be reproduced or quoted extensively from without first obtaining permission in writing from the author

The content must not be changed in any way or sold commercially in any format or medium without the formal permission of the author

When referring to this work, full bibliographic details including the author, title, awarding institution and date of the thesis must be given

Enlighten: Theses
https://theses.gla.ac.uk/
research-enlighten@glasgow.ac.uk

WAVEGUIDES WITH NON-PARALLEL PLANAR BOUNDARIES.

A Thesis
submitted to the Faculty of Engineering
of the University of Glasgow
for the degree of

Doctor of Philosophy

by

Andrew Peter Ansbro.

January 1989

© A.P. Ansbro 1989

ProQuest Number: 10999315

All rights reserved

INFORMATION TO ALL USERS
The quality of this reproduction is dependent upon the quality of the copy submitted.

In the unlikely event that the author did not send a complete manuscript
and there are missing pages, these will be noted. Also, if material had to be removed,
a note will indicate the deletion.

ProQuest 10999315

Published by ProQuest LLC (2018). Copyright of the Dissertation is held by the Author.

All rights reserved.
This work is protected against unauthorized copying under Title 17, United States Code
Microform Edition © ProQuest LLC.

ProQuest LLC.
789 East Eisenhower Parkway
P.O. Box 1346
Ann Arbor, MI 48106 – 1346

Contents.

ACKNOWLEDGEMENTS 5
SUMMARY 6
INTRODUCTION 7

CHAPTER 1: WAVE PROPAGATION IN NON-UNIFORM WAVEGUIDES.
Introduction 10
1.1: Adiabatic Mode Theory 11
1.2: Coupled Mode Theory 14
1.3: The Beam Propagation Method 17
1.4: The Parabolic Equation Method 20
Conclusions 22

CHAPTER 2: FORMULATION OF THE WEDGE GREEN'S FUNCTION AND THE INTRINSIC MODE.
Introduction 23
2.1: The Derivation Of The Scattering Equation 24
2.2: The Intrinsic Mode 28
2.3: Rigorous Analysis Of The Resolving Spectra 30
2.4: The 2-Dimensional Wedge Green's Function 36
2.5: The Convergence Of The Source Induced Spectra 41
Conclusions 44

CHAPTER 3: NUMERICAL IMPLEMENTATION OF SPECTRALLY SYNTHESISED FIELDS.
Introduction 45
3.1: The FFT Algorithm 45
3.2: Canonical Wedge Environments 47
3.3: The Transverse (x) FFT 49
3.4: The Longitudinal (z) FFT 50
3.5: Parallel And Perpendicular FFTs 52
3.5.1: The η-directed FFT 53
3.5.2: The ξ-directed FFT 54
Conclusions 56

CHAPTER 4: GEOMETRICAL AND MATHEMATICAL INTERPRETATION OF THE INTRINSIC MODE FIELD

Introduction 57
4.1: The Exact Intrinsic Mode 57
4.2: The Geometrical Approach 58
4.3: Mathematical Analysis Of The Intrinsic Mode 61
4.3.1: A Well Guided Local Normal Mode 62
4.3.2: The Critical Transition Region 66
4.3.3: The Radiating Regime 68
Conclusion 70

CHAPTER 5: NUMERICALLY CALCULATED INTRINSIC MODE FIELDS.

Introduction 71
5.1: Derivation Of The Optical Boundary Conditions 72
5.2: FFT Evaluation Of Optical Intrinsic Modes 74
5.3: Derivation Of The Acoustical Boundary Conditions 79
5.4: FFT Evaluation Of Acoustical Intrinsic Modes 81
5.5: Quantitative Comparisons With The BPM And PEM 85
5.6: The Conservation Of Total Power 90
Conclusions 97

CHAPTER 6: THE WEDGE GREEN'S FUNCTION.

Introduction 98
6.1: Derivation Of The WGF For The Global Wedge Geometry 98
6.2: The Spectral Structure 103
6.2.1: Continuity Of The Observed Field 103
6.2.2: Continuity Of The Observed Field For Different WGFs 110
6.2.3: Reciprocity 112
6.3: Asymptotic Analysis Of The WGF 115
6.3.1: The Modal Spectrum 115
6.3.2: The Initial Field 128
Conclusions 131

CHAPTER 7: APPLICATIONS OF THE WEDGE GREEN'S FUNCTION.

Introduction 132
7.1: Green's Theorem 132
7.2: Application To The Wedge Environment 133
7.3: The Gaussian Beam Input 135
7.4: The Adiabatic Mode Input 138

7.5: A Simple Connected Structure 142
Conclusions 144

CONCLUSIONS AND FUTURE CONSIDERATIONS 146

APPENDIX A: Asymptotic forms of the Euler–Maclaurin Remainder 151

APPENDIX B: Asymptotic properties of Reflection Coefficients 154

APPENDIX C: Proof Of Exactness Property Of The Intrinsic Mode 156

APPENDIX D: Stationary Phase Evaluation Of The Intrinsic Mode 158

APPENDIX E: Asymptotic Evaluation Of The Intrinsic Mode Throughout
The Critical Transition region 161

APPENDIX F: Calculation Of The Initial Fields For Global WGF 164

APPENDIX G: Proof Of The Satisfaction Of The Boundary Conditions
By The WGF 167

APPENDIX H: Evaluates The Properties Of The Spectral Phase
Function Of The WGF 173

APPENDIX I: Demonstrating The Reciprocity Property Of The WGF 176

APPENDIX J: Asymptotic Analysis Of The WGF 181

APPENDIX K: Asymptotic Analysis Of The Initial Fields 183

REFERENCES 185

ACKNOWLEDGEMENTS.

I wish to express my gratitude towards Dr. J.M. Arnold for his help, guidance and encouragement throughout this second degree 'education', and the non-trivial task of proof reading this work. My thanks extend to the Computing Service team in the Rankine Building for their efforts and useful advice throughout the duration of this work. I would also like to thank Dr. J.J. Gribble for many interesting discussions on this topic and many others.

SUMMARY.

The major part of this work is concerned with spectrally synthesised fields, in two dimensional tapered waveguides with planar boundaries. The derivation of the spectral objects of interest are from work by Arnold and Felsen [1], in which the tracking of plane wave species throughout the wedge environment is manipulated into a modal form. The collective form of the ray species (mode) is facilitated by the application of the Euler–Maclaurin summation formula [2]. The application of this summation formula furnishes the concept of an Intrinsic Mode and a source induced field which is maintained to be a Green's function for the tapered geometry.

Numerical calculation of Intrinsic Modes has been a feature of several authors' work [3,4,5,6], but in this exposition a highly efficient numerical algorithm is developed, by using Fast Fourier Transform routines [7], which exploit the oscillatory nature of the spectrum. This high efficiency enables confirmation of the power conserving property of the Intrinsic Mode on a transverse cross–section as it traverses the cut–off region of the Adiabatic Mode, provided that at least an asymptotic form of the Euler–Maclaurin remainder is included.

The Intrinsic Mode and the source induced spectral field are shown to be exact solutions of the tapered geometry (excluding the apex) and the latter is demonstrated to possess all the properties of a Green's function.

This work also examines derivations and properties of four different contemporary theories, and attaches plane wave significance to their approximations by consideration of their wave vector loci. The marching algorithm methods – Beam Propagation Method [8] and the Parabolic Equation Method [9] – are compared and assessed with the Intrinsic Mode and the Green's function for the wedge environment (calculated using Fast Fourier Transforms).

The final section deals with applications of the Green's function using the Kirchhoff integral representation. Here propagation of fields represented on a boundary are investigated. A method of calculating reflection loss from simple connected structures is also examined.

INTRODUCTION.

Wave propagation in many forms can be adequately described, in numerous instances, by the scalar Helmholtz equation. When considering environments in which the configuration coordinates can be decoupled, using appropriate separability parameters, the method of separation of variables [10] or transform approaches [11] will suffice. Many interesting practical problems cannot be solved using the above methods because the symmetry of the structures will not allow a decoupling of coordinates. Particular attention is focused on two dimensional non-separable geometries, in which a slow change in the longitudinal field is permissible, termed weakly range dependent. In the 1960s weakly range dependent fields were examined by Pierce [12]. Unfortunately this approach is unable to model certain physical phenomena, such as mode disappearance, as sufficient information about the propagating field is not present. However, the advent of modern computers facilitates fast, stable numerical algorithms which 'solve' many analytically intractable problems, approximately. Numerical modelling of weakly range dependent acoustical fields in fluids has developed mainly from approximate analytical analysis by Tappert [9]. In the above work Tappert derives approximate equations, possessing parabolic wave vector loci, which represent the elliptic Helmholtz equation in nearly-separable structures. These parabolic equations form the backbone of approximate numerical algorthims in acoustics, in which recent developments have produced more esoteric theories [13].

In optical environments the main approximate numerical machinary for examining wave propagation phenomena is the Beam Propagation Method (BPM), developed by Baets and Lagasse [8], which has been further enhanced to accommodate weakly non-linear wave propagation [14]. Feit and Fleck have also carried out extensive numerical work using the BPM [15,16]. All these numerical approaches essentially convert the boundary value problem, of the elliptic equation, into an initial value problem. This transformation is obtained by assuming approximate parallel propagation and weak confinement in the plane transverse to the propagation direction. These qualitative constraints imply that the range of applicability of these algorithms is not precisely known, as the true physical nature of the field is obscured. This lack of information about the wave nature of the field is highlighted in the investigation of geodesic lenses [17]. Here the focal shift computed using the BPM was different from the exact analytical solution. The discrepancy, after detailed analysis using Geometrical Optics [18], was attributed to the approximations inherent in the BPM algorithm. This inability to determine precisely the nature of the field has been the motivation for analytically approximate methods [19,20] and numerical approximations of coupled mode analysis [21]. In these approaches the ocean acoustics problem of Jensen and Kuperman [22] is addressed,

in which a slowly varying wedge shaped ocean overlies a fluid ocean floor. The work by Pierce [19] uses a boundary layer method [23] where matching of the guided mode field to the radiation field is made. This produces a uniform asymptotic representation of the field throughout the wedge environment.

All these methods, whether analytical or numerical, do not represent exactly any field propagating in a non-separable geometry. This reason is the main impetus in the search for a different representation of the field inside a non-separable environment. This search leads inevitably to the examination of other wave propagation phenomena. Particular interest is placed on the theory of diffraction [24], where the source fields are often represented in angular plane spectrum form [25]. This angular plane wave spectrum is used in many diffraction problems [26,27,28], and its representation of fields is essentially an integral over plane waves, parameterised by the propagation angle from a chosen datum. Indeed this method was used by Sommerfeld to calculate the diffracted field from a perfectly conducting half plane [29,30]. More recently this spectral approach has been used in an approximate manner [31], by exploiting the principle of stationary phase [32]. This type of patching has led to more esoteric representations (differential forms) of a global theory of diffraction [33]. The evolution of this spectral formulation is discussed comprehensively by Arnold [34]. However, in the class of approximate solutions there is one non-separable wave propagation environment which can be calculated exactly [1]; this being the two dimensional tapered waveguide with planar boundaries. The solution to this problem draws on several well known formulations. Firstly the source field is represented by the angular plane wave spectrum. The scattered field is then the sum of all possible image points of the source, with the information of the number of reflections and refractions contained in each spectral function. This slowly converging ray series is then manipulated using the Poisson summation formula [2] into a modal form. Several publications on the importance of this summation formula have recently been published [35,36,37]. It is of interest to note that the construction of this type of field is based, loosely, on the field due to a source point placed between two parallel, perfectly conducting, infinte planes [10].

This thesis is concerned with the analysis and evaluation of the spectral objects in the exactly soluble wedge geometry. This interest is motivated by a necessity to produce benchmark solutions with which to compare other approximate algorithms and assess their performance.

The first chapter considers four different standard approximate methods of solving the wedge environment. Here examination of the derivations, with specific emphasis placed on the plane wave content present in these representations, by discussion of their appropriate wave vector loci, is given.

A rigorous derivation of the Intrinsic Mode concept and the Green's function for the wedge environment are given as a demonstration of the necessary detail,

essential if elimination of all approximations is desired.

Having derived the appropriate spectral objects a method of exploiting the oscillatory nature of the spectrum by using the Fast Fourier Transform (FFT) methods [7] is developed. This exploitation reveals more efficient 'intrinsic' directions when calculating these spectral objects, which are dependent upon the plane wave structure of the field. A physical description of the plane wave structure of the Intrinsic Mode field demonstrates its ability to be calculated by this FFT approach.

The newly developed highly efficient algorthims are then used as a comparative tool in assessing the performance of other theories against the Intrinsic Mode for the Jensen–Kuperman (J–K) ocean [22] by examination of the field along the interface between the ocean and the ocean floor. The discrepancies in the field are accounted for by using the simplistic plane wave approach adopted in the first chapter. Also Intrinsic Mode fields are generated for TE and TM propagation in optical tapers. The Intrinsic Mode field is demonstrated to conserve power numerically across a transverse cross–section as the mode propagates upslope provided at least an aymptotic form of the Euler–Maclaurin remainder term is included.

Analysis of the source free and source induced fields is given which demonstrates that both representations are exact solutions of the Helmholtz equation, the latter possessing Green's function properties. Asymptotic analysis of these spectral objects shows agreement with other derivations and approaches upto the first order in the wedge angle. The calculation of the Green's function is demonstrated using the FFT method developed previously. Also gaussian and normal mode fields were propagated using Green's theorem [38] in two dimensions. A method is then discussed for calculating the reflected field, in principle exactly, from a simple connected structure, consisting of a parallel guide joined to an expanding wedge structure.

Chapters 2 and 4, and the asymptotic forms of the modal spectrum in chapter 6, together with the appropriate calculations (Appendices A, B, D, E, J) are this authors' interpretation of previous work by Arnold and Felsen [1,39,40]. The other wave propagation theories, discussed within a plane wave framework, are already well documented. All other work is by this author.

Introduction.

Weakly range dependent wave fields can be modelled by a variety of different techniques [8,9,12]. There are many publications demonstrating numerical results, implementation and rigorous detail. Here, four of the main types of technique are examined with specific attention placed on the physical anomalies arising out of their inherent approximations. The inability of all these theories to exactly model the planar wedge environment is greatly stressed as it is the prime motivation for the spectral synthesis approach discussed in chapter 2. The defficiencies of these methods in calculating the solution of

$$\left[\nabla^2 + n^2(z,x)k^2 \right] U(z,x) = 0 \qquad (1.1)$$

for non-separable two dimensional scalar fields are examined using simple spectral domain analysis. The theories under consideration in this chapter assume that the field varies arbitrarily in the transverse (x) direction and slowly over a wavelength scale in the longitudinal (z) direction. The four theories scrutinised are;

(1) Adiabatic Mode Theory (AMT).
(2) Coupled Mode Theory (CMT).
(3) Beam Propagation Method (BPM).
(4) Parabolic Equation Method (PEM).

These techniques, and most of the other wave propagation theories not discussed here, can be placed into two categories each having a different underlying philosophy. The first two theories are born out of the same type of approach. In this instance the field is modelled by using known solutions of the range independent problem at each cross-section and massaging these in such a way as to account for the weak range dependence (non-separablity) in an approximate manner. Indeed, coupled mode theory is a natural mathematical progression from the standard adiabatic mode theory as more information about the wave processes is retained.

The last two techniques are created from a totally different philosophical standpoint. Here, the advent of fast computers has allowed algorithms to develop that are computer-oriented. The boundary value problem is approximated by utilising a numerically stable, initial value alogrithm. The last two methods discussed are from this category of approach and the consequences of assumptions used to generate the algorithms are examined in $\underline{k}$-space.

1.1: Adiabatic Mode Theory.

This section discusses the basic assumptions used in adiabatic mode theory in a general weakly non-separable environment. It then highlights its severe limitations and how these may be overcome by employing a patching method, with particular reference to the specific geometry of Jensen and Kupermann [22]. Consider a general slowly varying structure in the longitudinal direction as shown in Figure 1.1.1

Figure 1.1.1: A General Range Dependent Environment.

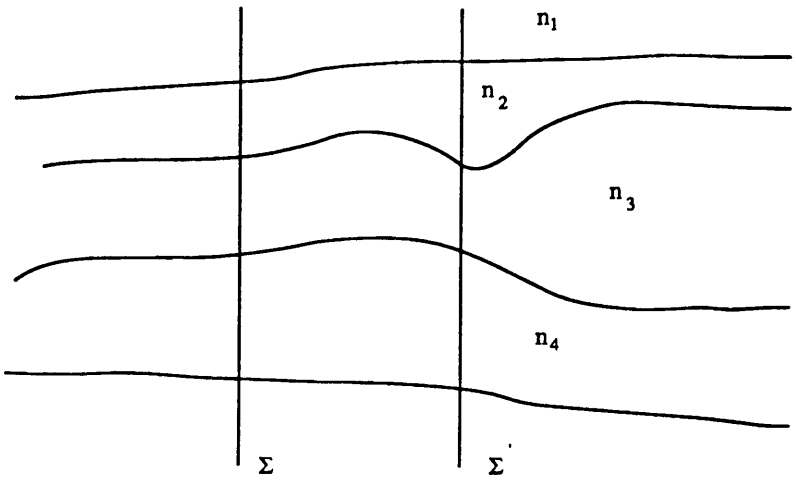

The field at a general transverse cross-section, $\sum$, can be decomposed into its transverse modal components at that cross-section. In AMT the field is assumed to consist only of the discrete guided mode set $\Phi_q(\epsilon z,x)$ of each transverse plane. The use of ϵz as an argument in any function expresses in a formal representation its weak dependence on the longitudinal parameter z. Thus the field, U(z,x), can be approximated globally by,

$$U(z,x) \approx \sum_q \Phi_q(\epsilon z,x) e^{i\Psi_q(z)} \qquad (1.1.1)$$

with the phase of each mode represented explicitly. Substituting this approximate expression into the wave equation (1.1) yields two one dimensional equations.

$$\left[\frac{d^2}{dx^2} + n^2(\epsilon z,x)k^2 - \beta_q^2 \right]\Phi_q(\epsilon z,x) = 0 \qquad (1.1.2)$$

$$i\frac{d^2\Psi_q}{dz^2} - \left[\frac{d\Psi_q}{dz}\right]^2 + \beta_q^2 = 0 \qquad (1.1.3)$$

The first equation confirms the constraint that $\Phi_q(\epsilon z,x)$ forms a discrete orthonormal set for each cross-section $\sum$ with the inner product relation defined as,

$$<\Phi_q(\epsilon z,x),\Phi_p(\epsilon z,x)> = \delta_{qp} \qquad (1.1.4)$$

The second differential equation can be simplified by imposing the constraint of slow variation of field in the longitudinal direction, which allows for the neglect of the second z derivative of the phase, $\Psi_q(z)$. Equation (1.1.3) then has the approximate solution,

$$\Psi_q(z) = \pm\int_{z_0}^{z}\beta_q(z')dz' \qquad (1.1.5)$$

A connection between each transverse mode at $\sum$ flowing into the transverse modes of a cross-section $\sum'$ is required. In AMT a mode, indexed by the integer q, is assumed to flow in a manner that retains the invariance of q. This effectively states that power is retained in a mode q throughout the geometry under consideration (hence the term adiabatic). A mode propagating in the z-direction must conserve the quantity

$$\mathrm{Im}\left[\, U(z,x)\frac{\partial U^*(z,x)}{\partial z}\right]$$

across each transverse plane (see chapter 5), where * represents complex conjugate. The adiabatic mode field propagating upslope can then be represented by,

$$U(z,x) = \sum_q \beta_q^{-\frac{1}{2}}(z)\Phi_q(\epsilon z,x)\exp\left[i\int_{z_0}^{z}\beta_q(z')dz'\right] \qquad (1.1.6)$$

This approach has been used by Pierce [12] to examine acoustic pressure fields in non-separable structures in which a ray tracing technique has been employed. There is a severe limitation to this theory which will be discussed with particular reference to the planar wedge configuration depicted in Figure 1.1.2. The discrete mode set at each cross-section is easily found to be [41],

$$\Phi_q(\epsilon z,x) = \begin{cases} A_q(\epsilon z)\sin\left[\gamma_q(h-x)\right] & 0<x<h(\epsilon z) \\ A_q(\epsilon z)\sin(\gamma_q h)e^{\tau_q x} & x<0 \end{cases} \qquad (1.1.7)$$

and where

$$\gamma_q^2 = n^2k^2 - \beta_q^2 \qquad \tau_q^2 = \beta_q^2 - n_1^2k^2 \qquad -d\gamma_q\cot(\gamma_q h) = d_1\tau_q$$

h is the local guide height and d and d_1 are the densities inside and outside guiding duct.

Figure 1.1.2: The Jensen -Kuperman Wedge Environment

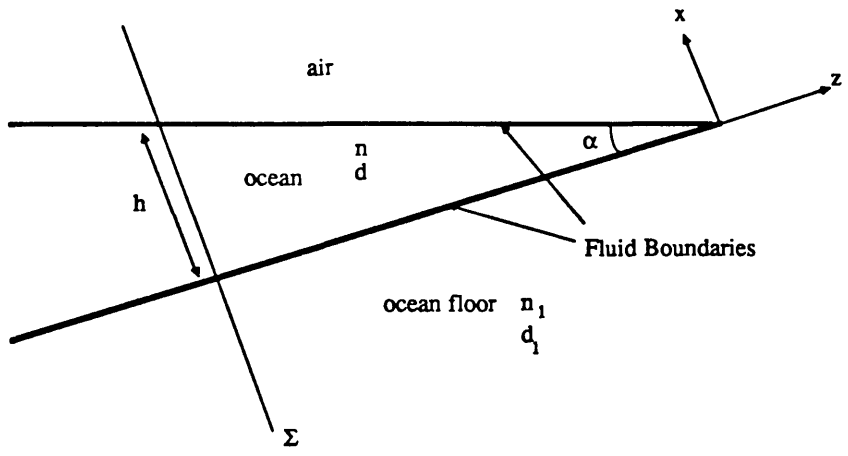

The inner product relation is given as [42],

$$\langle \Phi_p, \Phi_q \rangle = \frac{1}{d} \int_0^{h(\epsilon z)} \Phi_p^*(x)\Phi_q(x)dx + \frac{1}{d_1}\int_{-\infty}^{0} \Phi_p^*(x)\Phi_q(x)dx \qquad (1.1.8)$$

The orthonormality of this inner product relation when the densities in both media are equal to 1, together with the energy requirements, implies that,

$$A_q(\epsilon z) = \left[\frac{\tau_q}{1 + \tau_q h}\right]^{-\frac{1}{2}} \exp\, i\int_{z_0}^{z} \beta(z')dz' \qquad (1.1.9)$$

Thus the adiabatic mode field propagating upslope for the wedge region is,

$$U(z,x) = \left[\frac{\tau_q}{\beta_q(1+\tau_q h)}\right]^{-\frac{1}{2}} \exp\, i\int_{z_0}^{z} \beta(z')dz' \begin{cases} \sin\left[\gamma_q(h-x)\right] & 0<x<h(\epsilon z) \\ \sin(\gamma_q h)e^{\tau_q x} & x<0 \end{cases} \qquad (1.1.10)$$

As stated previously, for this theory to be valid, the environment must have slow dependence on the longitudinal variable. However, Jensen and Kuperman [22] have demonstrated numerically that, regardless of weak non−separability, the field changes rapidly over a wavelength scale in the longitudinal direction as the mode approaches cut−off. In this instance the evanescent field tends to a constant value and to compensate for the adiabatic nature of the theory leads $A_q(\epsilon z)$ to tend to zero. Thus

at and beyond cut−off there is no description of the field. This collapse in the theory is due to considering only the discrete spectrum corresponding to the modal field. As the mode approaches cut−off the modal angle θ_q tends to the critical angle θ_c. When θ_q is close to the critical angle, θ_c, the guided mode field couples strongly to the radiation spectrum. In AMT this continuous radiation spectrum is not considered and consequently the field calculations in this region are invalid.

Pierce [20] has shown that a critical transition region such as the one discussed above can be modelled by using a boundary layer technique [23]. This effectively expands the critical transition region so that the field can be said to be slowly varying with respect to a chosen parameter in this region and approximated asymptotically. This is then matched to the asymptotic form of the adiabatic mode before entering the critical transition region. Pierce [43] has augmented this method by using a collective form of this approach to model a point source in the Jensen − Kuperman (J−K) ocean [22]. The analysis of Pierce in this instance is in good agreement with the parabolic equation method of Jensen and Kuperman.

1.2: Coupled Mode Theory.

There are two main avenues of approach for generating coupled mode field solutions. The first method attempts generation by constructing numerically stable algorithms, which unfortunately obscure the physical processes occuring in the non−separable environment. This is the approach adopted by Evans [21] wherein the introduction of reflecting boundaries, sufficiently far from the transverse region of interest, facilitates an approximate method of sectioning through the discrete and continuous spectrum. The sectioning is achieved by evaluating all the discrete modes of the pseudo cross−section, at each cross−section, and applying the connection rules used in the Adiabatic Mode process. This method produces a stable algorithm and accurate results provided a large cross−section is used to generate the pseudo cross−section. This limitation has the effect of generating more pseudo modes and consequently field calculations require a large amount of computer time.

The second type of approach used to examine CM fields is derived from a purely mathematical background [42], which is the obvious extension of AMT. In this instance the continuous and discrete modal spectra are not subjected to a further boundary condition as above. Individual modes in the continuous spectrum do not satisfy the radiation conditions at infinity; it is possible, however, to contruct a radiation field which is not only convergent, but also satisfies the desired radiation condition by superposition of the modes in the continuous spectrum [44]. To complete a formal representation of the coupled mode equations requires the introduction of

extra orthogonality relations,

$$\langle \Phi_q, \Phi_\mu \rangle = 0 \qquad \langle \Phi_\mu, \Phi_\nu \rangle = \delta(k_\mu - k_\nu) \tag{1.2.1}$$

where k_μ represents the transverse wave number (of the μth radiation mode $\Phi_\mu(x)$) in the medium which extends to infinity. The above relations together with equation (1.1.4) allow the guided field and the continuous spectrum to form a complete basis for that particular transverse cross-section. Thus it is possible to represent the field at any transverse plane by,

$$U(\underline{x}) = \sum_q A_q(z)\Phi_q(\underline{x}) + \int_{-\infty}^{\infty} A_\mu(z)\Phi_\mu(\underline{x})dk_\mu \tag{1.2.2}$$

To ease notation the modal description of the field in (1.2.2) is represented formally as,

$$U(\underline{x}) = \sum_q' A_q(z)\Phi_q(\underline{x}) \tag{1.2.3}$$

Substituting this into equation (1.1) and employing the orthogonality relations leads to the representation of the Helmholtz equation given in equation (1.2.4)

$$\frac{\partial^2 A_p}{\partial z^2} + \sum_q' \left[2\langle \Phi_p, \frac{\partial \Phi_q}{\partial z} \rangle \frac{\partial A_p}{\partial z} + \langle \Phi_p, \frac{\partial^2 \Phi_q}{\partial z^2} \rangle A_q \right] + \beta_p^2 A_p = 0 \tag{1.2.4}$$

where p and q extend over into the radiation spectrum and β_p is the eigenvalue of the pth transverse mode. If just the discrete mode set is considered then this expression is identical to the equations (4), (5) and (6) given by Pierce [12]. Again in the limit of negligible coupling (the inner product terms in (1.2.4) are made zero) and considering only the discrete mode spectrum will generate the approximate solution given in equation (1.1.6), with positive and negative signs in the exponent indicating fields propagating to the right and left respectively. The assumption may then be made that each A_p consists of two modes, one propagating to the left, the other to the right. This assumption together with the ability to express the second order partial differential equation of (1.2.4), in terms of two coupled first order equations, gives (1.2.4) in matrix notation as,

$$\frac{\partial X}{\partial z} + MX = iBX \tag{1.2.5a}$$

with,

$$X = \begin{bmatrix} X^{+} \\ X^{-} \end{bmatrix} \qquad B = \begin{bmatrix} \beta & 0 \\ 0 & -\beta \end{bmatrix} \tag{1.2.5b}$$

with $X^{\pm}$ representing the amplitudes of the modes propagating to the right (+) and left (−), and

$$M = \begin{bmatrix} \frac{1}{2}(\beta^{\frac{1}{2}}\kappa\beta^{-\frac{1}{2}}+\beta^{-\frac{1}{2}}\kappa\beta^{\frac{1}{2}}) & \frac{1}{2}(\beta^{\frac{1}{2}}\kappa\beta^{-\frac{1}{2}}-\beta^{-\frac{1}{2}}\kappa\beta^{\frac{1}{2}})+\frac{1}{2}\beta^{-1}\frac{\partial\beta}{\partial z} \\ \frac{1}{2}(\beta^{\frac{1}{2}}\kappa\beta^{-\frac{1}{2}}-\beta^{-\frac{1}{2}}\kappa\beta^{\frac{1}{2}})+\frac{1}{2}\beta^{-1}\frac{\partial\beta}{\partial z} & \frac{1}{2}(\beta^{\frac{1}{2}}\kappa\beta^{-\frac{1}{2}}-\beta^{-\frac{1}{2}}\kappa\beta^{\frac{1}{2}}) \end{bmatrix} \tag{1.2.5c}$$

where,

$$\kappa_{pq} = \langle \Phi_p, \frac{\partial \Phi_q}{\partial z} \rangle \tag{1.2.5d}$$

and β is the diagonal operator which contains on the qth diagonal $\beta_q A_q$. Thus equations (1.2.5) represent exactly the Helmholtz equation (1.1). A full derivation of this formalism in terms of a composite Hilbert space containing the discrete and continuous spectrum is given in [42]. Equations (1.2.5) express concisely and exactly the modal processes occuring at each cross−section in a translationally variant structure. A simple understanding of these equations can be obtained by examination of a single mode; in this case the pth discrete mode propagating to the right. Suppressing the coupling matrix M, then the pth mode will propagate with a phase factor $\exp(i\beta_p z)$, which is as expected. Introducing the matrix M, it is clear that the pth mode interacts with all other fields propagating to the right and to the left, with κ encapsulating all possible mode coupling at a particular cross−section; discrete to continuous, discrete to discrete, continuous to discrete and continuous to continuous.

The authors of [42] state that successive diagonalisation of the coupled mode equations in (1.2.5) leads to successively more adaptable functions of the non−separable environment. It is suggested that the series obtained from this diagonalisation procedure can in principle furnish more adaptable modes (i.e. modes containing less intermode coupling). The computation of these functions is obviously faster than numerical solutions of the coupled mode equations as intermode coupling between these more adaptable modes is reduced. The disadvantage of this approach is that implementation of the analytic diagonalisation procedure is time consuming. In [42] Arnold and Felsen show that the coupled mode equations decoupled to $O(\alpha)$ are equivalent to the asymptotic form of the Intrinsic Mode derived in chapter 2. Indeed it is believed that this Intrinsic Mode will satisfy the coupled mode equations decoupled to any order α as this function is 'intrinsic' to its defined environment.

1.3: The Beam Propagation Method.

The BPM was placed on a stable numerical basis by Baets and Lagasse [14] and theoretical analysis, using integral equations and Green's functions, of the approximations, given by Van Roey, van der Donk and Lagasse [45]. However, both these expositions do not attempt to give physical descriptions of the approximations used for successful implementation of the BPM algorithm. The BPM and an altered BPM code (used to simulate the PEM) are used as a comparative tool in the assessment of the performance of the Intrinsic Mode concept. The finer points of implementing the BPM are omitted as interest is in analytical approximations which affect the physical nature of the model.

The elliptic equation is a boundary value problem and as such requires the field and its derivative normal to the boundary to be known on the boundary enclosing the region of interest. To make algorithms easier to generate, the field is assumed to consist only of forward propagating (positive z) fields, which is effectively stating the weak range dependence criterion in another guise. This does however mean that backward reflected fields and gratings cannot be modelled using this type of approach. The satisfaction of the radiation condition for a finite spectral domain, used in these methods, is achieved numerically by including an absorbing index profile (imaginary refractive index) at a sufficient distance from the region of interest. This profile must be such that no strong reflections occur back into the desired environment and in all computations the profile was of the form exp(cosx), where x is a transverse coordinate from a fixed point at a sufficiently isolated distance from the region of interest. The last restriction on the geometry is that the refractive index profile must be expressible in the form,

$$n(z,x) = n_0(x) + \delta n(\epsilon z, x) \qquad (1.3.1)$$

This states that the index profile must be representable in the form of a transverse index structure with a small perturbation representing the weak non-separability. The practical implementation of the BPM makes $n_0(x)$ a constant and equal to the background index. These preceeding statements imply that the global change of index must be small compared to the background index. Using the above assumptions a derivation of the BPM algorithm to calculate the field from a transverse plane at $z = z_0$ to a plane $z_0 + \delta z$ is given with all the ensuing approximations.

The field at the plane $z = z_0 + \delta z$ can be represented by,

$$U(z_0+\delta z, x) = W(z_0+\delta z, x) e^{F(z,x)} \qquad (1.3.2)$$

Substituting this into Helmholtz equation (1.1) and allowing,

$$\left[\nabla^2 + n_0^2 k^2 \right] W(z,x) = 0 \qquad (1.3.3)$$

Leaves the relationship,

$$W\nabla^2 F + W(\nabla F)^2 + 2\nabla W.\nabla F + k^2(n^2-n_0^2) = 0 \qquad (1.3.4)$$

If the stepsize in z (δz) is made small enough so that separability can be assumed then F(z,x) can be represented by,

$$F(z,x) = A(x)\,\delta z \qquad (1.3.5)$$

where A(x) is constant throughout δz. Baets and Lagasse treat F(z,x) as a series expansion in δz. However, if δz is assumed small, the equality of (1.3.5) will be satisfactory for a first order solution of (1.3.4). Substituting (1.3.5) into equation (1.3.4) means that A(x) must satisfy the quadratic,

$$A^2 + \frac{2}{W}\frac{\partial W}{\partial z} A + k^2(n^2-n_0^2) = 0 \qquad (1.3.6)$$

Solving this equation gives A(x) as,

$$A(x) = \frac{1}{W}\frac{\partial W}{\partial z}\left[-1 + \left[1 - k^2(n^2-n_0^2)W^2\left[\frac{\partial W}{\partial z}\right]^{-2}\right]^{\frac{1}{2}}\right] \qquad (1.3.7)$$

If the index pertubation is small then the second term under the square root can be assumed to be small and thus the square root term can be expanded to give the approximate value of A(x) as,

$$A(x) = -\frac{k^2}{2}(n^2-n_0^2)W\left[\frac{\partial W}{\partial z}\right]^{-1} \qquad (1.3.8)$$

This quantity can be calculated numerically, but to increase speed and numerical stability, paraxiality is introduced. The homogeneous field is said to consist of plane waves travelling almost parallel to the z axis in the background medium, allowing W(z,x) to be well approximated by $\exp(in_0 kz)$, n_0 being the background refractive index. This makes F(z,x) the standard approximation for thin lenses [46].

$$F(z,x) = e^{ik\frac{n^2-n_0^2}{2n_0}\delta z} \qquad (1.3.9)$$

Using the constraint of equation (1.3.1) and retaining terms upto $O(\delta n)$, then the BPM field at the cross-section $z = z_0 + \delta z$ from (1.3.2) is given by,

$$U(z_0+\delta z,x) = W(z_0+\delta z,x)e^{ik\delta n(x)\delta z} \tag{1.3.10}$$

To examine the algorithm in more detail it is advantageous to derive a BPM wave equation. The above formalism suggests that the BPM field consists of plane waves of the form,

$$V(z,x) = B(k_z,k_x)e^{i(k_z + k\delta n(x))z}e^{ik_x x} \tag{1.3.11}$$

where from (1.3.3) the dispersion relation is,

$$k_x^2 + k_z^2 = n_0^2k^2$$

The BPM wave equation can derived [18] by noting that,

$$\nabla^2V(z,x) = -\left[k_x^2 + (k_z + k\delta n(x))^2\right]V(z,x)$$

$$= -\left[n_0^2k^2 + 2k\delta n(x)(k_z + k\delta n(x)) - k^2\delta n^2(x)\right]V(z,x)$$

Using an obvious first order differential equation in z and considering all possible plane waves gives the BPM wave equation as,

$$\left[\ \nabla^2 - 2ik\delta n(x)\frac{\partial}{\partial z} + k^2(n_0^2-\delta n^2(x))\ \right]U(z,x) = 0 \tag{1.3.12}$$

As the field is weakly range dependent the second derivative with respect to z is neglected which gives the dispersion relation,

$$k_x^2 + \left[\ k_z + k\delta n(x)\right]^2 = n_0^2k^2 \tag{1.3.13}$$

In Figure 1.3.1 the dispersion relation is shown for the case when $\delta n(x)\neq 0$. The diagram gives a clear indication of how the BPM approximates the elliptic equation. At the cross-section z_0 the field is transformed into the plane wave spectrum propagating in the positive z direction. The phase for each plane wave, denoted by $k_z\delta z$, propagating from z_0 to the plane $z_0+\delta z$ in the background medium is,

$$\exp(ik_z\delta z) = \exp\ in_0k\left[\ 1 - \frac{k_x^2}{n_0^2k^2}\ \right]^{\frac{1}{2}}\delta z \tag{1.3.14}$$

To obtain the configuration space field the plane wave spectrum must be inverse Fourier transformed. In the spectral domain, at $z=z_0+\delta z$, this procedure corresponds to a semi-circular wave vector locus of radius n_0k and centre at the origin. However, to account for the perturbation of the medium the phase factor of the thin

lens approximation,

$$e^{ik\delta n(x)\delta z} \tag{1.3.15}$$

is added. This has the effect of shifting the plane wave locus to the right by $k\delta n(x)$ and from the diagram it is observed that this is a good paraxial approximation to the true elliptic field.

Figure 1.3.1: The Plane Wave Locus of the BPM

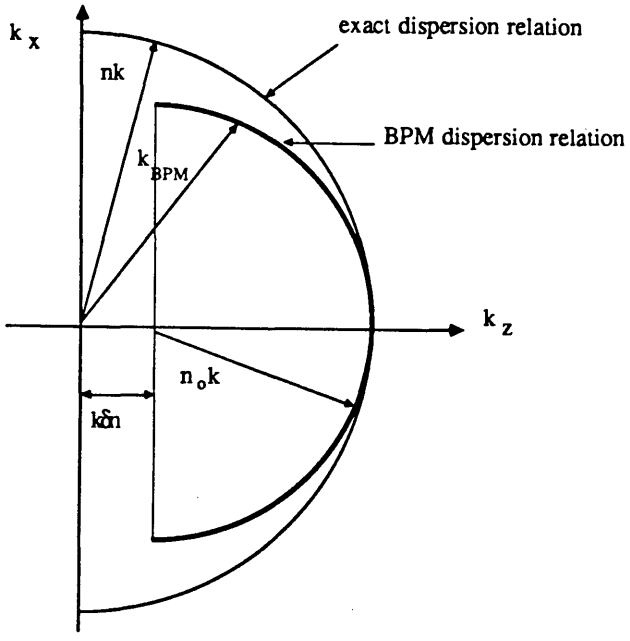

1.4: The Parabolic Equation Method.

There is a variety of different types of parabolic equation [9], but all are grouped as parabolic because they possess parabolic dispersion relations. A simple derivation of the PEM used later in the thesis is given by firstly assuming that all the field propagates as though it were in the background medium and travelling almost parallel to the z axis. Thus the field can be represented by,

$$U(z,x) = G(\epsilon z,x)e^{in_0kz} \tag{1.4.1}$$

Substituting this expression into the elliptic wave equation (1.1) implies that $G(\epsilon z,x)$

satisfies,

$$\left[\frac{\partial^2}{\partial x^2} + \frac{\partial^2}{\partial z^2} + 2in_0 k \frac{\partial}{\partial z} + k^2(n^2-n_0^2) \right] G(\epsilon z, x) = 0 \qquad (1.4.2)$$

exactly. Noting the implied slowness of G in the z direction means that the problem can transformed into an initial value problem by the neglect of the second z derivative of G. This gives the parabolic dispersion relation as,

$$k_x^2 + 2n_0 k k_z = (n^2-n_0^2)k^2 \qquad (1.4.3)$$

Figure 1.4.1 shows how this dispersion relation approximates the elliptic equation dispersion relation.

Figure 1.4.1: Parabolic Equation Dispersion Relation

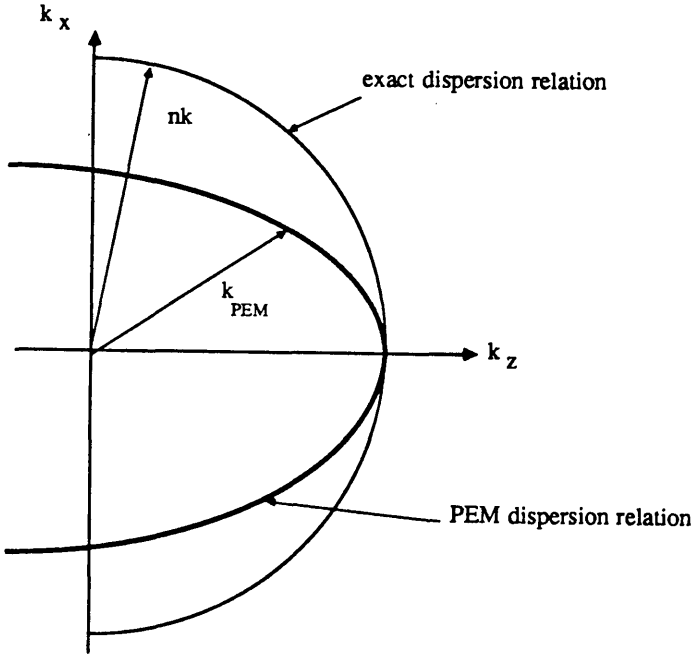

To emulate the PEM, the BPM framework can be used. If the phase change of each plane wave as it propagates from one plane to the next is changed from (1.3.14) to,

$$\exp(ik_z \delta z) = \exp in_0 k \left[1 - \frac{k_x^2}{2n_0^2 k^2} \right] \delta z \qquad (1.4.4)$$

and the thin lens approximation accounting for the perturbation is changed from (1.3.15) to,

$$\exp\, ik\left[\, \delta n(x) + \frac{\delta n^2(x)}{2n_o} \,\right]\delta z \qquad (1.4.5)$$

the BPM algorithm will then generate approximate solutions to the parabolic equation given in (1.4.2). To facilitate this emulation requires changing only two lines of code in the BPM alogrithm.

Conclusions.

The analytical approaches of AMT and CMT examine closely the wave propagation phenomenon by employing previous knowledge of similar separable structures. This type of method allows for arbitrary varying media in the transverse plane to be modelled accurately while still retaining physical insight as the wave field moves through critical transition regions. Unfortunately, because of the necessary examination of each geometry, each algorithm generated is specific to that environment. Consequently immediate versatility of algorithms is limited, even though the actual validity of application to many structures is possible.

The marching algorithm methods, where boundary value problems are transformed into initial value problems, have great versatility provided that weak guidance in the transverse plane and weak range dependence are encountered. These methods can be applied easily to the class of structures mentioned above, but it must be noted that these methods do not solve the exact elliptic wave equation of (1.1). These types of methods which solve different, but approximately similar, wave equations lead to difficulties when the comparison of data is required, because different conserved quantities exist in each particular wave equation. The effect of these approximations has been observed when predicted focal lengths of geodesic lenses using the BPM have not agreed precisely with exact analytical results [17]. Geometrical optics analysis by Gribble and Arnold [47,48] has adequately accounted for the discrepancies in the predictions of these focal lengths.

All these methods are under the umbrella of approximate solutions, which prompts research into new methods that may obtain exact solutions of specific non−separable geometries. The spectral synthesis approach used extensively throughout the following chapters allows for an exact solution of the planar wedge environment to be obtained.

Chapter 2: FORMULATION OF THE WEDGE GREEN'S FUNCTION AND THE INTRINSIC MODE.

Introduction.

Wave propagation in range independent media is a well explored phenomenon [24], the solutions of which are obtained by either of several standard techniques. Arguably the most powerful of these techniques is the separation of variables method. However, in range dependent environments the symmetry necessary for the decoupling of the wave equation to coordinate first order ordinary differential equations is not present and the above techniques cannot be applied. Most of the previous methods used to examine wave propagation in these structures can be divided into two main categories as mentioned in the previous chapter. Unfortunately while these methods may have reliable solutions for many slowly varying geometries, they lack a precise physical interpretation of the exact geometry, which will be intrinsic to the structure of the problem. This chapter presents a detailed account of the method of solution of the scalar Helmholtz equation for a wedge shaped refractive index profile for both the source–free and source excited cases. The method outlined in the following sections is that of spectral synthesis. This approach involves the introduction of a ray integral representation of the field from a source point. The ray integrals are such that their asymptotic forms behave locally like ray fields [11]. The field at an observation point in a wedge shaped structure is then said to consist of the direct ray integral field and all the multiple reflected ray integral fields. While this interpretation will in principle yield an exact solution, a large number of ray integral terms are required. To make the infintie series of ray integrals more rapidly convergent the ray field is transformed into a modal field, the passage to which is achieved by interchanging sum and integral and then applying the Euler–Maclaurin formula [2]. The presentation in this chapter is in the form of five main sections based on several publications by Arnold and Felsen [1,39,40].

The first section derives the scattering equation and explains the foundation of two cases of interest (i.e. source free and source excited cases). The second section examines the source free (Intrinsic Mode) case for the desired geometry of Figure 2.1.1. The third section is concerned with the niceties of mathematical detail necessary for a rigorous theory. The fourth section explores in detail the field due to a point source inside the guiding structure. This solution is the Green's Function for the wedge environment. The fifth section is again concerned with mathematical niceties, this time for the source excited geometry and demonstrates that the field can indeed be constructed for any open subset of the wedge geometry, excluding the apex.

The third and fifth sections, while being of great mathematical importance,

place the Intrinsic Mode theory on a solid analytical background. It is therefore unnecessary to examine the fine detail of these sections to obtain an understanding of the principles and concepts involved in the derivation. However, the results at the end of these two section need to be understood so as to realise the applicability of the derived spectral objects.

2.1: The Derivation Of The Scattering Equation

The decomposition of fields into an angular plane wave spectrum is a mathematical procedure employed to solve many diffraction problems [30], which not only furnishes great geometrical insight, but it can often afford more rigorous analysis to be implemented. Indeed this is the case for the geometry of interest shown in Figure 2.1.1.

Figure 2.1.1: 2-D Planar Wedge Environment.

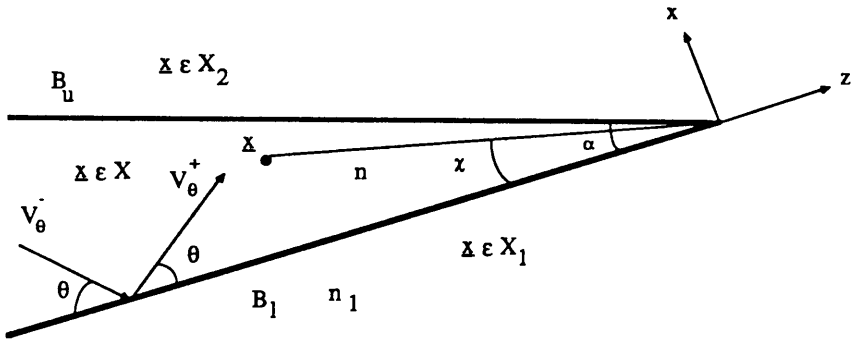

In the wedge interior the scalar field at a point $\underline{x}$ is expressible as the sum of both an upward propagating and a downward propagating plane wave field at that point. Let the upward and downward fields be $H^+(\underline{x})$ and $H^-(\underline{x})$ respectively. This statement may be represented in a spectral integral form by,

$$H^{\pm}(\underline{x}) = \int_{C^{\pm}} U^{\pm}(\theta) V_{\theta}^{\pm}(\underline{x}) d\theta \qquad (2.1.1)$$

where $U^{\pm}(\theta)$ is the spectral amplitude of each plane wave component,

$$V_\theta^{\pm}(\underline{x}) = e^{-ikr\cos(\theta \pm \chi)} \qquad \underline{x} \in X \qquad (2.1.2)$$

with the positive and negative signs denoting the upward and downward plane wave fields respectively. $C^{\pm}$ are infinite contours which terminate at $\pm i\infty$ and in sectors which make the integrands of (2.1.1) decay.

The application of this spectral approach has effectively transformed the problem into the spectral (θ) domain. With this transformation the evaluation of the spectral amplitude functions $U^{\pm}(\theta)$ is now addressed. The transformation to the θ– domain has altered the boundary conditions in such a way that they may be expressed in a linear operator notation. Let R_u and R_l be the linear reflection operators for the upper and lower boundaries respectively, which will act on plane waves in the manner shown below,

$$R_l V_\theta^-(\underline{x}) = e^{i\Phi_l(\theta)} V_\theta^+(\underline{x}) \qquad (2.1.3a)$$

$$R_u V_\theta^+(\underline{x}) = e^{i\Phi_u(\theta+\alpha)} V^-_{\theta+2\alpha}(\underline{x}) \qquad (2.1.3b)$$

where $\Phi_l(\theta)$ is the phase change at the lower boundary and $\Phi_u(\theta)$ the phase change at the upper boundary, for a wave incident at an angle θ. Two other reflection operators may be similarly defined which represent the phase changes induced after two reflections have occured, depending upon which boundary the plane wave was first incident.

$$R^+ = R_l R_u \qquad (2.1.4a)$$

$$R^- = R_u R_l \qquad (2.1.4b)$$

These composite reflection operators act in the obvious way to yield,

$$R^{\pm} V_\theta^{\pm}(\underline{x}) = e^{i\Phi^{\pm}(\theta)} V^{\pm}_{\theta+2\alpha}(\underline{x}) \qquad (2.1.5a)$$

$$\Phi^+(\theta) = \Phi_u(\theta+\alpha) + \Phi_l(\theta+2\alpha) \qquad (2.1.5b)$$

$$\Phi^-(\theta) = \Phi_u(\theta+\alpha) + \Phi_l(\theta) \qquad (2.1.5c)$$

The action of these operators on appropriate plane waves is depicted in Figure 2.1.2.

Figure 2.1.2: Geometrical Representation of the Reflection and Transmission Operators.

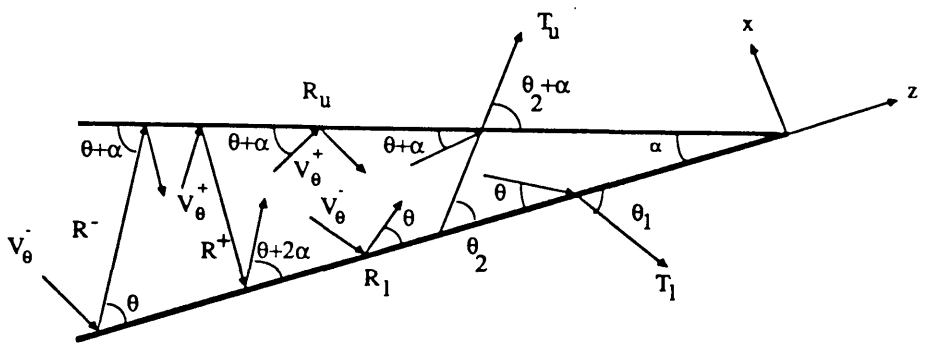

As the media of immediate concern are linear in nature, then it is possible to superpose plane waves to represent the total upward and downward fields, after one reflection, inside the guide by,

$$R_1 H^-(\underline{x}) = \int_{C^-} U^-(\theta)\, e^{i\Phi_1(\theta)} V^+_\theta(\underline{x})\, d\theta \qquad (2.1.6a)$$

$$R_u H^+(\underline{x}) = \int_{C^+} U^+(\theta)\, e^{i\Phi_u(\theta+\alpha)} V^-_{\theta+2\alpha}(\underline{x})\, d\theta \qquad (2.1.6b)$$

respectively. By a trivial extension the upward and downward field after two reflections can be expressed as,

$$R^\pm H^\pm(\underline{x}) = \int_{C^\pm} U^\pm(\theta)\, e^{i\Phi^\pm(\theta)} V^\pm_{\theta+2\alpha}(\underline{x})\, d\theta \qquad (2.1.7)$$

inside the guide. However, to facilitate the construction of the field outside the guide, the concept of transmission operators must be introduced. Firstly, plane waves outside the guide and travelling away from the higher refractive index can be represented by,

$$V_{1\theta_1}^-(\underline{x}) = e^{-in_1 k r\cos(\theta_1-\chi)} \qquad \underline{x} \in X_1 \qquad (2.1.8a)$$

$$V_{2\theta_2}^+(\underline{x}) = e^{-in_2 k r\cos(\theta_2+\chi)} \qquad \underline{x} \in X_2 \qquad (2.1.8b)$$

where θ_1 and θ_2 are the angles the plane waves make with the lower boundary

(see Figure 2.1.2). In a procedure similar to obtaining the field inside the guide, the total refracted field outside the guide can be expressed as

$$T_l H^-(\underline{x}) = \int_{C^-} U^-(\theta)\left[\, 1 + e^{i\Phi_l(\theta)} \,\right] V_{1\theta}^-(\underline{x})\,d\theta \qquad \underline{x} \in X_1 \qquad (2.1.9a)$$

$$T_u H^+(\underline{x}) = \int_{C^+} U^+(\theta)\left[\, 1 + e^{i\Phi_u(\theta+\alpha)} \,\right] V_{2\theta}^+(\underline{x})\,d\theta \qquad \underline{x} \in X_2 \qquad (2.1.9b)$$

Here T_u and T_l are the transmission operators at the upper and lower boundaries respectively (c.f. Figure 2.1.2).

The same strategy may be employed to evaluate fields due to plane waves incident on the guide structure from outside and will be explored in more detail in chapter 6. By invoking the spectral strategy above it is possible to synthesize the source field in the wedge environment. The source field is given in the usual notation by,

$$H_o^{\pm}(\underline{x}) = \int_{C^{\pm}} U_o^{\pm}(\theta) V_\theta^{\pm}(\underline{x})\,d\theta \qquad (2.1.10)$$

An intuitive physical interpretation of the problem states that the observed field $U(\underline{x})$ is the sum of the direct field at $\underline{x}$ plus the infinite number of possible reflected wave fields. This can be expressed by a scattering equation in the form below.

$$H^{\pm}(\underline{x}) = H_o^{\pm}(\underline{x}) + R^{\pm}H_o^{\pm}(\underline{x}) + \left[\, R^{\pm} \,\right]^2 H_o^{\pm}(\underline{x}) + \ldots . \qquad (2.1.11)$$

This expression represents the incident field, and all possible <u>evenly</u> reflected incident fields. While this notation greatly simplifies the problem it is not obvious if the infinite sum of (2.1.11) converges, nor is there any precise indication of the effect of truncating the series. However, this scattering equation can be expressed in closed form — the motivation for the operator notation — which can be solved exactly without the need to address the above stated problems. The scattering equation expressed in this closed form is,

$$\left[\, 1 - R^{\pm} \,\right] H^{\pm}(\underline{x}) = H_o^{\pm}(\underline{x}) \qquad (2.1.12)$$

for which (2.1.11) is the formal solution by iteration. In this form there are two distinct modes to the scattering problem, one being the homogeneous case (i.e. $H_o = 0$) and the other the inhomogeneous problem (i.e. $H_o \neq 0$). The examination of the former case gives rise to pure Intrinsic Modes, which are <u>exact</u> solutions of the

source free Helmholtz equation and are discussed in the ensuing section. The solution to the more complicated latter problem is fomulated in a later section which gives an exact Green's Function for the geometry described in Figure 2.1.1.

2.2: The Intrinsic Mode.

The solution of the source free scattering equation is facilitated by transforming to the spectral domain. The explicit representations for the scattering equation are given by equations (2.1.1) and (2.1.7). If the evenly reflected field (2.1.7) is shifted by 2α and a permissible deformation back to the original contours $C^{\pm}$ is made, then the spectral form of the scattering equation is

$$\int_{C^{\pm}} \left[U^{\pm}(\theta) - U^{\pm}(\theta-2\alpha) e^{i\Phi^{\pm}(\theta-2\alpha)} \right] V^{\pm}_{\theta}(\underline{x}) d\theta = 0 \qquad (2.2.1)$$

The deformation of the contours is permissible by invoking Cauchy's integral theorem for infinite contours, whereon the integrands vanish at infinity, provided no singularities are crossed in the deformation. For notational convenience the substitution $\theta \rightarrow \theta + 2\alpha$ is employed. As $V_{\theta}(\underline{x})$ is an arbitrary solution of the wave equation, and provided that convergence of the integrals is maintained, the spectral domain scattering equation is,

$$U^{\pm}(\theta+2\alpha) = U^{\pm}(\theta)\, e^{i\Phi^{\pm}(\theta)} \qquad (2.2.2)$$

For clarity it is desirable to employ the substitution,

$$U^{\pm}(\theta) = e^{iS^{\pm}_{q}(\theta)} \qquad (2.2.3)$$

This transforms equation (2.2.2) to,

$$S^{\pm}_{q}(\theta+2\alpha) - S^{\pm}_{q}(\theta) = \Phi^{\pm}(\theta) - 2q\Pi \qquad (2.2.4)$$

If another variable is defined as

$$S^{\pm}_{o}(\theta) = S^{\pm}_{q}(\theta) + \frac{1}{2}\Phi^{\pm}(\theta) + \frac{q\Pi\theta}{\alpha}\,, \qquad (2.2.5)$$

then equation (2.2.4) becomes,

$$S_o^{\pm}(\theta+2\alpha) - S_o^{\pm}(\theta) = \frac{1}{2}\left[\Phi^{\pm}(\theta+2\alpha) + \Phi^{\pm}(\theta)\right] \qquad (2.2.6)$$

The right hand side of equation (2.2.6) can be expressed <u>exactly</u> up to an arbitrary periodic function (with period 2α) by using the Euler–Maclaurin formula [2] given below,

$$\frac{1}{2}\left[f(\theta+2\alpha) + f(\theta)\right] = \frac{1}{2\alpha}\int_{\theta}^{\theta+2\alpha} f(s)ds + E(\theta+2\alpha,\theta) \qquad (2.2.7a)$$

where

$$E(\theta+2\alpha,\theta) = \frac{1}{2\alpha}\sum_{\substack{q=-\infty \\ q\neq 0}}^{\infty}\int_{\theta}^{\theta+2\alpha} f(s)\, e^{\frac{iq\Pi(s-\theta)}{\alpha}}\, ds \qquad (2.2.7b)$$

Identifying $\Phi^{\pm}$ with f, the solution of (2.2.6) can be extricated. It then follows that the solution of the desired equation (2.2.4) can be obtained by the substitution of equation (2.2.5) to yield,

$$S_q^{\pm}(\theta) = -\frac{\Phi^{\pm}(\theta)}{2} + \frac{1}{2\alpha}\int_{\theta_c}^{\theta}\Phi^{\pm}(s)ds - \frac{q\Pi\theta}{\alpha} + E^{\pm}(\theta,\theta_q) \qquad (2.2.8a)$$

$$E^{\pm}(\theta,\theta_q) = \frac{1}{2\alpha}\sum_{\substack{q=-\infty \\ q\neq 0}}^{\infty}\int_{\theta_q}^{\theta}\Phi^{\pm}(s)\, e^{\frac{iq\Pi(s-\theta)}{\alpha}}\, ds \qquad (2.2.8b)$$

The abitrary lower endpoints θ_c and θ_q are allowable provided the integrals of (2.2.8) converge. This arbitrariness is possible because the periodicity of the spectral scattering equation is equal to range of integration of the Euler–Maclaurin formula. Thus the solution of (2.2.2) is exact upto arbitrary periodic functions of θ. The upward and downward phases $S_q^{\pm}(\theta)$ are unrelated upto period functions of θ (period 2α). To maintain consistency with upward and downward fields it is profitable to find $S_q^{-}(\theta)$ and then construct $S_q^{+}(\theta)$ by applying one of the boundary conditions, the obvious one to impose being the lower. i.e.

$$H^{+}(\underline{x}) = R_1 H^{-}(\underline{x}) \qquad (2.2.9)$$

which gives the consistency condition,

$$S_q^{+}(\theta) - S_q^{-}(\theta) = \Phi_1(\theta) \qquad (2.2.10)$$

Consequently the Intrinsic Mode for the planar wedge geometry may be represented by,

$$W_q(\underline{x}) = \begin{cases} \sum_{-\mp} \int_{C^{\pm}} e^{iS_q^{\pm}(\theta)} e^{-ikr\cos(\theta \pm \chi)} d\theta, & \underline{x} \in X \\ \int_{C^-} e^{iS_q^-(\theta)} \left[1 + e^{i\Phi_l(\theta)}\right] e^{-ikr_1\cos(\theta_1 - \chi)} d\theta, & \underline{x} \in X_1 \\ \int_{C^+} e^{iS_q^+(\theta)} \left[1 + e^{i\Phi_u(\theta+\alpha)}\right] e^{-ikr_2\cos(\theta_2 + \chi)} d\theta, & \underline{x} \in X_2 \end{cases} \qquad (2.2.11)$$

The exact nature of the contours $C^{\pm}$ with the appropriate E–M remainder terms is examined in the next section, and in chapter 4 the physical significance of these contours and remainders is discussed. With this formalism, it is now essential, for mathematical completeness, to examine rigorously the properties of the resolving spectra of equation (2.2.8b).

2.3: Rigorous Analysis Of The Resolving Spectra.

In this section the convergence properties of the spectra in equation (2.2.8b) are examined, for equation (2.2.8a) will only hold if the series in (2.2.8b) is convergent throughout the range of integration. This section analyses the possible integration contours which will maintain convergence of the spectral series (2.2.8b). To analyse the sum in (2.2.8b) it is necessary to further specify the form of the phase function $\Phi^{\pm}(\theta)$, and to define a choice of θ_q for the lower endpoints of the integrals. These endpoints are essentially arbitrary because of the permissible indeterminancy of the Euler–Maclaurin formula.

Firstly, to ease analysis it is useful to define a generic function $\Phi(\theta)$ which possesses the analytical properties of physical realisable phase functions. These functions have several common properties;

(1) Algebraic growth anywhere in the complex plane.
This is a mathematical necessity which allows the spectral representation of the field to be governed by the plane wave terms.

(2) Possesses branch points of order $\frac{1}{2}$ at $\theta = \pm\theta_c$, $\Pi \pm \theta_c$
These branch points represent mathematically the critical angle at which total internal reflection occurs.

(3) Periodic in 2Π

This condition is necessary for consistency.

(4) $\Phi(\theta) = \Phi(\Pi - \theta)$

This condition is necessary for isotropic meida.

The Brewster phenomenon is not discussed in this exposition, but work by Arnold and Felsen [1] has shown that identical analysis can be used provided the singularity at the Brewster angle is removed and treated separately. Thus the generic form of equation (2.2.8b) is,

$$E(\theta,\theta_q) = \frac{1}{2\alpha}\sum_{\substack{q=-\infty \\ q\neq 0}}^{\infty}\int_{\theta_q}^{\theta}\Phi(s)M(qs-q\theta)ds \tag{2.3.1a}$$

with

$$M(\zeta) = e^{\frac{i\Pi\zeta}{\alpha}} \tag{2.3.1b}$$

As $\Phi(\theta)$ is defined as having no more than algebraic growth at infinity, the integral in (2.3.1a) is dominated by the exponential term. Thus the integral will converge at the lower limit if

$$\theta_q = i\infty \qquad q>0 \tag{2.3.2a}$$

$$\theta_q = -i\infty \qquad q<0 \tag{2.3.2b}$$

For the complicated non-trivial case where the phase function has a branch point, analysis is eased by splitting the sum in (2.3.1a) into positive and negative q parts and summing explicitly to yield,

$$E(\theta) = E_p(\theta,\theta_q) + E_n(\theta,\theta_q) \tag{2.3.3a}$$

where

$$E_p(\theta,\theta_q) = \frac{1}{2\alpha}\int_{i\infty}^{\theta+i\delta}\frac{\Phi(s)M(s-\theta)ds}{1-M(s-\theta)} \tag{2.3.3b}$$

$$E_n(\theta,\theta_q) = \frac{1}{2\alpha}\int_{-i\infty}^{\theta-i\delta}\frac{\Phi(s)M(-s+\theta)ds}{1-M(-s+\theta)} \tag{2.3.3c}$$

where δ is a small positive constant. Using this formalism the integration contour passes above the branch point in the first integral and below the branch point in the second integral. The above integrals diverge at $s = \theta$, but are self cancelling as $\delta \to 0$.

Figure 2.3.1: Contours of Integration for the E-M Remainder.

Figure 2.3.1(a)

$-\theta_c < Re\,\theta < \theta_c$

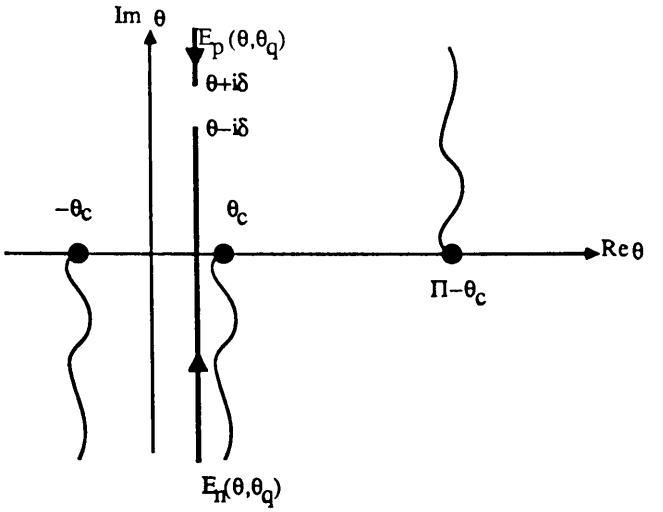

Figure 2.3.1(b)

$\theta_c < Re\,\theta < \Pi - \theta_c$

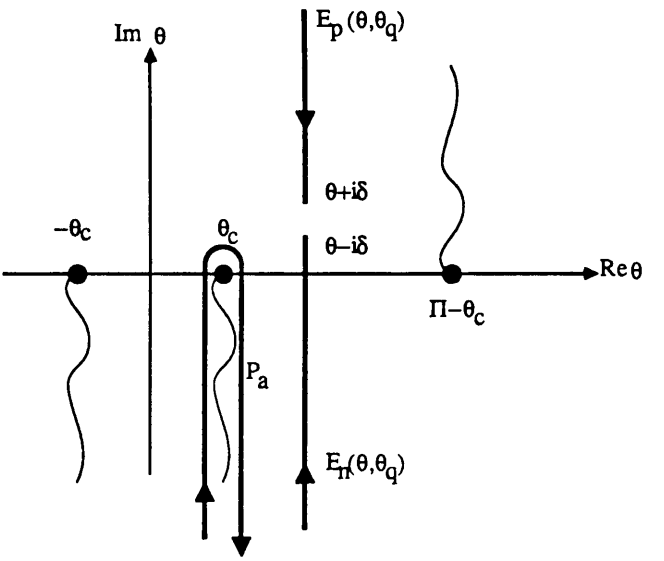

Figure 2.3.1(c)

$\Pi - \theta_c < Re\,\theta < \Pi + \theta_c$

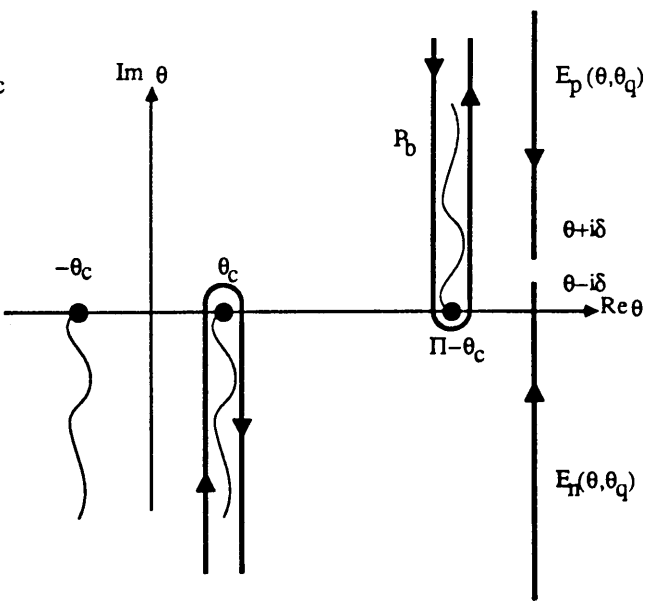

Applying Cauchy's theorem for infinite integrals it is possible to deform the lower end–points of both integrals to $\theta \pm i\infty$ appropriately, provided that,

$$| \, Re(\theta) \, | < \theta_c$$

(i.e. no singularities are crossed in the deformation of the contour). From complex analysis [51] the analytic properties possessed by an integral are entirely determined by the integrand, and as such $E(\theta)$ inherits the properties of $\Phi(\theta)$. This is shown diagramatically in Figure 2.3.1.

The convention for the branch cuts in Figure 2.3.1 will be discussed in later chapters. The diagram of Figure 2.3.1(a) shows clearly that $E(\theta)$ can be analytically continued to arbitrary complex values of θ, provided it does not cross the branch cuts at $|Re(\theta)| = \theta_c$. However, to retain <u>continuity</u> across the branch cut at $Re(\theta) = \theta_c$ it is necessary to add a branch cut integral $F_1(\theta)$ to $E(\theta)$. Hence $E(\theta)$ becomes,

$$E(\theta) = E_p(\theta, \theta_q) + E_n(\theta, \theta_q) + F_1(\theta) \qquad \theta_c < Re(\theta) < \Pi - \theta_c \qquad (2.3.4a)$$

where,

$$F_1(\theta) = \frac{1}{2\alpha} \int_{P_a} \frac{\Phi(s) M(-s+\theta) ds}{1 - M(-s+\theta)} \qquad (2.3.4b)$$

and where P_a is the contour encircling the branch cut at $Re(\theta) = \theta_c$ as seen in Figure 2.3.1(b). Due to the nature of the generic phase function $\Phi(\theta)$ it is obvious that,

$$F_1(\theta) \to 0 \quad \text{as} \quad Im\theta \to \infty \qquad (2.3.5)$$

The function $F_1(\theta)$ is periodic with respect to θ and has a period of 2α. It is very important at this juncture to stress that the addition of this branch cut integral term is <u>not</u> analytic continuation in the complex analysis sense, it is merely an exploitation of the indeterminacy of the Euler–Maclaurin solutions to correct the discontinuity of $E(\theta)$ sectionally. On crossing the branch cut at $Re(\theta) = \Pi - \theta_c$ another periodic function must be introduced to give continuity to $E(\theta)$. This case is observed in Figure 2.3.1(c) and is represented by,

$$E(\theta) = E_p(\theta, \theta_q) + E_n(\theta, \theta_q) + F_1(\theta) + F_2(\theta) \qquad (2.3.6a)$$

when

$$\Pi-\theta_c < \mathrm{Re}(\theta) < \Pi+\theta_c$$

and

$$F_2(\theta) = \frac{1}{2\alpha}\int_{P_b}\frac{\Phi(s)M(s-\theta)ds}{1 - M(s-\theta)} \qquad (2.3.6b)$$

Again imposing the properties of the generic phase function it is clear that $F_2(\theta)$ is dependent on the exponent in the integrand of (2.3.6b) and so

$$F_2(\theta) \to 0 \qquad \mathrm{Im}(\theta) \to -\infty \qquad (2.3.7)$$

It is useful at this stage to examine the reason for the above procedures. The previous manipulations are an attempt to evaluate the properties of the Euler–Maclaurin remainder over the complex θ–plane. The nature of the solutions – periodic indeterminacy – require that appropriate periodic functions are added to $E(\theta)$, so that $E(\theta)$ remains <u>continuous</u> across a branch line, these periodic functions being the corresponding branch cut integrals. While the addition of these functions is not analytical continuation it will make the E–M remainder $E(\theta)$ consistent throughout the θ–plane upto an arbitrary periodic function of θ, with a period of 2α. The mathematical sectioning can be represented by,

$$E(\theta) = \begin{cases} E_o(\theta), & -\theta_c < \mathrm{Re}(\theta) < \theta_c \\ E_o(\theta) + F_1(\theta), & \theta_c < \mathrm{Re}(\theta) < \Pi-\theta_c \\ E_o(\theta) + F_1(\theta) + F_2(\theta), & \Pi-\theta_c < \mathrm{Re}(\theta) < \Pi+\theta_c \end{cases} \qquad (2.3.8a)$$

with

$$E_o(\theta) = E_p(\theta,\theta_q) + E_n(\theta,\theta_q) \qquad (2.3.8b)$$

This analysis has exploited the Euler–Maclaurin indeterminacy <u>sectionally</u> so as to construct a consistent Euler–Maclaurin remainder term $E(\theta)$ throughout the θ–plane. However, it is also possible to exploit this indeterminacy <u>globally</u> by adding to $E(\theta)$ a periodic function in every sector shown in Figures 2.3.1. This procedure is equivalent to placing the lower endpoints θ_q of the integrals $E_n(\theta,\theta_q)$ and $E_p(\theta,\theta_q)$ in different sectors of the complex θ–plane as can easily be observed from Figure 2.3.1. If the periodic branch cut integral $F_1(\theta)$ is subtracted from each sector then $E(\theta)$ can be represented by

$$E(\theta) = \begin{cases} E_o(\theta) - F_1(\theta), & -\theta_c < Re(\theta) < \theta_c \\ E_o(\theta), & \theta_c < Re(\theta) < \Pi - \theta_c \\ E_o(\theta) + F_2(\theta), & \Pi - \theta_c < Re(\theta) < \Pi + \theta_c \end{cases} \qquad (2.3.9)$$

It is desirable to know the asymptotic nature of $E(\theta)$ as $\alpha \to 0$. The properties of the three functions $E_o(\theta)$, $F_1(\theta)$ and $F_2(\theta)$ are obtained in Appendix A and the results are summarised below,

$$\begin{aligned} E_o(\theta) &\sim O(\alpha), && |\, Im(\theta)\, | \to \infty \\ F_1(\theta) &\sim O(\alpha^{\frac{1}{2}}), && Im(\theta) > 0, \quad \theta \neq \theta_c \\ F_2(\theta) &\sim O(\alpha^{\frac{1}{2}}), && Im(\theta) < 0, \quad \theta \neq \theta_c \end{aligned} \qquad (2.3.10)$$

It can also be shown that the above equations hold even for $\theta = \theta_c$ [1]. As the functions $F_1(\theta)$ and $F_2(\theta)$ inherit the branching structure of the phase function $\Phi(\theta)$ to the right of their generating branch cuts, continuation deep into these sectors should be avoided. Using equations (2.3.8), (2.3.9), (2.3.10) and Appendix A, it is noticed that the two remainder terms have only algebraic growth in the shaded regions shown in Figure 2.3.2.

The first E−M remainder term defined by equation (2.3.8a) is denoted by $E_a(\theta)$ and the E−M remainder defined by equation (2.3.9) is denoted as $E_b(\theta)$. As the two E−M remainders have algebraic growth in the above sectors the convergence of the Intrinsic Mode is dominated by the plane wave terms,

$$e^{-ikr\cos(\theta \pm \chi)}$$

Therefore when observation points are inside the wedge the allowable contours must tend to infinity in the sectors,

$$\begin{aligned} -\alpha < Re(\theta) < \Pi - \alpha, && Im(\theta) \to \infty \\ -\Pi + \alpha < Re(\theta) < -\alpha, \quad \Pi + \alpha < Re(\theta) < 2\Pi - \alpha, && Im(\theta) \to -\infty \end{aligned} \qquad (2.3.11)$$

Two possible contours C_a and C_b depicted in Figure 2.3.2 will maintain convergence of the Intrinsic Mode field. The Intrinsic Modes calculated using the contour C_a and $E_a(\theta)$ correspond to upslope propagating fields, while integrating over C_b and using $E_b(\theta)$ represents downslope propagating fields (c.f. chapter 4). The summation of both these types of field gives the Intrinsic Mode contour $C^{\pm}$ of equations (2.2.11).

Figure 2.3.2: Regions of Algebraic Growth of the two Sectionally Continuous E-M Remainders and possible contours of the IM

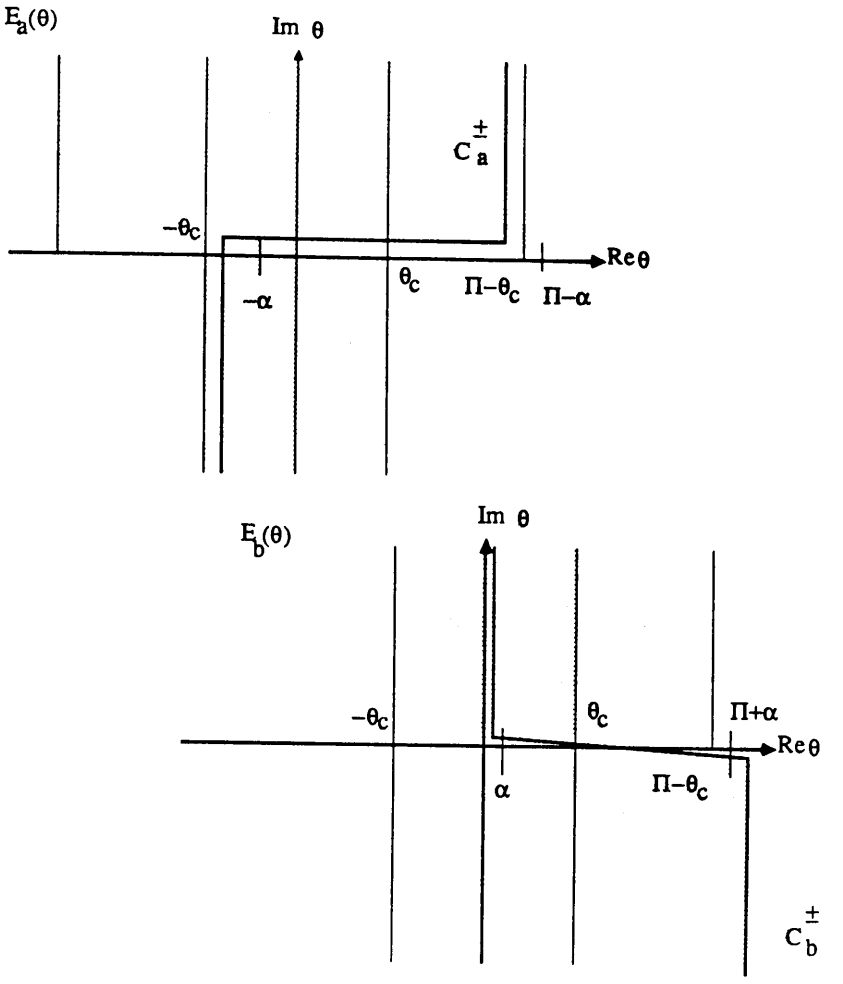

2.4: The 2– Dimensional Wedge Green's Function.

This section is concerned with evaluating the field of a line source in a wedge environment. The observed field in this case is equivalent to the solution of the inhomogeneous scattering equation (2.1.12). As the wedge structure is quasi two dimensional (i.e. the geometry is invariant in the y– direction) the line source may be represented in two dimensions by a delta function. The free space field at a point due to the line source can be represented in the spectral synthesis notation of equation (2.1.10). While this notation may at first appear the obvious choice for the source term of equation (2.1.12) it is inadvisable to apply it in this form, because of convergence difficulties in the final representation. Instead, it is more desirable to use source fields that converge even when the observation point is coincident with the source point.

It was mentioned in the first section of this chapter that the solution to the scattering equation consisted of an initial field and all possible even reflected initial fields. Using this scattering equation, it can then be seen that to represent only the total scattered field, the initial field for the scattering equation must contain four wave species. These four wave species are the fields after the direct field has been reflected in the upper and lower boundaries both an odd and even number of times and are depicted in Figure 2.4.1.

Figure 2.4.1: The Initial fields for the Scattering equation

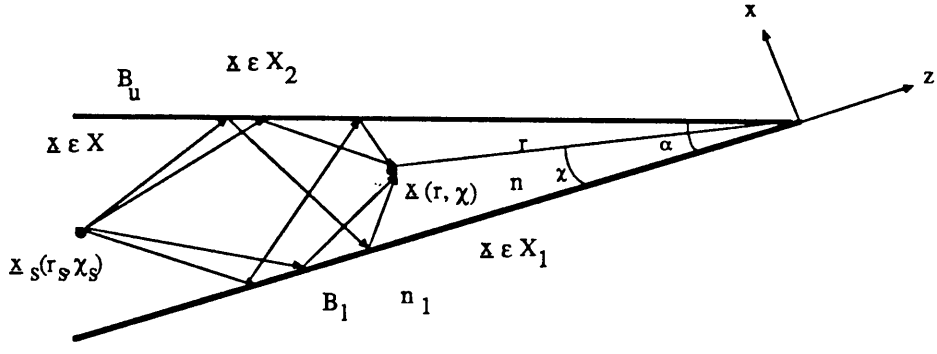

With these reflected fields as the source terms in the scattering equation all possible reflections are defined. To obtain the Green's Function for the wedge environment requires the addition of the direct term to the total scattered field of equation (2.1.12).

The upward and downward fields in free space can be represented by,

$$H_o^+(\underline{x}) = \int_{C^+} W_o^+(\theta) V_\theta^+(\underline{x}) d\theta \qquad (2.4.1a)$$

$$H_o^-(\underline{x}) = \int_{C^-} W_o^-(\theta) V_\theta^-(\underline{x}) d\theta \qquad (2.4.1b)$$

where

$$W_o^\pm(\theta) = e^{ikr_s \cos(\theta \pm \chi_s)} \qquad (2.4.1c)$$

and V_θ are the plane waves defined by equation (2.1.2). The contours are the Sommerfeld contours depicted in Figure 2.4.2, which may be freely shifted to obtain convergence over the whole space.

Figure 2.4.2: The Standard Sommerfeld Contour.

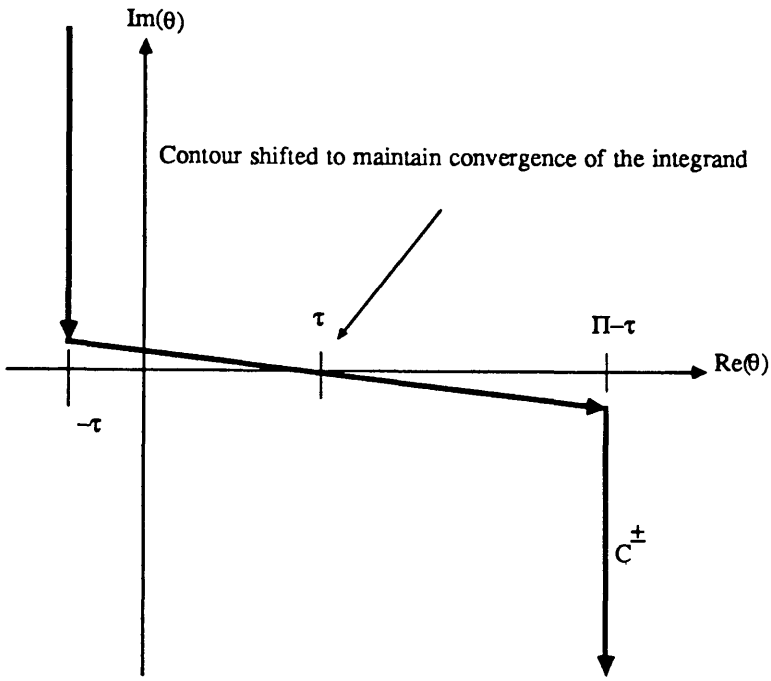

This shifting of the contour in the $\theta-$ plane corresponds to a rotation of axes in the configuration space domain. The integrals of equation (2.4.1) can now be operated on using the reflection operators defined in the first section of this chapter. The total upward initial incident field is the sum of the single and double reflected fields. i.e.

$$R_1 H_o^-(\underline{x}) + R^+ H_o^+(\underline{x}) = \int_{C^-} W_o^-(\theta) e^{i\Phi_1(\theta)} V_\theta^+(\underline{x}) d\theta + \int_{C^+} W_o^+(\theta) e^{i\Phi^+(\theta)} V^+_{\theta+2\alpha}(\underline{x}) d\theta \qquad (2.4.2a)$$

Similarly the downward field, inside the guide, after one and two reflections is,

$$R_u H_o^+(\underline{x}) + R^- H_o^-(\underline{x}) = \int_{C^+} W_o^+(\theta) e^{i\Phi_u(\theta+\alpha)} V^-_{\theta+2\alpha}(\underline{x}) d\theta + \int_{C^-} W_o^-(\theta) e^{i\Phi^-(\theta)} V^-_{\theta+2\alpha}(\underline{x}) d\theta \qquad (2.4.2b)$$

The contours $C^\pm$ may be freely shifted and provided no singularities are crossed in this shifting process the integrals will remain equivalent. Thus with an obvious change of variables in equations (2.4.2) the incident fields can be brought into the form of (2.1.10). The incident field spectral amplitudes then become,

$$U_o^+(\theta) = W_o^-(\theta)e^{i\Phi_l(\theta)} + W_o^+(\theta-2\alpha)e^{i\Phi^+(\theta-2\alpha)} \qquad (2.4.3a)$$

$$U_o^-(\theta) = W_o^+(\theta-2\alpha)e^{i\Phi_u(\theta-\alpha)} + W_o^-(\theta-2\alpha)e^{i\Phi^-(\theta-2\alpha)} \qquad (2.4.3b)$$

With these definitions of incident field the scattering equation (2.1.12) becomes in the spectral domain,

$$U^{\pm}(\theta+2\alpha) - U^{\pm}(\theta)e^{i\Phi^{\pm}(\theta)} = U_o^{\pm}(\theta+2\alpha) \qquad (2.4.4)$$

where the obvious shift of 2α to left has been applied. This is in the form of equation (2.2.4), but for ease of notation it is desirable to introduce some definitions. Firstly let,

$$U^{\pm}(\theta) = Y^{\pm}(\theta)e^{iS^{\pm}(\theta)} \qquad (2.4.5)$$

where

$$S^{\pm}(\theta+2\alpha) - S^{\pm}(\theta) = \Phi^{\pm}(\theta) \qquad (2.4.6)$$

If the incident field is defined in a similar manner,

$$U_o^{\pm}(\theta) = Y_o^{\pm}(\theta)e^{-iS^{\pm}(\theta)} \qquad (2.4.7)$$

equation (2.4.4) becomes,

$$Y^{\pm}(\theta+2\alpha) - Y^{\pm}(\theta) = Y_o^{\pm}(\theta+2\alpha) \qquad (2.4.8)$$

The solution to the scattering problem in the spectral domain without the direct term is simply the sum of $U^+(\theta)$ and $U^-(\theta)$. The calculation of these two terms requires the solution of the four difference equations of (2.4.6) and (2.4.8). As in the Intrinsic Mode section these difference equations can be solved exactly, upto arbitrary periodic functions of θ, using the Euler–Maclaurin formula. The solution of (2.4.6) is identical to the solution of (2.2.4) with $q = 0$. Thus $S^{\pm}(\theta)$ becomes,

$$S^{\pm}(\theta) = -\frac{1}{2}\Phi^{\pm}(\theta) + \frac{1}{2\alpha}\int_{\theta_c}^{\theta}\Phi^{\pm}(s)ds + E^{\pm}(\theta,\theta_q) \qquad (2.4.9)$$

Again due to the indeterminacy of the Euler–Maclaurin formula, it is more practicable to evaluate $S^-(\theta)$ and impose a boundary condition to obtain a consistent

$S^+(\theta)$, the most appropriate being the lower boundary. i.e. imposing,

$$S^+(\theta) - S^-(\theta) = \Phi_1(\theta) \tag{2.4.10}$$

The solution $Y^{\pm}(\theta)$ of equation (2.4.8) can be solved in a similar manner to yield,

$$Y^{\pm}(\theta) = \frac{1}{2} Y_o^{\pm}(\theta) + \frac{1}{2\alpha} \sum_{q=-\infty}^{\infty} \int_{\theta_{q\infty}}^{\theta} Y_o^{\pm}(s) e^{\frac{-iq\Pi(\theta-s)}{\alpha}} \, ds \tag{2.4.11}$$

The limits $\theta_{q\infty}$ are arbitrary because of the indeterminacy of the Euler–Maclaurin formula. Returning to the original functions $U^{\pm}(\theta)$ via (2.4.5) and (2.4.6) produces,

$$U^{\pm}(\theta) = \frac{1}{2} U_o^{\pm}(\theta) + \frac{1}{2\alpha} \sum_{q=-\infty}^{\infty} \int_{\theta_{q\infty}}^{\theta} U_o^{\pm}(s) e^{iS^{\pm}(\theta) - iS^{\pm}(s) - \frac{iq\Pi(\theta-s)}{\alpha}} \, ds \tag{2.4.12}$$

This expression is arbitrary upto periodic functions of θ and obviously the convergence of $E^{\pm}(\theta)$ in $S^{\pm}(\theta)$ is required. As shown in the previous section there are several ways to construct the remainder so that $E(\theta)$ has no more than algebraic growth in some sectors. As θ ranges over the Sommerfeld contour of Figure 2.4.2 then it can be observed that only the b–type remainder is convergent and the remainder $E(\theta)$ must be interpreted as $E_b(\theta)$. This then gives the scattered field for observation points inside the guide as,

$$G_s(\underline{x},\underline{x}_s) = \sum_{+-} \int_C \left[\frac{1}{2} U_o^{\pm}(\theta) + \frac{1}{2\alpha} \sum_{q=-\infty}^{\infty} \int_{\theta_{q\infty}}^{\theta} U_o^{\pm}(s) e^{iS^{\pm}(\theta) - iS^{\pm}(s) - \frac{iq\Pi(\theta-s)}{\alpha}} \, ds \right] V_{\theta}^{\pm}(\underline{x}) \, d\theta \tag{2.4.13}$$

The Green's function is now the sum of this scattered field and the direct field given in equation (2.4.1). Therefore the Wedge Green's function is,

$$G(\underline{x},\underline{x}_s) = H_o^+(\underline{x}) + G_s(\underline{x},\underline{x}_s) \tag{2.4.14}$$

The extension to this procedure for points anywhere within this wedge region excluding the apex can be obtained straightforwardly by application of the above outlined theory. All that is now required is mathematical rigour in which the convergence properties of this function are examined. This rigour is necessary to give the theory a solid foundation and is tackled in the next section.

2.5: The Convergence Of The Source Induced Spectra.

It is important to mention that there is one basic assumption made in the last section which is fundamental to the theory and has no mathematical grounding. This section will now correct this inadequacy in essentially two main ways. The assumption made was that the contours of the total scattered field integral $G_S(\underline{x},\underline{x}_S)$ (equation (2.4.13)) and the initial source field integrals (equations (2.4.2)) could be deformed into a common contour, while maintaining convergence and crossing no singularities in the deformation. This central idea is necessary so that reduction to the spectral plane is possible and hence the procedures of previous sections applicable. The first terms $U_0(\theta)$ in the expression for $G_S(\underline{x},\underline{x}_S)$ are identical to the initial field and the contours are obviously equivalent. However, the properties of the double integral terms are not so clear. Let,

$$U_q^{\pm}(\theta) = \int_{\theta_{q\infty}}^{\theta} U_o^{\pm}(s) e^{iS^{\pm}(\theta)-iS^{\pm}(s)-\frac{iq\Pi(\theta-s)}{\alpha}} ds \qquad (2.5.1)$$

The analysis of the above integrals, which form part of the spectral amplitude functions for the observed field, is divided into two main categories. The first category is concerned with showing that the integrals $U_q(\theta)$ are convergent on the same contours as the initial field. This is achieved by firstly examining the significance of the lower limit $\theta_{q\infty}$ and then the convergence of these integrals when multiplied by their appropriate plane wave fields with θ ranging over the Sommerfeld contour shown in Figure 2.4.2. The second stage of analysis then demonstrates that while each individual integral term is convergent, the total infinite sum of these integrals is also convergent.

As previously stated the limits $\theta_{q\infty}$ are arbitrary, however, for convergence of the sum in equation (2.5.1) these limits must be such that the exponential term involving q decays. i.e.

$$\begin{aligned} &Im(\theta_{q\infty}) > Im(\theta), \qquad q > 0 \\ &Im(\theta_{q\infty}) < Im(\theta), \qquad q < 0 \end{aligned} \qquad (2.5.2)$$

and since θ ranges over the infinite Sommerfeld contour C_0 (C_0 representing either of the contours $C^{\pm}$) the convergence of all q terms can only be secured if,

$$\begin{aligned} &Im(\theta_{q\infty}) = \infty, \qquad q > 0 \\ &Im(\theta_{q\infty}) = -\infty, \qquad q < 0 \end{aligned} \qquad (2.5.3)$$

$\mathrm{Im}(\theta_{q\infty})$ has been defined to facilitate the decay of the exponent involving the q term in equation (2.5.1), but the exponential form of the remaining integrand has not been accounted for. It can be seen through equations (2.4.9) and (2.4.3) that the convergence of each integral in (2.5.1) is governed by plane waves of the form,

$$e^{ikr_s\cos(s+w)} \tag{2.5.4}$$

where w can represent either $\pm\chi_s$ or $-2\alpha\pm\chi_s$ depending on which term of $U_o(\theta)$ is being considered. These exponential terms vanish exponentially in the sectors,

$$\begin{aligned} -w < \mathrm{Re}(s) < \Pi-w, \qquad & \mathrm{Im}(s) < 0 \\ -\Pi-w < \mathrm{Re}(s) < -w, \qquad & \mathrm{Im}(s) > 0 \end{aligned} \tag{2.5.5}$$

When the source point is in the guide, this being the Green's function of immediate interest, then χ_s, the polar source variable is less than α. In equation (2.4.13) there are four plane wave species and the sector for which all these terms converge is obtained from (2.5.4) and the definition of w, to give

$$\begin{aligned} -3\alpha < \mathrm{Re}(s) < \Pi-3\alpha, \qquad & \mathrm{Im}(s) < 0 \\ -\Pi-3\alpha < \mathrm{Re}(s) < -3\alpha, \qquad & \mathrm{Im}(s) > 0 \end{aligned} \tag{2.5.6}$$

To assure convergence in the lower limit $\theta_{q\infty}$, the limits should be restricted to the conditions above. Hence to achieve this the lower limits should be continued off to infinity in the shaded sectors of Figure 2.5.1.

The Regions Of $\theta_{q\infty}$ Which Maintain The Convergence Of U_q In The Lower Limit.

Figure 2.5.1:

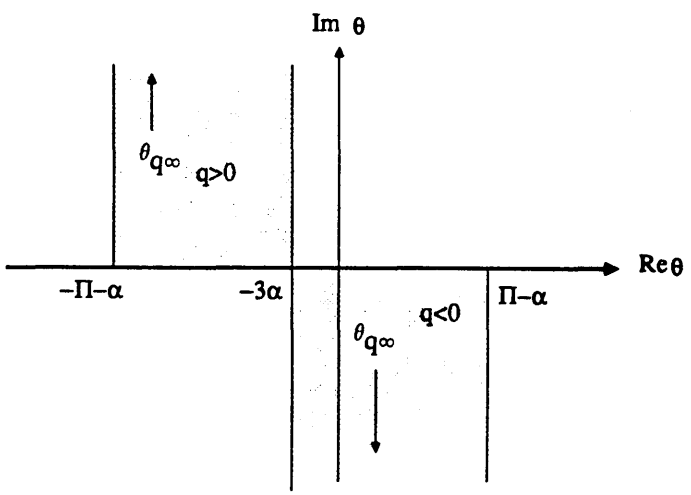

Now the convergence of these separate integrals needs to be explored as $|\theta| \to \infty$. θ ranges along the infinite Sommerfeld contour C_0 and these are regions where the plane waves of (2.5.4) diverge. It must be established, for convergence, that the plane wave terms, $V_\theta(\underline{x})$, in the spectrum decay faster than the rate at which the integrals, $U_q(\theta)$, diverge. An estimation of the increase of these integrals can be found by the application of Laplace's method for asymptotic evaluation of integrals [2]. This yields the asymptotic value of the integrals $U_q(\theta)$ for $|\theta| \to \infty$,

$$U_q^{\pm}(\theta) \sim U_o^{\pm}(\theta)\left[-ikr_s\sin(\theta+w) \right]^{-1} \tag{2.5.7}$$

This is an estimation of the spectral amplitude function and so the approximation to the integrand of the scattered field integral is,

$$U_q^{\pm}(\theta)V_\theta^{\pm}(\underline{x}) \sim U_o^{\pm}(\theta)\left[-ikr_s\sin(\theta+w) \right]^{-1} V_\theta^{\pm}(\underline{x}) \tag{2.5.8}$$

for $|\theta| \to \infty$. Thus it is plainly observed that the convergence of the separate double integrals of $G_s(\underline{x},\underline{x}_s)$ is secured in the regions where,

$$U_o^{\pm}(\theta)V_\theta^{\pm}(\underline{x})$$

decay to zero. This sector of convergence is obviously the same as the initial fields in the source term of the scattering equation, because the above functions are identical to the integrands of (2.4.2). The above analysis has shown that each separate integral, $U_q(\theta)$, is dominated by the upper endpoint θ. It has not given any indication that the infinite sum over q of $U_q(\theta)$ is convergent. Employing the same procedure as in section 2.3, this infinite sum can be re-written in the form

$$\sum_{q=-\infty}^{\infty} U_q^{\pm}(\theta) = \int_{\theta_{q\infty}}^{\theta+i\delta} \frac{Y_o^{\pm}(s)M(s-\theta)ds}{1 - M(s-\theta)} + \int_{\theta_{q\infty}}^{\theta-i\delta} \frac{Y_o^{\pm}(s)M(-s+\theta)ds}{1 - M(-s+\theta)} \tag{2.5.9}$$

where $\theta_{q\infty}$ are defined as in Figure 2.5.1. The divergences of these integrals as $\delta \to 0$ are self cancelling. The representation $G_s(\underline{x},\underline{x}_s)$ has now been shown to be convergent in the appropriate sectors, which implies that this function is a bonafide solution of the Helmholtz wave equation in the wedge environment.

Conclusions.

This chapter is an attempt to show the philosophy of the Intrinsic Mode and its subsequent application to the source induced field problem. The mathematical complexities have not been avoided, in an attempt to show the reader the necessary mathematical considerations for a 'watertight' theory. This theory is based on the ability of the slowly converging ray integral field to be manipulated using the Euler–Maclaurin formula into a rapidly converging modal field. This theory does not account for the diffracted field at the apex of the wedge and as such the field near this point cannot be accurately represented. A future publication by Arnold and Felsen is planned to alleviate this shortcoming. It may seem at first sight that this theory is too esoteric to be of any significant use, this however, is not the case. The apparent complexity in constructing the Intrinsic Mode field results, in reality, in an easier object to compute numerically than, say, a large number of ray integrals. Also, the Intrinsic Mode field is an exact solution of the wave equation, which implies that the inaccuracy incurred in evaluating the spectral object is entirely contained in the numerical implementation. This is not the case for all of the other theories to date. Another interesting point to mention at this time is that with this theory it is possible to evaluate the true conserved quantity (i.e. Poynting Vector) as shown in a forthcoming chapter. It may be observed that in evaluating the Green's Function for the wedge geometry, no reference was made to the properties of Green's Functions, or as to whether the spectral object of equation (2.4.14) possessed any of these properties. This is left until chapter 6 where the properties of Green's Functions are used in verifying the computer programme developed to compute this field.

There are still, however, several unaddressed questions in this theory and, while these are of no great importance in the ensuing chapters, it is desirable to understand their significance. The Euler–Maclaurin formula has periodic indeterminacy and as such the effect of adding periodic functions must be determined. Arnold and Felsen [1] have demonstrated that the arbitrariness of the Euler–Maclaurin formula can be explained simply. The solution to the inhomogeneous equation (2.1.13) consists of the solution to the homogeneous problem and the solution to the inhomogeneous problem. The arbitrariness in the solution of the inhomogeneous equation is then merely the addition of homogeneous solutions (i.e. Intrinsic Modes).

Chapter 3: NUMERICAL IMPLEMENTATION OF SPECTRALLY SYNTHESISED FIELDS.

Introduction

The derivation of the spectral objects in chapter 2 require some form of numerical evaluation. Standard integration techniques can be employed [5], but they do not exploit fully the nature of the spectral fields.

The numerical evaluation of both the Intrinsic Mode field and the Green's Function in a wedge environment are addressed in this chapter. To demonstrate clearly the method of implementation a generalised spectral integral is considered, wherein the desired properties for this type of analysis are assumed. The calculation of both these spectral objects is achieved by the application of a Fast Fourier Transform (FFT) algorithm [7] from the NAG software support library, the properties of which are easily derivable from a knowledge of Fourier Series [54]. From these properties and the ensuing procedures it will become apparent that any field which may be well approximated by a finite oscillatory integral can be evaluated using this FFT procedure.

The first section describes, abstractly, how an arbitrary spectral integral may be numerically manipulated so that application of the FFT algorithm is possible. The next sections are concerned with demonstrating how the desired spectral objects for the wedge geometry can be calculated using differently 'directed' FFTs.

In the subsequent sections it will be observed that if the spectral field is to be amenable to the FFT approach then it must satisfy some basic properties. In this chapter it is assumed that the Intrinsic Mode and the Wedge Green's Function possess these properties. The justification for these assumptions is given in the relevant chapters discussing each spectral object.

3.1: The FFT Algorithm

Consider an integral of the form,

$$F(\beta) = \int_{-\infty}^{\infty} f(\theta) e^{i2\Pi\beta\theta} d\theta \qquad (3.1.1)$$

and assume it has the dominant part of the integrand in an interval (0,T), say. The integral may then be approximated by,

$$F(\beta) \approx \int_0^T f(\theta) e^{i2\Pi\beta\theta} d\theta \qquad (3.1.2)$$

To evaluate this integral numerically for a fixed β any number of standard techniques may be employed [53]. However, for suitable accuracy and ease of implementation Bode's Rule [54] was used. This five point rule states that a finite integral may be calculated by applying the formula,

$$\int_0^T G(\theta,\beta) d\theta = \frac{T}{90}\left\{7G(\beta,0)+32G(\beta,\frac{T}{4})+12G(\beta,\frac{T}{2})+32G(\beta,\frac{3T}{4})+7G(\beta,T)\right\} + O(T^7) \qquad (3.1.3)$$

To evaluate (3.1.2) and as such approximate the integral of equation (3.1.1), for each point β in the appropriate admissible space, the algorithm of equation (3.1.3) would have to be repeatedly applied, for each β, with a sufficient number of points for accuracy. If $G(\beta,\theta)$ is of a slowly varying nature, then the evaluation of such a space using the procedure of (3.1.3) will be adequate. When $G(\beta,\theta)$ is either rapidly oscillatory, or non-negligible in a wide range of θ, or both, a large number of data points will be required. If this is the case then it is desirable to find a more efficient method of evaluating the field $F(\beta)$.

The desired improved efficiency can be generated in two significant areas. The obvious way to increase the efficiency would be to use a more accurate integration rule. It is obvious, however, that the application of a more accurate integration rule could not achieve a significant improvement in efficiency and remain sufficiently adaptable. Due to this minimum gain in efficiency research into more complicated integration algorithms was felt to be unfruitful. The other approach is to exploit the periodicity of the integrand and use an FFT routine. The algorithm used for this particular application is from the software support library on the GEC 4180 computer. The form of the FFT algorithm is very general and as such some manipulation of the input data to this routine is required to satisfy its initialisation procedure. It is therefore desirable to obtain a clear understanding of the properties of the FFT algorithm.

Let the function $f(\theta)$ of equation (3.1.2) be discretised into N equally spaced points in θ, f_j say. This being the case the FFT produces N data points F^k – using the butterfly method [7] – such that,

$$F^k = \sum_{j=0}^{N-1} f_j e^{\frac{i2\Pi jk}{N}} \qquad (3.1.4)$$

The spacing of the data points F^k corresponds to a spacing in the β-domian of

1/T (from the properties of Fourier Series [55]). The FFT procedure itself requires that $j=0$ corresponds to $\theta=0$ and the output space is such that $k=0$ is equivalent to $\beta=0$ and increasing k implies increasing β. There is one glaring defect in the above statements which needs rapid clarification. It is that the series in equation (3.1.4) is not equivalent to the integral of equation (3.1.2), it is merely the addition of all the f_j values with a corresponding phase change. The required equivalence between (3.1.4) and $F(\beta)$ can be obtained simply by evaluating the integral of (3.1.2) by the trapezium rule (i.e. multiplying output of algorithm by $T/N^{\frac{1}{2}}$). It is, however more accurate and also tractable to 'window' the input data field so that the 'five point' integration rule of (3.1.3) is used to evaluate the integral of equation (3.1.2). This 'windowing' is achieved by the weighting of the $\theta-$ domain f_j values by the amounts indicated in equation (3.1.3).

With equivalence now achieved accurately between (3.1.4) and (3.1.2) it is necessary to be able to adjust the spacing of the data points in the $\beta-$ domain so a desirable $\beta-$ space may be computed. To achieve this property a quasi finite interval T_s is constructed, the construction of which is given below. Assume that the desired spacing in β is $1/T_s$ and the non- negligible interval of integration is T, which is discretised into K+1 points. Thus the θ distance between each f_j is $\theta_s = T/K$. If K_a zeros are then added to the $\theta-$ domain K+1 field points the quasi interval of non- negligible integration is then,

$$(K+1+K_a)\frac{T}{K} \tag{3.1.5}$$

which must be equal to T_s and as such a variable spacing between the points in the $\beta-$ domian is achieved by the formula,

$$\beta_s = \frac{K}{T(K+1+K_a)} \tag{3.1.6}$$

with β_s being the β spacing and K+1 the true non- negligible field points of θ and K_a the number of added zero field points. Now that a versatile routine has been developed for evaluating finite oscillatory integrals it only remains to discuss its application to spectrally synthesised Intrinsic Mode type fields.

3.2: Canonical Wedge Environments.

There are many different configurations in which two infinite planar interfaces intersect. However, this exposition is only concerned with the excitation of two- dimensional non- separable geometries by an infinite line source. Obviously

there are many examples of Intrinsic Mode fields to examine, but they are all evaluated by using either of two canonical wedge environments, which only depened upon the type of upper boundary. If the upper boundary has a reflection coefficient which is constant and equal to -1 then the recipe for solution will be of type A say. If, however, the reflection coefficient on the upper boundary is a function of the incident plane wave and environmental parameters, a more complicated procedure is required to evaluate the field (recipe B). From the previous chapter a general form for the Wedge Green's Function or the Intrinsic Mode, when the reflection coefficient is a constant and equal to -1 on the upper boundary, is,

$$W_q(\underline{x}) = \begin{cases} \sum_{-+} \int_{C^{\pm}} I^{\pm}(\theta,\underline{x}_s) V^{\pm}_{\theta}(\underline{x}) d\theta, & \underline{x} \in X \\ \int_{C^-} I^-(\theta,\underline{x}_s)\left[1 + e^{i\Phi_1(\theta)}\right] V^-_{1\theta_1}(\underline{x}) d\theta, & \underline{x} \in X_1 \end{cases} \tag{3.2.1}$$

while for the type B field (variable reflection coefficient of the upper boundary) the spectral fields can be represented in the form

$$W_q(\underline{x}) = \begin{cases} \sum_{+-} \int_{C^{\pm}} I^{\pm}(\theta,\underline{x}_s) V^{\pm}_{\theta}(\underline{x}) d\theta, & \underline{x} \in X \\ \int_{C^-} I^-(\theta,\underline{x}_s)\left[1 + e^{i\Phi_1(\theta)}\right] V^-_{1\theta_1}(\underline{x}) d\theta, & \underline{x} \in X_1 \\ \int_{C^+} I^+(\theta,\underline{x}_s)\left[1 + e^{i\Phi_u(\theta+\alpha)}\right] V^+_{2\theta_2}(\underline{x}) d\theta, & \underline{x} \in X_2 \end{cases} \tag{3.2.2}$$

Here $I^{\pm}(\theta,\underline{x}_s)$ are the appropriate spectral amplitudes depending on which global object is being considered and in which particular subset of the wedge geometry. The plane wave components V_{θ} can be expressed in a more useful Cartesian coordinate system which facilitates efficient evaluation of the fields along the new configuration space axes. The plane waves become,

$$V^{\pm}_{\theta}(\underline{x}) = e^{-ikr\cos(\theta\pm\chi)} = e^{ik(z\cos\theta\pm x\sin\theta)} \tag{3.2.3}$$

$$V^-_{1\theta_1}(\underline{x}) = e^{-in_1 k\cos(\theta_1-\chi)} = e^{ikz\cos\theta - in_1 kx\sin\theta_1} \tag{3.2.4}$$

$$V^+_{2\theta_2}(\underline{x}) = e^{-in_2 k\cos(\theta_2+\chi)} = e^{ikz\cos\theta_2 + in_2 kx\sin\theta_2} \tag{3.2.5}$$

where z and x are the coordinates given in Figure 2.1.1 of chapter 2. It is apparent that there is the possiblity of exploiting the periodicity of these oscillatory functions in two orthogonal directions. There are however, difficulties in implementation of either of these two possible directions, which will be outlined. Consider firstly exploiting the transverse (x) periodicity of a type A field.

3.3: The Transverse (x) FFT.

Manipulating the integrals of equations (3.2.1) into a form more sutiable in which to explain the substitutions required to allow the application of the FFT leads to,

$$W_q(\underline{x}) = \begin{cases} \sum_{+-} \int_a^b \overset{+}{G}(\theta,z,\underline{x}_s) e^{\pm inkxsin\theta}\, d\theta, & \underline{x} \in X \\ \int_a^b \bar{G}(\theta,z,\underline{x}_s)\left[1 + e^{i\Phi_1(\theta)}\right] e^{-in_1kxsin\theta}\, d\theta, & \underline{x} \in X_1 \end{cases} \qquad (3.3.1)$$

where $\overset{\pm}{G}(\theta,z,\underline{x}_s)$ are the appropriate functions easily obtainable from equations (3.1.1) and the interval (a,b) is assumed to be sufficiently large in some sense (see later chapters). These integral forms must be massaged into a canonical form for the FFT application. To show analysis succinctly it is easier to consider the upward propagating field inside the guide ($\underline{x} \epsilon X$) initially. With the change of variable,

$$2\Pi s = nk(\sin\theta - \sin a) \qquad (3.3.2)$$

the integral of (3.3.1) is transformed into,

$$e^{inkxsina} \int_0^{\frac{nk}{2\Pi}\left[sinb-sina\right]} \frac{d\theta}{ds} G(\theta,z,\underline{x}_s) e^{i2\Pi xs}\, ds \qquad (3.3.3)$$

which is amenable to FFT exploitation provided in evaluation s is stepped through in equal increments. The downward field can be transformed in a similar manner.

The field in the lower medium consists of the transmitted field due to plane waves from the guiding medium incident on the lower boundary. As some of the plane waves have an incident angle less than the critical angle (θ_c), the field must be split into two sections.

$$\int_{a}^{\theta_c} + \int_{\theta_c}^{b} G(\theta,z,\underline{x}_s)\left[1 + e^{i\Phi_1(\theta)}\right]e^{-in_1 kx\sin\theta_1}d\theta \qquad (3.3.4)$$

The first integral is a sum of inhomogeneous plane waves (as $\sin\theta_1$ is purely positive imaginary) which correspond to wave fields trapped inside the guiding medium. These fields have lost their x periodicity – they constitute the evanescent field – and consequently the FFT cannot be applied to this region. However, the integral over the interval (θ_c,b) is plane wave in nature (this is the refracted field) and as such can be manipulated into the form,

$$\int_{0}^{C(b)} \frac{d\theta}{d\theta_1}\frac{d\theta_1}{ds} G(\theta,z,\underline{x}_s)\left[1 + e^{i\Phi_1(\theta)}\right]e^{i2\Pi xs}ds \qquad (3.3.5a)$$

with

$$C(b) = \frac{nk}{2\Pi}\sin\left[\cos^{-1}\left[\frac{n\cos b}{n_1}\right]\right] \qquad (3.3.5b)$$

where the FFT may then be applied. Fortunately the substitution (3.3.2) is such that the spacing between the points in the θ domain around zero is decreased to $O(\delta s)$ where δs is the equal increment in s space. This implies that the number of points required to evaluate the integral accurately would be the same as if the substitution (3.3.2) had not occurred, as the dominant part of the field is situated near zero (c.f. chapters 4 and 6). The lack of being able to evaluate the spectal object outside the guide by using the FFT exclusively has the effect of increasing run times, because an integral must now be evaluated for every point considered outside the guide. The useful substitution of (3.2.2) does not compensate for having to calculate the evanescent field by a standard method and so overall efficiency, while being significantly greater than a standard integration technique, does not utilise fully the periodicity of the spectral fields.

3.4: The Longitudinal (z) FFT.

As stated in the previous section the evanescent field has no x–periodictiy associated with it. However, this field still retains its longitudinal (z) periodicity – due to the tangential components of the field being continuous at an interface – so that exploitation by the FFT method with respect to the z ordinate may be employed. With this knowledge it is obvious that the field can be calculated

everywhere in the type A wedge configuration by using this longitudinal FFT alone. This type of FFT 'direction' is termed the 'intrinsic direction' for the geometry, because it exploits fully the intrinsic nature of the wedge environment. Thus the spectral objects may be represented by

$$W_q(\underline{x}) = \begin{cases} \int_a^b K_1(\theta,x,\underline{x}_s)e^{inkzcos\theta}d\theta, & \underline{x} \in X \\ \int_a^b K_2(\theta,x,\underline{x}_s)e^{inkzcos\theta}d\theta, & \underline{x} \in X_1 \end{cases} \qquad (3.4.1)$$

with $K_1(\theta,x,\underline{x}_s)$ and $K_2(\theta,x,\underline{x}_s)$ being the kernels calculated from equations (3.2.1). The desired substitution to allow this periodic exploitation is,

$$2\Pi s = nk(\cos\theta - \cos b) \qquad (3.4.2)$$

The application of this substitution to equations (3.4.1) gives rise to the formalism,

$$e^{inkzcosb} \int_0^{\frac{nk}{2\Pi}[cosa-cosb]} \frac{d\theta}{ds} K(\theta,x,\underline{x}_s)e^{i2\Pi zs}ds \qquad (3.4.3)$$

Here the $K(\theta,x,\underline{x}_s)$ is the function $K_1(\theta,x,\underline{x}_s)$ or $K_2(\theta,x,\underline{x}_s)$ depending on whether the observation point is inside or outside the guide. This approach appears at first sight to have no disadvantages. Unfortunately this is not the case. The substitution (3.4.2) has the effect that as $s \to nk/2\Pi$, and thus $\theta \to 0$, the equal spacing in the s− domain (δs) causes the spacing in the θ− domain to increase. The spacing in the θ− domain is

$$\delta\theta \approx \left[\frac{2\Pi\delta s}{\sqrt{[n^2k^2 - 4\Pi^2s^2]}} \right] \qquad (3.4.4)$$

The θ− domain spacing around zero obviously increases dramatically and unfortunately this is where the dominant contribution to the field occurs. To circumvent this problem the region of integration is truncated in such a manner that important spectral topologies (c.f. chapter 4 and 6) are sufficiently far away from the endpoints. An asymptotic approximation (in terms of wedge angle) is then added to correct this truncation.

The previous two sections have dealt with FFT directions depicted in Figure 2.1.1 of chapter 2. There are many other possible directions which may be considered, but they have the obvious disadvantage of having to calculate some form of evanescent field.

3.5: Parallel and Perpendicular Directed FFTs.

The type B fields can be evaluated using the FFT methods of sections 3.3 and 3.4. However, when the observation point is in the superstrate ($\underline{x} \epsilon X_2$) the evanescent field cannot be calculated totally by the FFT method and standard integration techniques, as used in section 3.3, are necessary to calculate the remainder of the evanescent field. Thus to calculate the total field above the guide by using only the FFT method requires an FFT direction which runs parallel to the upper boundary. To achieve this different FFT 'direction' a rotation of axes is required (see Figure 3.5.1 below).

Figure 3.5.1: Rotation of Cartesian Coordinates.

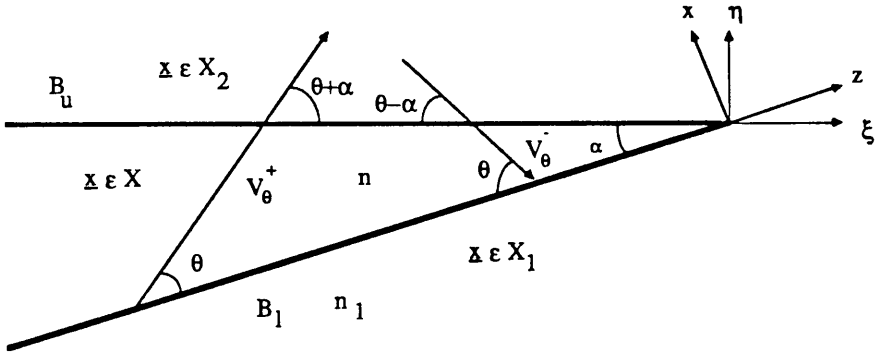

The different orientation of these new orthogonal axes depicted above can be represented in terms of the Cartesian coordinates of sections 3.3 and 3.4 in matrix form by,

$$\begin{bmatrix} \cos\alpha & -\sin\alpha \\ \sin\alpha & \cos\alpha \end{bmatrix} \begin{bmatrix} z \\ x \end{bmatrix} = \begin{bmatrix} \xi \\ \eta \end{bmatrix} \qquad (3.4.1)$$

Thus the plane wave species of equations (3.2.3), (3.2.4) and (3.2.5) can be expressed in the rotated co−ordinate system as,

$$V_\theta^{\pm}(\underline{x}) = e^{ink(\xi\cos(\theta\pm\alpha)+\eta\sin(\alpha\pm\theta))} \qquad (3.5.2)$$

$$V_{1\theta}^{-}(\underline{x}) = e^{in_1k(\xi\cos(\theta_1-\alpha)-\eta\sin(\theta_1-\alpha))} \qquad (3.5.3)$$

$$V_{2\theta}^{+}(\underline{x}) = e^{in_2k(\xi\cos(\theta_2+\alpha)+\eta\sin(\theta_2+\alpha))} \qquad (3.5.4)$$

Although the primary reason for this rotation of co−ordinates is the efficient

evaluation of fields in a type B geometry, another useful FFT direction arises.

3.6: The η– directed FFT.

Examine firstly the η– directed FFT (useful for calculating fields in integrated optical structures). The field in the guiding duct can then be manipulated into the form,

$$\sum_{+-} e^{ink\eta sin(\alpha\pm a)} \int_0^{\frac{nk}{2\Pi}\left[sin(\alpha\pm b)-sin(\alpha\pm a)\right]} \frac{2\Pi}{nkcos(\alpha\pm\theta)} L^{\pm}(\theta,\xi,\underline{x}_s) e^{i2\Pi\eta s} ds \qquad (3.6.1)$$

The field outside the guide must be split up into the evanescent and plane wave spectrum as previously shown to give,

$$\int_a^{\theta_c} + \int_{\theta_c}^{b} L^{-}(\theta,\xi,\underline{x}_s)\left[1+e^{i\Phi_1(\theta)}\right] e^{-in_1 k\eta sin(\theta_1-\alpha)} d\theta \qquad (3.6.2)$$

in some subset of the wedge configuration. The obvious substitutions can be made for the second integral to give

$$\int_0^{C(b)} \frac{2\Pi L^{-}(\theta,\xi,\underline{x}_s)}{nkcos(\alpha-\theta)}\left[1+e^{i\Phi_1(\theta)}\right]\frac{d\theta}{d\theta_1} e^{i2\Pi s} ds \qquad (3.6.3a)$$

with

$$C(b) = \alpha + \frac{nk}{2\Pi} sin\left[cos^{-1}\left[\frac{ncosb}{n_1}\right]\right] \qquad (3.6.3b)$$

which can be evaluated using the FFT approach. The evanescent field must be evaluated by using Bode's rule, as periodicity in the η variable is not present. A similar representation may be obtained for the field above the guide, but for brevity this is omitted.

3.7: The $\xi-$directed FFT.

The $\xi-$directed FFT can be used to evaluate efficiently the field in both the guiding duct and the superstrate. It can be seen that this direction of FFT for evaluating the field inside and above the guide is the 'intrinsic direction', because it exploits fully the nature of the interaction of the fields between two linear media (c.f. longitudinal (z) FFT). In the guiding duct the field can be represented in the usual manner for FFT exploitation, as,

$$W_q(\underline{x}) = \int_a^b N(\theta,\eta,\underline{x}_s) e^{ink\xi\cos(\theta+\alpha)} d\theta, \qquad \underline{x} \in X \qquad (3.7.1)$$

With the obvious change of variables (3.7.1) becomes

$$W_q(\underline{x}) = e^{ink\xi\cos(b+\alpha)} \int_0^{\frac{nk}{2\Pi}\left[\cos(a+\alpha)-\cos(b+\alpha)\right]} \frac{2\Pi N(\theta,\eta,\underline{x}_s)}{nk\sin(\theta+\alpha)} e^{i2\Pi\xi s} ds, \qquad \underline{x} \in X \qquad (3.7.2)$$

Noting that the field must be continuous across the boundary, then,

$$n\cos(\theta+\alpha) = n_2\cos(\theta_2+\alpha) \qquad (3.7.3)$$

The field for $\underline{x} \in X_2$ can be manipulated into the similar form of,

$$W_q(\underline{x}) = e^{ink\xi\cos(b+\alpha)} \int_0^{\frac{nk}{2\Pi}\left[\cos(a+\alpha)-\cos(b+\alpha)\right]} \frac{2\Pi N_0(\theta,\eta,\underline{x}_s)}{nk\sin(\theta+\alpha)} e^{i2\Pi\xi s} ds, \qquad \underline{x} \in X_2 \qquad (3.7.4)$$

$N_0(\theta,\eta,\underline{x}_s)$ and $N(\theta,\eta,\underline{x}_s)$ are the obvious spectral amplitude coefficients derived from equations (3.22). All that now remains is to marry the z and ξ FFTs so that an efficient algorithm can be generated to calculate either of the spectrally synthesised linear fields.

To calculate the field in the total space the field below the upper boundary (guiding duct and substrate) is evaluated using the intrinsic z FFT. The field in the upper medium is evaluated using the $\xi-$directed FFT (intrinsic direction). However, it has been observed that the spacing in the configuration domain is dependent upon the interval of non$-$negligible integrand (0,T). This interval can be varied using the technique of the first section, but there is still the problem of calculating the fields at regular points in a two dimensional grid which is shown below.

Take the field points generated by the z$-$FFT to be the reference data points

in the two dimensional configuration as shown in Figure 3.7.1.

Figure 3.7.1: Generating a data Grid for the Global Wedge profile.

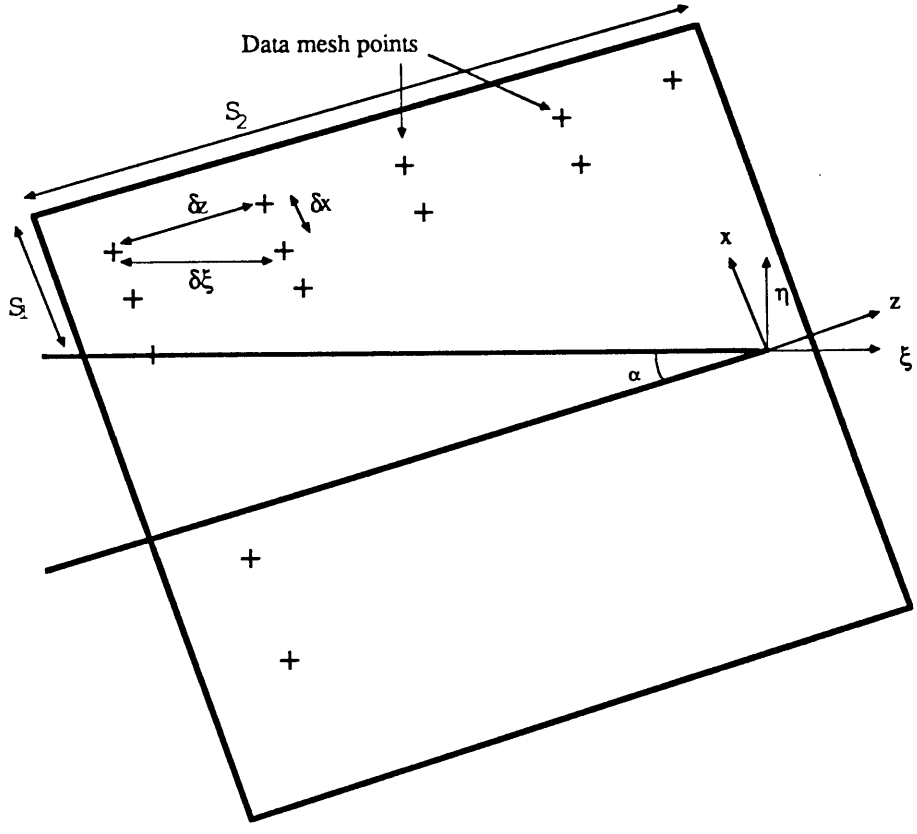

Here the mesh points are parallel and perpendicular to the lower boundary as would be expected with the z−FFT routine. In the upper medium this configuration of mesh points is required to be conserved, but the ξ−directed FFT generates points that are parallel to the upper interface. To ensure that the field points evaluated, lie on the reference mesh the spacing and the initial starting point of the ξ−directed FFT must be adjusted. From the diagram of Figure 3.7.1,

$$\delta\xi = (\delta x^2 + \delta z^2)^{\frac{1}{2}} \qquad (3.7.5)$$

with δx and δz being the spacial increments in x and z respectively and $\delta\xi$ the spatial increment in the ξ−directed FFT. The initial starting value for each of the ξ−FFTs is at data points of the mesh that lie on the Boundary sections S_1 and S_2. This technique utilises the 'intrinsic' nature of the z and ξ FFTs below and above the upper boundary respectively.

Conclusions.

This chapter has not offered any constructive arguments to demonstrate that the spectrally synthesised fields of interest possess the properties essential for this type of numerical evaluation. These arguments are left to the chapters were the appropriate spectral object is examined more closely. The efficient evaluation of spectral fields discussed in this chapter is achieved by exploiting the oscillatory nature of the fields. It is observed that the spectral amplitudes of the plane waves in each particular environment can be calculated without any positional dependence. The introduction of the positional dependence of the fields is expressed using Cartesian coordinate systems. Obviously the two 'intrinsic directions' z and ξ are the most efficient approach to field calculations using this method, as the evanescent field outside the guide is contained within the appropriate FFT evaluation. The other two directions are useful as comparisons of other field plots and for generating the input fields to other numerical algorithms. A large number of orientations of these systems are possible, but the four chosen directions of this chapter are the most numerically efficient when using the FFT method. It will also be noted that the plane polar orthogonal system (r,χ) used for the derivation of the Intrinsic Mode and the Wedge Green's Function was discarded. This rejection is because the numerical evaluation of the spectral amplitudes cannot occur without dependence on either the range or angle parameter.

Chapter 4: GEOMETRICAL AND MATHEMATICAL INTERPRETATION OF THE INTRINSIC MODE FIELD.

Introduction.

The preceeding two chapters discussed the derivation of the Intrinsic Mode field and its subsequent numerical implementation. In both these chapters several properties of the Intrinsic Mode field were stated without any apparent justification. This chapter attempts to rectify these omissions.

It was stated in chapter 2 that the Intrinsic Mode is an exact solution of the elliptic wave equation in the wedge shaped environment. This statement is extremely important for it is the first exact solution of this non-separable structure and as such it will allow detailed estimation of the errors incurred when calculating the Intrinsic Mode field numerically, this estimation being virtually impossible for any other method.

The numerical implementation of the Intrinsic Mode field assumes that the field is constructed in such a manner that it can be well approximated by a finite oscillatory integral. The grounds for this argument and other omissions from the spectral field are examined from both a physical and mathematical standpoint. In the interests of clarity a specific example, that of the Jensen-Kupermann ocean [22], has been chosen.

4.1: The Exact Intrinsic Mode.

The exactness of the Intrisic Mode field is examined for an arbitrary wedge environment. To achieve this, and before embarking on the physical interpretation of the Intrinsic Mode field, it must be demonstrated that this field satisfies the elliptic wave equation and the boundary conditions away from the apex exactly.

As the field is formulated in the spectral domain (each plane wave being an exact solution of the wave equation) and as the media are linear, allowing superposition, then the field must satisfy the wave equation exactly.

The field under scrutiny has been constructed in such a manner that the source free field may be represented in the form of a single spectral object. To demonstrate that this Intrnsic Mode satisfies the boundary conditions requires the use of Cauchy's theorem for closed contours and the application of the Euler-Maclaurin summation formula. This calculation, while essential, would only serve to cloud the issue. Accordingly only the geometrical interpretation of the procedure is outlined, with the mathematical detail given in appendix C. For clarity consider the bottom

boundary, knowing that identical analysis can be carried out on the upper boundary. Consider a downward propagating plane wave, after N internal reflections, approaching the lower boundary at an angle θ. The refracted field at the boundary is then this field with the $1+\exp(i\Phi_1(\theta))$ transmission coefficient attached. The reflected field corresponding to this particular plane wave after interaction with the lower boundary is the N+1 reflected upward propagating field. Obviously there is an infinity of reflected and refracted plane wave fields. Thus to satisfy the lower boundary condition it must be demonstrated that any refracted field, which has undergone N internal reflections (where N is from 1 to ∞), must be equal to the upward field after N+1 reflections, and the Nth reflected downward field inside the guide evaluated on the boundary.

It now only remains to show how the geometrical interpretation and the mathematical analysis of the field can explain phenomena associated with this form of spectral construction.

4.2: The Geometrical Approach.

To be able to apply the FFT algorithm to evaluate the Intrinsic Mode integral it is essential that the infinite integral must be well approximated by a finite oscillatory integral. This section examines the spectral Intrinsic Mode integral and demonstrates that it can be calculated accurately for the approximations necessary when implementing the FFT algorithm. Using a consistent notation the Intrinsic Mode field in the Jensen–Kupermann ocean can be represented by – see chapter 2 –,

$$W_q(\underline{x}) = \begin{cases} \sum_{+-} \int_C e^{iS_q^{\pm}(\theta)} V_\theta^{\pm}(\underline{x})\, d\theta, & \underline{x} \in X \\ \int_C e^{iS_q^{-}(\theta)} \left[1 + e^{i\Phi_1(\theta)}\right] V_{1\,\theta_1}^{-}(\underline{x})\, d\theta, & \underline{x} \in X_1 \end{cases} \qquad (4.2.1)$$

Section 2.3 of chapter 2 demonstrates that there are essentially two possible contours C_a and C_b, with corresponding Euler–Maclaurin remainder types, over which the spectral Intrinsic Mode field can be integrated. Integrating over the contour C_a accounts for an upslope propagating field and over C_b downslope propagation. It was demonstrated in appendix A that the two E–M remainders are $O(\alpha^{\frac{1}{2}})$ along their respective contours and consequently in all subsequent analysis and assessment in this chapter these E–M remainders are neglected. The neglect of these remainder terms allows the two contours of Figure 2.3.2 of chapter 2 to be added together to give C as in Figure 4.2.1.

Figure 4.2.1 The Intrinsic Mode Contour

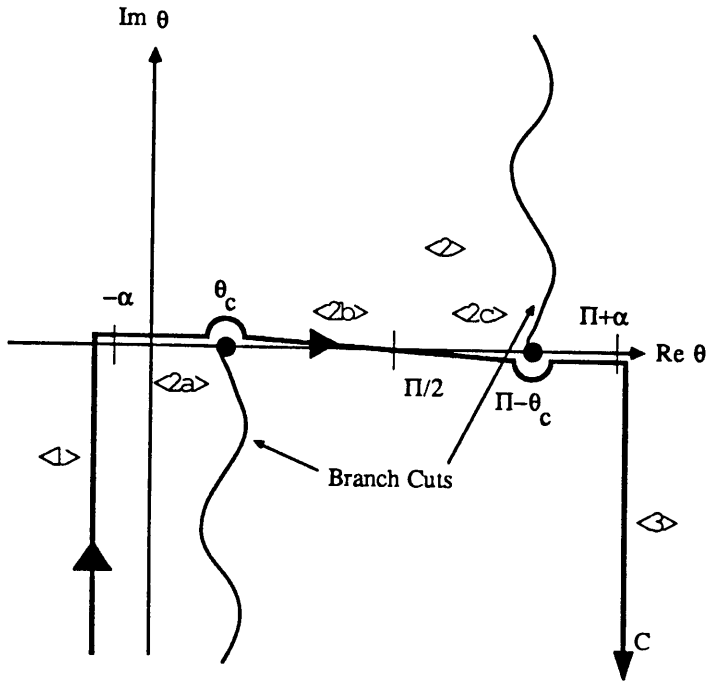

It is instructive to examine the nature of the plane wave fields along different portions of the contour C. The contour allows two different types of plane wave propagation to exist, essential for mathematical completeness, which give rise to the exactness property of the Intrinsic Mode. The field due to the two complex portions of the contour, <1> and <3>, represent inhomogeneous plane wave propagation, while the field due to the integration along the real axis gives rise to a homogeneous plane wave field inside the guide and both an inhomogeneous and homogeneous plane wave field outside the guide.

The inhomogeneous plane wave field has two forms of propagation associated with it. On the contours <1> and <3> the integrands of (4.2.1) are dominated by the exponential decay of the plane wave terms,

$$e^{-inkr\cos(\theta\pm\chi)} \quad \text{and} \quad e^{-in_1kr\cos(\theta_1-\chi)}$$

for observation points inside and outside the guide respectively. The integral over the interval <1> corresponds to the inhomogeneous plane wave field which propagates upslope and is obviously significantly less than the homogeneous contribution to the field, due to its exponential decay. The field arising from the interval <3> represents the inhomogeneous plane wave field which is propagating downslope because of a large number of internal reflections which have rotated the direction of the propagation.

The homogeneous plane wave propagation inside the guide has three distinct categories of propagation shown by <2a>, <2b> and <2c>. To aid clarity it is useful to examine these categories in the spectral domain. The diagram of Figure 4.2.2 indicates the forms of homogeneous wave propagation inside and outside the guiding duct.

Figure 4.2.2: Different Plane Wave Species of Region <2>

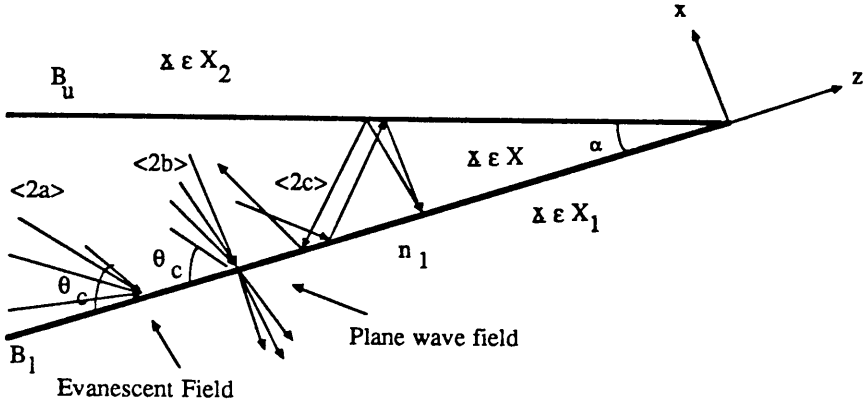

In region <2a>, ($\theta < \theta_c$) the plane waves are totally internally reflected (i.e. they are trapped in the higher index medium at the local cross–section). In this region there will be specific plane waves at angles, θ_q say, which interfere constructively to generate a modal field. The angles θ_q are asymptotically the local normal mode angles at the local observation cross–section (see later for verification). Outside the guide these modal angles produce an evanescent field. The remaining continuous spectra form ray bundles which decay in the usual manner, but are trapped inside the guide at this particular observation point and so give rise to inhomogeneous wave propagation outside the guide (as $\sin\theta_1$ is purely imaginary).

In the second region, <2b>, the plane waves can refract out into the lower medium and so leak energy out of the guiding layer. The greater the angle of incidence the greater the amount of energy which leaks out of the guide. The refracted field is truely plane wave in nature and will form ray bundles which will decay accordingly.

Region <2c> corresponds to plane waves which have travelled past the local cross–section towards the apex and have been rotated – by the angled boundaries – to such a degree that they are now travelling away from the wedge apex. The plane waves of region <2c> have undergone many reflections where the incident

angle is greater than θ_c and will consequently be carrying little energy in the guiding duct. The field outside the guide is homogeneous, but after a large number of reflections (and hence refraction loss) there is little energy present.

4.3: Mathematical Analysis of the Intrinsic Mode.

The geometrical interpretation given above – while convincing – requires some form of mathematical rigour, so that estimates of the order of magnitude of particular regions of the spectral function may be obtained. To facilitate analysis and for notational simplicity it is useful to note that the range parameter z can be asymptotically ordered in wedge angle α to,

$$z = -\frac{h}{\alpha}\left[\, 1 + O(\alpha^2) \,\right] \tag{4.3.1}$$

with h being the local hieght of the guide. This leads to an asymptotic form of the Intrinsic Mode,

$$W_q(\underline{x}) \sim \begin{cases} \sum_{+-} \int_C F^{\pm}(\theta)\, e^{\frac{iZ_q(\theta)}{\alpha}}\, d\theta, & \underline{x} \in X \\ \int_C F^{o}(\theta)\, e^{\frac{iZ_q(\theta)}{\alpha}}\, d\theta, & \underline{x} \in X_1 \end{cases} \tag{4.3.2a}$$

with,

$$Z_q(\theta) \sim \frac{\Pi\theta}{2} + \frac{1}{2}\int_{\theta_c}^{\theta} \Phi_1(s)ds - q\Pi\theta - nkh\cos\theta \tag{4.3.2b}$$

and

$$F^{\pm}(\theta) = e^{i\left[\, \pm\frac{\Phi_1(\theta)}{2} - \frac{\Pi}{2} \pm nkx\sin\theta \,\right]} \tag{4.3.2c}$$

$$F^{o}(\theta) = \left[\, 1 + e^{i\Phi_1(\theta)} \,\right] e^{i\left[\, -\frac{\Phi_1(\theta)}{2} - \frac{\Pi}{2} - n_1 kx\sin\theta_1 \,\right]} \tag{4.3.2d}$$

The Euler–Maclaurin remainder term is omitted for the reasons discussed in section

4.2. The asymptotic analysis of the Intrinsic Mode field is achieved by examining three different local cross–sections of the guide (i.e. the field as the observation point moves upslope). There are fortunately several different ways to view the same phenomena and in this section these approaches will be blended together to form a coherent picture of the wave field structure. The approach will be as mathematically sparse as possible so that concepts can be discussed clearly. However, most of the results are of significant importance and the derivations are placed in appendices.

4.3.1: A Well Guided Local Normal Mode.

Firstly consider an observation point in a particular cross–section with local guide height (h) large enough to support the local normal mode of interest. In a translationally invariant guide this mode would consist of two counter–propagating plane waves with an angle of incidence θ_q to the lower boundary which interfere. This modal angle is obtained from the standard eigenvalue equation for open waveguides. To calculate the asymptotic field in the wedge, for small wedge angle, the method of steepest descents [32] is applied and the appropriate deformation of the contour C is shown in Figure 4.3.1.1.

Figure 4.3.1.1: Steepest Descent Paths of the Intrinsic Mode when the Adiabatic Mode is well guided.

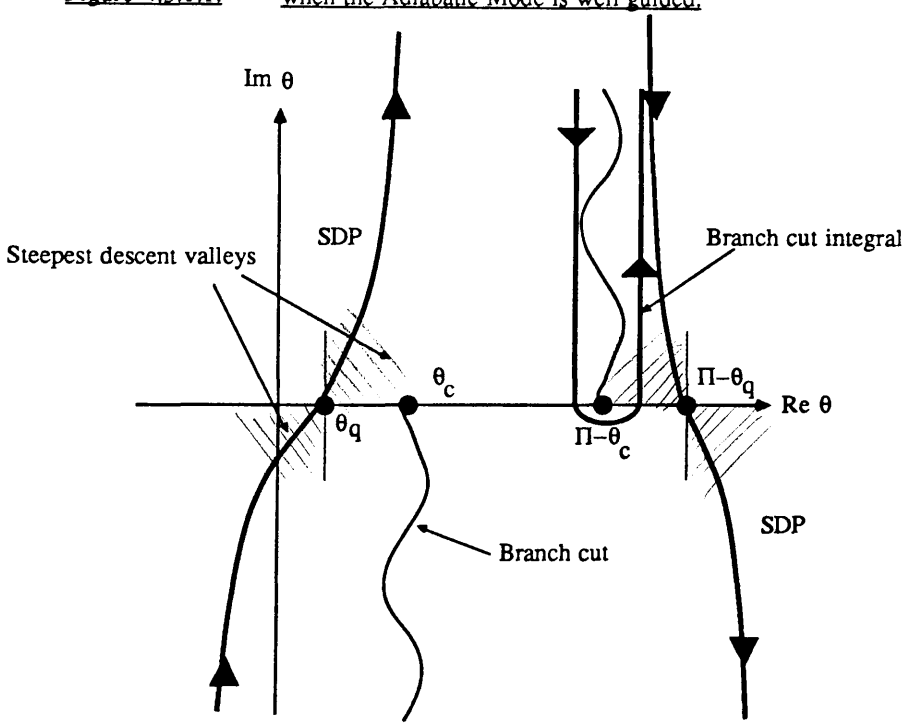

The steepest descent sectors around a stationary point, θ_s, are easily found by using the conditions,

$$\text{Imag}\left[\frac{d^2 Z_q(\theta_s)}{d\theta^2}(\theta-\theta_s)^2 \right] > 0$$
$$\text{Real}\left[\frac{d^2 Z_q(\theta_s)}{d\theta^2}(\theta-\theta_s)^2 \right] = 0 \qquad (4.3.1.1)$$

These steepest descent regions are shown as the shaded sectors in Figure 4.3.1.1. Due to the symmetry of the reflection coefficient there are two stationary phase points at θ_q and $\Pi - \theta_q$ which are defined by

$$\frac{dZ_q(\theta_s)}{d\theta} = 0 \qquad (4.3.1.2a)$$

where θ_s is either θ_q or $\Pi - \theta_q$. Using (4.3.2b) gives the condition,

$$\Pi + \Phi_1(\theta_q) + 2nkh\sin\theta_q = 2q\Pi \qquad (4.3.1.2b)$$

The above condition is also recognisable as the eigenvalue equation for the transverse wave number of the local parallel guide. When the local normal mode is well guided, $\theta_q < \theta_c$ the asymptotic field to first order in wedge angle can be evaluated by considering the isolated stationary phase points θ_q and $\Pi - \theta_q$, and the branch cut integral around $\Pi - \theta_c$. The asymptotic description of the upslope propagating field is, from appendix D,

$$W_q(\underline{x}) = \begin{cases} \left[\frac{8\Pi\alpha}{-\frac{d^2 Z_q}{d\theta^2}(\theta_q)} \right]^{\frac{1}{2}} e^{\frac{iZ_q(\theta_q)}{\alpha} - \frac{i\Pi}{4}} \sin\left[[h-x]nk\sin\theta_q \right], & \underline{x} \in X \\ \left[\frac{8\Pi\alpha}{-\frac{d^2 Z_q}{d\theta^2}(\theta_q)} \right]^{\frac{1}{2}} e^{\frac{iZ_q(\theta_q)}{\alpha} - \frac{i\Pi}{4}} \sin\left[nkh\sin\theta_q\right] e^{-inkx\sin\theta_{q_1}}, & \underline{x} \in X_1 \end{cases} \qquad (4.3.1.3)$$

Here θ_{q_1} is the refracted stationary phase point angle. This asymptotic form can be shown [39] to be equal to the Adiabatic Mode of Pierce (chapter 1 equation (1.1.9)), by using the procedure in appendix D. It was stated previously that the field due to the stationary phase point at $\Pi - \theta_q$ and the branch cut integral at $\Pi - \theta_c$, correspond to the Adiabatic Mode and the lateral ray field propagating downslope respectively. The plane waves that constitute these phenomena are indicated in Figure 4.2.2, where physically it is obvious that they must be significantly smaller than the upslope asymptotic field because of the large accumulated refraction loss. It can be shown (appendix D) that the downward asymptotic field amplitude and phase from the stationary phase point at $\Pi - \theta_q$ are,

$$\left[\frac{8\Pi\alpha}{\frac{d^2Z_q(\theta_q)}{d\theta^2}+R(\theta_q)}\right]^{\frac{1}{2}} e^{\frac{-iZ_q(\theta_q)}{\alpha}-i\frac{\Pi}{4}} \exp\, i\left[\frac{\Pi^2}{2}(1-2q) + \frac{1}{2\alpha}\sum_{q=-\infty}^{\infty}\int_{\theta_c}^{\Pi-\theta_c} \Phi_1(s)e^{\frac{iq\Pi(s-\theta)}{\alpha}}\, ds\right]$$

This extra integral term has a large positive imaginary part which confirms the physical predictions of the nature of the fields. Note also the change of sign of the phase indicating an outward propagating field. The branch cut integral at $\Pi-\theta_c$ arises when $\theta_q<\theta_c$ because the observation point must be downslope of the point at which the mode couples to the lateral wave. The previous arguments allow the asymptotic field to consist of only upslope propagation and consequently the fields due to the stationary phase point $\Pi-\theta_q$ and the branch cut integrals at $\Pi-\theta_c$ are neglected, but will be formally retained in the steepest descent analysis to demonstrate the completeness of the theory. A visual demonstration of the above arguments can be seen numerically by examination of the real part of the downward spectrum against incident angle for observation points inside and outside the guide (depicted in Figure 4.3.1.2).

Figure 4.3.1.2:

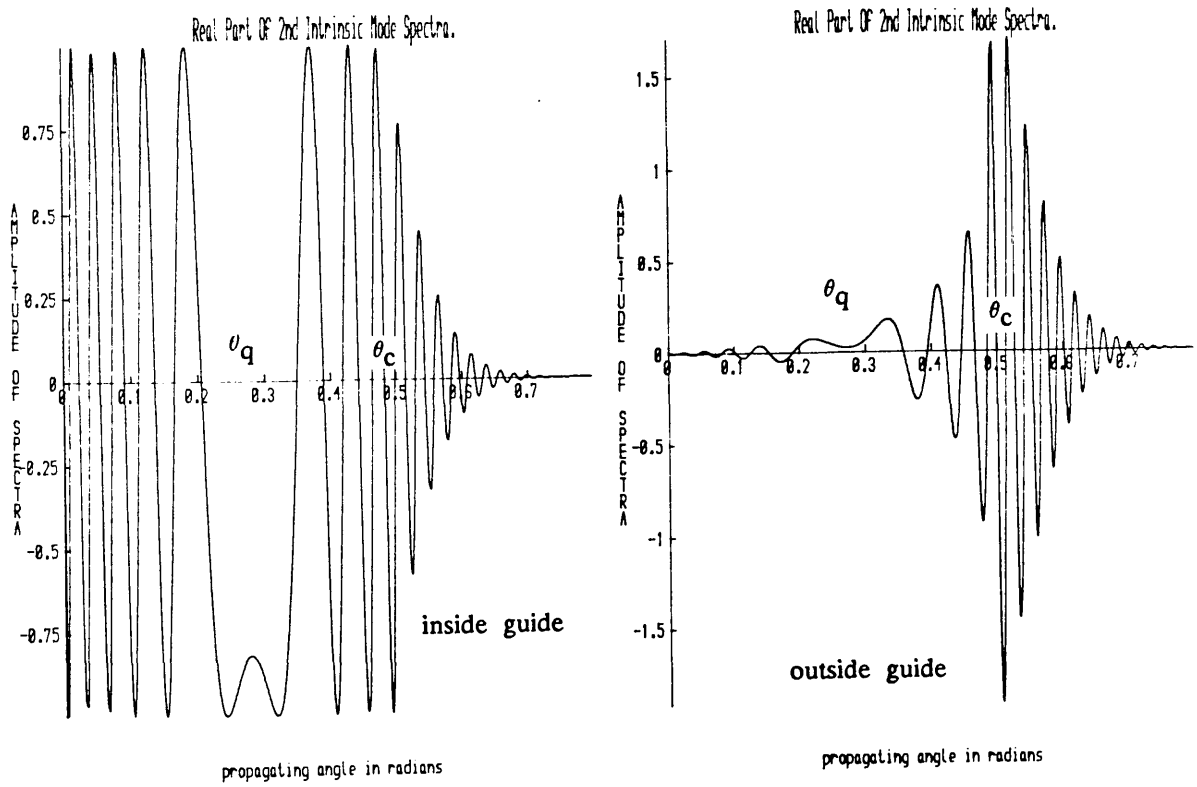

The Intrinsic Mode field at this cross–section was calculated using and x 'directed' FFT routine. For observation points inside the guide a lower endpoint correction, evaluated using Laplace's method in appendix D was added to the field. This addition is necessary because when employing the FFT method the integrand should be negligible outside the interval of integration. The diagram of Figure 4.3.1.2 indicates clearly that this necessity is not met for points inside the guide, but if the endpoint is a sufficient distance from the stationary phase point the endpoint correction in appendix D will be a good approximation to the remaining field not accounted for by the FFT algorithm. The field at this cross–section is shown in Figure 4.3.1.3.

Figure 4.3.1.3:

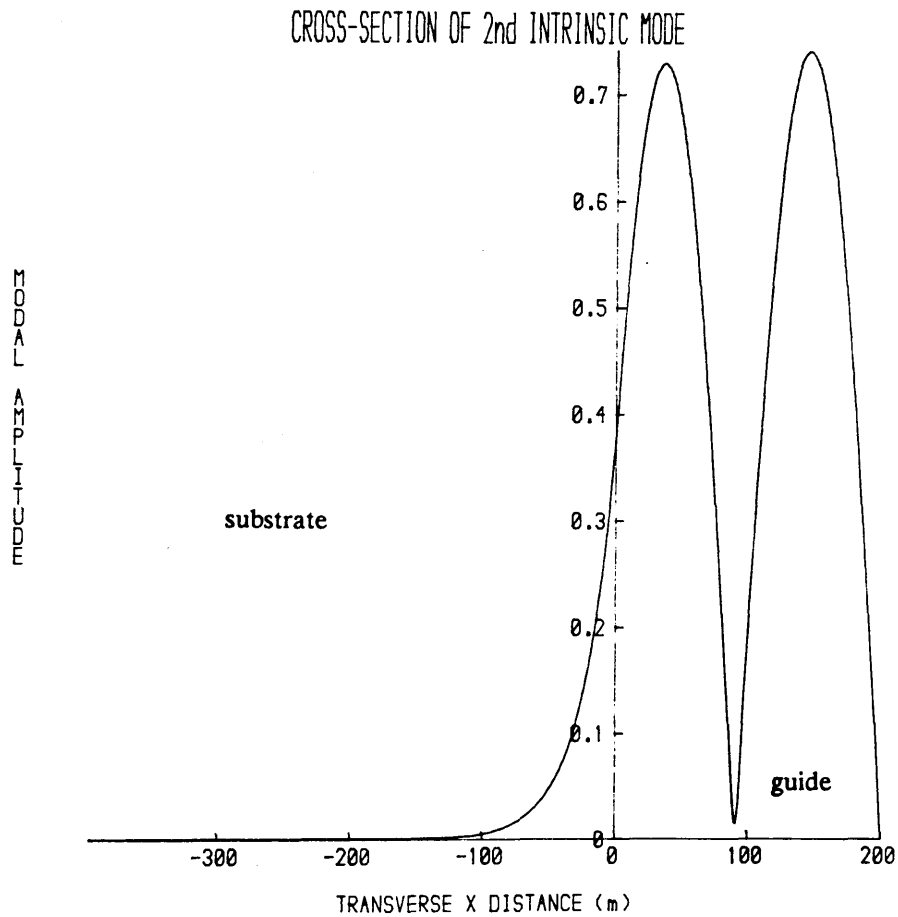

4.3.2: The Critical Transition Region.

In configuration space this region corresponds to the local guide height approaching the critical hieght h_c for the particular mode; the critical height being where the local structure will no longer support that mode. In spectral terms this is when the stationary phase point lies close to the branch point of the reflection coefficient (i.e. $\theta_q \approx \theta_c$). The asymptotic analysis is slightly more complicated than before because the effect of the branch point must be accounted for; this being interpreted as the region in which the Intrinsic Mode couples to the lateral ray. The contour deformed into its Steepest Descent Path (SDP) is shown in Figure 4.3.2.1.

Figure 4.3.2.1: Steepest Descent Paths of the Intrinsic Mode in the Critical transition region.

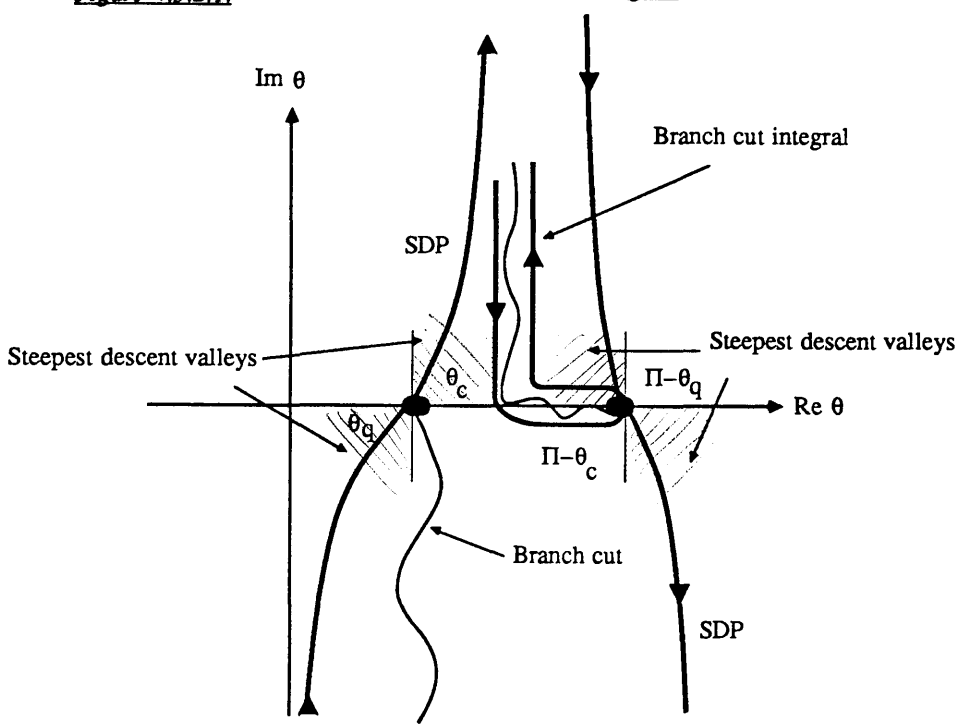

In this region the asymptotic analysis is eased greatly by mapping the $\theta-$ plane to the t− plane via the function $t = \sqrt{(\theta - \theta_c)}$, which transforms the branch point in the $\theta-$ domain into a saddle point, at $t = 0$, in the t− plane. Using the method of Chester, Friedman and Ursell [2] a uniform asymptotic expansion, with respect to α, can be obtained. The upslope field inside the guide (from appendix E) in this region is approximated by,

$$W_q(\underline{x}) = \sum_{\pm} \frac{F^{\pm}(\theta_c)\alpha}{2Z_q'(\theta_c)} e^{\frac{iZ_q(\theta_c)}{\alpha}} \left[\frac{6}{\alpha(2\cot\theta_c)^{\frac{1}{2}}} \right] \int_{C_s} Se^{-iBS^2/2 - S^3/3} dS \qquad (4.3.2.1)$$

Again plotting the real part of the downgoing Intrinsic Mode field for observation points inside and outside the guide, at a cross–section within the critical transition region is given in Figure 4.3.2.2.

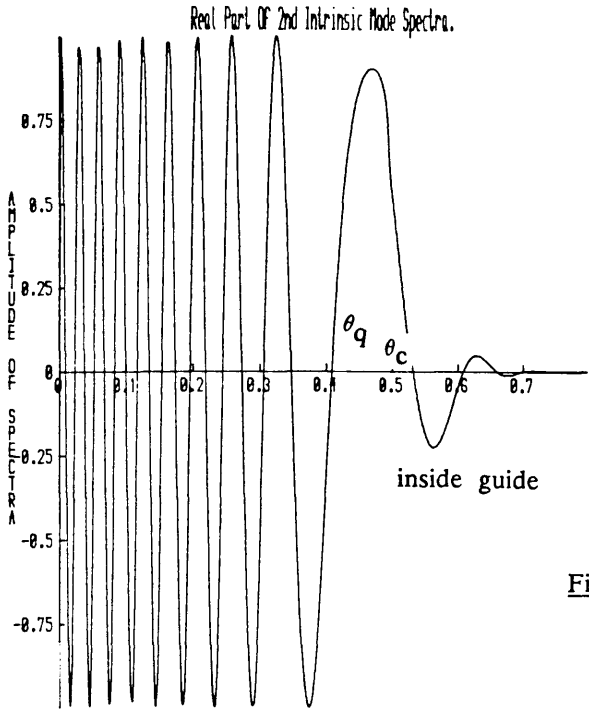

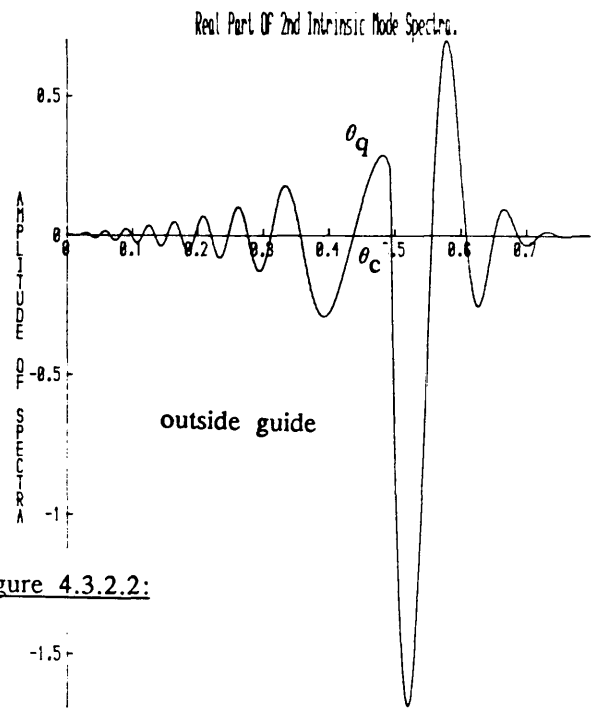

Figure 4.3.2.2:

From the above diagrams it is obvious that the dominant contribution to the field in this region is the plane waves propagating at angles around the critical angle θ_c. The field in this region was numerically calculated using the method outlined in the section 4.3.1 and is shown in Figure 4.3.2.3.

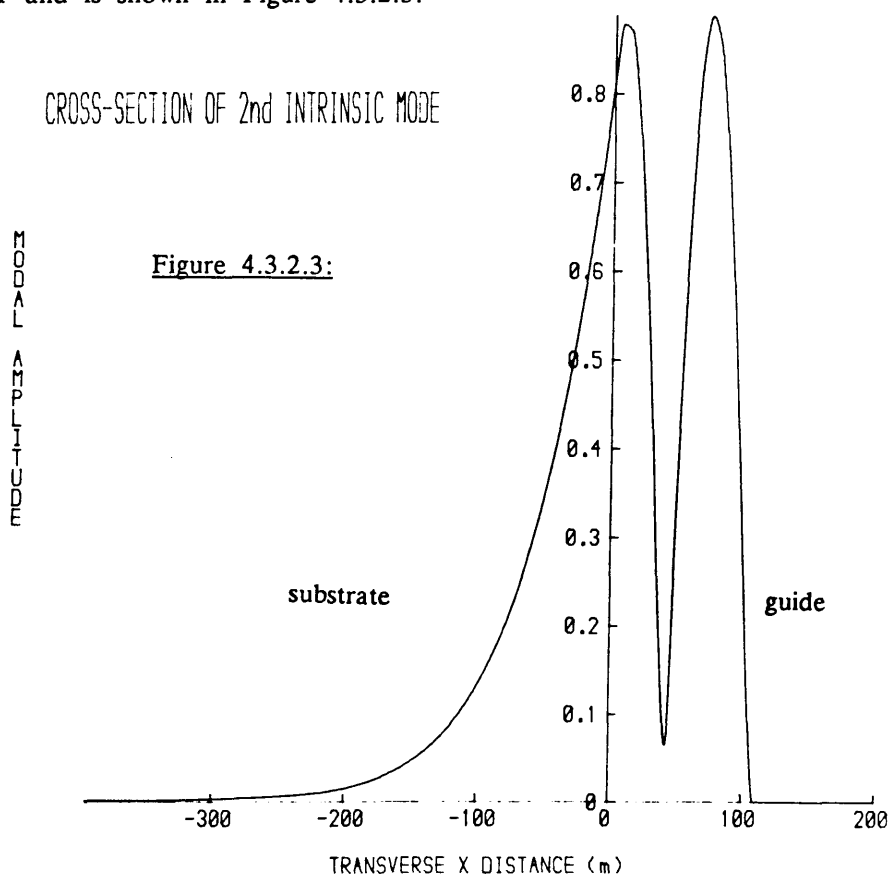

Figure 4.3.2.3:

4.3.3: The Radiating Regime.

In this situation the local guide height is less than the critical height for that particular mode and the local normal mode no longer exists. In this region the stationary phase point becomes complex and $\theta_q > \theta_c$ and $\mathrm{Im}(\theta_q) < 0$ to maintain exponential decay in the propagating direction. The diagrams of Figure 4.3.3.1 show the steepest descent paths for this particular region in the wedge environment.

Figure 4.3.3.1: Steepest Descent Paths of the Intrinsic Mode for the Radiating regime

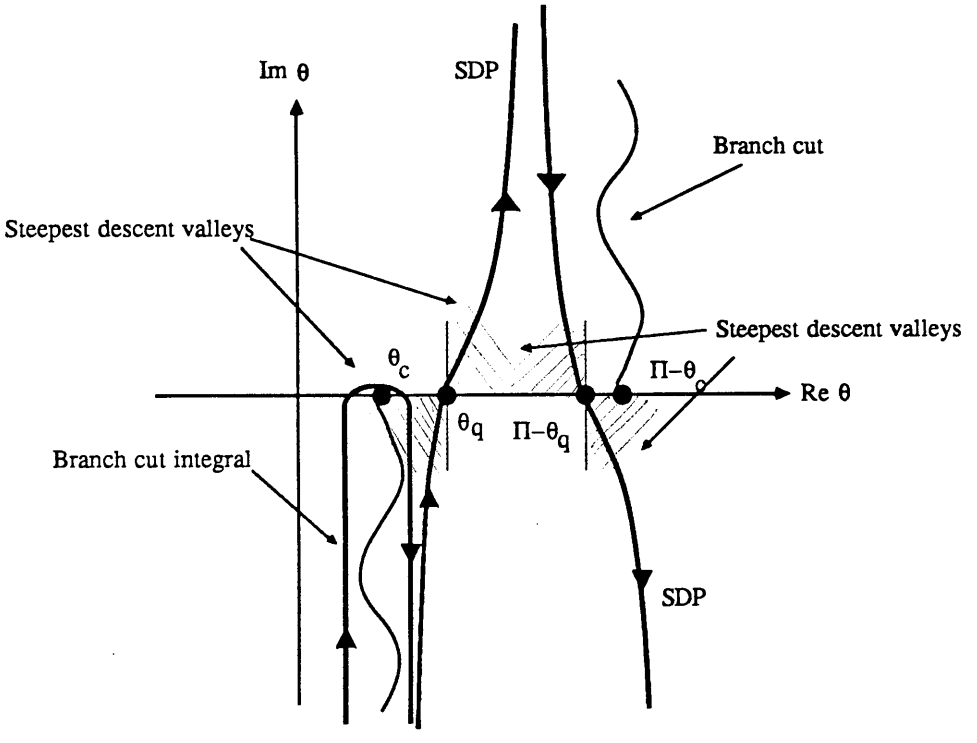

In this radiating regime θ_q and θ_c are isolated points which are then amenable to separate analysis. The branch cut integral term, which represents the launching of a lateral ray, is retained in the asymptotic expression for the field, as θ_q is now a complex solution of the transverse resonance condition giving rise to a decaying field. The calculation of the lateral ray field using the stationary phase point method, inside the guide is easily achieved [39]. The real part of the downward field contribution to the Intrinsic Mode, as a function of angle of incidence, for observation points inside and outside the guide is given in Figure 4.3.3.2.

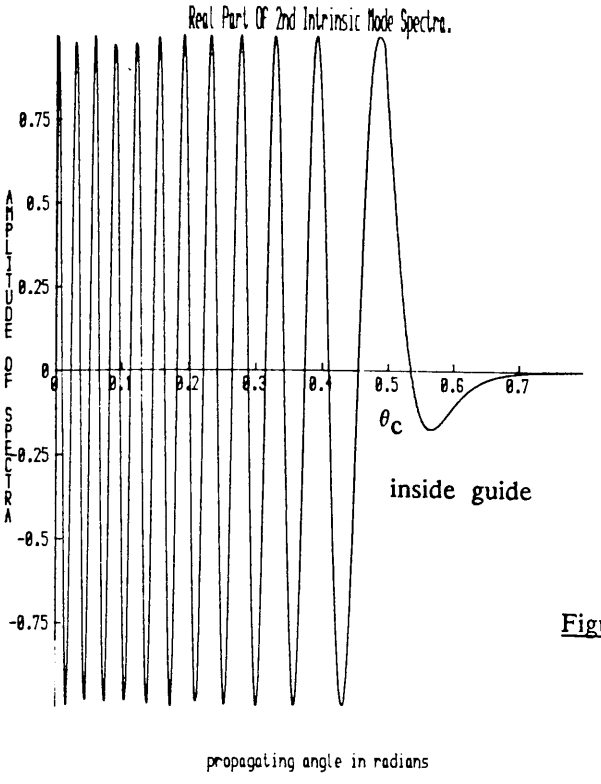

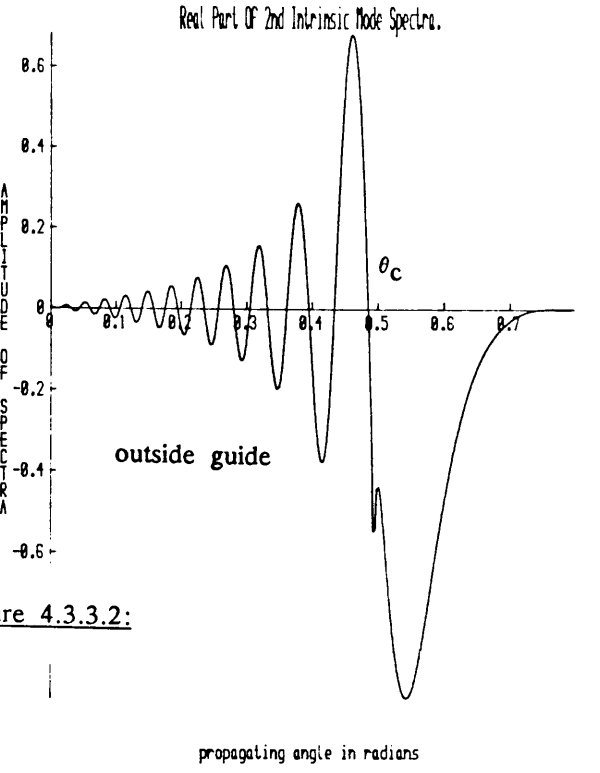

Figure 4.3.3.2:

It is observed that the rapid oscillation of these integrands implies that the contribution to the field is from plane waves around the critical angle, which is in agreement with the asymptotic analysis. Also, it is interesting to note that there is no longer a branch cut integral at $\Pi - \theta_c$ as the observation point now lies upslope of this lateral ray launch. The field in this region is mostly outside the guide (see Figure 4.3.3.3).

Figure 4.3.3.3:

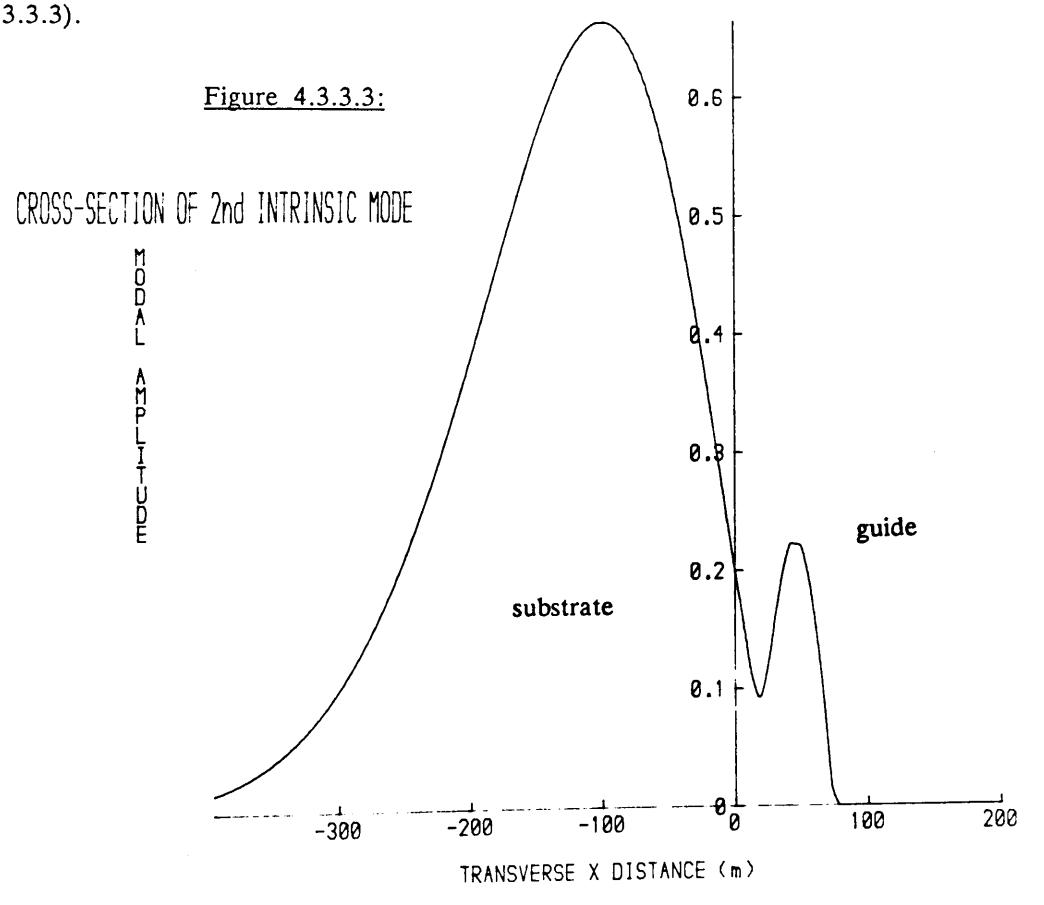

Conclusion.

In this chapter, the physical significance and numerical confirmation of the asymptotic analysis of the Intrinsic Mode field have been given, by firstly examining the nature of the plane wave fields on each different segment of the contour C. Although the physical significance of the fields is of prime concern in this chapter it is important to stress that these asymptotic forms agree with the analysis of Pierce [20] and that of Kamel and Felsen [55].

The numerical computation of the field at a local cross–section was achieved by using the x 'directed' FFT. The interval of integration was from 0 to .8 radians along the real axis and the CPU time required to generate a fifty data point field was about fifteen seconds, making the routine as efficient as the algorithms used by Xiang [5]. This however is not the most efficient method of calculation because of the necessity to calculate the evanescent field using Bode's rule. The transverse field profiles generated by Dendane and Arnold [6] using a standard integration rule, for the Jensen – Kuperman ocean were calculated using the above FFT direction and were found to be in good agreement.

Introduction.

This chapter is concerned with the propagation of pure Intrinsic Mode fields, using the numerical algorithms discussed in chapter 3, throughout different wedge environments. Obviously there is a plethora of wedge configurations that could be investigated. However, to indicate succinctly the differences between field propagation methods requires only a limited number of pure Intrinsic Mode geometries. In the chosen structures, of either Integrated Optics or Ocean Acoustics, the diffracted field from the apex is ignored so that the source free field can be represented as in chapter 2 by,

$$W_q(\underline{x}) = \begin{cases} \sum_{+-} \int_{C^{\pm}} e^{iS_q^{\pm}(\theta)} e^{-ikr\cos(\theta \pm \chi)} d\theta, & \underline{x} \in X \\ \int_{C^-} e^{iS_q^-(\theta)} \left[1 + e^{i\Phi_1(\theta)}\right] e^{-in_1 kr\cos(\theta-\chi)} d\theta, & \underline{x} \in X_1 \\ \int_{C^+} e^{iS_q^+(\theta)} \left[1 + e^{i\Phi_u(\theta+\alpha)}\right] e^{-in_2 kr\cos(\theta+\chi)} d\theta, & \underline{x} \in X_2 \end{cases} \qquad (5.1a)$$

with,

$$S_q^-(\theta+2\alpha) = \frac{\Phi^-(\theta)}{2} + \frac{1}{2\alpha} \int_{\theta_c}^{\theta} \Phi^-(s)ds - \frac{q\Pi\theta}{\alpha} + E_b^-(\theta, \theta_q) \qquad (5.1b)$$

and,

$$S_q^+(\theta) - S_q^-(\theta) = \Phi_1(\theta),$$
$$\Phi^-(\theta) = \Phi_1(\theta) + \Phi_u(\theta+\alpha), \qquad n\cos\theta = n_1\cos\theta_1. \qquad (5.1c)$$

The neglect of the diffracted field from the apex means that the Intrinsic Mode does not satisfy the boundary conditions in the vicinity of the apex. The only configuration–dependent quantities are the reflection coefficients at the two infinite planar interfaces. A brief summary of the derivation of these spectral functions is now given for the Integrated Optical and Ocean Acoustical wave propagation environments.

Using appropriate scaling of wavelength and configuration space scales; optical fields can be transformed into acoustical fields and vice versa. It can thus be argued

that the type of wave phenomena discussed is independent of the actual wave field in these cases and as such actual physical dimensions are unimportant. This approach has been used by Xiang, Cada and Felsen [5], but it loses some physical contact as all scales are normalised to wavelength. In this exposition this approach has not been adopted so that a demonstration of the true dimensions of the fields can be given, with the knowledge that it is trivial to convert acoustical fields to optical fields in the manner discussed above. Sections 5.1 and 5.2 show qualitative plots of both optical and acoustical fields. The qualitative statements made in these sections are quantified in section 5.3. Section 5.4 discusses an essential numerical calculation of power, necessary for demonstrating that the Intrinsic Mode is an exact solution of the elliptical wave equation.

5.1: Derivation Of The Optical Boundary Conditions.

There are two types of electromagnetic propagation of interest, that of TE and TM propagation in linear isotropic dielectric media. A brief derivation of the spectral boundary conditions for each type of propagation is given. Consider the diagram of Figure 5.1.1, where the interface between the two media lies along $x = 0$ and the plane of incidence is the $xz-$ plane.

Figure 5.1.1: Plane Wave Striking an Infinite Planar boundary

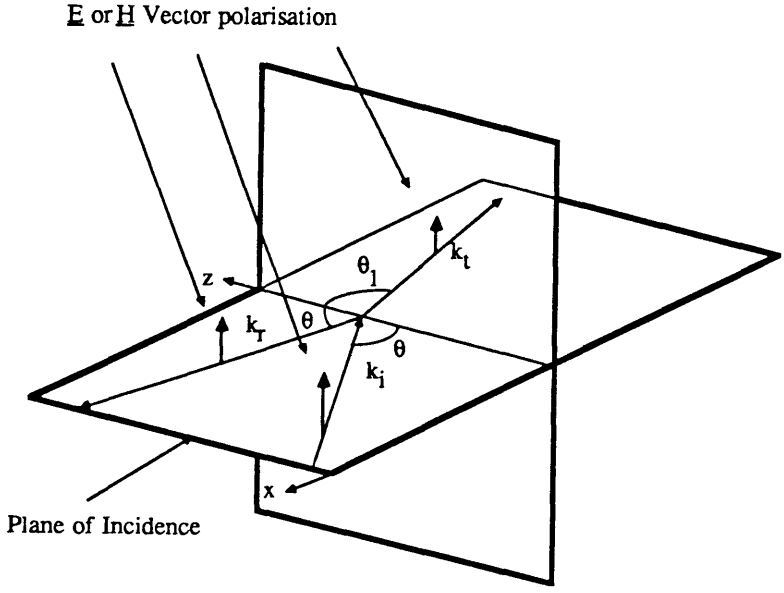

Let the incident field be plane polarised so that its $\underline{E}$ field is perpendicular to the plane of propagation. This field can be represented by,

$$\underline{E}_i = \underline{j}E_i e^{i\underline{k}_i \cdot \underline{r} - i\omega t} \tag{5.1.1}$$

where E_i may be complex and $\underline{j}$ is the unit vector in the y direction. The reflected and refracted fields may be similarly represented by,

$$\underline{E}_r = \underline{j}E_r e^{i\underline{k}_r \cdot \underline{r} - i\omega t} \qquad \underline{E}_t = \underline{j}E_t e^{i\underline{k}_t \cdot \underline{r} - i\omega t} \tag{5.1.2}$$

respectively. The two boundary conditions needed to evaluate the spectral reflection coefficients are that the tangential components of the $\underline{E}$ and $\underline{H}$ field must be continuous [57]. The first condition gives,

$$E_i e^{i\underline{k}_i \cdot \underline{r}} + E_r e^{i\underline{k}_r \cdot \underline{r}} = E_t e^{i\underline{k}_t \cdot \underline{r}} \tag{5.1.3}$$

If this equation is to be consistent for every point in the interface then,

$$\underline{k}_i \cdot \underline{r} = \underline{k}_r \cdot \underline{r} = \underline{k}_t \cdot \underline{r} \qquad \underline{r} \in \{x=0\} \tag{5.1.4}$$

this being the vector representation of Snell's law. The second condition, regarding the $\underline{H}$ field can be transformed using,

$$\nabla \wedge \underline{E} = -\frac{\partial \underline{B}}{\partial t} \tag{5.1.5}$$

into a condition for $\underline{E}$ which is that the continuity of the tangential component of

$$\frac{1}{i\omega\mu_0}\frac{\partial \underline{E}}{\partial x} \tag{5.1.6}$$

must be conserved. Applying this condition and using equation (5.1.3) leads to the expression of the Fresnel reflection coefficient for an $\underline{E}$ field perpendicular to the plane of incidence to be,

$$\frac{E_r}{E_i} = e^{i2\tan^{-1}\left[\frac{in_1\sin\theta_1}{n\sin\theta}\right]} \tag{5.1.7}$$

When the $\underline{E}$ field is parallel to the plane of incidence (no component of the $\underline{E}$ field is in the y direction) it is easier to consider the $\underline{H}$ field, which will be normal to the plane of incidence. As the tangential components of the $\underline{H}$ field must be continuous the same equation as (5.1.3) is obtained when $\underline{E}$ is interchanged with $\underline{H}$. To satisfy the continuity requirements of the $\underline{E}$ field in terms of $\underline{H}$ requires the use of,

$$\nabla_{\wedge}\underline{H} = \epsilon_0\epsilon_r\frac{\partial\underline{E}}{\partial t} \qquad (5.1.8)$$

This then has the condition on the $\underline{H}$ field that the tangential components of,

$$\frac{1}{i\omega\mu_0\epsilon_0\epsilon_r}\frac{\partial\underline{H}}{\partial x} \qquad (5.1.9)$$

must be continuous across the interface. Applying (5.1.9) and the analogy of (5.1.3) for the $\underline{H}$ field and implementing (5.1.8) gives the reflection coefficient for $\underline{E}$ fields parallel to the plane of incidence as,

$$\frac{E_r}{E_i} = e^{i2\tan^{-1}\left[\frac{in\sin\theta_1}{n_1\sin\theta}\right]} \qquad (5.1.10)$$

These derivations of the spectral boundary conditions for the two modes of propagation now fully specify the electromagnetic field anywhere in the two–dimensional structure, excluding the apex. There is little difference in the reflection coeffients for the TM and TE propagation if a weak guiding regime is considered and this is demonstrated in the field plots.

5.2: FFT Evaluation Of Optical Intrinsic Modes.

The fields of this section have a free space wavelength of 1.55μm, a semiconductor laser line, and the taper angle is 3^0. All the optical fields calculated in this section are evaluated using the B type field routines, with the appropriate endpoint corrections described in the previous chapter. This type of field calculation shows clearly the advantage of greater efficiency of the FFT approach over conventional integration methods. The Intrinsic Mode field for these types of geometries using a standard integration technique would take approximately ten seconds of CPU time to produce fifty data points [5]. Employing the FFT method a data grid of 256 transverse points by 512 longitudinal points could be generated in under two minutes. In fact altering the number of longitudinal data points does not greatly effect run times, as the rate determining step in the program is the calculation of the spectral integrand over the desired spectral interval and not the time taken for the FFT routine. In the plots shown below the number of transverse and longitudinal field points is 256 and 1024 respectively. There is redundancy generated in these field constructions because of the large number of points obtained from the FFT algorithms and although this increases run times to around 4 minutes, better accuracy is attained. If a direct application of the type B method of solution is used the lower boundary of the guide will be parallel to the upper boundary of

plot. To construct the field so that the upper boundary is parallel to the upper boundary of the plot (the standard representation of the fields) requires the interchanging of the substrate and superstrate indices which also reduces efficiency.

Consider a strong asymmetry in the guiding structure where the guide index is 1.54, substrate index is 1.2 and the superstrate index is 1.47. The diagrams in Figures 5.2.1 are of fields when the electric vector is perpendicular to the plane of incidence (TE). The plots are normalised by taking the peak height of the field on the initial plane as one, and all contours are in −4dB intervals from 0dB (all contour plots have this interval). The diagrams in Figure 5.2.2 show the Intrinsic Mode field in the above described geometry with the electric vector parallel to the plane of incidence (TM).

Figure 5.2.1(a):

TE field plots

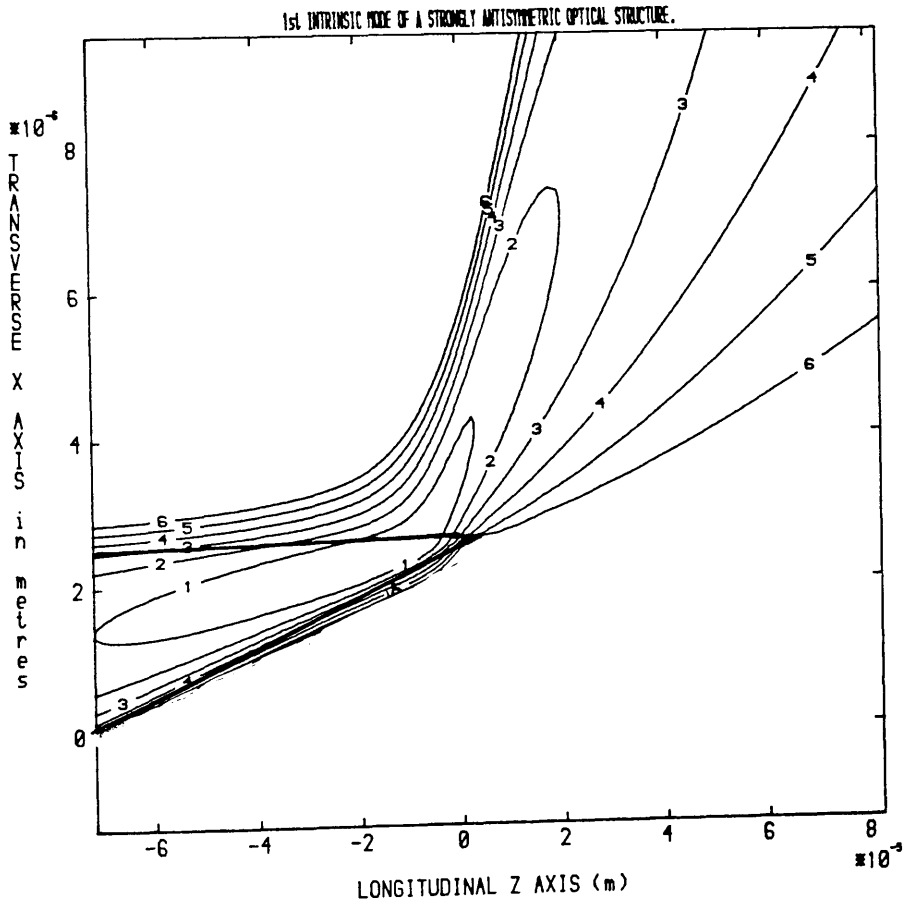

Figure 5.2.1(b):

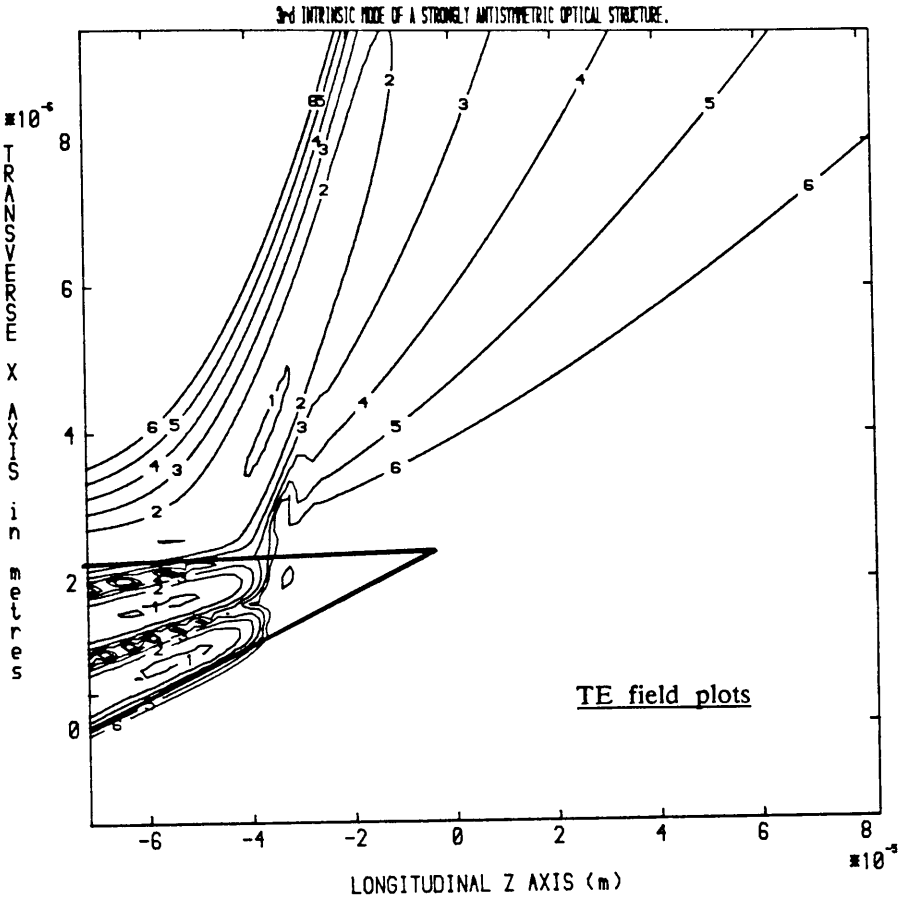

Figure 5.2.1(c):

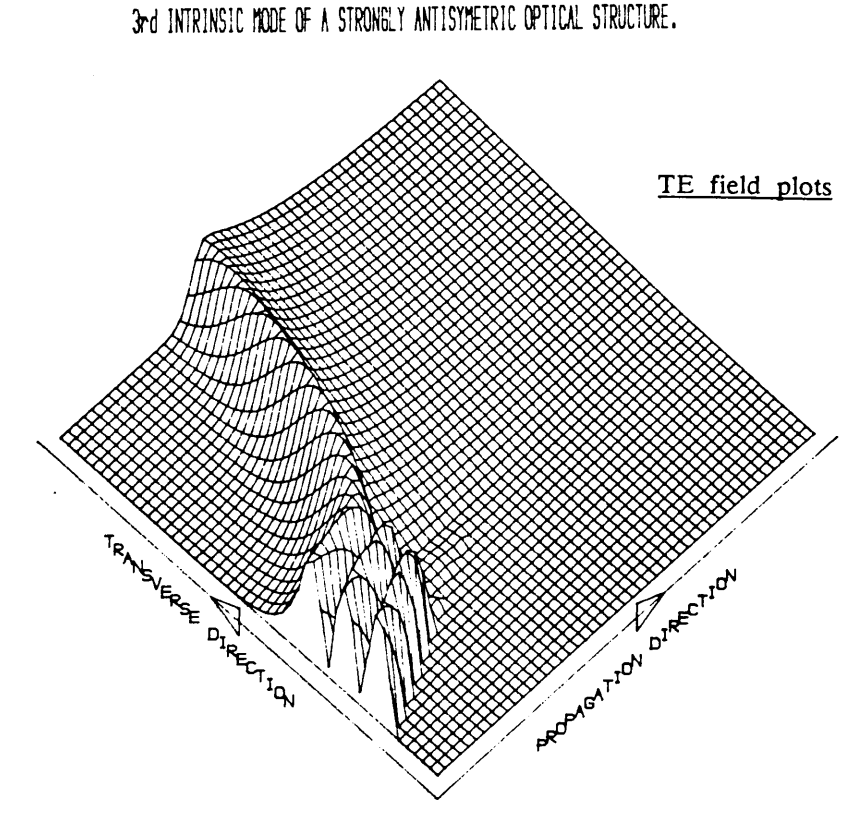

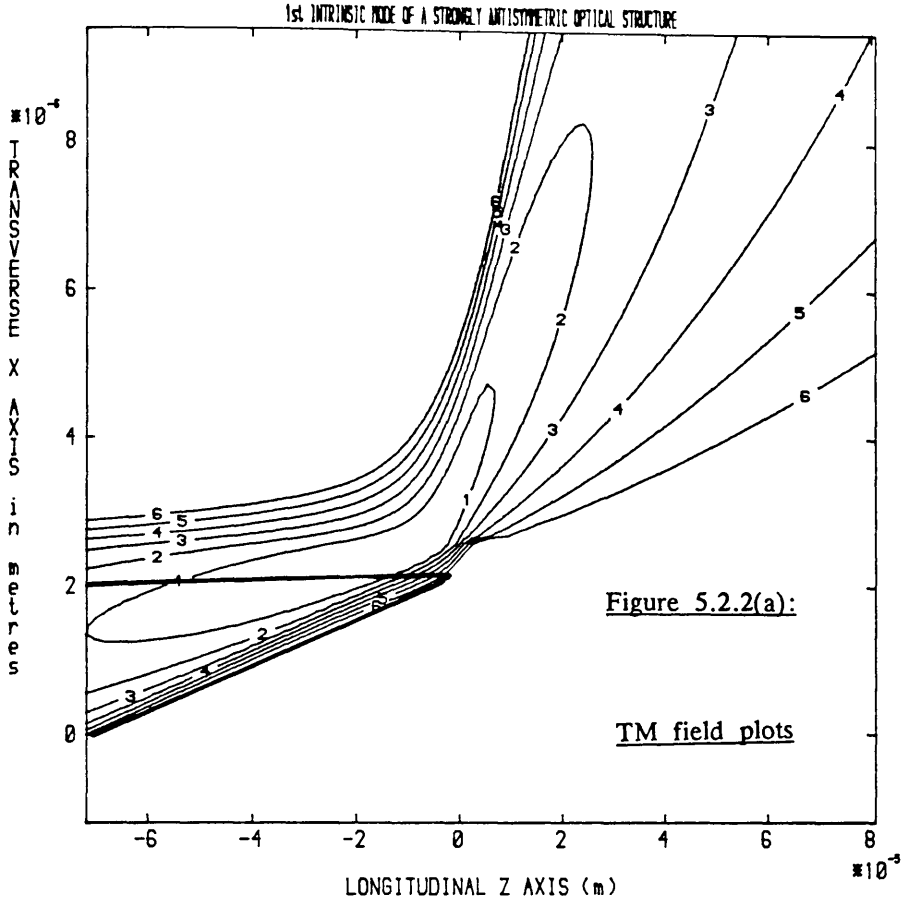

Figure 5.2.2(a):

TM field plots

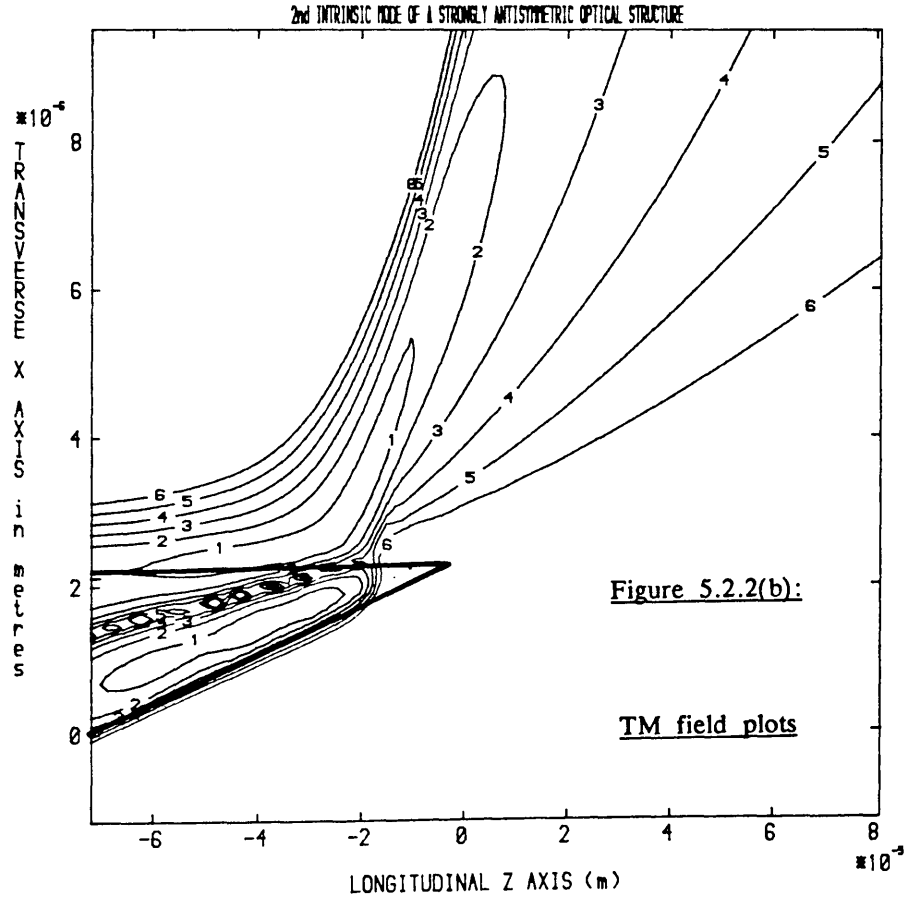

Figure 5.2.2(b):

TM field plots

From these field plots the power transfer of the fields from the guide to the substrate occurs around the critical height for the corresponding Adiabatic Mode defined in this case by

$$h_c = \frac{(q - \frac{1}{2})\Pi - \Phi(\theta_{ci}+\alpha)}{k(n^2 - n_i^2)^{\frac{1}{2}}} \qquad (5.2.1)$$

where i=1,2 depending on which is the higher index of n_i and $\Phi(\theta_{ci}+\alpha)$ is the phase of the reflection coefficient at the interface with the larger refractive index change and θ_{ci} is the critical angle at the other boundary. The phenomenon is as expected from chapter 4 as the asymptotic forms to first order are the Adiabatic Mode fields in the guiding region. Figures 5.2.3(a), 5.2.3(b) shows the Intrinsic Mode field of a weakly asymmetric structure where the guide index is as before and the substrate index and the superstrate index are 1.47 and 1.5 respectively. Both TE and TM propagation are shown.

Figure 5.2.3(a)

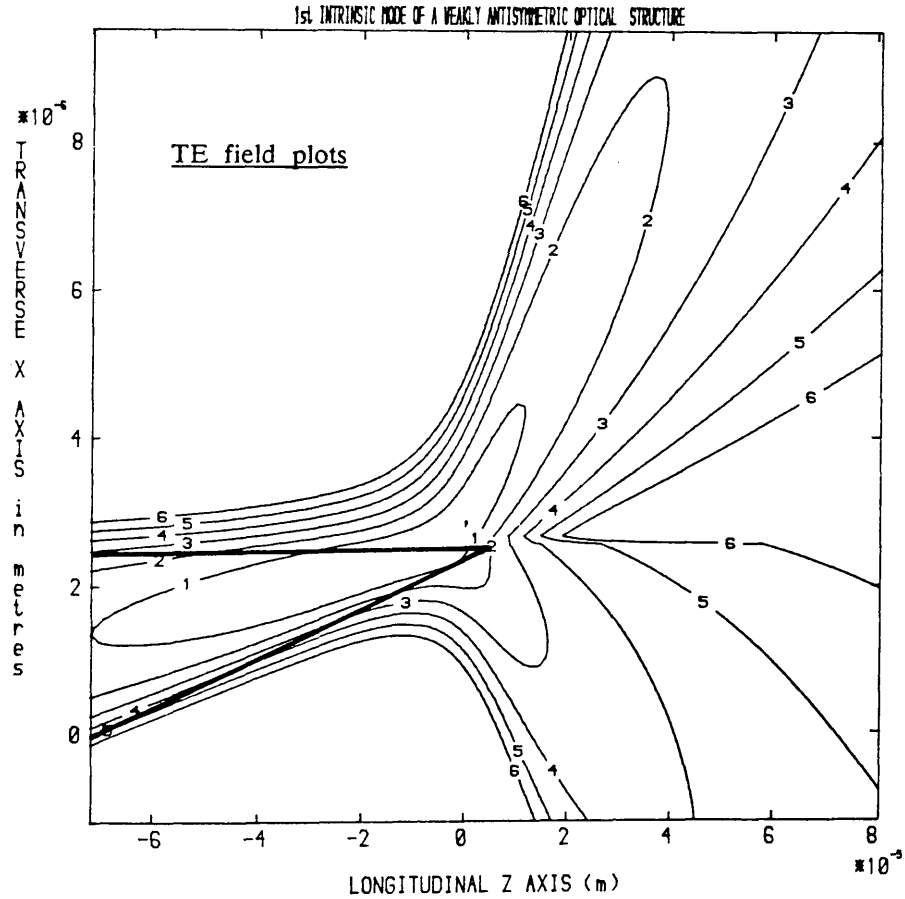

Figure 5.2.3(b):

TM field plots

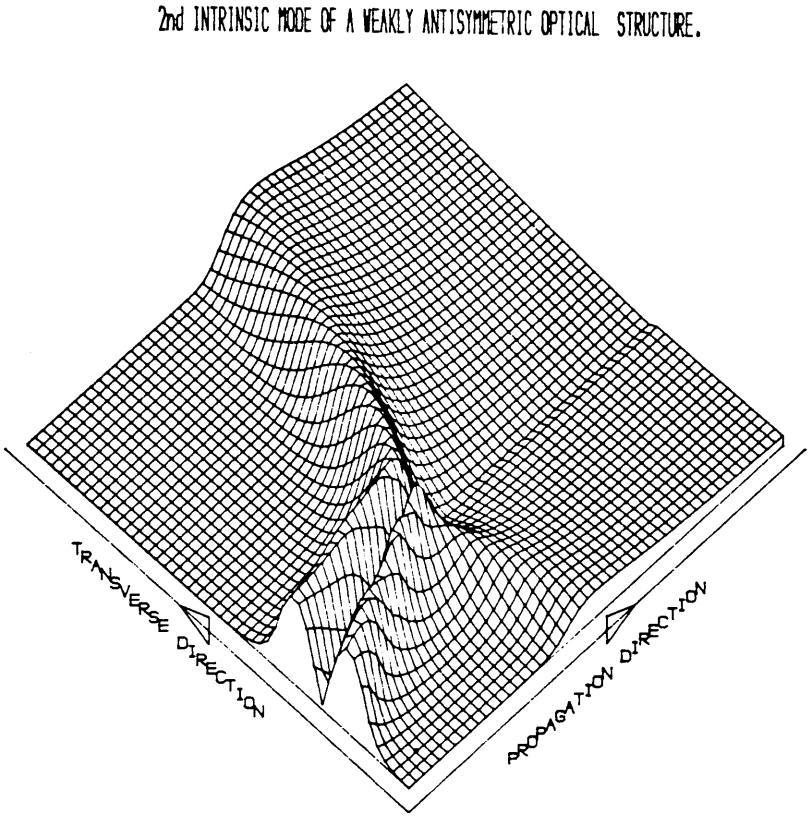

Another interesting feature of these fields is that although the TM and TE fields have almost identical cut−off widths, the leakage of power into the substrate is greater for TM propagation.

5.3: Derivation Of The Acoustical Boundary Conditions.

In this thesis attention is placed on the pressure acoustic fields in fluids, as the J−K ocean of interest is assumed to behave as two immiscible fluids. This assumption implies that no shear forces are present in the structure under consideration. A simple continuity equation can be developed in fluids by examinig the flow of matter through a vanishingly small cube [57] to give,

$$-\frac{\partial \rho}{\partial t} = \nabla.(\rho \underline{v}) \qquad (5.3.1)$$

where ρ is the density of the fluid and $\underline{v}$ the velocity of the particles constituting the

fluid. The above equation states that the rate of change of matter is equal to the net flow of matter throughout an infinitesimally small volume, with the minus sign indicating matter flowing away from volume element. Applying Newton's third law to this cube gives,

$$\rho\frac{\partial \underline{v}}{\partial t} = -\nabla P \qquad (5.3.2)$$

where P is the pressure field. Differentiating equation (5.3.1) and substituting in (5.3.2) leads to,

$$\frac{\partial^2 \rho}{\partial t^2} = \nabla^2 P - \nabla.(\underline{v}\nabla.(\rho\underline{v})) \qquad (5.3.3)$$

The second term in the right hand side of (5.3.3) generates second order terms and is neglected. Assume also that the density and pressure are related by a first order effect $P = c^2\rho$ then the equation of motion of the pressure field to first order is,

$$\nabla^2 P = \frac{1}{c^2}\frac{\partial^2 P}{\partial t^2} \qquad (5.3.4)$$

Consider a pressure field incident on a boundary in a similar fashion to that demonstrated in Figure 5.1.1. Then the transmitted pressure field must be equivalent to the incident and reflected pressure field at the boundary as a build up of pressure at the boundary is non-physical. Thus suppressing the time dependence this can be expressed as,

$$P_i e^{i\underline{k}_i\cdot\underline{r}} + P_r e^{i\underline{k}_r\cdot\underline{r}} = P_t e^{i\underline{k}_t\cdot\underline{r}} \qquad (5.3.5)$$

with the same notation as in section 5.1. The change in velocity of the particles from one medium to the other must be continuous which gives,

$$\underline{v}_i e^{i\underline{k}_i\cdot\underline{r}} + \underline{v}_r e^{i\underline{k}_r\cdot\underline{r}} = \underline{v}_t e^{i\underline{k}_t\cdot\underline{r}} \qquad (5.3.6)$$

Using (5.3.5) and (5.3.6) and the relationship (5.3.1) the reflection coefficient for acoustic pressure fields can be expressed as,

$$\frac{P_r}{P_i} = e^{i2\tan^{-1}\left[\frac{in_1\rho\sin\theta_1}{n\rho_1\sin\theta}\right]} \qquad (5.3.7)$$

Thus if $\rho = \rho_1$ this reflection coefficient is analogous to the optical case when the $\underline{E}$-vector polarisation is perpendicular to the plane of incidence (TE). When $\rho = n/n_1$ and $\rho_1 = n_1/n$ the pressure field is analogous to the optical case when the $\underline{E}$-vector is parallel to the plane of incidence (TM).

5.4: FFT Evaluation Of Acoustical Intrinsic Modes.

The Intrinsic Mode fields for the J−K ocean were generated using the same algorithms used for the optical structures above, although in this instance the density of the two fluids was varied. The J−K ocean has a pressure release upper boundary, which implies that the pressure field on this boundary is zero. It must be noted that the BPM and the PEM can only model structures with small perturbations of the medium. This restriction implies that these methods applied in the standard way cannot model accurately the zero boundary condition. There is a method which will circumvent this problem for a number of geometries. The zero boundary condition is attained by reflecting the desired environment in the interface with the zero boundary condition, so that antisymmetric modes propagating in the new structure will have a zero boundary condition in the desired environment. The input data to these new expanded models must also be antisymmetric, to obtain only antisymmetric fields. The antisymmetry on the input data is achieved by reflecting the desired input of the J−K ocean in the upper boundary and attaching a phase change of Π, and summing.

Using the η − FFT method, of chapter 3, the Intrinsic Mode fields were generated and used as inputs to the BPM and PEM using the antisymmetrising procedure outlined above. In all comparisons the densities of all media are equal to one. The field plots in Figure 5.4.1 are 1st order Intrinsic Mode fields propagating through the wedge environment using BPM, PEM and IM numerical algorithms. Figures 5.4.2 show the propagation of the 3rd Intrinsic Mode through the J−K ocean.

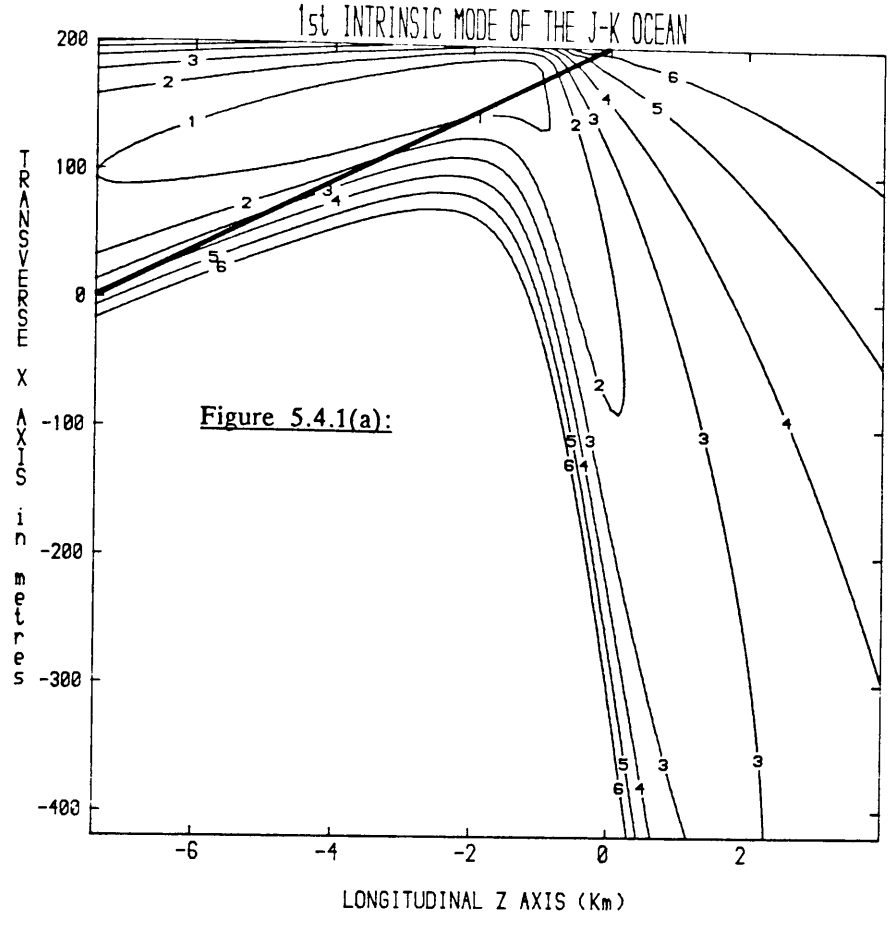

Figure 5.4.1(a):

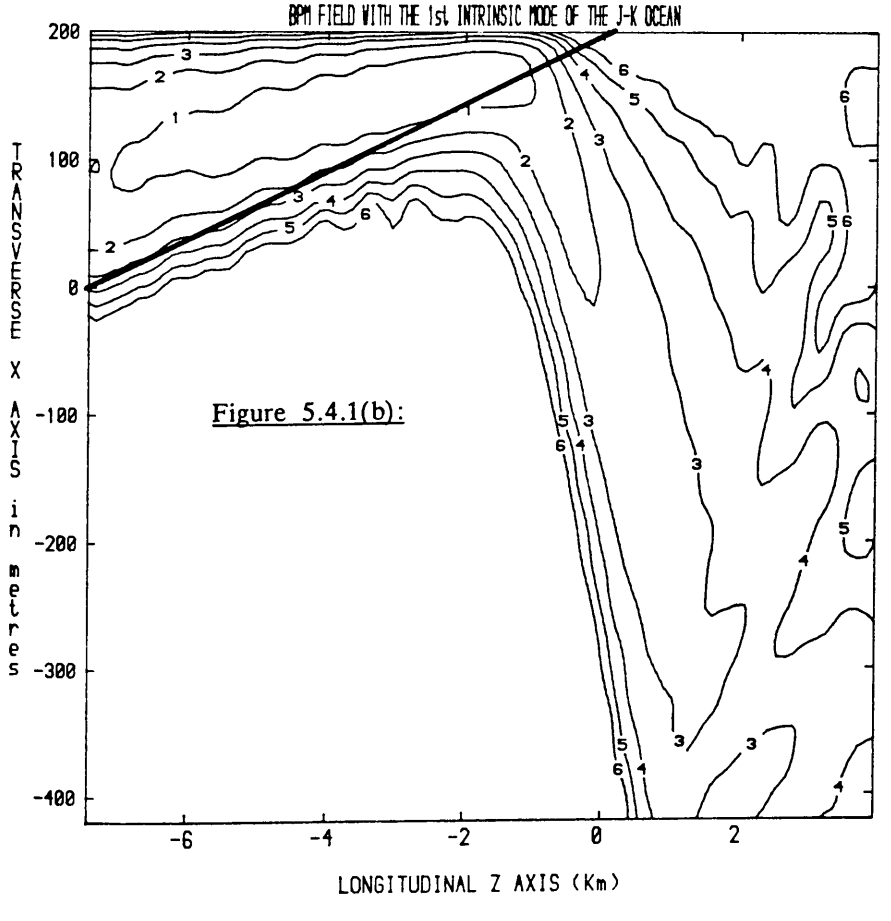

Figure 5.4.1(b):

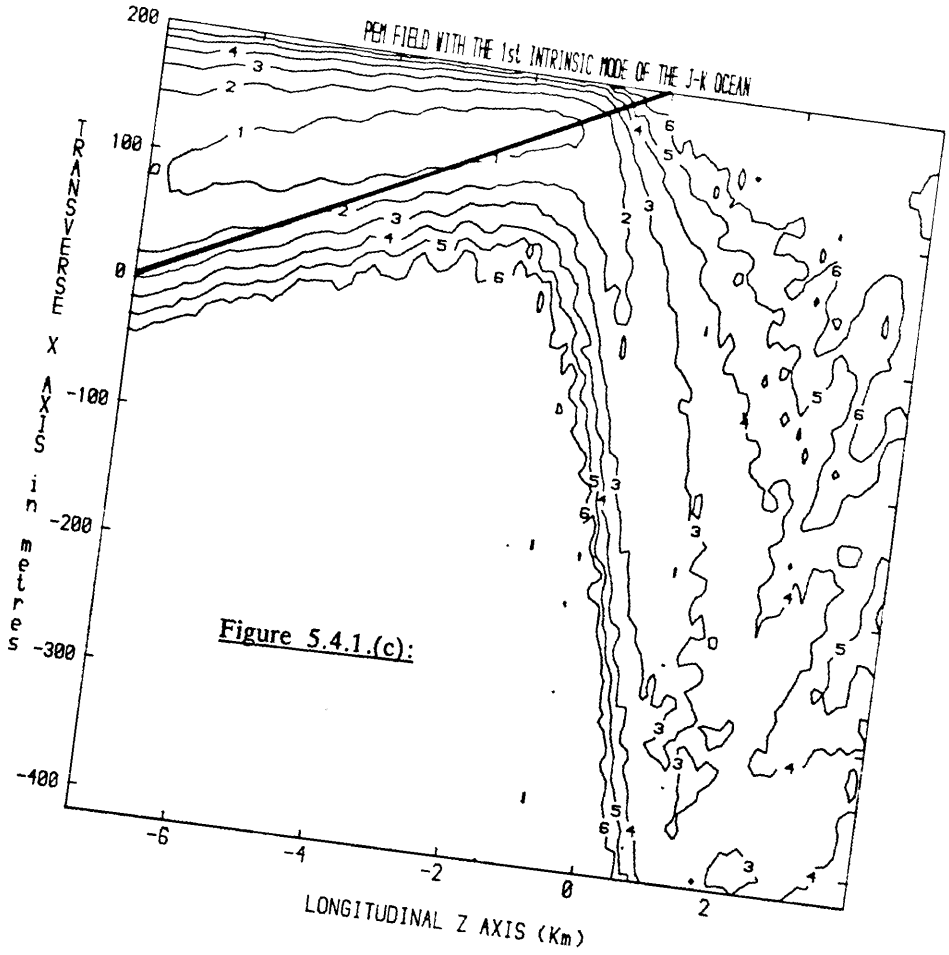

Figure 5.4.1.(c):

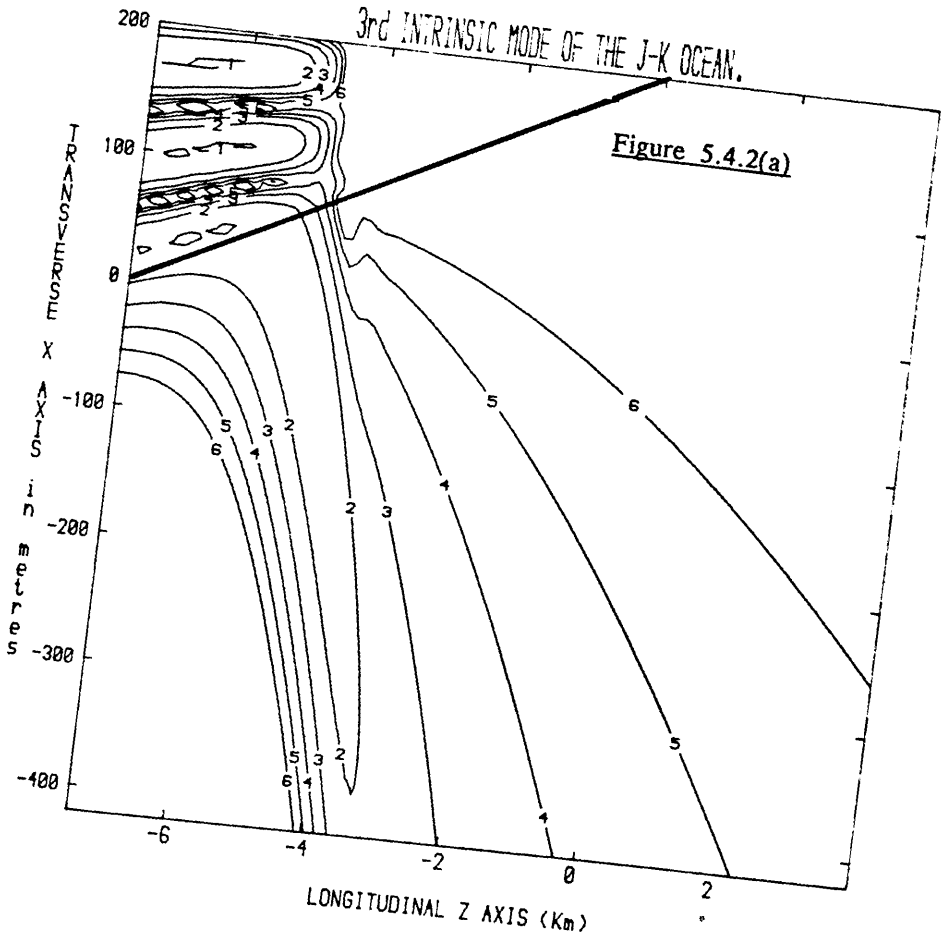

Figure 5.4.2(a)

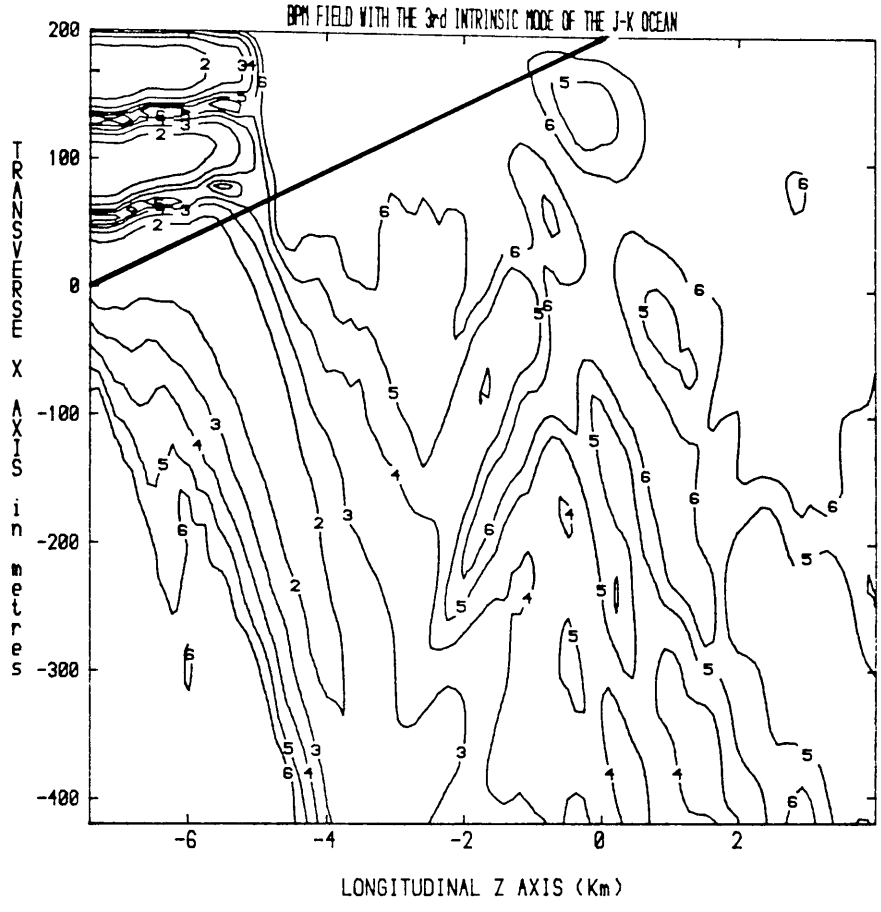
BPM FIELD WITH THE 3rd INTRINSIC MODE OF THE J-K OCEAN
TRANSVERSE X AXIS in metres
200
100
0
-100
-200
-300
-400
-6
-4
-2
0
2
LONGITUDINAL Z AXIS (Km)

Figure 5.4.2(c):

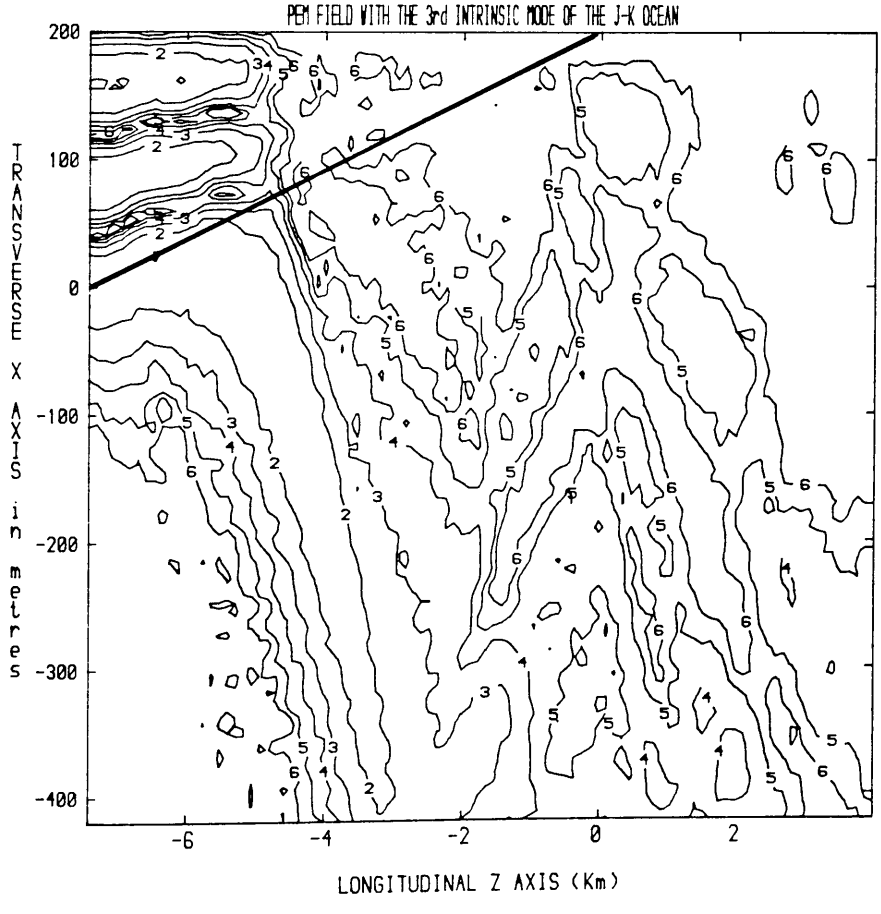
PEM FIELD WITH THE 3rd INTRINSIC MODE OF THE J-K OCEAN
TRANSVERSE X AXIS in metres
200
100
0
-100
-200
-300
-400
-6
-4
-2
0
2
LONGITUDINAL Z AXIS (Km)

The BPM and PEM fields have significantly more noise associated with them than the IM fields. This can be explained by an overall intrinsic mode strategy. As stated in chapter 1, the BPM and the PEM solve particular equations. In principle it is possible to construct intrinsic modes for the BPM equation and the PEM equation in the J−K environment. These new intrinsic modes will be exact solutions of their respective equations. Thus when a pure IM is input into these BPM and PEM environments a set of BPM or PEM intrinsic modes will be excited and these new intrinsic modes may not exhibit the same properties. In the case of the PEM the cut−off point of the field and leakage into the lower medium agree well with the IM fields. The BPM intrinsic mode field is noticably different from the IM field in that the leakage of energy in the lower medium is weaker and the cut−off point for each mode is further away from the apex. These methods of comparison are poor as the orders of the discrepancies in the field are of the order of the plot interval of the fields and consequently a more quantitative approach is required.

5.5: Quantitative Comparisons with B.P.M. and P.E.M.

The quantity examined most readily for the comparison of wave propagation programmes, in the J−K ocean, is the variation in the widths of the guiding layer when the adiabatic mode cuts off (cut−off heights). As an adiabatic mode propagates upslope, the modal angle (θ_q) rotates until it eventually equals the critical angle (θ_c), at which point the mode is said to be cut−off. An examination of the transverse spectral content of the field at each cross−section should give an indication of the variations in local cut−off heights. Unfortunately, this method is redundant as the IM is formed by spectral synthesis and the BPM and PEM consist of a set of their own intrinsic modes (c.f. previous section), so that the spectral content of the fields are high.

As stated previously, as the mode approaches cut−off then $\theta_q \to \theta_c$ and the magnitude of the longitudinal component of wave vector of the mode tends to the magnitude of the wave vector in the substructure (i.e $\beta \to n_1 k$). Using this fact combined with the transverse resonance condition, the component of the gradient of the adiabatic field normal to the interface between the two media (from chapter 1) is,

$$\frac{\partial w_q(\underline{x})}{\partial n} = \left[\frac{2\tau_q}{(1 + \tau_q h)\beta(z)} \right]^{\frac{1}{2}} \sin\left[\frac{\Phi(\theta_q)}{2} \right] e^{i\int_{z_0}^{z} \beta(z)\,dz} \qquad (5.5.1)$$

Noting that $\Phi_1(\theta_c) = 0$ and $\tau_q = 0$ at $\theta_q = \theta_c$, then it is obvious that the component

of the gradient normal to the interface is zero at mode cut−off. Thus the comparisons of the cut−off points with respect to the local guide height can be achieved by the plotting of the gradient of the field normal to the interface, at a point along the interface of the two media. This argument while correct is limited because the physics of the marching algorithm methods are such that the pure IM input consists of BPM (or PEM) intrirnsic modes. Consequently modal interference will occur which may cause the gradient of the field normal to the boundary to be zero at points away from the actual cut−off. To find the appropriate quantity the physics of the phenomenon must be examined more closely.

As the mode approaching cut−off has to spread its energy over an effectively smaller and smaller cross−section (as the mode is guided) the energy density will increase. From adiabatic mode theory the peak value of the field on the boundary is at the point before cut−off (just before the evanescent field in the substrate becomes constant). In the true physical situation the zero field after cut−off, which the AM theory predicts, does not occur. The condition for maximum field to occur on the boundary is coincident with a zero value of the normal derivative of the field, and is termed the cut−off condition.

Accounting for all these arguments implies that the field at the interface is required as a function of local guide height; the occurence of maximum field corresponds to adiabatic mode cut−off.

The Adiabatic Mode cut−off height is easily calculated by letting $\beta \rightarrow n_1 k$ in the transverse resonance condition of the J−K ocean (equation (4.3.1.2) chapter 4), and is

$$h_c = \frac{(q - \frac{1}{2})2\Pi}{k(n^2 - n_1^2)^{\frac{1}{2}}} \qquad (5.5.2)$$

This is asymptotically equivalent up to $O(\alpha)$ to the IM staionary phase point description of the local cut−off height (c.f. chapter 4). Thus the IM cut−off height should correspond to the AM cut−off height. The denominator in equation (5.5.2) is the transverse wave number in the guiding layer. Consequently the cut−off height for a particular mode using a particular algorithm depends only on the evaluation of the transverse wave vector in the guiding medium.

In the BPM the wave vector locus derived in chapter 1 and the cut−off wave number for a particular mode is shown in Figure 5.5.1 below.

Figure 5.5.1: The BPM Transerse Wave Vector At Adiabatic Mode Cut-off.

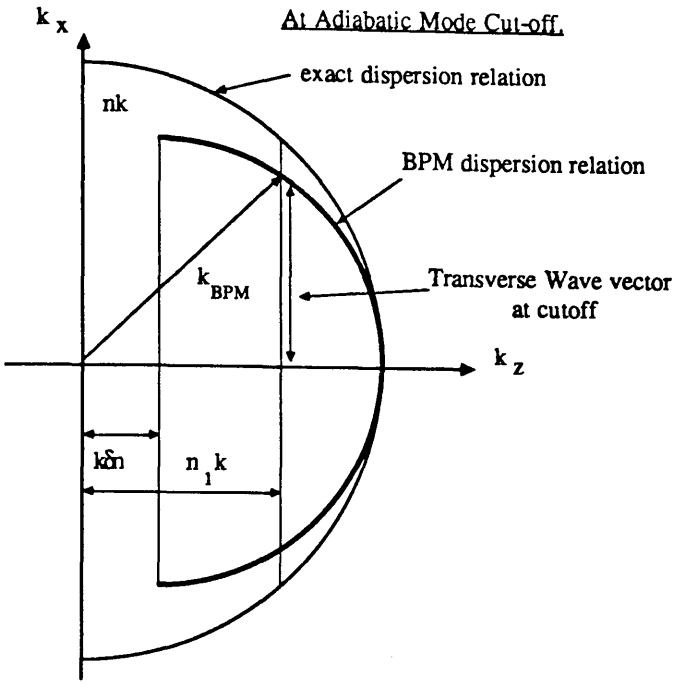

From this diagram the magnitude of the transverse wave vector in the guiding medium can be seen to be,

$$k_{BPM} = k(\delta n(2n_1 - \delta n))^{\frac{1}{2}} \qquad (5.5.3)$$

and so the BPM cut−off height is,

$$h_{c_{BPM}} = \frac{(q - \frac{1}{2})2\Pi}{k(\delta n(2n_1 - \delta n))^{\frac{1}{2}}} \qquad (5.5.4)$$

By contrast, the parabolic equation method (PEM) of chapter 1 is such that the field is assumed to have a wave vector equivalent to the wave vector in the background medium, with a perturbation to this wave vector attached. This means that at the adiabatic mode cut−off this perturbation of wave vector must be zero and hence the parabolic equation method correctly defines this cut−off point.

The table below indicates the shifting of the cut−off points for the three modes considered in the J−K ocean problem.

Figure 5.5.2 Local Cut-off heights for the J-K ocean.

Mode Number	BPM cut-off height	PEM + IM cut-off heights
1	33.81m	31.57m
2	101.42m	94.72m
3	169.03m	157.87m

In Figures 5.5.3(a)(b)(c) field plots of the BPM, PEM and the IM along the interface between the two media are shown for the three different IM inputs. Also the corresponding AM field at the interface is shown so that qualitative comparisons can be made. All fields on the boundary are normalised at the local guide height of 200m.

Figure 5.5.3(a):

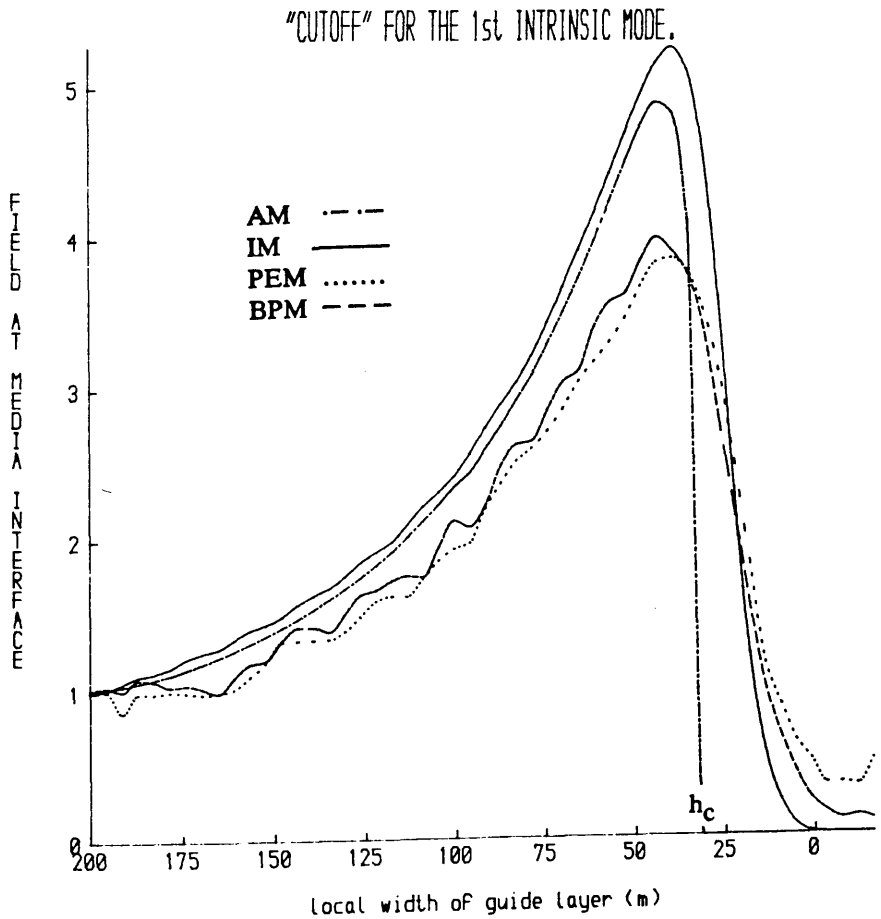

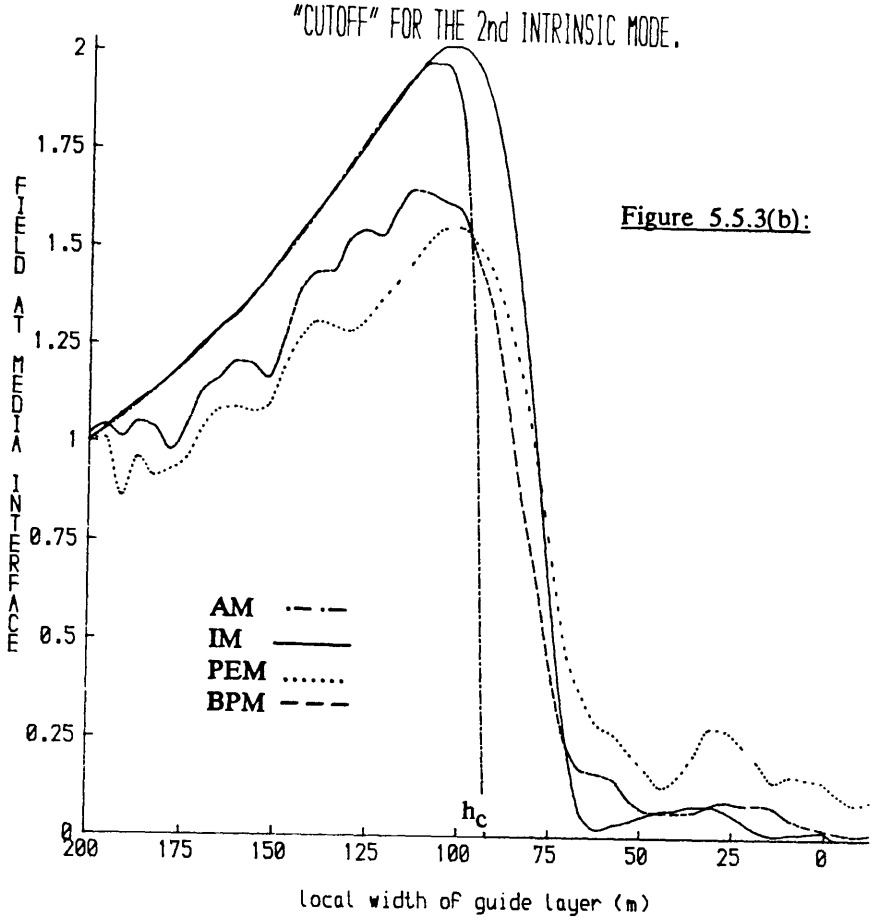

Figure 5.5.3(b):

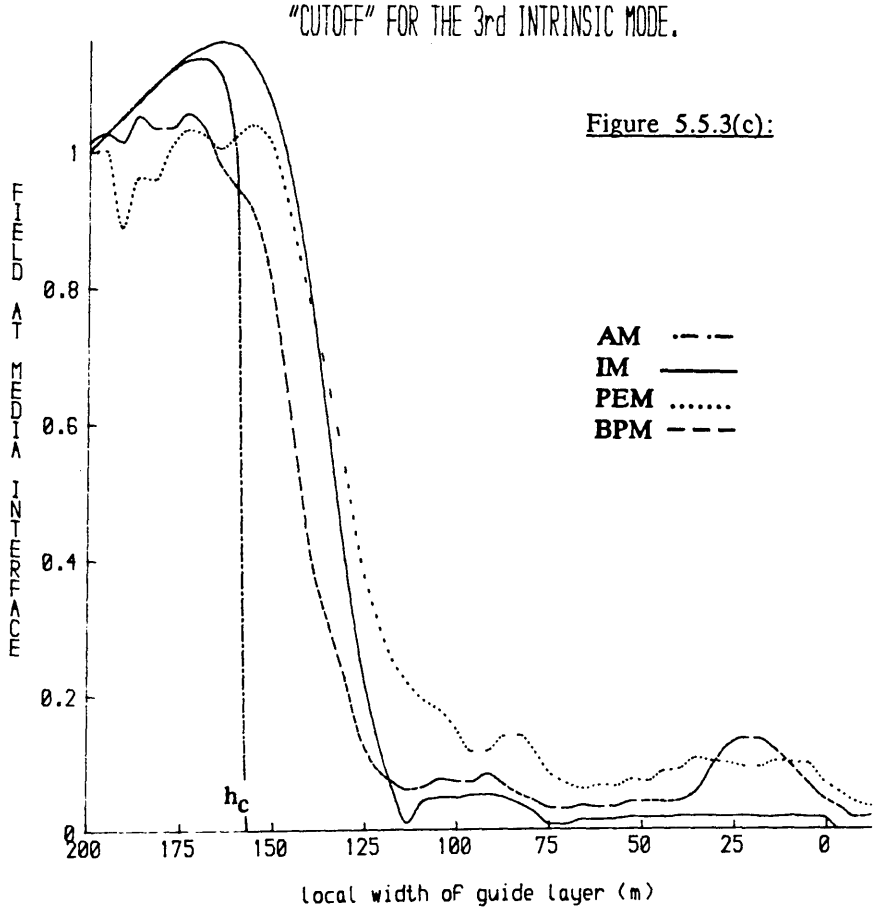

Figure 5.5.3(c):

An overall analysis best serves the discussion and interpretation of these plots, because the phenomena occuring are observed in each case. Immediately it can be noticed that the maximum height of the IM field corresponds to the adiabatic cut−off point as expected.

The obvious detail is that the BPM and PEM appear to possess a large amount of noise. Closer examination reveals a more fundamental structure confirming qualitative descriptions given in section 5.2. Firstly the maximum heights of the fields compare favourably with those predicted in Figure 5.5.2. Secondly the pure IM input can be decomposed into an infinite set of BPM or PEM intrinsic modes where applicable. As a consequence of this, the three dominant BPM (or PEM) intrinsic modes can be seen cutting off at their correct heights for each pure IM input and are indicated on the diagrams. This adds considerable weight to the intrinsic mode arguments of the preceeding two sections.

5.6: The Conservation of Total Power.

A further requirement of the Intrinsic Mode if it is to be an exact solution of the elliptic wave equation is that no net flow of power can occur across any closed surface (excluding the apex). This power calculation has been carried out by Xiang, Cada and Felsen [5] and discrepancies of the order of 0.6dBs occured when the Adiabatic mode was still guiding; after cut−off more substantial errors were incurred, these being attributed to several causes. This section explains how and why the inclusion of certain terms will describe adequately the propagation through the transition region and subsequent conservation of power. Let $U(\underline{x})$ be a solution of the elliptic equation,

$$\left[\begin{matrix} \nabla^2 + n^2k^2 \\ \nabla^2 + n^2k^2 \end{matrix} \right] U(\underline{x}) = 0 \qquad (5.6.1)$$

Then it follows that its complex conjugate $U^*(\underline{x})$ must also be a solution,

$$\left[\nabla^2 + n^2k^2 \right] U^*(\underline{x}) = 0 \qquad (5.6.2)$$

Multiplying (5.6.1) by $U^*(\underline{x})$ and (4.2) by $U(\underline{x})$ and subtracting gives,

$$U^*(\underline{x})\nabla^2 U(\underline{x}) - U(\underline{x})\nabla^2 U^*(\underline{x}) = 0 \qquad (5.6.3)$$

With the use of the vector indentity,

$$\nabla.\left[\ F\nabla G\ \right] = \nabla F.\nabla G + F\nabla^2 G \qquad (5.6.4)$$

equation (5.6.3) can then be expressed in the form,

$$\nabla.\left[\ \mathrm{Im}\ U(\underline{x})\nabla U^*(\underline{x})\right] = 0 \qquad (5.6.5)$$

Integrating this equation throughout the volume of interest and applying the divergence theorem leads to,

$$\iint_A \underline{S}.d\underline{A} = 0 \qquad (5.6.6)$$

where $\underline{A}$ is the unit normal to the surface A enclosing the volume and

$$\underline{S} = \mathrm{Im}\left[\ U(\underline{x})\nabla U^*(\underline{x})\right] \qquad (5.6.7)$$

This states that if no sources are present in the volume, then no net flux of $\underline{S}$ crosses the total surface. To evaluate the power in the IM as it propagates upslope it is useful to introduce infinite contours which close the $\sum$ contour in the left hand quarter plane as the field is zero above the upper boundary. This contour is shown in Figure 5.6.1

Figure 5.6.1: Contour For Conservation Of Power Algorithm.

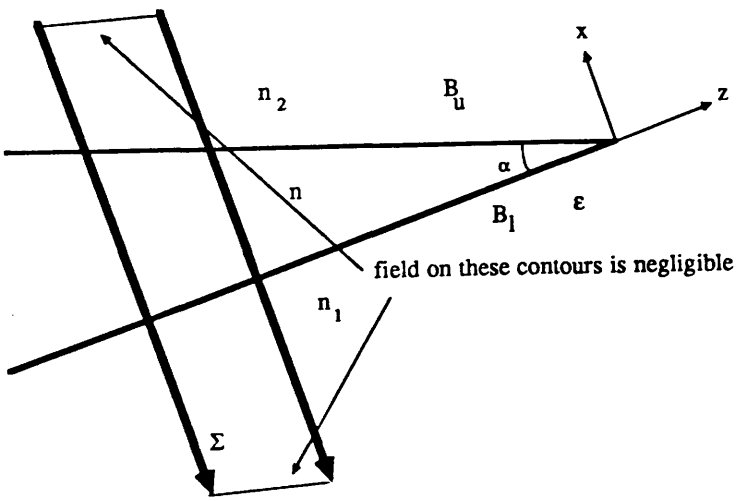

As equation (5.6.6) must be satisfied and the value of the field on the infinite portion of the contour must be zero then the power crossing the section $\sum$ is,

$$P = \int_{\sum} \underline{S}.d\underline{l} \tag{5.6.8}$$

where $\underline{l}$ is the unit normal to the cross-section $\sum$ depicted in Figure 5.6.1. The calculated quantity at each possible $\sum$ plane from the cartesian coordinates of Figure 5.6.1 is,

$$P = Im \int_{\sum} U(\underline{x}_0)\frac{\partial U^*}{\partial z}(\underline{x}_0)dx_0 \tag{5.6.9}$$

Previous authors [5,58] calculating the above conserved quantity did not include an expression for the E-M remainder. In this exposition, this remainder term has been asymptotically evaluated (appendix A), to give

$$E_b^-(\theta) = \begin{cases} E_0^-(\theta), & Re\theta < \theta_c \\ E_0^-(\theta) + F_1(\theta), & \theta_c < Re\theta < \Pi-\theta_c \end{cases} \tag{5.6.10}$$

where,

$$E_0^-(\theta) = \frac{\alpha}{6}\frac{d\Phi_1(\theta)}{d\theta} + O(\alpha^3) \tag{5.6.11}$$

$$F_1(\theta) \sim \frac{(2\alpha\cot\theta_c)^{\frac{1}{2}}}{2\Pi} e^{\frac{i\Pi(\theta-\theta_c)}{\alpha} - \frac{i\Pi}{4}} \tag{5.6.12}$$

This approximation will be sufficient for small wedge angle, which is a feature of the ocean acoustical problems. Figures 5.6.2 show the conservation of power in the acoustic pressure field crossing a desired cross-section $\sum$ in an ocean overlying a fluid bottom, wherein the wedge angle and the density of the fluid bottom are varied.

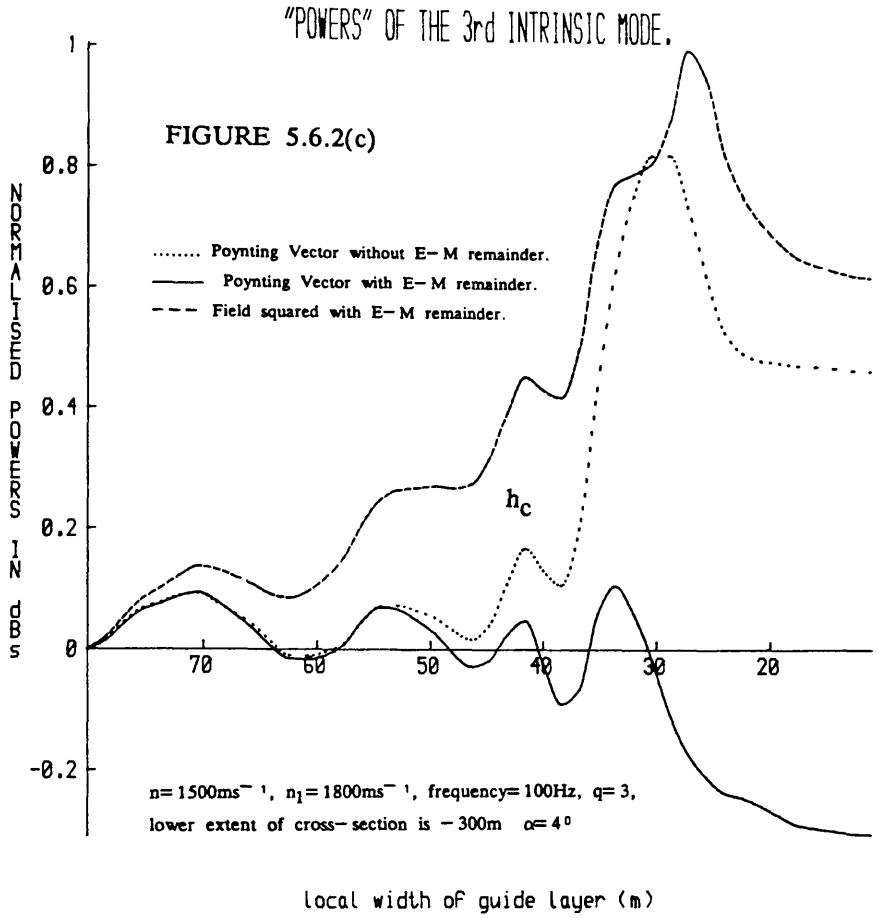
"POWERS" OF THE 3rd INTRINSIC MODE.
FIGURE 5.6.2(c)
..... Poynting Vector without E–M remainder.
—— Poynting Vector with E–M remainder.
– – – Field squared with E–M remainder.
NORMALISED POWERS IN dBs
1
0.8
0.6
0.4
0.2
0
-0.2
70
60
50
40
30
20
h_c
n= 1500ms^{-1}, n_1= 1800ms^{-1}, frequency= 100Hz, q= 3,
lower extent of cross–section is –300m α= 4°
local width of guide layer (m)

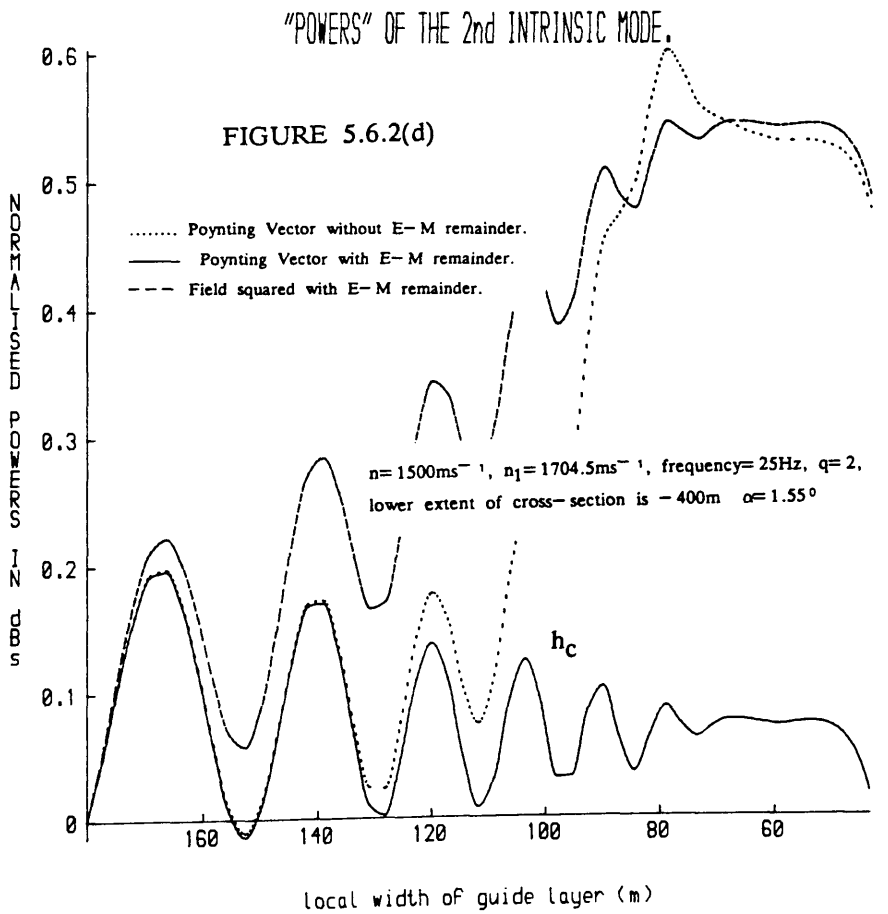
"POWERS" OF THE 2nd INTRINSIC MODE.
FIGURE 5.6.2(d)
..... Poynting Vector without E–M remainder.
—— Poynting Vector with E–M remainder.
– – – Field squared with E–M remainder.
NORMALISED POWERS IN dBs
0.6
0.5
0.4
0.3
0.2
0.1
0
160
140
120
100
80
60
h_c
n= 1500ms^{-1}, n_1= 1704.5ms^{-1}, frequency= 25Hz, q= 2,
lower extent of cross–section is –400m α= 1.55°
local width of guide layer (m)

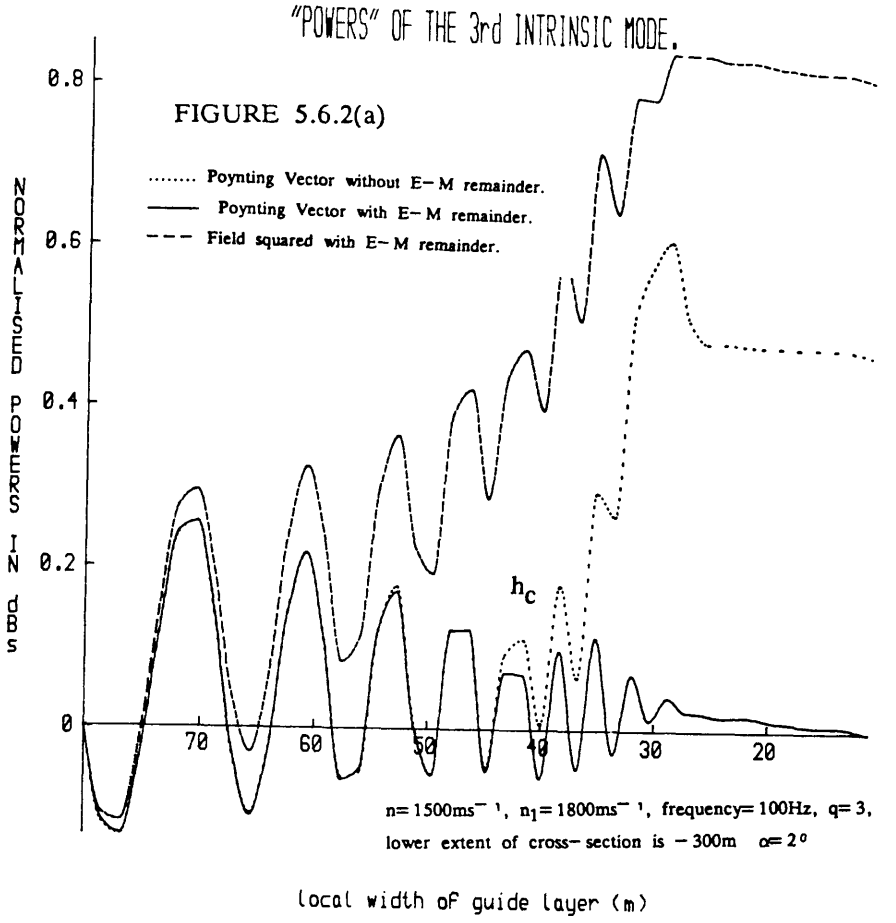
"POWERS" OF THE 3rd INTRINSIC MODE.
FIGURE 5.6.2(a)
..... Poynting Vector without E-M remainder.
—— Poynting Vector with E-M remainder.
– – – Field squared with E-M remainder.
NORMALISED POWERS IN dBs
0.8
0.6
0.4
0.2
0
70
60
50
40
30
20
h_c
n=1500ms^{-1}, n_1=1800ms^{-1}, frequency=100Hz, q=3,
lower extent of cross-section is −300m α=2°
local width of guide layer (m)

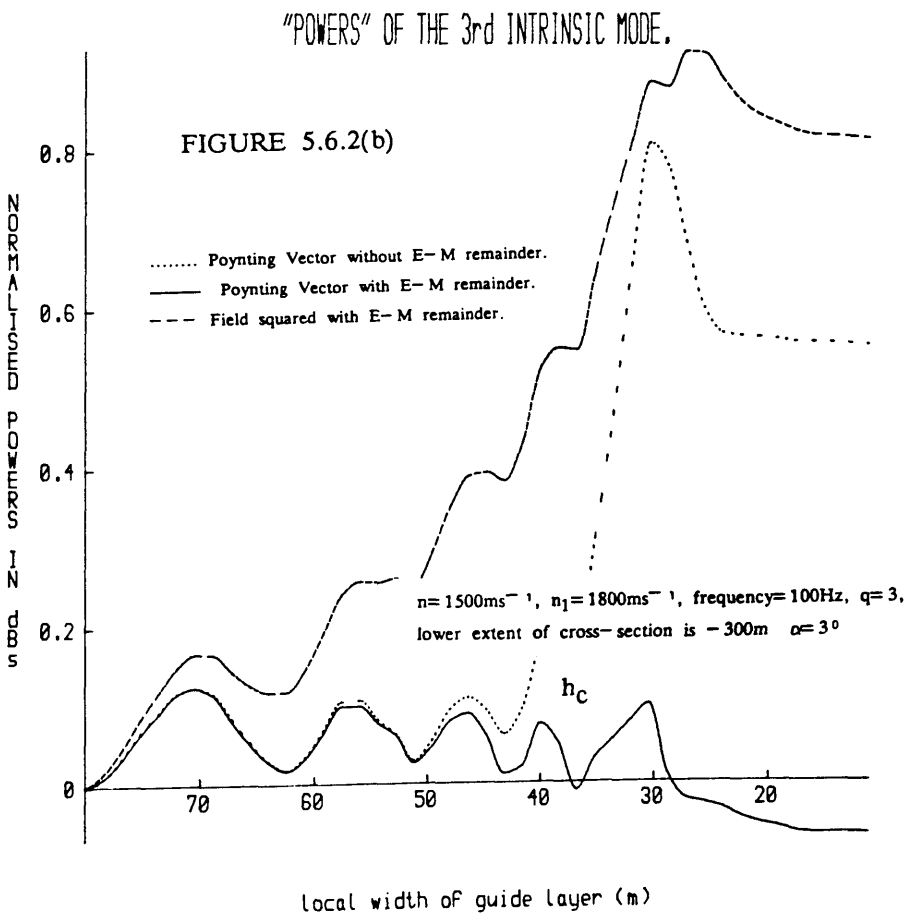
"POWERS" OF THE 3rd INTRINSIC MODE.
FIGURE 5.6.2(b)
..... Poynting Vector without E-M remainder.
—— Poynting Vector with E-M remainder.
– – – Field squared with E-M remainder.
NORMALISED POWERS IN dBs
0.8
0.6
0.4
0.2
0
70
60
50
40
30
20
h_c
n=1500ms^{-1}, n_1=1800ms^{-1}, frequency=100Hz, q=3,
lower extent of cross-section is −300m α=3°
local width of guide layer (m)

FIGURE 5.6.2(e)

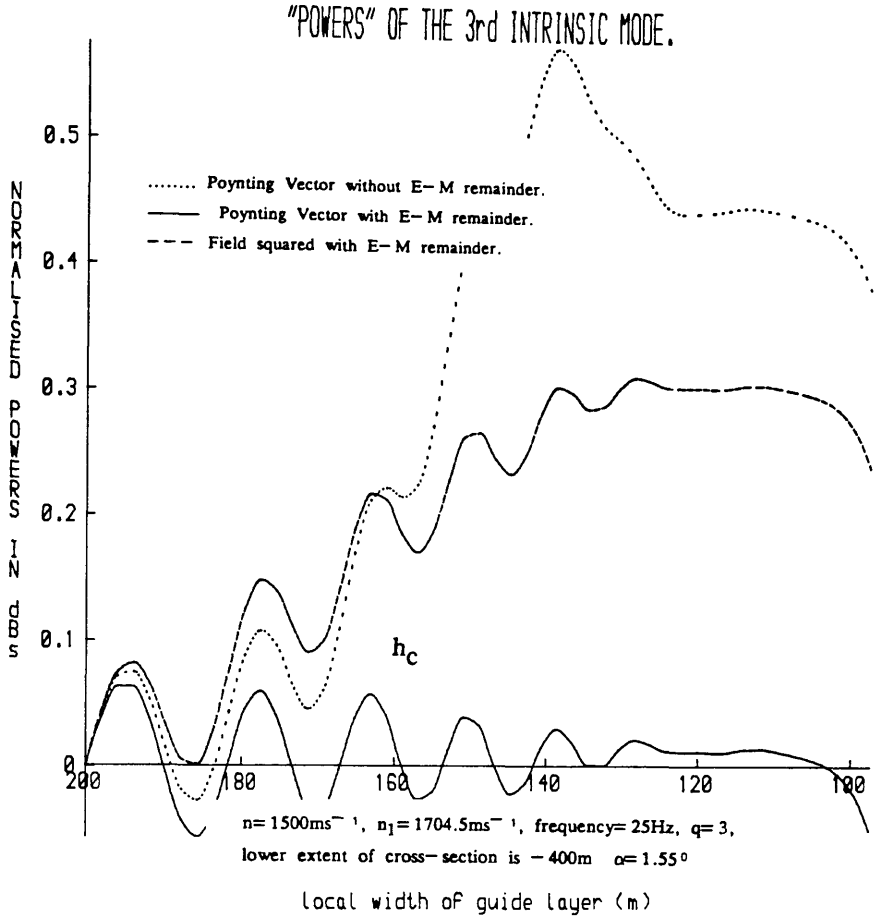

In each of these environments there are three calculated quantities, so as to demonstrate conclusively that the integral of the Poynting Vector $\underline{S}$, over $\sum$, including the Euler–Maclaurin remainder, is a conserved quantity. Using equation (5.6.9), and in the limit of small wedge angle, the conserved quantity for the Intrinsic Mode field can be approximated by,

$$P \approx \int_{\sum} W_q(\underline{x}_0)\, ink\cos\theta_q\, W_q^*(\underline{x}_0)\, d\underline{x}_0 \qquad (5.6.13)$$

With the z dependence of the Intrinsic Mode obtained from equation (3.5.22) of chapter 3 and θ_q is the modal angle. Thus the conserved quantity is of the approximate form

$$P \approx \beta \int_{\sum} |W_q(\underline{x}_0)|^2 d\underline{x}_0 \qquad (5.6.14)$$

where β is the adiabatic mode propagation constant. Thus, as the cross-section $\sum$ passes through the adiabatic mode regime ($\beta \approx nk$) into a radiative regime ($\beta \approx n_1 k$), there must be a corresponding increase in the field to compensate for the decrease in β as P remains constant. In ocean acoustics the accuracy of numerical data is often checked by calculating the conserved quantity. Figures 5.6.2 and the derivation of the conserved quantity (equation (5.6.14)) demonstrate that the correct quantity must be calculated and that is not necessarily $|U|^2$. To make sure that this critical transition region is traversed fully it essential to calculate the local height of the guide where adiabatic cut-off occurs. The local cut-off height (h_c) for the q^{th} adiabatic mode can be calculated from the transverse resonance condition given in equation (5.5.2).

With the appropriate regions of interest calculated it only remains to examine and interpret the plots. It must be stated that all the plots start to decrease at the small local guide heights because the finite cross-section considered, at these points, does not span all the dominant contributions to the field.

The first three cases (Figures 5.6.2(a)(b)(c)) are slight variations of the wedge angle α on a specific geometry considered by Topuz and Felsen [3]. It is observed that the change in $|W_q|^2$ is equivalent to the ratio of the velocities in the two media. Also the inclusion of the asymptotic remainder accounts for previous discrepancies in Poynting Vector calculations [5]. However, as the wedge angle is increased, the asymptotic form of the remainder becomes insufficient. It is believed that a numerical computation of the remainder would improve accuracy, but it is adequate to demonstrate that the inclusion of this term verifies energy conservation for small wedge angles and there is no reason to suppose that successive approximations will not hold for $\alpha < \theta_c/2$. Figures 5.6.2(d)(e) demonstrate that the IM of wedge geometries with constant angle and varying media still conserve the quantity in equation (5.6.9).

Conclusions.

This chapter has demonstrated that the IM field derived in chapter 2 can be calculated very efficiently using the FFT algorithms of chapter 3. The accuracy of these field calculations was determined by a simplistic method; that of observing the required number of integration points to produce a zero boundary condition in the J-K ocean. Maintaining accuracy when examining other structures was achieved by a scaling of wavelength and refractive index to determine a sufficient number of integration points.

This efficient evaluation of the IM field has allowed previously time consuming calculations on this field to be accessible within the order of minutes. This facility is clearly demonstrated with the two dimensional field plots in the first two sections of this chapter. The IM field plots along the interface between the guide and the substrate for the J−K ocean were generated using the z−directed FFT of chapter 3, which allowed comparisons with the BPM, PEM and AM fields. These comparisions demonstrated quantitative discrepancies which were discussed using a simplistic wave vector approach and enabled the concept of BPM and PEM intrinsic modes to be introduced.

The final section on calculated power demonstrates the efficiency of these FFT routines, as previous calculations of this type required many hours of computer time [3], whereas now minutes are all that are needed. Indeed this last section has laid to rest any previous speculation [58] as to whether the IM conserves power as the observation point moves upslope through the cut−off of the appropriate AM. It is clearly shown that the with the inclusion of the asymptotic form of the E−M remainder, for small wedge angles, the IM field conserves power to within .2dBs.

The underlying message of this chapter is that a fast and accurate method of calculating the field inside a planar wedge has been obtained which may serve as a benchmark solution because errors can be quantified asymptotically.

Introduction.

The Green's function for translationally invariant structures can be calculated by a variety of different methods [44] ; usually in geometries of more than one dimension the simplest systematic approach is of a transform type [59] . However, in range dependent geometries this type of approach is inapplicable. The spectral synthesis approach of Arnold and Felsen [1], described in chapter 2, is claimed to produce an exact Green's function for the wedge structure, excluding the apex, and this spectral object is termed the Wedge Green's Function (WGF). The major aim of this chapter is to substantiate the above claim and in the process gain a greater understanding of the physical phenomena involved in the propagation of wave fields throughout a wedge environment.

The first two sections investigate the properties of the WGF for a general wedge configuration, by firstly deriving the WGF for all possible orientations of source and observation point, using analysis analogous to that in chapter 2. The derivation of this global WGF then permits a rigorous analysis of its properties by tracking individual plane wave fields.

With the identity of the WGF rigorously proved in the previous sections, it now remains to investigate asymptotically a WGF of a particular geometry. This analysis of the Jensen–Kupermann ocean [22] allows for the identification of previously defined global spectral quantities, necessary for a confirmation of a correct numerical algorithm.

The final section of this chapter examines the WGFs for several different wedge geometries and discusses the implications of the position of the source point.

6.1: Derivation of the WGF for the Global Wedge Geometry.

The derivation of the WGF in chapter 2 considered only source points inside the guiding wedge. However, for completeness and further analysis it is necessary to obtain the WGF for all the other possible configurations of source and observation points.

A close examination of the method employed in chapter 2, suggests that all the multiply–reflected fields can be expressed in the simple closed form of equation (2.4.13) (chapter 2), provided that all possible initial reflected fields are obtained. From equation (2.1.11) of chapter 2 it can be seen that the total scattered field is the sum of the initial field, plus all possible multiple even reflections of this initial field.

To obtain the total scattered field for all possible orientations of the source and observation point requires the identification of the initial fields of the scattering equation, which are necessary to correctly define the infinite reflection processes in a collective form. The WGF then consists of this scattered field and all other possible fields unaccounted for in the above collective form. In this chapter an examination of the convergence of the global WGF is omitted for brevity, with the knowledge that the analysis follows the same form as in chapter 2.

Consider firstly source points lying in the medium below the wedge–shaped high refractive index (denoted by 1). Figure 6.1.1 shows the initial plane wave species (<1> and <2>) which then undergo multiple reflections, and also the direct <4> and reflected <3> plane wave species when the observation point is in the lower medium.

Figure 6.1.1: Plane Wave Species for Source Points in the Substrate (medium 1)

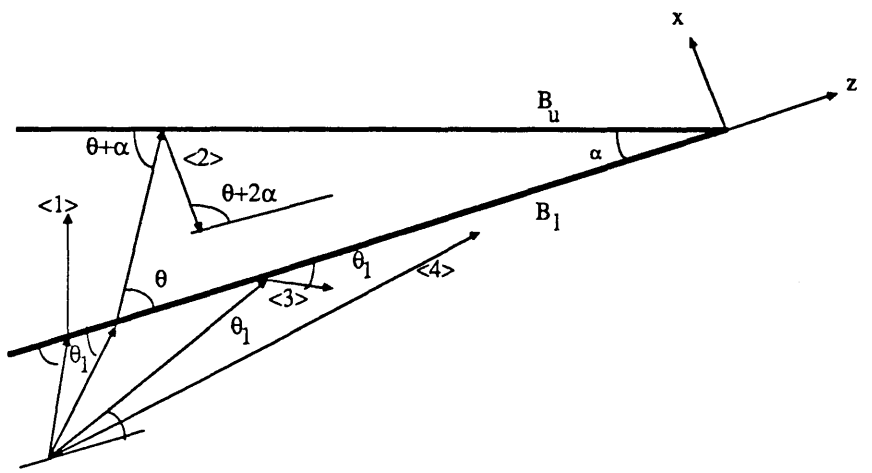

To interpret these fields mathematically requires the introduction of the quantities,

$$W_1^{\pm}(\theta_1) = e^{-in_1k(z_s\cos\theta_1 \pm x_s\sin\theta_1)} \qquad (6.1.1)$$

Let the transmission of a plane wave through the lower boundary be represented by the operator T_1 and the reflection at the upper boundary be R_u. Using the principle of superposition the initial upward field (path <1>) is then,

$$\int_C W_1^+(\theta_1)T_1V_\theta^+(\underline{x})d\theta_1 \qquad (6.1.2)$$

In a similar manner the initial downward field (path <2>) at the observation point can be represented by,

$$\int_C W_1^+(\theta_1)T_1R_uV_\theta^+(\underline{x})d\theta_1 \qquad (6.1.3)$$

with C being the appropriate Sommerfeld contour necessary for convergence. While these equations are correct they are not amenable to the collective procedure of chapter 2. (i.e. they must be in a form in which the observation plane wave is $V_\theta(\underline{x})$ and the integration variable is also θ). This manipulation, demonstrated in appendix F, gives the spectral amplitudes of the initial upward and downward fields at the observation point to be,

$$U_1^{\pm}(\theta) = \begin{cases} W_1^+(\theta_1)\left[1 + e^{i\Phi_1(\theta)}\right] \\ W_1^+(\theta_1')\left[1 + e^{i\Phi_1(\theta-2\alpha)}\right]e^{i\Phi_u(\theta-\alpha)} \end{cases} \qquad (6.1.4)$$

with,

$$n\cos\theta = n_1\cos\theta_1, \qquad n\cos(\theta-2\alpha) = n_1\cos(\theta_1')$$

(c.f. equation (2.4.3) of chapter 2). In this form these functions may be directly substituted into equation (2.4.13) to obtain the scattered field. If the observation point is in the same medium then the direct and reflected fields must be added. These fields are calculated in appendix F using Figure 6.1.1 and are found to be,

$$W_{d_1}(\underline{x},\underline{x}_s) = \int_C W_1^+(\theta_1)\frac{n\sin\theta}{n_1\sin\theta_1}V_{1\theta_1}^+(\underline{x})d\theta \qquad (6.1.5a)$$

$$W_{r_1}(\underline{x},\underline{x}_s) = -\int_C W_1^+(\theta_1)\frac{n\sin\theta}{n_1\sin\theta_1}e^{i\Phi_1(\theta)}V_{1\theta_1}^-(\underline{x})d\theta \qquad (6.1.5b)$$

The preceeding derivation of all the initial incident fields allows for a complete representation of the WGF for a source point in the lower medium.

When the source point is in the upper medium (denoted by 2) it is essential to introduce the plane wave terms,

$$W_2^{\pm}(\theta_2) = e^{-in_2k(z_s\cos\theta_2 \pm x_s\sin\theta_2)} \qquad (6.1.6)$$

so that the trajectories of the initial plane wave types of Figure 6.1.2 can be described mathematically.

Figure 6.1.2:

Plane Wave Species for Source Points in the Superstrate (medium 2)

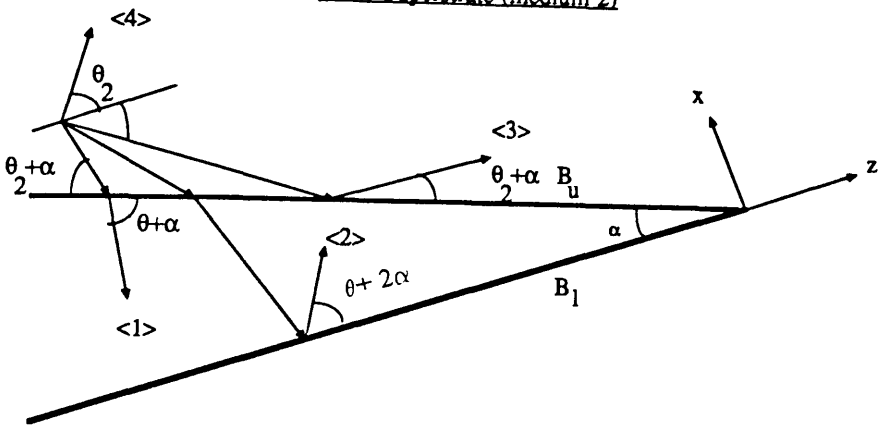

The expressions for the initial downward, **<1>**, and upward, **<2>**, plane wave field types at the observation point depicted in Figure 6.1.2 are,

$$\int_C W_2^-(\theta_2+2\alpha)T_2V^-_{\theta+2\alpha}(\underline{x})d\theta_2 \qquad (6.1.7)$$

$$\int_C W_2^-(\theta_2+2\alpha)T_2R_1V^-_{\theta+2\alpha}(\underline{x})d\theta_2 \qquad (6.1.8)$$

respectively, where T_2 and R_1 are the transmission and reflection operators for an incident plane wave. In a procedure analogous to the calculation of the initial spectral amplitudes of the previous WGF (appendix F) the upward and downward initial spectral amplitudes at the observation point are,

$$U_2^{\pm}(\theta) = \begin{cases} W_2^-(\theta_2'+\alpha)\left[1 + e^{i\Phi_u(\theta-\alpha)}\right]e^{i\Phi_l(\theta)} \\ W_2^-(\theta_2'+\alpha)\left[1 + e^{i\Phi_u(\theta-\alpha)}\right] \end{cases} \qquad (6.1.9)$$

with,

$$n\cos(\theta-\alpha) = n_2\cos(\theta_2') \qquad n\cos(\theta+\alpha) = n_2\cos(\theta_2+\alpha)$$

Again, as previously, these spectral amplitudes can only be used to evaluate the total reflected field and so that when the observation point is in the upper medium the WGF requires the addition of the direct <4> and single reflected <3> fields, shown in Figure 6.1.2, which are found to be,

$$W_{d_2}(\underline{x},\underline{x}_s) = \int_C W_2^+(\theta_2)\frac{n\sin(\theta+\alpha)}{n_2\sin(\theta_2+\alpha)}\, V^+_{2\theta_2}(\underline{x})d\theta \qquad (6.1.10a)$$

$$W_{r_2}(\underline{x},\underline{x}_s) = -\int_C e^{i\Phi_1(\theta+\alpha)}\, W_2^-(\theta_2+2\alpha)\frac{n\sin(\theta+\alpha)}{n_2\sin(\theta_2+\alpha)}\, V^+_{2\theta_2}(\underline{x})d\theta \qquad (6.1.10b)$$

respectively. With all the initial fields fully described for all possible orientations of the source and observation point the WGF can be defined as,

$$G^0_j(\underline{x},\underline{x}_o) = D_0 I_0 + \sum^{+}_{-}\int_C\left[\frac{1}{2}U^{\pm}_j(\theta)+\frac{1}{2\alpha}\sum_{q=-\infty}^{\infty}\int_{\theta_{q\infty}}^{\theta}U^{\pm}_j(s)F^{\pm}_q(\theta,s)ds\right]V^{\pm}_{\theta}(\underline{x})d\theta$$

$$G^1_j(\underline{x},\underline{x}_s) = D_1 I_1+\int_C\left[\frac{1}{2}U^-_j(\theta)+D_0W^-_o+\frac{1}{2\alpha}\sum_{q=-\infty}^{\infty}\int_{\theta_{q\infty}}^{\theta}U^-_j(s)F^-_q(\theta,s)ds\right]\left[1+e^{i\Phi_1(\theta)}\right]V^-_{1\theta_1}(\underline{x})d\theta \qquad (6.1.11a)$$

$$G^2_j(\underline{x},\underline{x}_s) = D_2 I_2+\int_C\left[\frac{1}{2}U^+_j(\theta)+D_0W^+_o+\frac{1}{2\alpha}\sum_{q=-\infty}^{\infty}\int_{\theta_{q\infty}}^{\theta}U^+_j(s)F^+_q(\theta,s)ds\right]\left[1+e^{i\Phi_u(\theta+\alpha)}\right]V^+_{2\theta_2}(\underline{x})d\theta$$

with,

$$F^{\pm}_q(\theta,s) = \exp i\left[\frac{\Phi^{\pm}(s)}{2}-\frac{\Phi^{\pm}(\theta)}{2}+\frac{1}{2\alpha}\int_s^{\theta}\Phi^{\pm}(\delta)d\delta-\frac{q\Pi(\theta-s)}{\alpha}+E^{\pm}_b(\theta,s)\right] \qquad (6.1.11b)$$

and where,

$$D_0 = (j-2)(j-1)\tfrac{1}{2}, \qquad D_1 = j(2-j), \qquad D_2 = j(j-1)\tfrac{1}{2}$$

Remembering that j ranges from 0 to 2 and that all quantities are as defined in chapter 2. The superscript and subscript of G denote the position of the observation and source positions respectively. The functions I_j are the direct and reflected fields in each case. i.e. I_0 is the direct field given in equation (2.4.1a) of chapter 2 and

$$I_1(\underline{x},\underline{x}_s) = W_{d_1}(\underline{x},\underline{x}_s) + W_{r_1}(\underline{x},\underline{x}_s)$$
$$I_2(\underline{x},\underline{x}_s) = W_{d_2}(\underline{x},\underline{x}_s) + W_{r_2}(\underline{x},\underline{x}_s) \qquad (6.1.12)$$

6.2: The Spectral Structure.

The expostion of the WGF for all configurations of source and obervation points in the above section facilitates the examination of its claimed properties. If the identity of the WGF is a true Green's function for the wedge geometry, excluding the apex, it must possess the following properties:–

(1) Satisfies the wave equation with a delta function source term.
(2) Continuity of the observed field and its normal derivative at each boundary.
(3) Continuity of the observed field for source points crossing each boundary.
(4) Reciprocity.

The first property in this rubric is considerably easier to prove than the others and is dealt with immediately, by noting that the WGF must be a solution of the homogeneous wave equation, as it is constructed spectrally, and in such a manner, that all the integrals are convergent. However, at the point $\underline{x}=\underline{x}_s$ the exponentials defining the plane wave fields and maintaining the convergence properties of the integrals cancel, causing the field to become infinite.

The last three properties are more compilcated to prove and are simplified if a systematic plane wave approach is adopted. This technique involves tracking single or collective plane wave species throughout the wedge environment. Using this approach still requires complicated mathematical expressions to be manipulated, the bulk of which are placed in appendices. This allows for a physical explanation of the procedures in the text using a diagramatical approach where, in the interests of clarity, a particular plane wave species is treated as a local phenomenon. The introduction of terminology, consistent with proceeding sections and chapters, aids the analysis of this section. The double integrals of equation (6.1.11a) will be termed the modal field, as its structure is such that it represents the infinity of wave processes inside the wedge environment by a rapidly convergent modal type series. The source terms required for the above modal field are termed the initial plane wave fields, and all other additional fields are labelled in an obvious manner.

6.2.1: Continuity of the Observed field.

Consider firstly the continuity of the field and its derivative at the upper boundary. This can be mathematically stated as,

$$G_j^0(\underline{x},\underline{x}_s) - G_j^2(\underline{x},\underline{x}_s) \qquad \frac{dG_j^0(\underline{x},\underline{x}_s)}{dn} - \frac{dG_j^2(\underline{x},\underline{x}_s)}{dn} \qquad \underline{x} \in B_u \qquad (6.2.1.1)$$

where n is the direction normal to the interface. At this upper boundary, B_u, the observation plane wave fields are found to be,

$$V_\theta^{\pm}(\underline{x}) = e^{ikz\frac{\cos(\theta\pm\alpha)}{\cos\alpha}} \qquad V_{\theta_2}^{\pm}(\underline{x}) = e^{in_2kz\frac{\cos(\theta_2\pm\alpha)}{\cos\alpha}} \qquad \underline{x} \in B_u \qquad (6.2.1.2)$$

The application of Snell's law on the upper boundary – given in equation (6.1.9) – to these plane wave terms gives an initial indication of the wave relationships occuring at B_u, which are governed by the identities,

$$V_\theta^+(\underline{x}) = V_{\theta+2\alpha}^-(\underline{x}) = V_{\theta_2}^+(\underline{x}) = V_{\theta_2+2\alpha}^-(\underline{x}) \qquad \underline{x} \in B_u \qquad (6.2.1.3)$$

Of the three WGFs, the simplest demonstration of the continuity of the observed field across the upper boundary, is when the source point is in the lower medium. In this case all the wave fields are contained in the initial and modal spectra, which is obvious from its construction. The diagram of Figure 6.2.1.1 describes the first two different types of plane wave field which are transmitted into the upper medium and the associated plane wave fields in the guiding layer.

Figure 6.2.1.1: Plane Wave Species for Source Points in medium 1 for the proof of the Upper boundary condition.

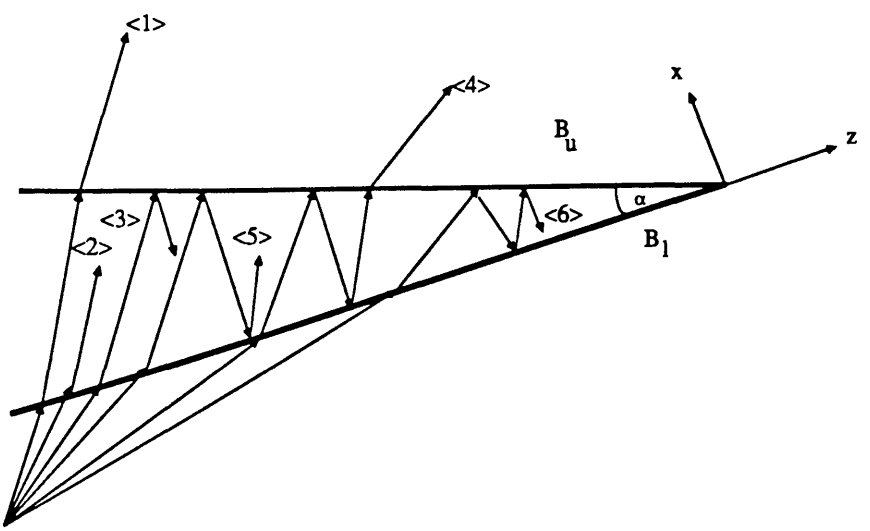

There is obviously an infinity of other different types of plane wave field transmitted into the upper medium. These other types of field differ from either <1> or <4> by an integer number of double reflections (reflected off B_u and B_l), an appropriate path length change and by a propagation direction rotated by $2n\alpha$, where n is an integer. All these different species of plane wave field are represented collectively as a specific plane wave field, which is the modal expression defined in (6.1.11). The preceeding description is applicable to all other infinite reflection processes represented collectively by a modal concept and discussed in this work. On examination of equations (6.1.11) and (6.2.1.3), in conjunction with Figure 6.2.1.1, it can be observed that a transmitted plane wave field (<1> or <4>) on B_u consists of the corresponding upward plane wave field (<2> or <5>), calculated in the guiding medium, with an appropriately defined transmission coefficient attached. The two types of plane wave field corresponding to the above transmitted field in the guiding layer consist of an upward field (<3> or <6>), orientated at the appropriate angle, and a downward field propagating with a defined angle 2α greater than the upward field. Using the above statements and equations (6.1.11), (6.2.1.3) the proof of the continuity of the observed field across B_u for the WGF, when the source point is in the substrate, requires that the downward field in medium $_0$, rotated by 2α, must be equivalent to the upward field in the same medium with the corresponding reflection coefficient attached. This equivalence is demonstrated in appendix G and hence the boundary condition is satisfied.

The next case to consider is when the source lies in the guiding medium, the problem being made slightly more difficult because of the necessary introduction of the direct and refracted fields. The diagrams of Figure 6.2.1.2 illuminate the presence of two distinct categories of plane wave field. The first category is comprised of fields where the plane waves are launched from the source in a negative x direction, the second category being where the plane waves are launched in a positive x direction. Figure 6.2.1.2(a) describes pictorially the general types of plane wave field in category one. Using identical analysis as for the previous WGF, it is found that for the proof of the continuity requirement it is necessary that the downward plane wave field (rotated by 2α) in the guide must equal the upward field in the guide with a sutiable reflection coefficient attached. This equality is demonstrated in appendix G. The second category of plane waves is more difficult to analyse. The simplest method for analysing this complicated wave category is diagramatically, noting from equation (6.1.11) that the direct field and the refracted direct field are twice the size of the initial and modal fields. Using Figure 6.2.1.2(b) the transmitted species <5>, on B_u, is equal to the two plane wave species <4> and <6> at the upper boundary. In a similar fashion the refracted type <1> is equal to the the direct species ,<2> and twice the initial species <3> at the upper boundary. It must be noted that <5> and <4> are initial species and <6> is part of the modal plane wave species. Consequently the

continuity of the observed field at B_u is preserved if the difference between the modal field inside the guide and the transmitted modal field (both evaluated at B_u) are equal to the downward initial field <3>, rotated by 2α, and the difference between the initial transmitted plane wave species, <5>, and the upward species <4>. This equality is demonstrated in appendix G and as a result the continuity requirements of the observed field for the upper boundary B_u when the source is in medium 0 are satisfied.

Figure 6.2.1.2(a,b): Plane Wave Species for Source Points in medium 0 for the proof of the Upper boundary condition.

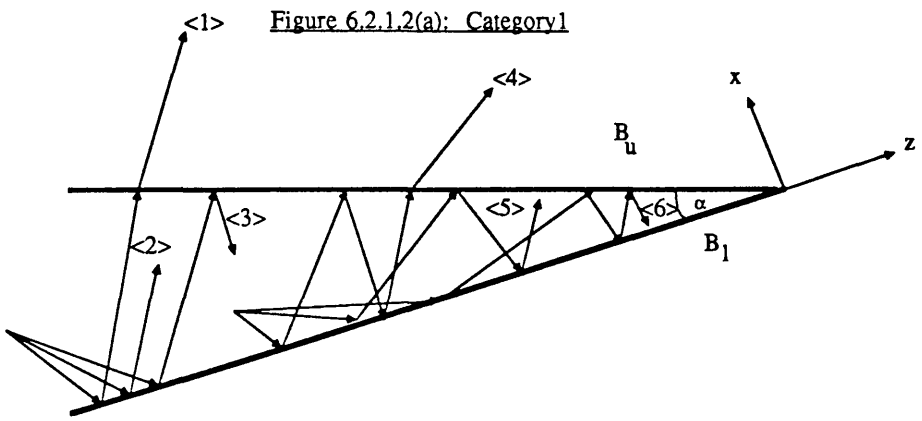

Figure 6.2.1.2(a): Category1

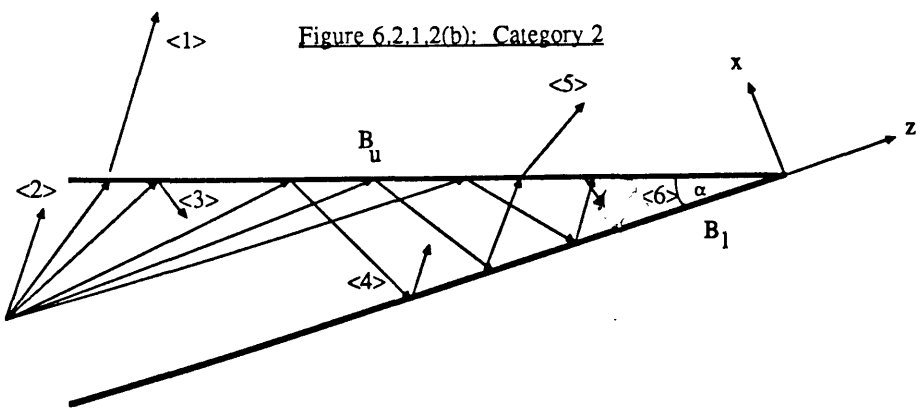

Figure 6.2.1.2(b): Category 2

The final case to examine is when the source point is in the upper medium. The first initial plane wave species are shown in Figure 6.2.1.3.

Figure 6.2.1.3: Plane Wave Species for Source Points in medium 2 for the proof of the upper boundary condition.

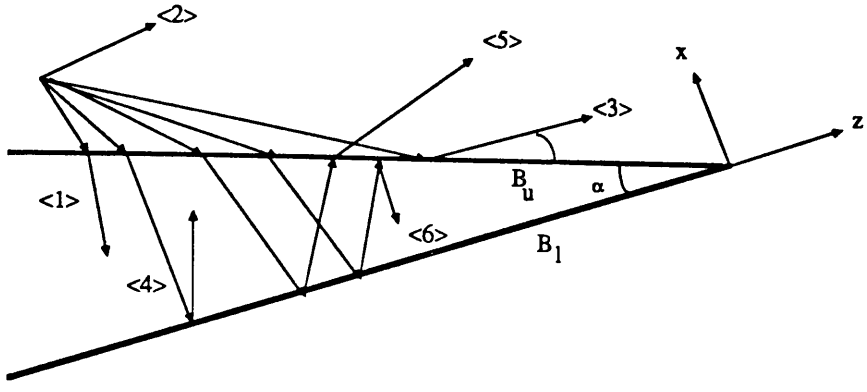

As with source points in the guiding medium, the proof of observed field continuity across B_u is eased greatly by using a schematic approach. The plane wave species are depicted for this situation in Figure 6.2.1.3. As previously it is apparent from equation (6.1.11) that the direct species, <2>, and the reflected species, <3>, are twice as large as all other plane wave species. Consequently from Figure 6.2.1.3 twice the transmitted field, <1>, must equal the direct field <2> and reflected field <3>. In a similar manner the transmitted species <5> must be equal to species <4> and <6> evaluated on B_u. The transmitted species <5> is represented by the initial fields, which is equal to the initial field <4> and a portion of the modal field <6>. Thus the continuity of the observed field requires that the difference between the modal field inside the guide and the transmitted modal field calculated at the boundary B_u must equal the initial downward field inside the guide and the difference between the initial transmitted field <5> and the initial upward field <4>. This equality is proved in appendix G and hence the WGF for source points in the upper medium possesses the correct boundary conditions at B_u.

At the lower boundary B_l the boundary conditions can be stated mathematically as,

$$G_j^0(\underline{x},\underline{x}_s) = G_j^1(\underline{x},\underline{x}_s) \qquad \frac{dG_j^0(\underline{x},\underline{x}_s)}{dx} = \frac{dG_j^1(\underline{x},\underline{x}_s)}{dx} \qquad \underline{x} \in B_l \qquad (6.2.1.4)$$

The proof of the lower boundary conditions follows a similar procedure as for the

upper boundary, which is discussed geometrically in the text and proved mathematically in appendix G. The observable plane wave identities for the lower boundary are found to be,

$$V_{\theta}^{+}(\underline{x}) - V_{\theta}^{-}(\underline{x}) - V_{1\theta_1}^{+}(\underline{x}) - V_{1\theta_1}^{-}(\underline{x}) \qquad (6.2.1.5)$$

As before the simplest case to examine is when the WGF can be represented totally by only initial and modal fields at the lower boundary. This situation arises for the WGF representing source points in the upper medium. Figure 6.2.1.4 depicts the plane wave species of this particular WGF incident on B_l.

Figure 6.2.1.4:

Plane Wave Species for Source Points in medium 2 for the proof of the Lower boundary condition.

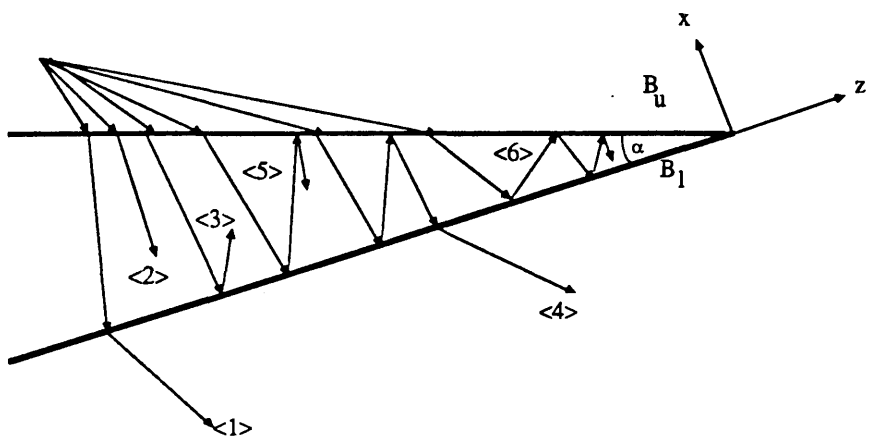

Examining Figure 6.2.1.4 it is immediately apparent that the initial transmitted field <1> is equal to the initial fields <2> and <3> evaluated on B_l. Similarly plane wave species <4> must equal <5> and <6>, all of which are represented in modal form. Thus to demonstrate the satisfaction of the lower boundary condition requires that the transmitted modal field equals the modal fields inside the guide, evaluated at B_l, and that the transmitted initial field is equivalent to the initial fields <2> and <3> on the boundary. These two equalities are demonstrated in appendix G.

The second case to consider is when the source point is in the guiding medium. In this case the same two categories described for the upper boundary exist, except here the second category can be treated as for the source point in the upper medium (shown in appendix G) and more complicated analysis has to be utilised for the first category.

Figure 6.2.1.5(a,b): Plane Wave Species for Source Points in medium 0 for the proof of the lower boundary condition.

Figure 6.2.1.5(a): Category 2

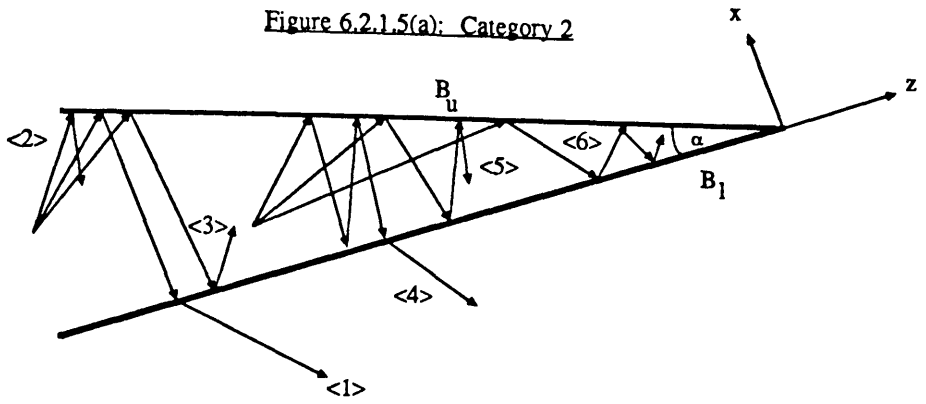

Figure 6.2.1.5(b): Category 1

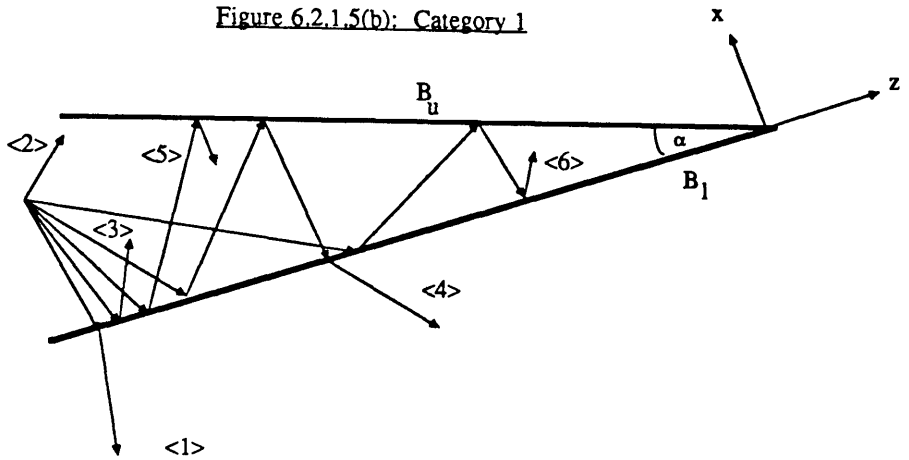

Using Figure 6.2.1.5(a), where category two is depicted it is immediately obvious that the transmitted initial species $<1>$ is equivalent to the the initial species $<2>$ and $<3>$. As $<4>$, $<5>$, and $<6>$ are represented in modal form in the WGF and the obvious equality (i.e. $<4>=<5>+<6>$ on B_l) must be preserved, then boundary condition is satisfied if total transmitted field equals field inside the guide evaulated at B_l. This property is shown in appendix G. Category one is slightly more complicated, however using a diagramatical approach (Figure 6.2.1.5(b)) the analysis of appendix G is made much simpler. In this instance the transmitted field, $<1>$, is equal to the direct field, $<2>$, and twice the reflected field, $<3>$, (from equation (6.1.11a)) calculated on the boundary B_l. In an analogous manner species $<4>$ must equal species $<5>$ and $<6>$ on the boundary. As the transmitted species $<4>$ and downward species $<5>$ are represented in the initial fields, then to demonstrate continuity of observed field requires that the difference in modal fields on B_l is equivalent to the initial field $<3>$ and the difference between the initial fields $<5>$ and $<4>$. The above requirement is proved in appendix G.

Figure 6.2.1.6: Plane Wave Species for Source Points in medium 1 for the proof of the lower boundary condition.

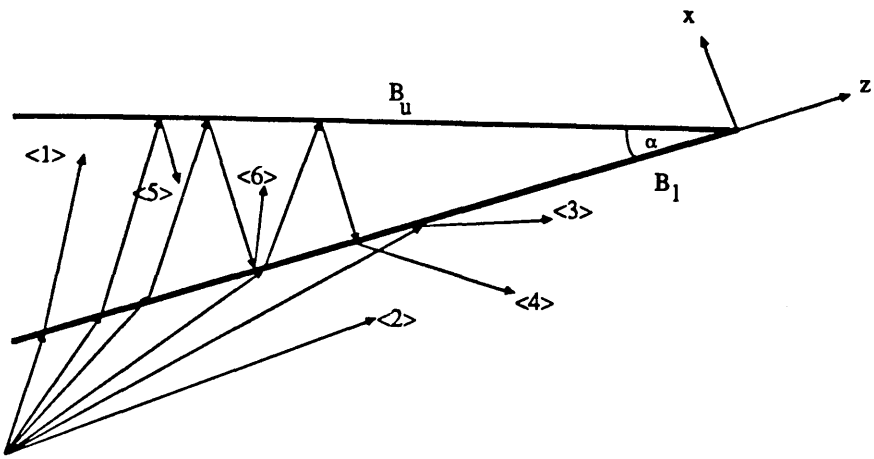

The last boundary condition to satisfy for the observed field is the lower boundary B_l when the source point is in the lower medium. Figure 6.2.1.6 displays the first few initial spectral species present in this situation. Again it is seen from equation (6.1.11) that the direct species $<2>$ and the reflected species $<3>$ are twice as large as all other plane wave types. Using Figure 6.2.1.6 twice the transmitted initial species, $<1>$, equals the plane wave species $<2>$ and $<3>$. Also the initial transmitted species $<4>$ must equal plane wave species $<5>$ and $<6>$. From the above two statements the continuity of the observed field is preserved if the difference in the modal fields is equal to the initial field of type $<1>$ and the difference between the field types $<4>$ and $<5>$. This is demonstrated in appendix G.

6.2.2: Continuity of the Observed Field for Different WGFs.

The preceeding analysis has demonstrated that the three independently derived WGFs satisfy the continuity requirements on the observed field at the upper and lower boundary. As the WGFs were constructed independently it is necessary to demonstrate that these functions are also consistent. In other words the evaluation of the observed field when a source point is coincident with a boundary must be independent of either of the two WGFs that may be legitimately applied. On first inspection it would appear

that six different categories need to be examined, because of two boundaries and three possible positions of the observation points. However, as the continuity of the observed field has been demonstrated, a single arbitrary observation point will be sufficient to demonstrate the continuity of the source field. Due to these properties of the WGFs only two cases need to be examined – i.e those for source on either of the two boundaries – with the arbitrary observation point placed in the guiding medium. Consider firstly the source points on the lower boundary. The different spectral species for the two WGF representations are shown in Figures 6.2.2.1

Figure 6.2.2.1: The Plane Wave Species for the Continuity of the Observed field as the source point traverses the lower boundary

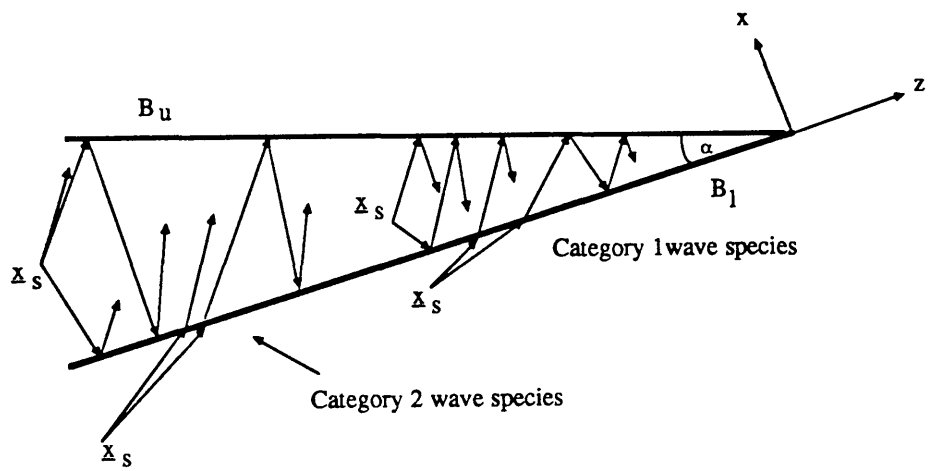

Using the geometrical representations in Figure 6.2.2.1 the source point inside the guide has the two categories defined for the proof of the observation boundary conditions. When the source point is on the lower boundary then the species of category 1 are either initial or modal fields and are all downward. Applying Snell's law for the lower boundary from equations (6.1.4) generates source plane wave identities,

$$W_1^-(\theta_1) = W_0^-(\theta) = W_1^+(\theta_1) = W_0^+(\theta) \qquad (6.2.2.6)$$

Using the above identities and appropriate shifts of 2α it is clearly seen that the downward field from source points outside the guide (equation (6.1.4)) is identical to the downward field for source points inside the guide (equation (2.4.3b)). Thus continuity of the observed downward field is maintained as the source point crosses the lower boundary. The category 2 plane wave species are such that the difference

between the two modal expressions for this category must equal the difference in the initial and direct fields. This equality is proved in appendix G.

Figure 6.2.2.2: The Plane Wave Species for the Continuity of the Observed field as the source point traverses the upper boundary

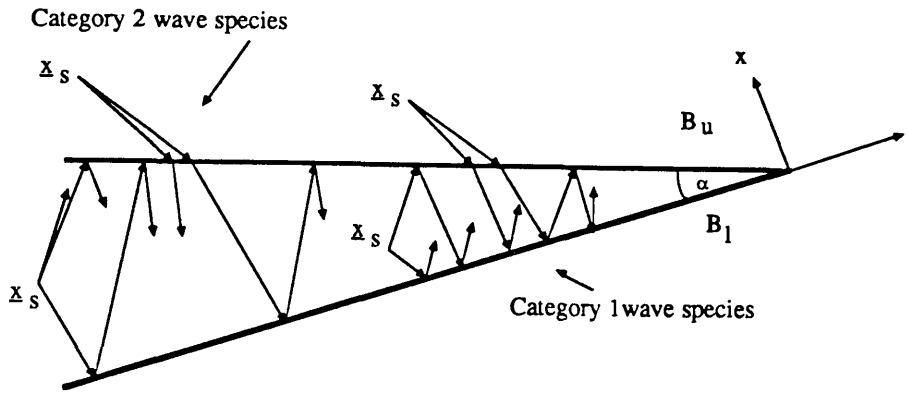

The upper boundary case is similiar in construction and is shown in Figure 6.2.2.2. Using the particular definitions of Snell's law on this boundary from equation (6.1.9), produces the source plane identities,

$$W_2^-(\theta_2' + \alpha) = W_0^-(\theta) \qquad W_2^-(\theta_2 + 2\alpha) = W_0^+(\theta) \qquad (6.2.2.7)$$

The upward field consists of only the initial and modal spectrum, and is shown pictorially as category 1 species. Applying shifts of 2α to the even−order reflected fields and using the identities (6.2.2.7) then it is clear that the upward field from the source point inside the guide (equation (2.4.3a)) is equal to the upward field from the source point in the upper medium (equation (6.1.9)). Category 2 fields must also be equivalent and this equality is proved in appendix G by noting that the difference in modal fields of the two representations is equal to the difference between their initial and direct fields.

6.2.3: Reciprocity.

The last property which needs to be proved is reciprocity. This can be stated mathematically in a simple way by,

$$G_n^j(\underline{x}, \underline{x}_s) = G_j^n(\underline{x}_s, \underline{x}) \qquad (6.2.3.1)$$

where n and j range from 0 to 2. There are nine equations in the representation of (6.2.3.1), but because of the properties of the WGFs necessitates only examination of one particular configuration of source and observation point. The case considered is when the source and observation point are in the guiding medium (medium 0). While this property can be stated simply as in equation (6.2.3.1), the proof is considerably more involved than any of the preceeding analysis. As previously the bulk of the mathematical analysis is in appendices, and a geometrical exposition of the proof is given in the text.

Figure 6.2.3.1: Different plane wave types for the proof of Reciprocity.

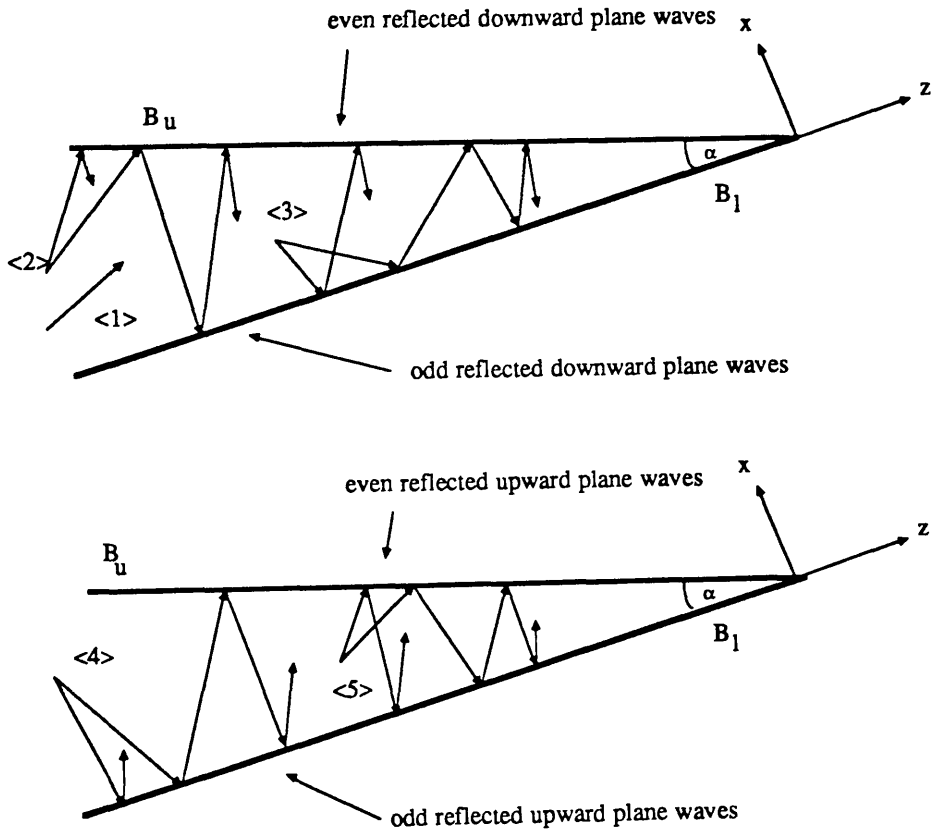

Reciprocity must be demonstrated for all plane wave species in the wedge geometry. The method of proof for reciprocity is achieved by the following analytical steps. The upslope WGF has its source and observation point interchanged and then substitutions are used (obtained from Figure 6.2.3.1) in conjunction with contour shifts to show that this is equivalent to the original upslope WGF formalism. The simplest case to prove is the direct field depicted as species <1> in Figure 6.2.3.1. The substitution $\theta - \Pi$ is applied to the direct field when source and observation points are interchanged, and then deforming the contour produces the original formalism of the direct field. All

other reflected field processes can be described by either an odd or even number of reflections. Using the diagram of Figure 6.2.3.1 there are two different cases to examine in each of the above reflection cases.

Consider firstly the odd reflected field which is downward at the observation point, represented as the plane wave species <2>. The initial and modal fields for this case can be represented by,

$$\int_C e^{ikr_s\cos(\theta-2\alpha+\chi_s)} e^{i\Phi_u(\theta-\alpha)} e^{-ikr\cos(\theta-\chi)} d\theta \qquad (6.2.3.9a)$$

$$\int_C \frac{1}{2\alpha} \sum_{q=-\infty}^{\infty} \int_{\theta_{q\infty}}^{\theta} F_q^-(\theta,s) e^{ikr_s\cos(s-2\alpha+\chi_s)} e^{i\Phi_u(s-\alpha)} ds\, e^{-ikr\cos(\theta-\chi)} d\theta \qquad (6.2.3.9b)$$

respectively. The source and obervation points are interchanged and then with the aid of Figure 6.2.3.1 the appropriate substitutions are made to show that this formalism is equal to (6.2.3.9a) and (6.2.3.9b). This is carried out in appendix I where similar analysis is used on the other odd field (denoted by species <4>).

The even reflected fields are slightly different as both the upward and downward fields are interelated. The upward even reflected initial and modal fields at the observation point (species <5>) are,

$$\int_C e^{ikr_s\cos(\theta-2\alpha+\chi_s)} e^{i\Phi^+(\theta-2\alpha)} e^{-ikr\cos(\theta+\chi)} d\theta \qquad (6.2.3.10a)$$

$$\int_C \frac{1}{2\alpha} \sum_{q=-\infty}^{\infty} \int_{\theta_{q\infty}}^{\theta} F_q^+(\theta,s) e^{ikr_s\cos(s-2\alpha+\chi_s)} e^{i\Phi^+(s-2\alpha)} ds\, e^{-ikr\cos(\theta+\chi)} d\theta \qquad (6.2.3.10b)$$

respectively. Interchanging the source and observation point and using the substitutions indicated by Figure 6.2.3.1 will give the same field as if the observed field were even reflected downwards <3>. This is demonstrated in appendix I as is the case when the original modal spectrum is downward at the observation point and interchanging the source and observation looks like the upward field at observation point <5>.

The above demonstration of the reciprocity of all the different plane wave types which constitute the WGF implies that this function itself possesses the reciprocity property.

6.3: Asymptotic Analysis of a Wedge Green's Function.

The above section dealt with the exact analytical proofs of the WGF. This section is concerned with approximate asymptotic forms of the WGF, which will allow further confirmation of a correct numerical algorithm. This analysis, although specific to the Jensen–Kupermann ocean problem and a WGF having a source point in the guiding duct, can be applied to any wedge environment. The method of approach involves treating the modal spectrum and the initial spectrum separately as different asymptotic parameters are employed in their evaluation. This analysis considers only source points which are in guide cross–sections much greater than the critical guide height h_c.

6.3.1: The Modal Spectrum.

Inspection of one particular term in the infinite modal sum allows for a cleaner exposition of the analysis. The modal term indexed by the integer q can be represented asymptotically with respect to the smallness parameter α as,

$$M_q(\underline{x},\underline{x}_s) \sim \begin{cases} \sum_{C}^{\pm} \int_{\theta_{q\infty}}^{\theta} H^{\pm}(\theta,s) e^{\frac{iB_q(\theta,s)}{\alpha}} \, ds d\theta + O(\alpha^2) & \underline{x}\epsilon X_0 \\ \int_{C} \int_{\theta_{q\infty}}^{\theta} \left[1 + e^{i\Phi_1(\theta)}\right] T(\theta,s) e^{\frac{iB_q(\theta,s)}{\alpha}} \, ds d\theta + O(\alpha^2) & \underline{x}\epsilon X_1 \end{cases} \qquad (6.3.1.1a)$$

where,

$$B_q(\theta,s) = \frac{1}{2} \int_{s}^{\theta} \Phi_1(\delta) d\delta - \Pi(q-\tfrac{1}{2})(\theta-s) - nk(h\cos\theta - h_s\cos s) + E_b^{-}(\theta,s) \qquad (6.3.1.1b)$$

and from equation (6.1.11) and using the analysis of appendix B,

$$H^{\pm}(\theta,s) \sim \begin{cases} e^{i\Phi_1(s)} \left[e^{ink x_s \sin s} - e^{ink(2h_s - x_s)\sin s} \right] e^{inkx\sin\theta} e^{iJ(\theta,s)} \\ \left[-e^{ink(2h_s - x_s)\sin s} - e^{i\Phi_1(s)} e^{ink(2h_s + x_s)\sin s} \right] e^{-inkx\sin\theta} e^{iJ(s,\theta)} \end{cases} \qquad (6.3.1.1c)$$

$$T(\theta,s) \sim \left[-e^{ink(2h_s - x_s)\sin s} - e^{i\Phi_1(s)} e^{ink(2h_s + x_s)\sin s} \right] e^{-in_1 kx\sin\theta_1} e^{iJ(s,\theta)}$$

and

$$J(\theta,s) = \frac{\Phi_1(\theta)-\Phi_1(s)}{2}$$

The reason for the $M_q(\underline{x},\underline{x}_s)$ being defined as the 'modal' term is now demonstrated. As stated previously the analysis of each modal term $M_q(\underline{x},\underline{x}_s)$ is concerned with instances when the source point, in the guiding layer, is in a region where the Adiabatic Mode, indexed by the integer q, exists. Although this analysis examines only a subset of possible source and observation point configurations, it is sufficient to indicate the nature of the field. The phase of the modal field $M_q(\underline{x},\underline{x}_s)$, with $q=2$, is shown in Figure 6.3.1.1.. In these diagrams the phase of the odd reflected upward field of $M_q(\underline{x},\underline{x}_s)$, for observation points inside the guide, is plotted against the propagation angle of the source and observation plane waves.

Figure 6.3.1.1(a):

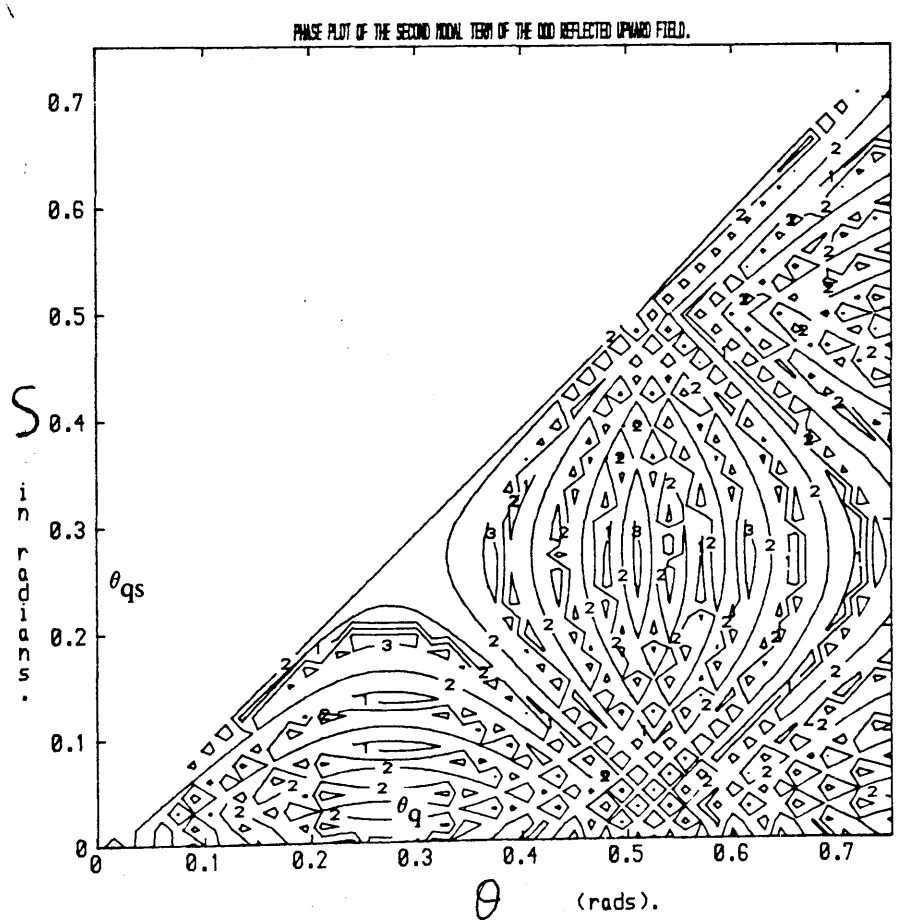

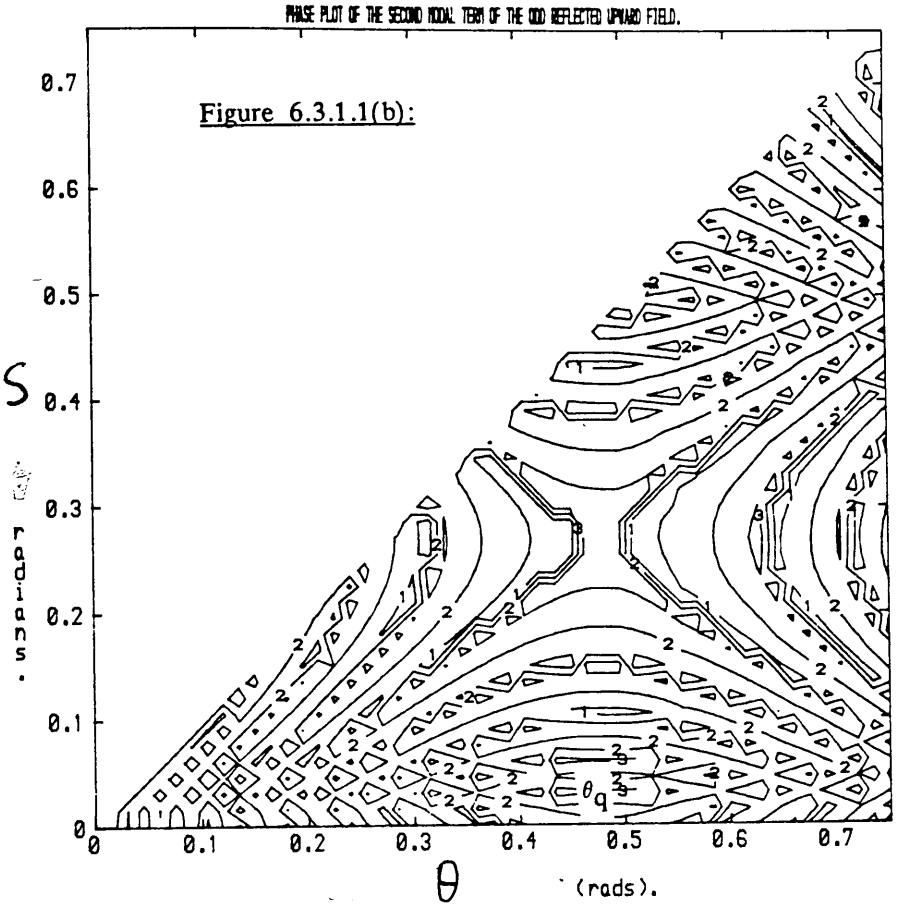

Figure 6.3.1.1(b):

Figure 6.3.1.1(c):

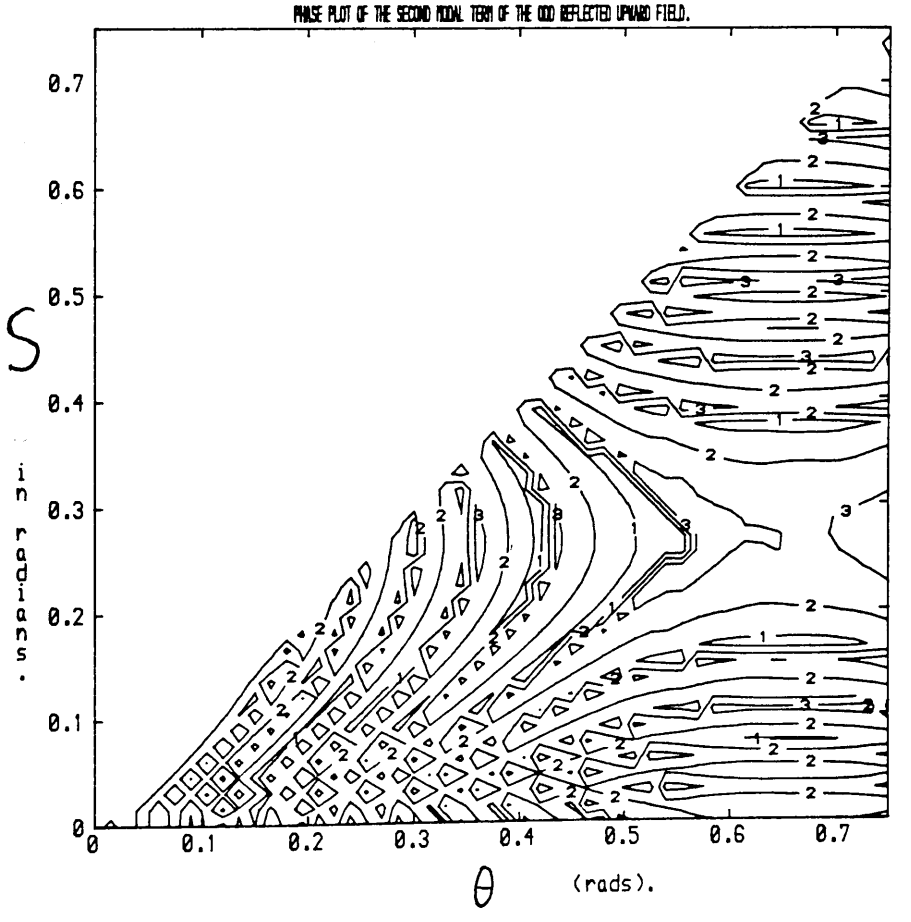

In the above two dimensional phase plots the source point is in a cross–section where the local guide height is 216m and the propagation angle of the second normal mode in a translationally invariant guide of this cross–section is .225 radians. In Figure 6.3.1.1(a) the observation point is at a range where the local guide cross–section is 200m, and the second AM at this point can be constructed by two counter–propagating plane waves at an angle .274 radians. Figure 6.3.1.1(b) has its observation point in a cross–section where the local guide height is 105m and the plane waves which constitute the second AM are propagating at an angle .4724 radians. Figure 6.3.1.1(c) has the observation point in a region where the local guide height is 94m, which is unable to support a second normal mode, and consequently the modal angle is now complex. In this case a two dimensional saddle point is still observed because the integrand will still be slowly varying around the real part of the complex angle if this modal angle possesses only a small imaginary part. From all three diagrams the two dimensional saddle points are positioned at (θ_q, θ_{qs}) where θ_q and θ_{qs} are the stationary phase points in the observation and source variables which solve the equations,

$$\frac{\partial B_q(\theta,s)}{\partial \theta} = 0 \qquad \frac{\partial B_q(\theta,s)}{\partial s} = 0 \qquad (6.3.1.2)$$

respectively. These equations are the transverse resonance conditions for the observation and source cross–sections respectively. The observed spectral content of $M_q(\underline{x},\underline{x}_s)$, for observation points inside the guide, reveals a modal structure which can be explained by a Intrinsic Mode interpretation of the wave processes. When the observation point is inside the guide, $M_q(\underline{x},\underline{x}_s)$ can be represented in the same notation as in equation (6.3.1.2) of chapter 4 by noting that $B_q(\theta,s) = Z_q(\theta,\underline{x}) - Z_q(s,\underline{x}_s)$, to give,

$$M_q(\underline{x},\underline{x}_s) = \sum_{-}^{+} \int_C F^{\pm}(\theta,\underline{x}) e^{\frac{iZ_q(\theta,\underline{x})}{\alpha}} \left[\sum_{-}^{+} \int_{\theta_{q\infty}}^{\theta} F^{\pm *}(s,\underline{x}_s) e^{-\frac{iZ_q(s,\underline{x}_s)}{\alpha}} ds \right] d\theta \qquad (6.3.1.3)$$

where * denotes complex conjugation and dependence on source or observation point is indicated explicitly. From equation (6.3.1.3) it is clear that if the bracketted term is a constant, D say, with respect to θ then the asymptotic modal term is merely the Intrinsic Mode field multiplied by D. It will be demonstrated later in this chapter that this assumption is approximately valid when the source and observation points are many wavelengths apart. There are three different regions which are examined asymptotically and these are determined by the position of the observation point, which can be situated in any of the following regions:–

(1) A region where the qth Adiabatic Mode exists.

(2) The critical transition region for the qth modal term.

(3) A purely radiative region.

and the source point is positioned at $z_s = -9$Km and $x_s = 50$m. This source position is such that it is a sufficient distance from any observation point of interest to enable the saddle point to be considered as isolated (this is the case for Figures 6.3.1.1(b)(c)). Consider firstly the case when the observation point is in region (1). This configuration produces the constraint $\theta_c > \theta_q > \theta_{qs}$. The spectral content of the observed odd reflected downward field inside and outside the guide for this situation is shown in Figure 6.3.1.2. noting that no topological differences occur in any of the other possible wave species.

Figure 6.3.1.2:

Real Part Of Odd Reflected Downward Field

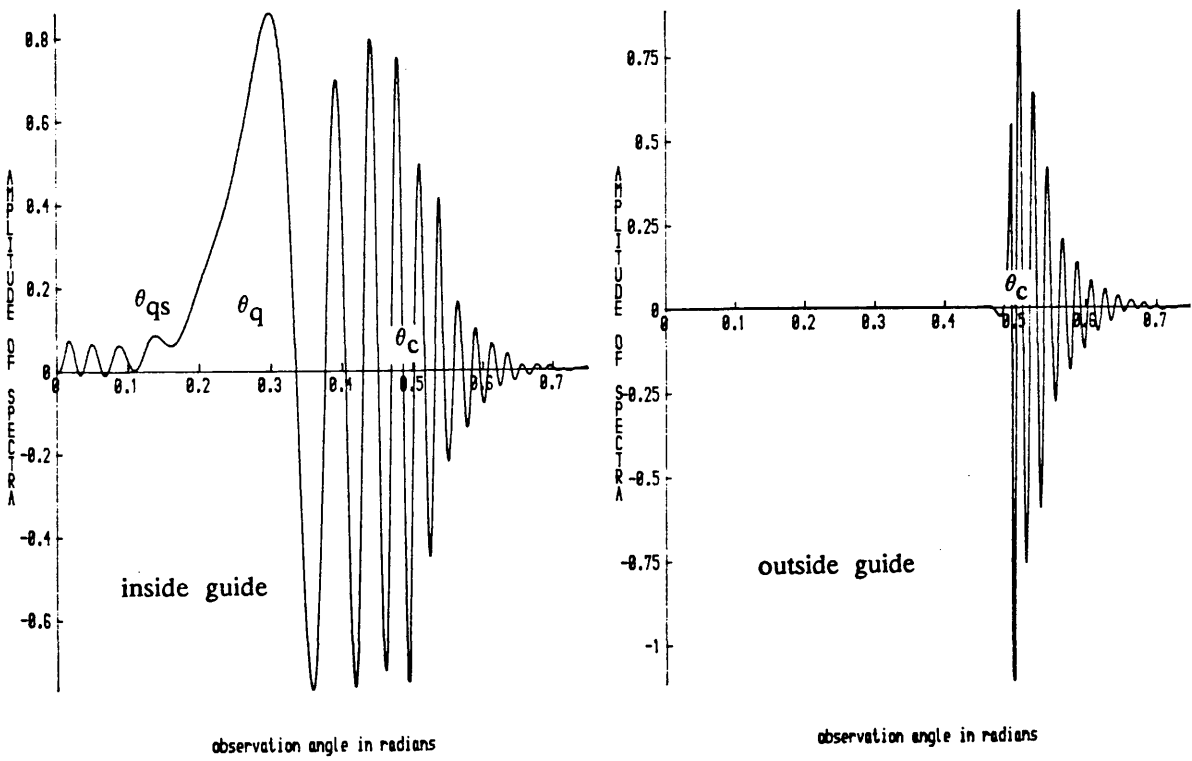

The steepest descent paths for this case are indicated in Figure 6.3.1.3

Figure 6.3.1.3:

Steepset Descent Paths of the Modal part of the WGF in the observation plane when the mode is well guided.

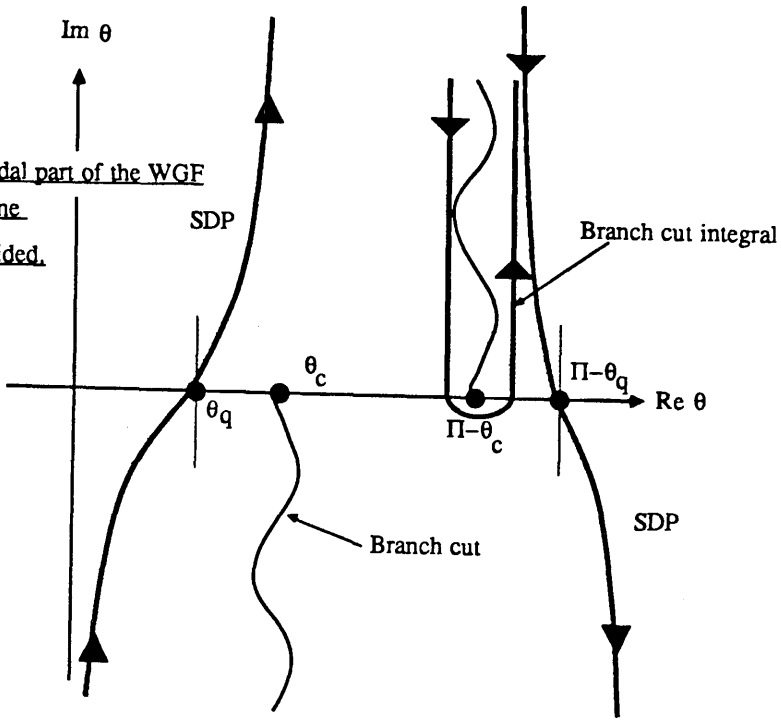

The field in this region can be asymptotically represented considering only the contribution from the stationary phase point at (θ_q, θ_{qs}) (see appendix J) which is,

$$M_q(\underline{x},\underline{x}_s) \sim w_q^*(\underline{x}_s)w_q(\underline{x})\left[1 - \Pi^{-\frac{1}{2}}\int_{-\infty}^{X} e^{-p_s^2}dp_s\right] \qquad (6.3.1.4)$$

where $w_q(\underline{x})$ is the asymptotic function defined in equation (4.3.1.3) of chapter 4. The remaining integral term in (6.3.1.4) corresponds to the saddle point being close to the endpoint of the source integral which is the case highlighted in Figure 6.3.1.1(a). The retention of the Fresnel integral term in (6.3.1.4) is necessary only when the source and observation point are in close proximity. As mentioned earlier the source and observation points are well separated and using appendix J for asymptotically small wedge angle it is found that $X \to -\infty$ and the Fresnel integral of (6.3.1.4) can be neglected. The neglect of the Fresnel integral is assumed for all the following analysis, which is justifiable because separation between source and observation point will be greater than when the observation point is in region (1).

It is useful to examine the nature of the modal term $M_q(\underline{x},\underline{x}_s)$ by investigating, in an asymptotic manner, the phenomena occuring at the source and observation cross-sections independently. The field from the source point which excites the modal field is the same for all positions of observation point so that this discussion of the wave processes at the source plane can be applied to the other two regions of interest. The steepest descent contours for the source variable, shown in Figure 6.3.1.4, are

similar to those for the reflected field from a source point above a half plane [43] which is as expected.

Figure 6.3.1.4:
Steepest Descent Paths of the Modal part of the WGF
in the source plane
for all positions of observation point considered.

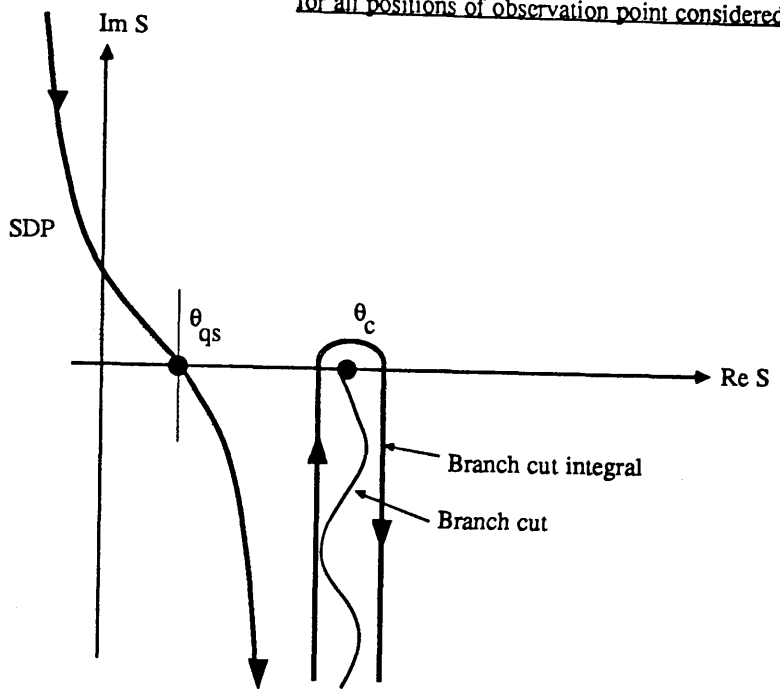

The contour integral around the branch point represents collectively the launching of all possible lateral rays and their further interaction with the planar boundaries. As the decay of these lateral ray fields is large compared to the modal field they are neglected from any asymptotic analysis. The source field from around θ_{qs} contributes significantly to the modal term which can easily be demonstrated by examination of the observed spectrum.

It must be remembered that the amplitude of each plane wave, propagating at an angle θ say, in this spectrum, has been obtained by an integral over the source field from $\theta_{q\infty}$ to θ and an Intrinsic Mode like amplitude function (see equation (6.3.1.3)). The above statement can now explain adequately the phase plots of Figure 6.3.1.2. When the observed plane waves are propagating at an angle less than θ_{qs} then the source integral does not contain a stationary phase point. Consequently the contribution from this integral to the field is asymptotically small, which is clearly seen

in Figure 6.3.1.2. When the plane waves are propagating at angles greater than θ_{qs} the endpoint of the source integral is greater than the stationary phase point and the integral contributes to significantly to the field. As there are no more features which will change the source integral contribution asymptotically for all $\theta > \theta_{qs}$, this integral can be regarded as a constant. Thus it is seen in Figure 6.3.1.2 that the spectrum of the observed field for angles greater than θ_{qs} is very similar to the spectrum of the Intrinsic Mode (c.f. Figure 4.3.3.1 of chapter 4) which is as predicted.

When the observation point is in the critical transition region for the qth Adiabatic Mode, the steepest descent paths for observation field are as shown in Figure 6.3.1.5.

Figure 6.3.1.5: Steepst decent path in the observation plane of the Modal part of the WGF when the observation point is in the critical transition region

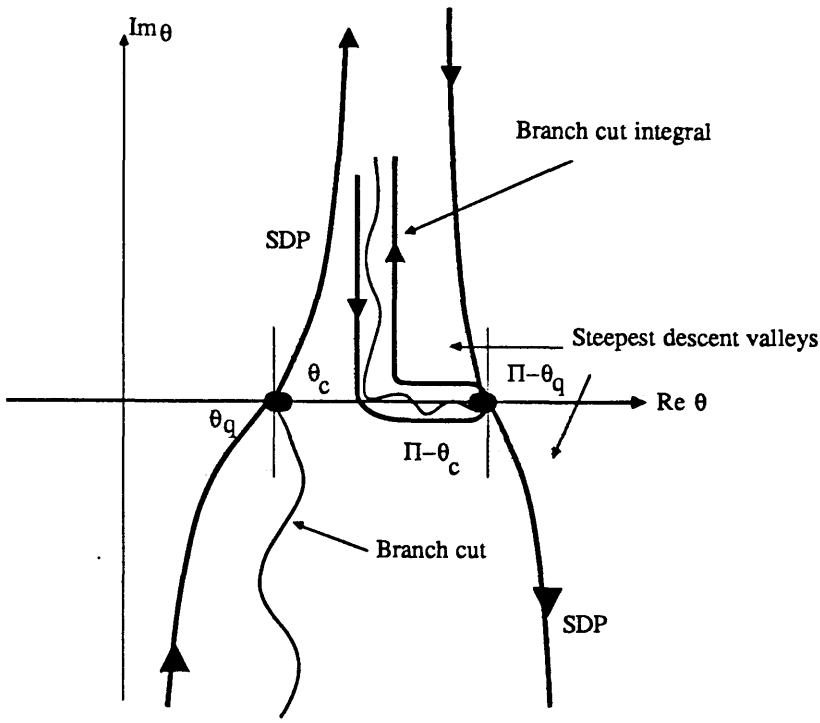

The observed spectral content for the odd reflected downward field, for observation points in region two is depicted in Figure 6.3.1.6, which are as expected similar, topologically speaking, to Intrinsic Mode spectral fields. The noise introduced in these amplitude plots is due to round off errors in the numerical evaluation as only single precision complex number representation was possible. This computer generated noise has little effect on the actual field as it has then to be integrated, which will have the effect of filtering this high frequency noise.

Figure 6.3.1.6:

Real Part Of Odd Reflected Downward Field

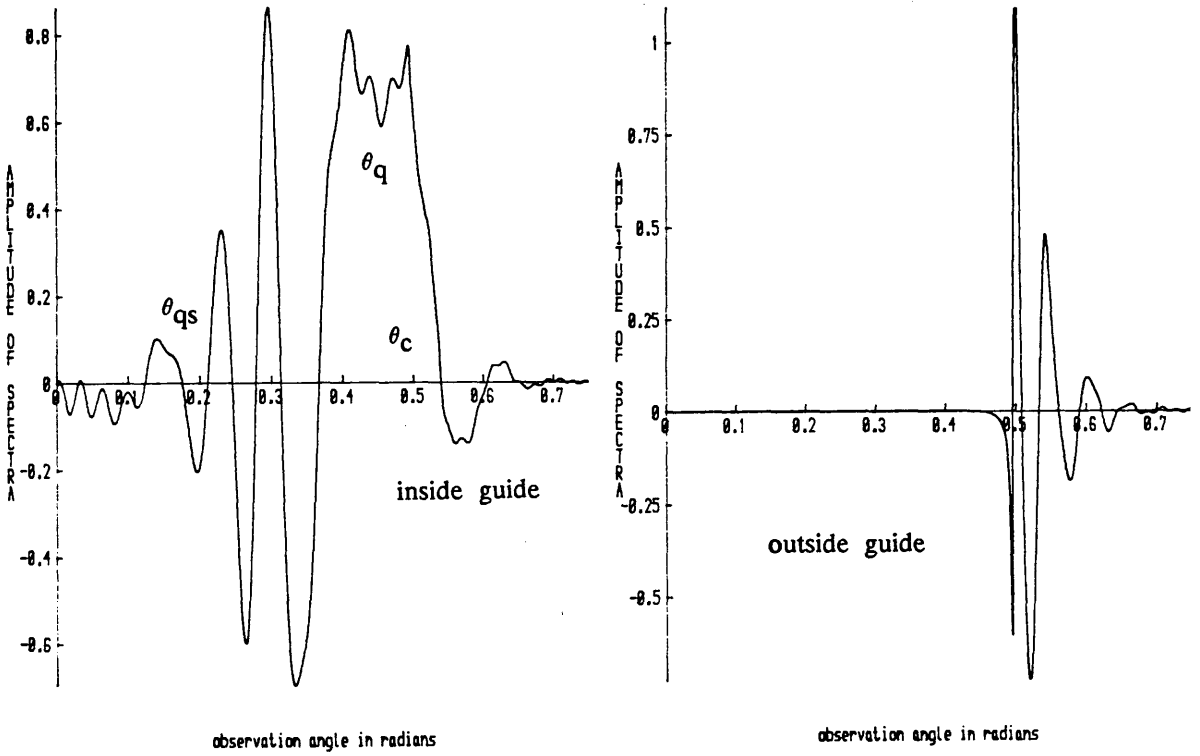

The field in this region can be calculated by the same method as the Intrinsic Mode field, given in appendix E, with the appropriate source weighting function attached. When the observation point is in region 3, the contribution to the modal term $M_q(\underline{x},\underline{x}_s)$, is dictated by the steepest descent paths shown in Figure 6.3.1.7

Figure 6.3.1.7: Steepst decent path in the observation plane of the Modal part of the WGF when observation point is in the Radiating Regime

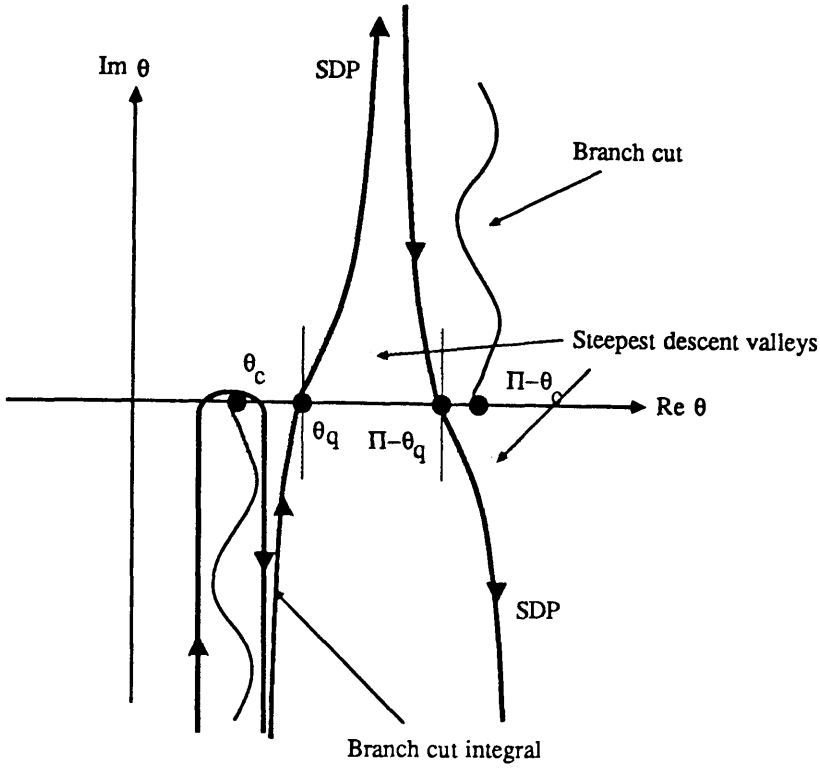

The appropriate spectrum of the observed odd reflected downward field for observation points inside and outside the guide is shown in Figure 6.3.1.8.

Real Part Of Odd Reflected Downward Field

Figure 6.3.1.8:

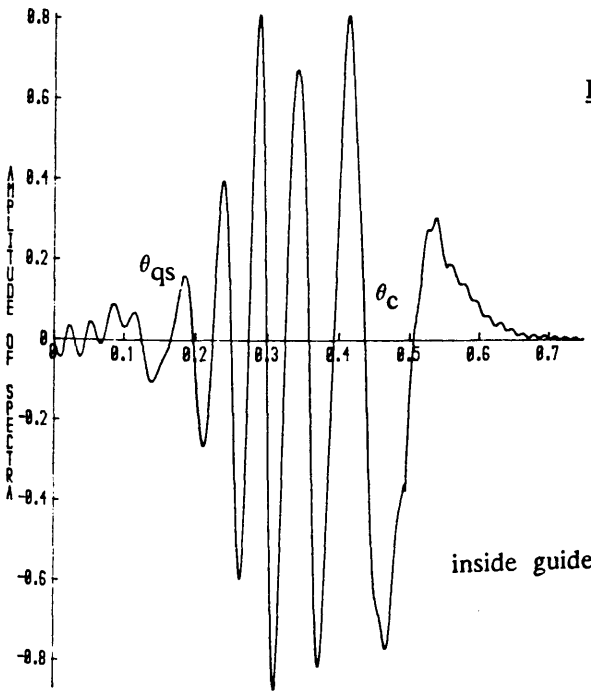

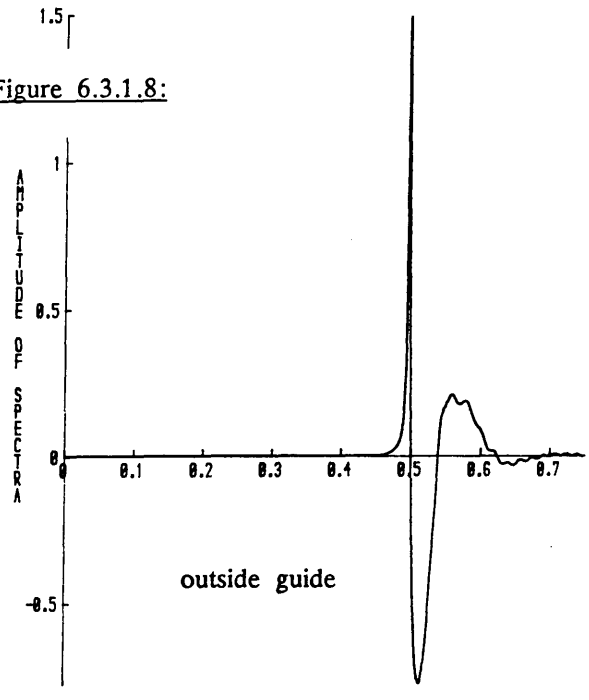

The asymptotic field in this region consists of the Adiabatic Mode coupling to the lateral field, arising from the branch cut integral and the radiation field from the complex stationary phase point. The field in this region is the same as in chapter 4 with the weighting function $w_q^*(\underline{x}_S)$ attached. Arnold and Felsen [24] have demonstrated that these asymptotic forms are asymptotically equivalent to the boundary layer approach of Pierce [20].

Having discussed the asymptotic forms and the physical implications of a part term in the modal portion of the WGF it would now be suitable to calculate this spectral term. Firstly the endpoint $\theta_{q\infty}$ was made equal to zero, which is allowable as, from Figures 6.3.1.2, 6.3.1.6, 6.3.1.8, any source plane wave propagating at an angle significantly less than θ_{qs} can be neglected. The most desirable property, in terms of numerical evaluation, of this spectrum is that the dominant contribution to the field occurs over a finite portion of the real axis and as such is amenable to the FFT approaches of chapter 3, without the need for any additional endpoint corrections. The speed of calculation of this modal term was increased by having a variable number of integration points for the source integral, whose number was dependent on the size of the integration range. In Figures 6.3.1.9 the second modal term has been calculated for the Jensen–Kuperman ocean with different source positions. To generate a 256 by 512 data field, integrating over the real axis from zero to .85 radians took approximately 40 minutes of CPU time.

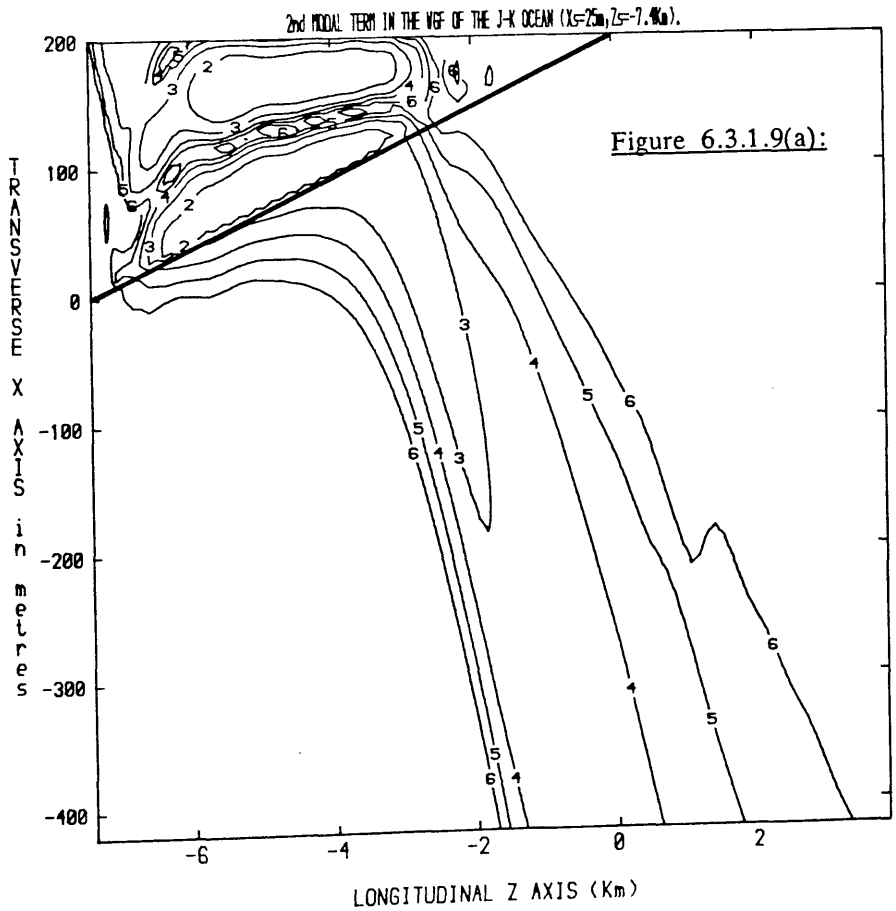

Figure 6.3.1.9(a):

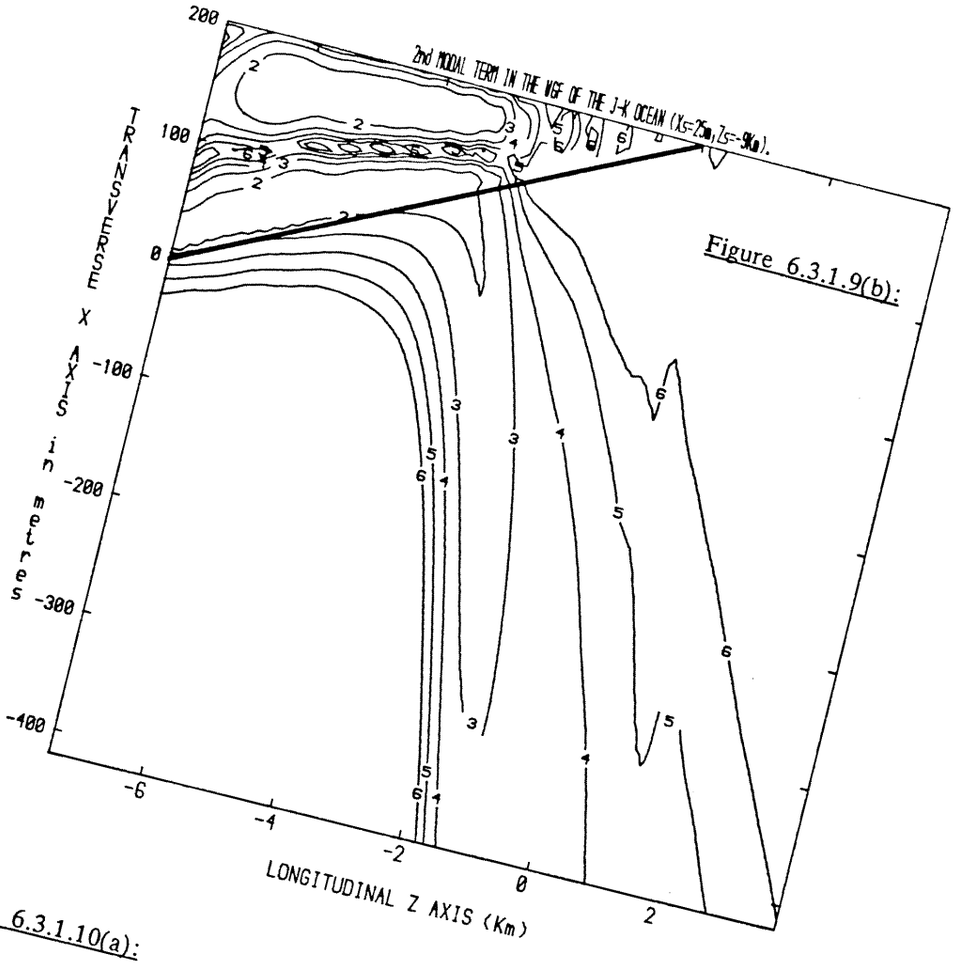

Figure 6.3.1.9(b):

Figure 6.3.1.10(a):

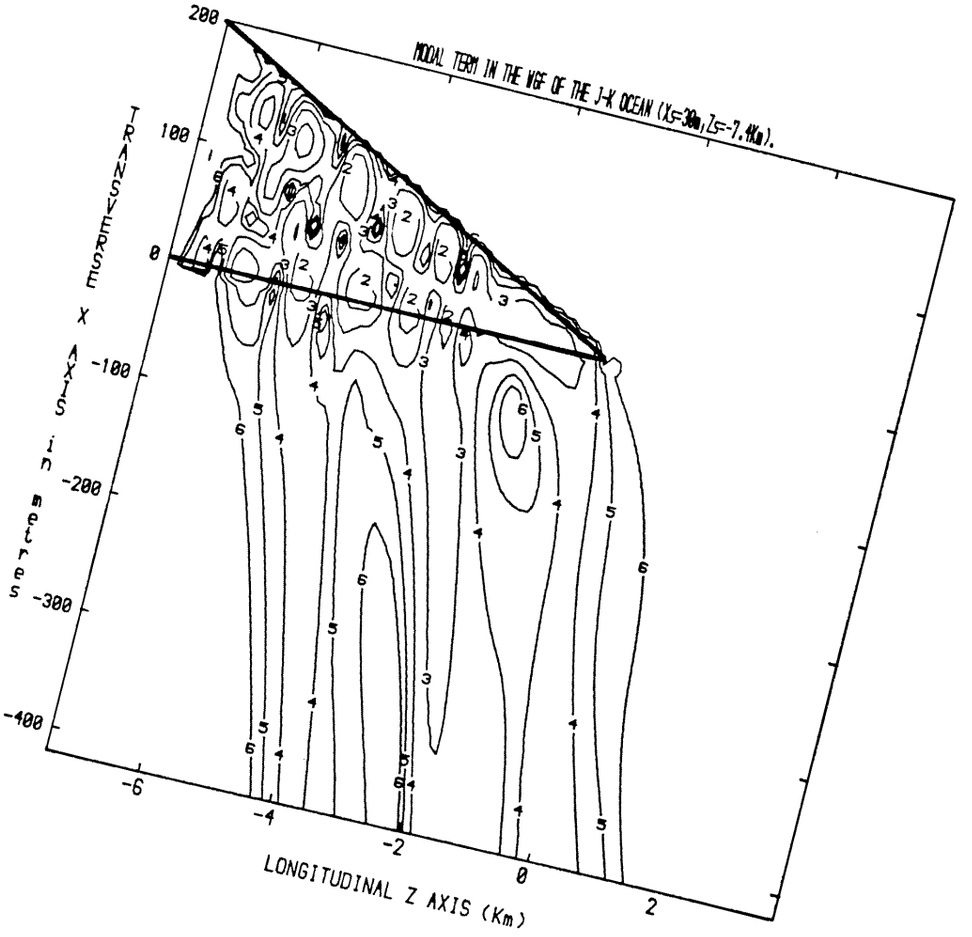

The above Figures confirm previous descriptions of a single modal field as the observation point moves upslope. This modal term is small when the source and observation point are close, as the saddle point is now near the endpoint of the source integral and the Fresnel integral in (6.3.1.4) must be retained. A physical interpretation of this is enlightening. As this modal term represents the scattered field which has undergone more than one reflection, the angle of propagation of any plane wave represented in this collecteive form must be close to normal incidence. Consequently as the plane waves represented in the modal term have propagating angles greater than the modal angle at that cross–section they are unable to generate a modal type field.

It will also be noticed that as the source point is positioned further away from the apex of the wedge, the observed field of interest asymptotically satisfies the boundary conditions.

Another property of the total modal field can be demonstrated if the source point is moved along a fixed cross–section as depicted in Figure 6.3.1.10. In these diagrams only the z–directed FFT is implemented as this reduces run times by half, but as a consequence the data field has been rotated by α.

Figure 6.3.1.10(b):

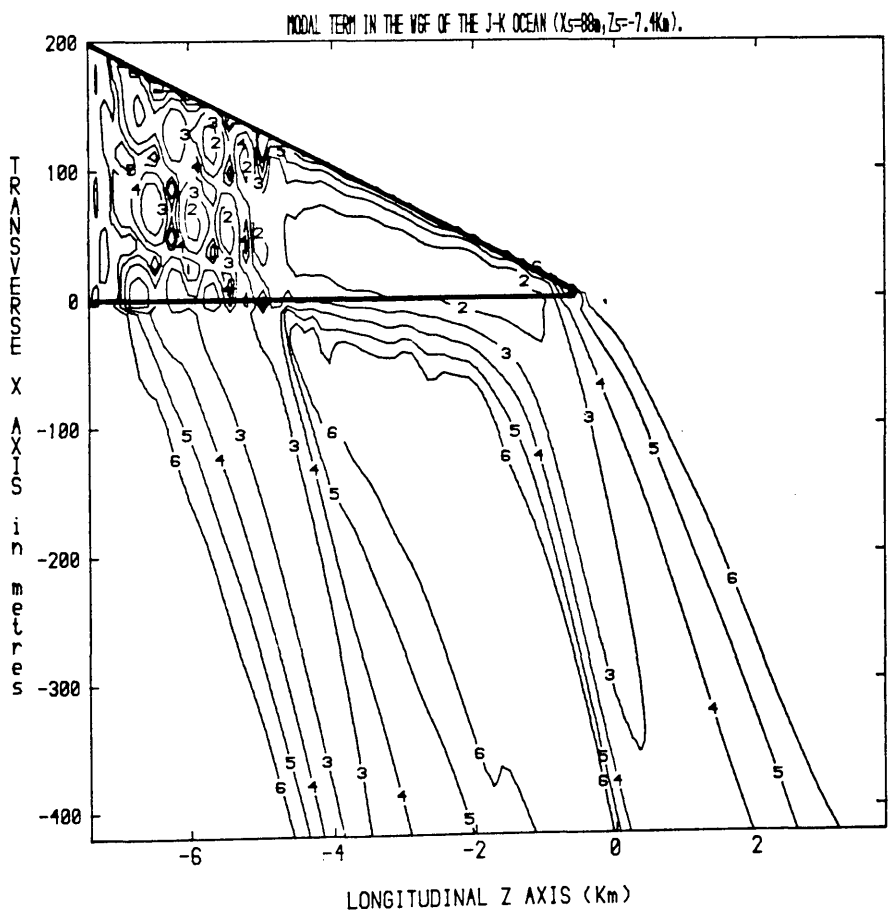

In Figure 6.3.1.10(a) a source point is placed in the desired cross–section in such a manner that all the Adiabatic Modes of the structure are excited. The modal interference and their corresponding cut–off points are clearly seen. In Figure 6.3.1.10(b) the source point was placed at the null of the second Adiabatic Mode in that cross–section and it is clear that in this situation no excitation of this mode occurs. This phenomenon is expected from the asymptotic nature of the field due to the $w_q^*(\underline{x}_s)$ term. The form of the asymptotic results of this section suggest that when the source and observation points are well separated the WGF may be well approximated by,

$$\sum_q W_q^*(\underline{x}_s) W_q(\underline{x}) \qquad (6.3.1.5)$$

where $W_q(\underline{x})$ is the standard Intrinsic Mode. This effectively states that the WGF can be said, in the far field, to consist of all possible Intrinsic Mode fields. The modal contribution to the field for a strongly asymmetric optical structure is shown in Figure 6.3.1.11.

Figure 6.3.1.11:

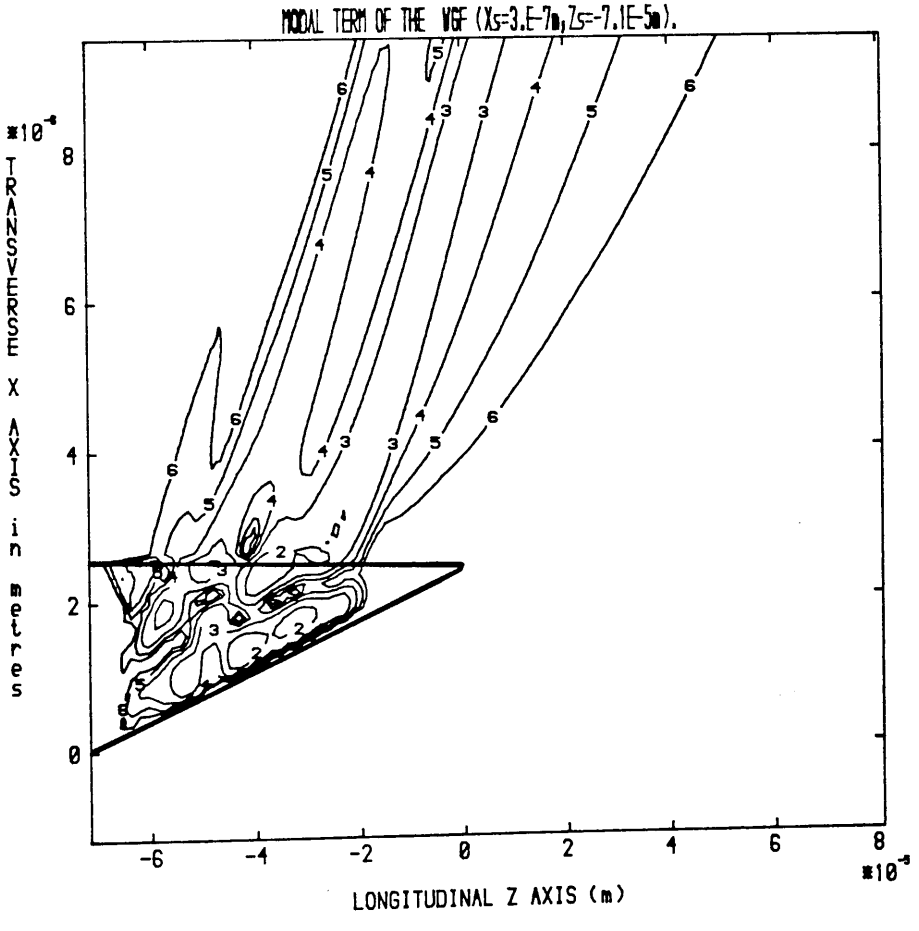

6.3.2: The Initial Field.

This section deals with a systematic approach to the calculation and confirmation of the correct initial fields. The direct field which has not been refracted can be calculated straightforwardly, by using the asymptotic approximations of the Hankel functions for large and small argument given in [54]. The remaining initial fields for observation points inside the guide can be mainpulated into the form,

$$I(R,\tau) = \int_{C_0} A(\theta) e^{inkR\cos(\theta-\tau)} d\theta \qquad (6.3.2.1)$$

where nkR is the optical path length from source to observer and τ is the corresponding stationary phase point. $A(\theta)$ represents phase changes due to the reflection processes inside the guide (see equation (2.4.3)). This analysis is concerned with generating some measure of the initial fields. To simplify this approach a single term representing the single reflected upward field is examined. In this case,

$$A(\theta) = e^{i\Phi_1(\theta)} \qquad R^2 = (z-z_s)^2 + (x+x_s)^2 \qquad (6.3.2.2)$$

It will be immediately noticed that the asymptotic parameter is no longer $1/\alpha$, but is the optical path length nkR. Thus when the source and observation point are separated by many wavelengths the Sommerfeld contour C_0 can be deformed so that the field consists of a ray field (generated from the stationary phase point τ) and a lateral ray field (from plane waves around the critical angle). Subsequent reflections of the lateral ray field are neglected. The asymptotic analysis for the ray field from appendix K is,

$$I_r(R,\tau) \sim \left[\frac{2\Pi}{inkR} \right]^{\frac{1}{2}} A(\tau) e^{inkR - i\Pi/4} \left[1 + \frac{e^{\frac{-i\Pi}{2}}}{8inkR} \left[\frac{8A_{\theta\theta}(\tau)}{A(\tau)} + 1 \right] \right] \qquad (6.3.2.3)$$

where $A_\theta(\tau)$ is the derivative of $A(\theta)$ with respect to θ evaluated at τ. The lateral ray field is calculated to be,

$$I_b(R,\tau) \sim \frac{C_1 \sqrt{\Pi} e^{inkr\cos(\theta_c-\tau) - i\Pi/4}}{(nkR\sin(\theta_c-\tau))^{3/2}} \qquad (6.3.2.4)$$

A uniform asymptotic expansion as τ traverses θ_c can be obtain by using Bleisteins method [60]. However, when nkR is large τ will always be well separated from θ_c as the wedge angle α is small and the uniform approach of Bleistein is not required. The combination of the two fields of (6.3.2.3) and (6.3.2.4) will now be used, in conjunction with another approach, to verify a correct numerical algorithm for the calculation of the initial fields.

The numerical evaluation of the initial fields was achieved by employing the FFT routines of chapter 3. There are underlying difficulties with this method of calculation as the dominant contribution to the field is not contained in a finite portion of the real axis. This problem is circumvented, when nkR is large, by using Laplace's method to correct for the endpoint contributions as used in chapter 5 and calculated in appendix D. The finite interval of integration for the FFT was shifted to be from $-.3$ radians to .8 radians, so that the Laplace's approximations will be accurate.

Two different checks were then carried out on this FFT evaluation of the initial fields when the optical path length is large. Firstly, comparisons between the FFT method and the asymptotic field given in (6.3.2.3) and (6.3.2.4) were taken and found to be in good agreement with even the first term of (6.3.2.3) provided that nkR is >15. The second check on the initial fields when nkR is large can be developed from exact analysis of the boundary conditions given in this chapter. It is observed that certain combinations of plane wave species satisfy particular boundary conditions independently of the modal field. Using this knowledge it was observed that the boundary conditions were satisfied to within approximately 3% of the maximum value of the field provided that nkR was >15. From these two tests it can be concluded that provided the source and observation point were separated by more than fifteen wavelengths the WGF can be accurately calculated using the FFT methods of chapter 3.

When the optical path length is small asymptotic forms become difficult to obtain as the evanescent wave fields contribute significantly to the field. Thus with no asymptotic form to compare any reflected field the confirmation of a correct algorithm was only obtainable through the satisfaction of the boundary conditions. The evaluation of the initial fields in this instance consists of the FFT method along the real θ axis and a small portion of the evanescent spectrum was calculated using Simpson's rule for a contour progressing into the complex plane. The satisfaction of the boundary conditions was $\approx 10\%$ for nkR <10, and as only far fields were of interest this restriction is adequate.

The analysis of the modal field and the initial field leads to the conclusion that accurate and efficient generation of the WGF field can be obtained using the FFT method provided the source and observation point are separated by more than 15 wavelengths. In Figure 6.3.2.1 the WGF for the J−K ocean is demonstrated. The first diagram shows that the source point was positioned at the null of the second local mode in the source local cross−section. The last diagram shows the excitation of all modes present in the wedge environment. It is clearly seen that the initial fields are significantly smaller than the modal field as this field is easily recognised.

Figure 6.3.2.1.

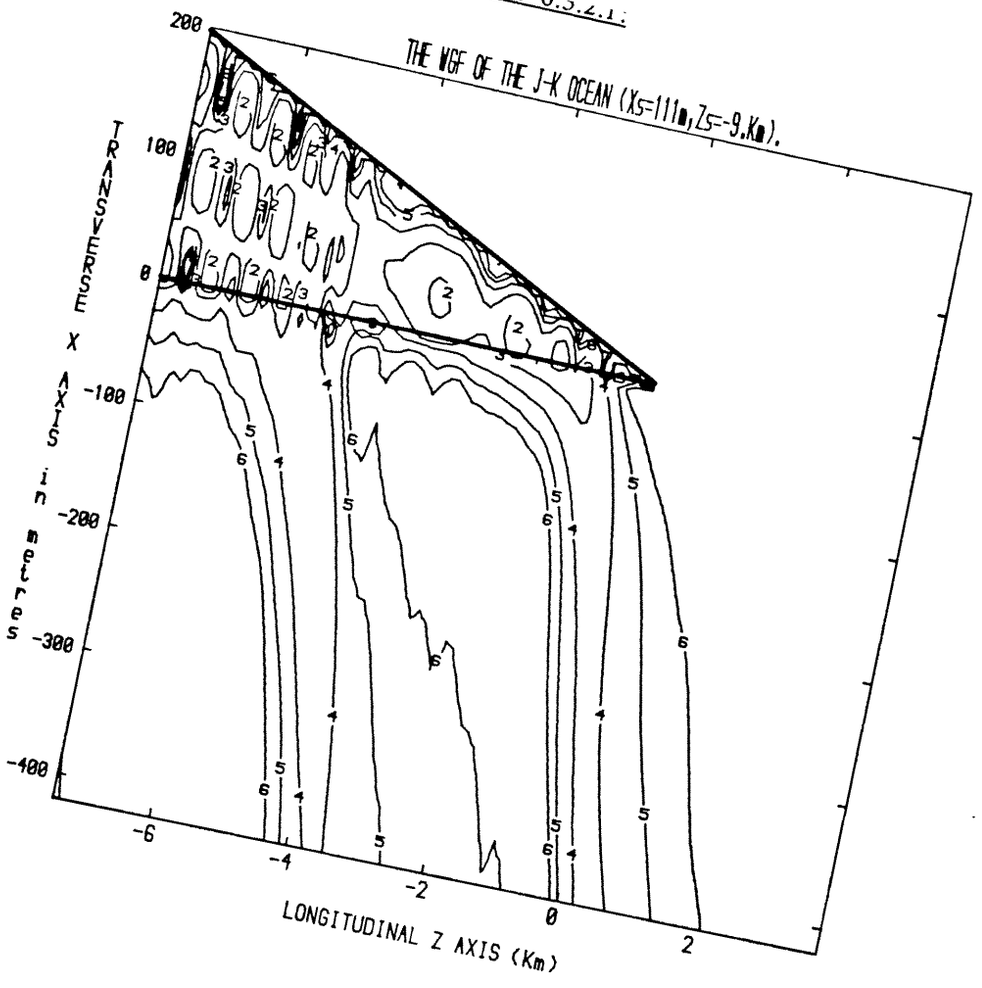
THE VGF OF THE J-K OCEAN (Xs=111m,Zs=-9.Km).
TRANSVERSE X AXIS in metres
200
100
0
-100
-200
-300
-400
-6
-4
-2
0
2
LONGITUDINAL Z AXIS (Km)

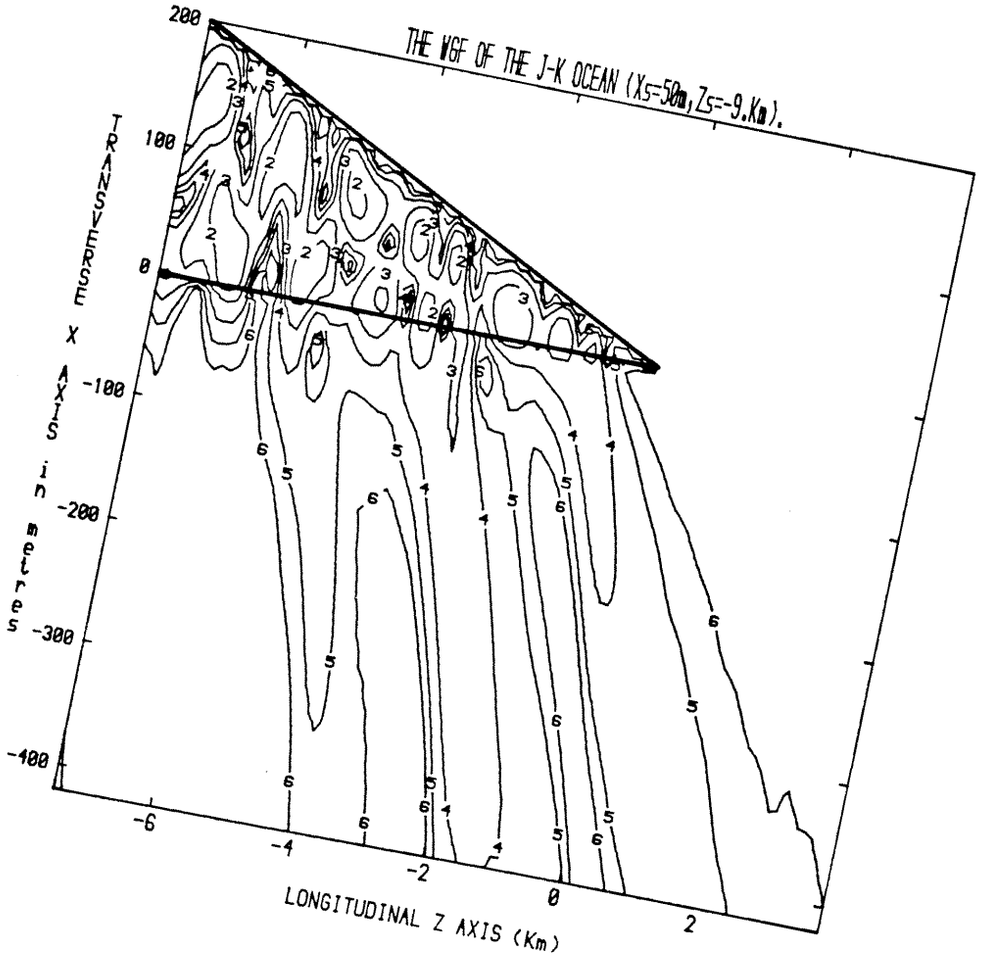
THE VGF OF THE J-K OCEAN (Xs=50m,Zs=-9.Km).
TRANSVERSE X AXIS in metres
200
100
0
-100
-200
-300
-400
-6
-4
-2
0
2
LONGITUDINAL Z AXIS (Km)

Conclusions.

This chapter has examined closely the properties of the source induced global object of chapter 2. This examination has proved rigorously that the global object in question is the true Green's function for the wedge environment, excluding the apex of the wedge. A by–product of this analysis, together with asymptotic forms, has enabled a systematic approach to the confirmation of a correct numerical algorithm. The asymptotic forms facilitated another confirmatory test on the FFT evaluation of the WGF, while also demonstrating the dominant wave processes.

The final two sections demonstrate the close physical links between the pure IM and the WGF. However the nature of the WGF suggests that all possible IMs does not form a complete set in the wedge environment. This chapter has also demonstrated that an accurate calculation of the modal field can be obtained everywhere in the wedge geometry (excluding the apex) due to the finite nature of the spectral field. This statement is confirmed numerically by examination of the boundary conditions for specific plane wave species in the modal sum. A qualitative comparison between the WGF and the BPM and the PEM is left to the next chapter as difficulties in generating a delta function occur in the marching algorithm methods. In conclusion it is interesting to discuss the behaviour of the initial and modal fields throughout a typical wedge environment. The modal field close to the source point is small for the reasons discussed above and the initial fields are the dominant field terms. In this region it is apparent that the initial fields will be a good approximation to the WGF and will satisfy the boundary conditions in this region. As the optical distance between source and observation point is increased, the initial fields decay at least as fast as R^{-1}, yet the modal term increases. Thus in the far field the WGF is well approximated by the asymptotic modal field given in (6.3.1.5).

Chapter 7: APPLICATIONS OF THE WEDGE GREEN'S FUNCTION.

Introduction.

This chapter explores methods which exploit the properties of Green's functions to solve the elliptic wave equation in a non-separable environment. The central principle is that of being able to represent the field inside an enclosed surface by an integral over the surface. This idea has extensive use in diffraction problems [30]. The first section of this chapter derives briefly this boundary integral representation of a field enclosed by the said boundary.

This formalism is then applied to the two dimensional planar wedge configuration of interest, where a description of a suitable contour, necessary for a good approximate solution, is given. In the following sections, input fields are placed on the prescribed contours and the propagation of these input fields throughout the wedge structure is examined. The final section shows how, using similar structures to those developed in preceeding sections, it is possible to model simply connected structures. While this is future work, arguments are given for and against pursuing this course of action further.

7.1: Green's Theorem.

Consider a volume V enclosed by a surface S, which has an associated 3-dimensional vector Green's function $\underline{G}(\underline{x},\underline{x}_s)$. This Green's function is constrained in such a manner as to satisfy the equation [10],

$$\left[\nabla^2_{\underline{x}_s} + n^2(\underline{x}_s)k^2 \right]\underline{G}(\underline{x},\underline{x}_s) = \delta(\underline{x}_s-\underline{x}) \qquad (7.1.1)$$

with the subscript $\underline{x}_s$ denoting differentiation with respect to the source variable $\underline{x}_s$, and ∇^2 taken as acting on each component of the vector Green's function. The wave vector magnitude is k and the refractive index $n(\underline{x}_s)$. A solution, $\underline{U}(\underline{x}_s)$, of the homogeneous elliptic equation can be mathematically described by,

$$\left[\nabla^2_{\underline{x}_s} + n^2(\underline{x}_s)k^2 \right]\underline{U}(\underline{x}_s) = 0 \qquad (7.1.2)$$

If equation (7.1.1) is multiplied by $\underline{U}(\underline{x}_s)$ and equation (7.1.2) multiplied by the Green's function, then subtracting these two altered equations gives,

$$\underline{U}(\underline{x}_S)\delta(\underline{x}_S-\underline{x}) = \underline{U}(\underline{x}_S)\nabla^2_{\underline{x}_S}\underline{G}(\underline{x},\underline{x}_S) - \underline{G}(\underline{x},\underline{x}_S)\nabla^2_{\underline{x}_S}\underline{U}(\underline{x}_S) \qquad (7.1.3)$$

If this equation is then integrated throughout the entire volume V in conjunction with the sampling property of the delta function, gives the field anywhere in the volume V is given as,

$$\underline{U}(\underline{x}) = \iiint_V \left[\underline{U}(\underline{x}_S)\nabla^2_{\underline{x}_S}\underline{G}(\underline{x},\underline{x}_S) - \underline{G}(\underline{x},\underline{x}_S)\nabla^2_{\underline{x}_S}\underline{U}(\underline{x}_S)\right] dV \qquad (7.1.4)$$

Using the vector identity (equation (5.4.4)) and the divergence theorem, then the field inside and on the boundary S is given by,

$$\underline{U}(\underline{x}) = \iint_S \left[\underline{U}(\underline{x}_S)\nabla_{\underline{x}_S}\underline{G}(\underline{x},\underline{x}_S) - \underline{G}(\underline{x},\underline{x}_S)\nabla_{\underline{x}_S}\underline{U}(\underline{x}_S)\right].d\underline{S} \qquad (7.1.5)$$

where $\underline{S}$ is the unit outward normal to the surface S. This diffraction integral can be interpreted physically by using the Kirchoff–Huygens concept. The field anywhere inside or on the surface S (which does not enclose any sources) can be said to consist of the field from appropriately weighted source points from every point on S.

7.2: Application to the Wedge Environment.

Figure 7.2.1: Enclosing Contour shape for modelling Wave Propagation by Boundary integral method.

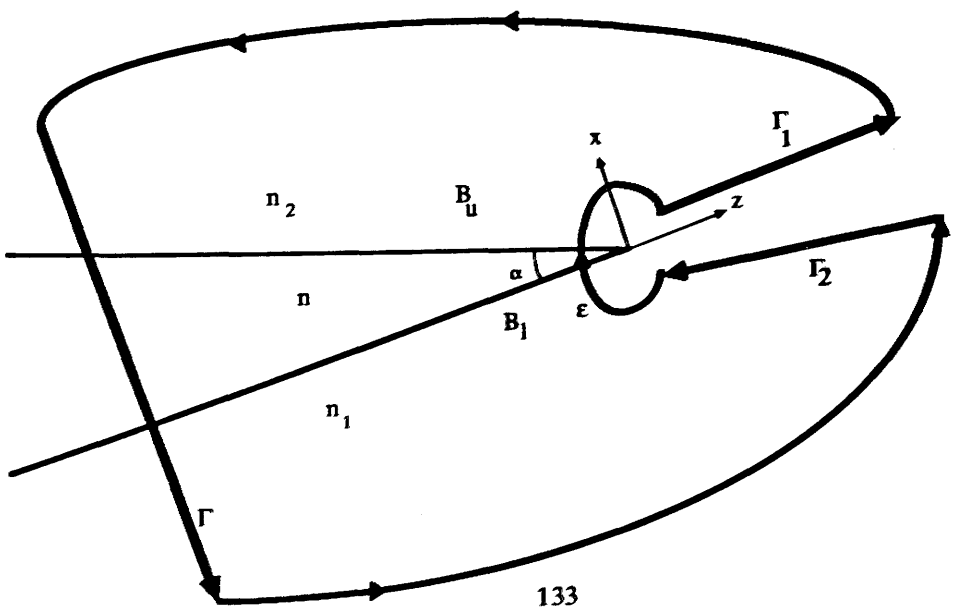

Armed with the above representation of the field in a region where the Green's function is known, the field in the wedge region can be calculated. The applicability of the WGF is such that the apex of the wedge must not be included in the interior or situated on the the contour enclosing the region of interest. This constraint motivates the contour shape depicted in Figure 7.2.1. In this representation Γ_1 and Γ_2, sections of the enclosing contour, are coincident and as they are in different directions their field contribution is zero. Γ_1 and Γ_2 meet Γ at infinity where the radiation condition holds. Thus the contributions from the sections of the contour at infinity are zero. As a consequence the field in the wedge region with no source points can be represented exactly as the integral over the Γ and ϵ contours shown in Figure 7.2.1. If the mode is propagating upslope the field incident on the apex will be small. Also if the observation points are many wavelengths away from ϵ then its contribution can be neglected. Thus the field in the wedge away from the wedge apex can be given approximately by,

$$U(\underline{x}) \sim \int_{\Gamma} \left[U(\underline{x}_s) \frac{dG(\underline{x},\underline{x}_s)}{dn} - G(\underline{x},\underline{x}_s) \frac{dU(\underline{x}_s)}{dn} \right] d\Gamma \qquad (7.2.1)$$

n is the outward normal to Γ, and the vector representation has been removed as only scalar fields are of interest. The fields $U(\underline{x})$ could be evaluated numerically by the above method, but the calculation of the Green's function for source and observation points in close proximity is difficult and also would require a vast amount of CPU time, as the WGF would have to be calculated for every point on Γ for every observation point. A more efficient algorithm can be generated, without the singularity difficulty of the WGF, if the Γ source integral is calculated first. This route can be followed if the contour Γ and the angular spectrum integral over θ are interchanged, which is plausible as the field is convergent. Using the standard coordinate system used in Figure 7.2.1 for the wedge geometry the field can then be represented as,

$$U(\underline{x}) \sim \int_{C} \int_{\Gamma} \left[U(\underline{x}_s) \frac{dI(\underline{x},\underline{x}_s,\theta)}{dz_s} - I(\underline{x},\underline{x}_s,\theta) \frac{dU(\underline{x}_s)}{dz_s} \right] dx_s d\theta \qquad (7.2.2)$$

where I is the plane wave spectrum of the appropriate WGF. Inspection of the spectral function $I(\underline{x},\underline{x}_s,\theta)$ (from equation (6.1.11) of chapter 6) it is apparent that the $\underline{x}_s$ dependence is only present in the source plane wave terms. Therefore to calculate the field in this boundary integral efficiently requires the evaluation of the WGF with the source plane wave terms, $W_i^{\pm}(\delta)$, replaced by,

$$\int_{\Gamma}\left[U(\underline{x}_s)\frac{dW_i^{\pm}(\delta)}{dz_s} - W_i^{\pm}(\delta)\frac{dU(\underline{x}_s)}{dz_s}\right]dx_s \qquad (7.2.3)$$

7.3: The Gaussian Beam Input.

This section is concerned with initiatiing fields into the wedge environment which enable at least qualitative comparisons with the BPM and PEM discussed in chapter 1. Discussion in the previous chapter highlighted the difficulties involved when comparing the WGF with other methods, due to the difficulty of modelling the source point. To circumvent this problem, consider a two dimensional gaussian field with its peak (z_p,x_p) and a 1/e point of d, is used as an input to all numerical routines, at the cross-section $z=z_p$, the form of which is given in equation (3.1).

$$U(\underline{x}) = \frac{1}{d^2\Pi}\, e^{-((x-x_p)/d)^2 - ((z-z_p)/d))^2} \qquad (7.3.1)$$

In the usual manner letting $d\to 0$ implies that $U(\underline{x})\to\delta(x-x_p)\,\delta(z-z_p)$. Thus using this type of input with a finite value of d avoids the singularity problem incurred when comparing the WGF. To successfully model a field due to a delta function the width of the gaussian must be considerably less than the wavelength of the field in the guide. Also to simplify the problem only cases where the majority of the gaussian is inside the guide will be examined, although there is no loss of generality to the principle in this constraint. If the Γ contour is placed at $z_s=z_p$ then the field evaluation requires the source plane waves $W_0^{\pm}(\delta)$ to be replaced by,

$$\frac{-ikcos\delta}{\Pi d^2}\, e^{-ikz_p cos\delta}\int_0^{h(z_p)}\left[\, e^{\mp ikx_s sin\delta} e^{-((x_s-x_p)/d)^2}\right]dx_s \qquad (7.3.2)$$

Completing the square in the exponent gives the integral in the form

$$\frac{-ikcos\delta}{\Pi d^2} e^{-ik(z_p cos\delta \pm x_p sin\delta)-(dksin\delta/2)^2}\int_0^{h(z_p)} e^{-\left[\frac{x_s-x_p \mp ikdsin\delta}{d} \over 2\right]^2} dx_s \qquad (7.3.3)$$

Applying the substitution,

$$t = (x_s-x_p)/d \mp (ikdsin\delta)/2$$

and noting that the beam is well contained in the guide cross-section (allowing the

endpoints to be taken to $\pm\infty$) alters the source plane waves to

$$\frac{-ink\cos\delta}{\Pi^{\frac{1}{2}}d}e^{-ink(z_p\cos\delta\pm x_p\sin\delta)-(dnk\sin\delta/2)^2} \qquad (7.3.4)$$

As the gaussian profile is well contained inside the guiding duct, then to generate an accurate field structure throughout the wedge environment requires the $G_0^i(\underline{x},\underline{x}_s)$ WGF. The gaussian beam was positioned at 88m above the J−K ocean floor at an ocean depth of 200m (i.e. $x_p=88$m, $z_p=-7391$m for $\alpha=1.55^0$) which corresponds to the null of the second order mode in a translationally invariant guide possessing this local transverse plane. The 1/e point of the gaussian is 20m and was used as an input to the BPM and PEM algorithms in the same manner as used in chapter 5. Figure 7.3.1 depicts the field throughout the J−K wedge shaped ocean for the particular input

Figure 7.3.1(a):

Gaussian Input Using Boundary Integral Method.

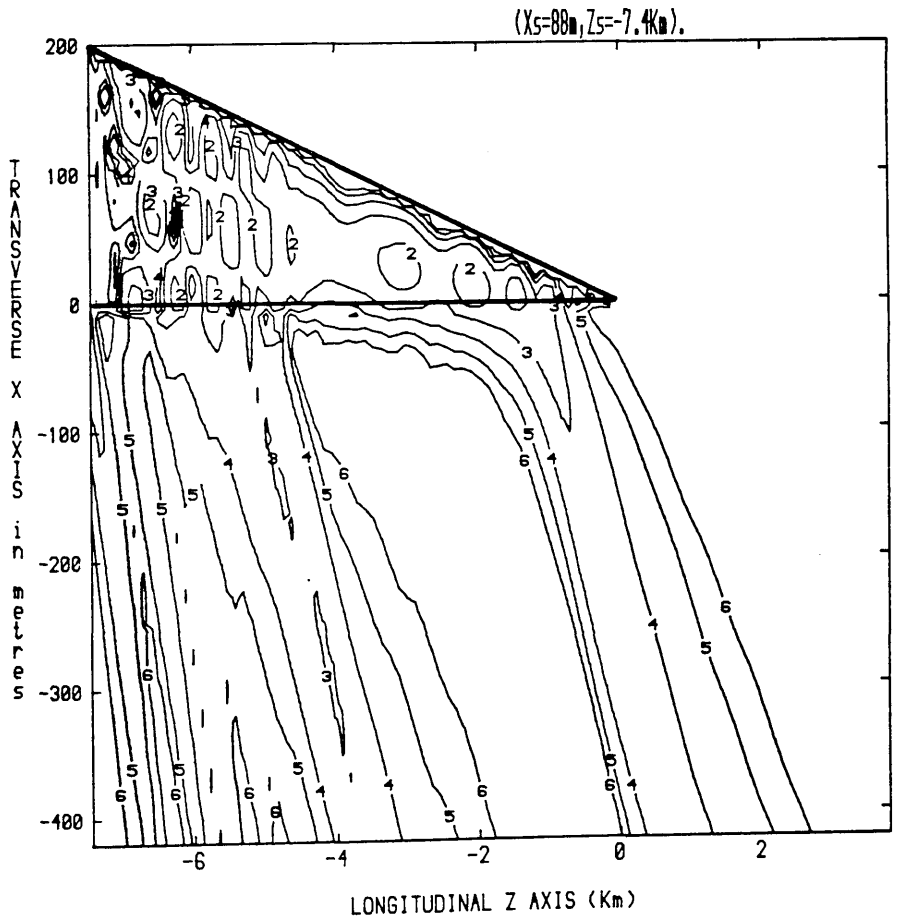

Figure 7.3.1(b):

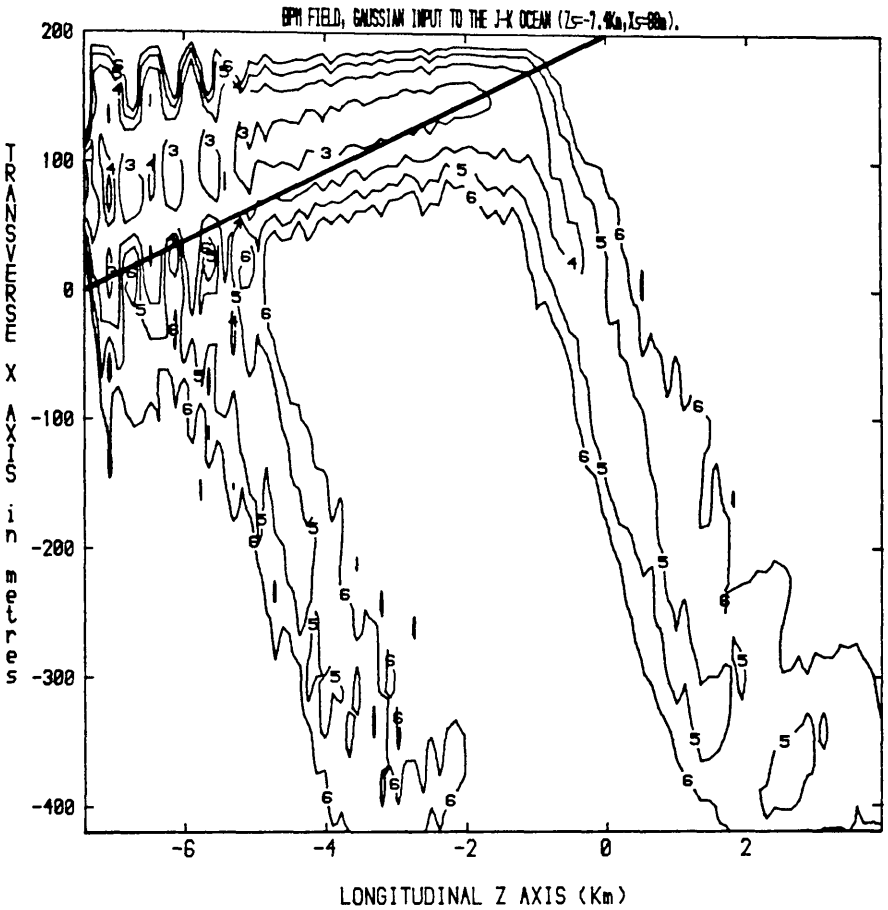

Figure 7.3.1(c):

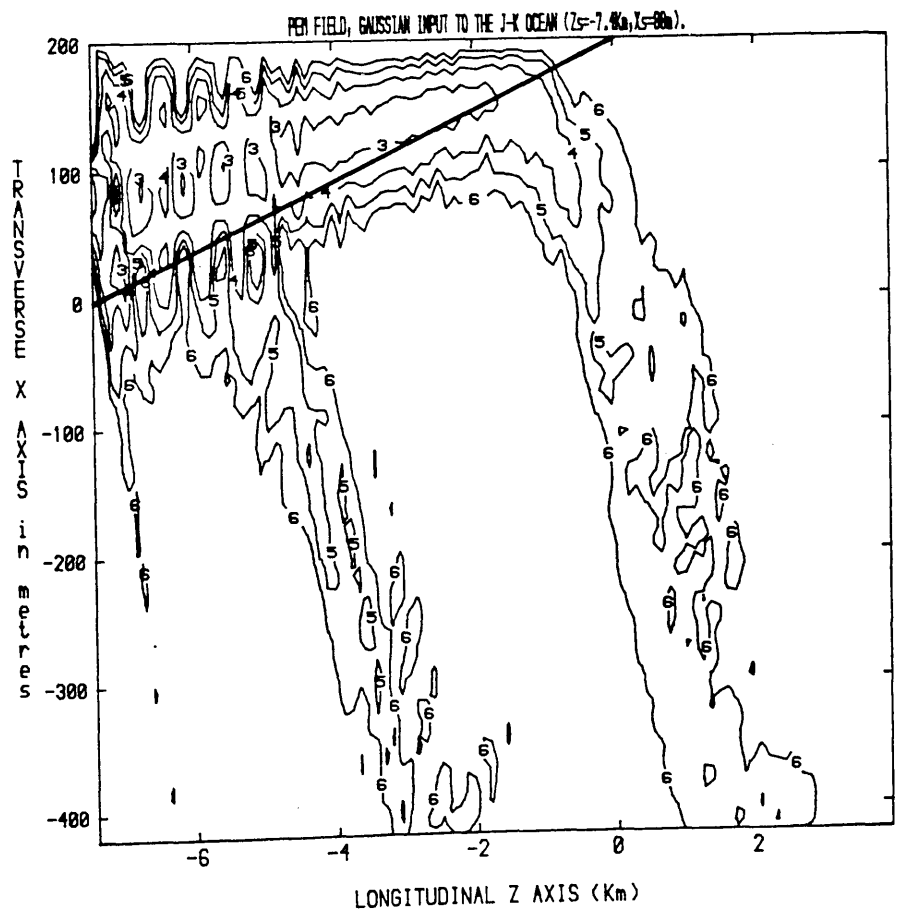

It is first noticed that the WGF field is orientated at an angle α to the other marching algorithm fields, which is merely a consequence of employing the z−directed FFT only so that a fast generation of the data field was possible. Quantitative comparisons of the fields would require a similar approach to section 5.3 of chapter 5 and to avoid repetition this is neglected. In a qualitative description of the fields this rotation of α in the WGF field is of little consequence as it is the confirmation of the global effects which is of importance.

All three plots of Figure 7.3.1 demonstrate clearly non−excitation of the second normal mode which is as expected for this position of the narrow gaussian beam. Also the appropriate cut−off points of each mode (calculated in chapter 5) for each different propagating field method are still maintained, even though their determination is approximate. The inconsistency in the penetration of the field into the substrate for each different algorithm can be attributed to two main causes. Firstly, the discrepancy is in part due to the method of normalisation of the plots: the zero dB point is the maximum value of the field in the wedge geometry. The second cause is purely physical. It can be argued that the input field, in this case the gaussian, in each algorithm excites the appropriate intrinsic modes, be they pure, BPM or PEM. As a consequence of this coupling into different intrinsic modes their excitation amplitudes can be altered. Unfortunately, as for the WGF, only observation points that are greater than 15 wavelengths away could be computed with any sureity, as the same problems in calculating the initial fields for the WGF befall this boundary approach.

7.4: The Adiabatic Mode Input.

It would be useful to demonstrate that a pure IM field input on the boundary would propagate as a pure IM. The calculation of this input involves evaluating triple integrals: one for the IM and two for the WGF together with an analytically calculated configuration space integral. Due to this complexity the evaluation of this field required more CPU time than was permissible on the computer available and consequently this approach was abandoned. However, a simpler case can be considered which will approximate well the IM input, and will prove useful in future work. If a transverse section of the wedge is taken where the local normal mode is well guided, then the IM field will be well approximated by this local normal mode. Thus the Adiabatic Mode of the J−K ocean,

$$w_q(\underline{x}) = \begin{cases} A(z)\sin\left[\gamma_q(h-x)\right] & 0<x<h(z) \\ A(z)\sin\gamma_q h e^{\tau_q x} & x<0 \end{cases} \qquad (7.4.1)$$

into the wedge configuration by the Green's function boundary value approach, where A(z) is such as to normalise the inner product for the wedge. The boundary Γ is situated at $z = zp = -7391$m and the field upslope of Γ, away from the wedge apex, can be approximated by,

$$U(\underline{x}) \sim \int_{-\infty}^{h(z_p)} \left[\frac{dG(\underline{x},\underline{x}_s)}{dz_s} - i\beta_q G(\underline{x},\underline{x}_s) \right] w_q(\underline{x}_s) dx_s \qquad (7.4.2)$$

This integral can be can then be split into two parts, for source fields above and below the interface between the ocean and the ocean floor, to give the field as,

$$\begin{aligned} U(\underline{x}) \sim & \int_{0}^{h(z_p)} \left[\frac{dG_0^j(\underline{x},\underline{x}_s)}{dz_s} - i\beta_q G_0^j(\underline{x},\underline{x}_s) \right] \sin(\gamma_q(h-x_s)) dx_s \\ & + \int_{-\infty}^{0} \left[\frac{dG_1^j(\underline{x},\underline{x}_s)}{dz_s} - i\beta_q G_1^j(\underline{x},\underline{x}_s) \right] \sin(\gamma_q h) e^{i\tau_q} dx_s \end{aligned} \qquad (7.4.3)$$

where the $G_n^j(\underline{x},\underline{x}_s)$ are as defined in chapter 6. In a similar manner to the gaussian input the source plane wave terms for points inside the guide, $W_0^{\pm}(\delta)$ must be replaced by,

$$i(\beta_q + nkz_p\cos\delta) e^{-inkz_p\cos\delta} \int_{0}^{h(z_p)} e^{\mp inkx_s\sin\delta} \sin(\gamma_q(h-x_s)) dx_s \qquad (7.4.4)$$

to generate an Adiabatic mode field on the boundary. This integral can be evaluated easily by noting that the normal mode and the plane waves are solutions of particular one dimensional wave equations. Using the Sturm–Louiville approach [10] requires that the source plane waves be replaced by,

$$\frac{i(\beta_q + nkz_p\cos\delta)}{n^2k^2\sin^2\delta - \gamma_q^2} e^{-inkz_p\cos\delta} \left[\gamma_q\cos(\gamma_q h) \mp inks\sin\delta\sin(\gamma_q h) - \gamma_q e^{\mp inkhs\sin\delta} \right] \qquad (7.4.5)$$

This is indeterminate when δ is equal to modal angle and applying L'Hopital's rule gives the plane wave species at this particular δ as,

$$\frac{i\beta_q}{\gamma_q} e^{-i\beta_q z_p}\left[\mp\sin(\gamma_q h) - \gamma_q h e^{\mp i\gamma_q h} \right] \qquad (7.4.6)$$

When the boundary is in the lower medium (the ocean floor) the plane wave terms of $G_1^j(\underline{x},\underline{x}_s)$, given as $W_1^{\pm}(\delta)$, need to be replaced by,

$$i(\beta_q+nkz_p\cos\delta)\sin(\gamma_q h)e^{-inkz_p\cos\delta}\int_{-\infty}^{0} e^{(\tau_q-in_1kx_s\sin\delta_1)x_s}dx_s \qquad (7.4.7)$$

where δ_1 is the refracted angle calculated from Snell's law (equation (6.1.4) of chapter 6). Evaluating this integral implies that the source plane wave terms for input fields in the ocean for must be replaced by,

$$\frac{i(\beta_q+nkz_p\cos\delta)}{(\tau_q-in_1k\sin\delta_1)} \sin(\gamma_q h)e^{-inkz_p\cos\delta} \qquad (7.4.8)$$

Again, as in the evaluation of the WGF and the gaussian boundary value problem, the calculation of the initial fields can be considered as accurate only when the distance between the boundary and the observation point is greater than 15 wavelengths. It is sufficient for the purposes of this thesis to examine the modal terms in this boundary value problem, so that possible future work can exploit this known accurate field calculation.

Figure 7.4.1(a):

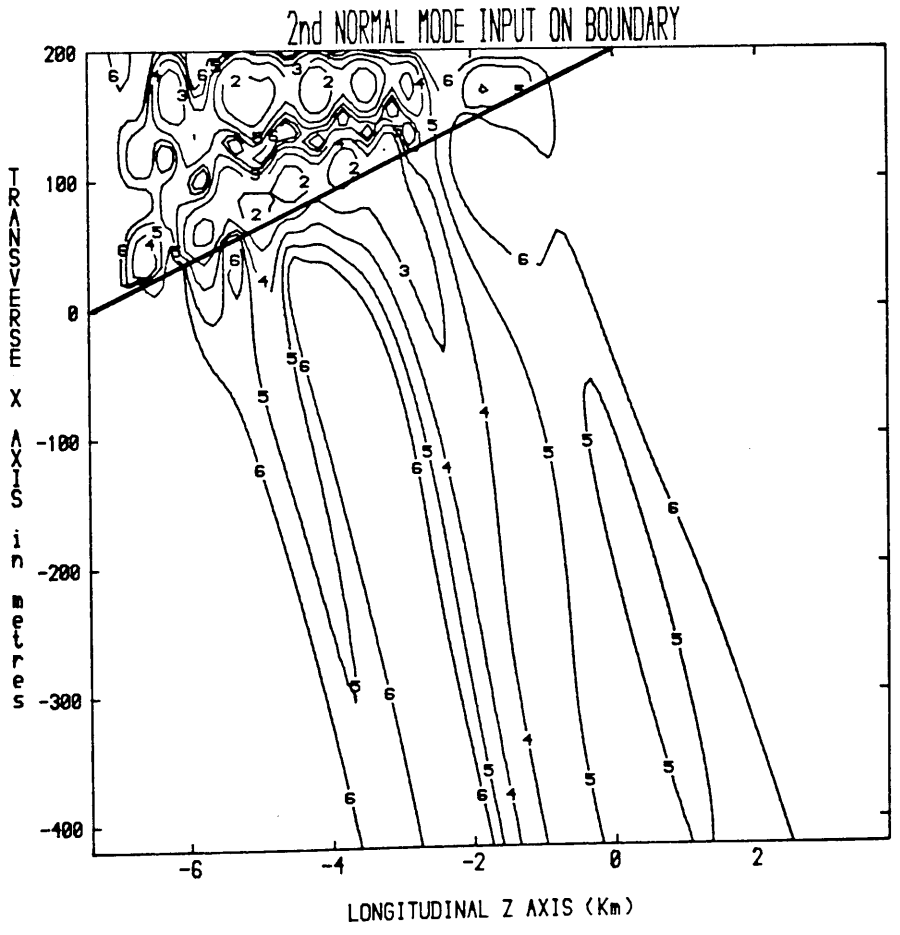

Figure 7.4.1(b):

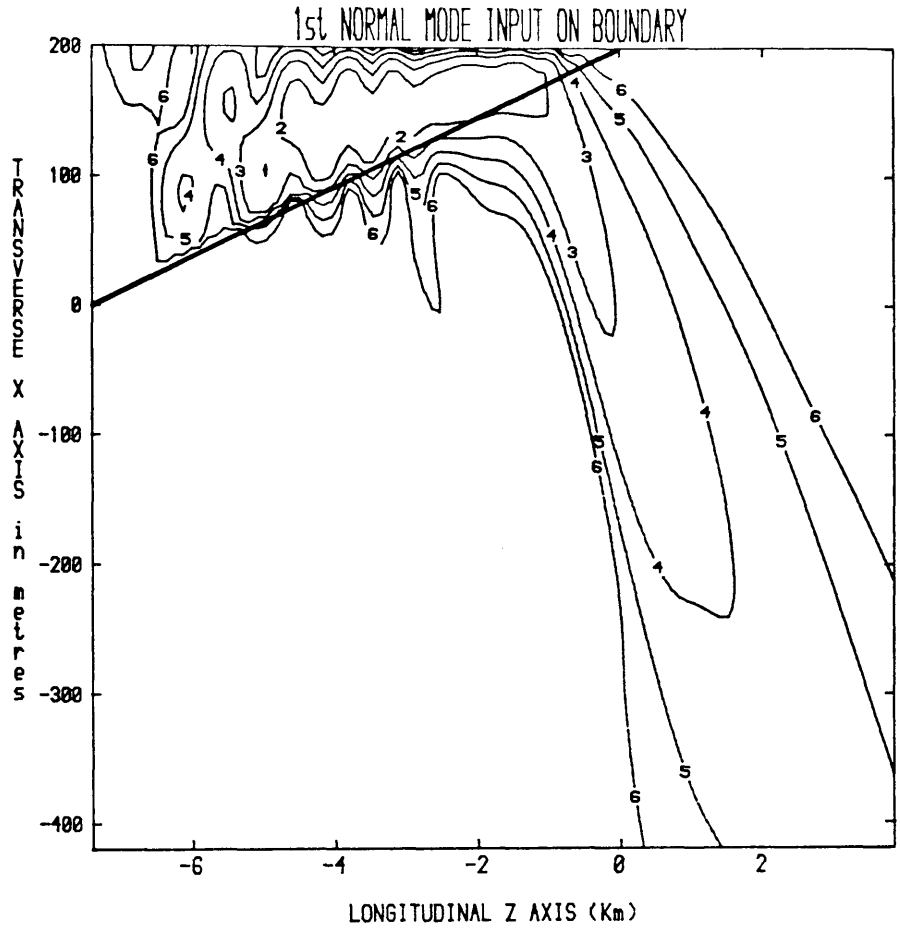

In Figure 7.4.1 it is clearly seen that the AM input does not propagate as one would expect a pure IM to propagate. This discrepancy in the expectation of the two inputs is due to two main effects. The first effect is non–physical and is due to numerical error in the calculation of the fields, as the new source plane wave terms are significantly more complicated than for the WGF. This type of error could be easily eradicated by using double precision complex numbers, which was unfortunately unobtainable on the machine available.

The second and more profound reason for the AM input not behaving as an IM input would be expected to behave can be explained by examination of the boundary value expresssion. If the IM were input on the same boundary as the AM, then the kernel of this spectral integral would obviously differ from the kernel produced by initiating the AM. Thus at each point, upslope of Γ, the field expression has retained the exact nature of the input field. This last statement confirms that everywhere in the wedge environment the information of the coupling of the input field to the IM field is retained. These above statements then facilitate an understanding of the field plots in Figure 7.4.1. In these diagrams the first mode is well guided and will consequently be a good approximation to the IM at the boundary cross–section so that a pure IM is generated. The second mode is less well

guided than the first mode and consequently will not approximate its corresponding IM as well, thus exciting other IMs.

The above concept has significant ramifications in that in the IM the information of the field on any boundary is retained at any point inside the enclosing boundary. This retention of information, necessary for exact field evaluation, implies that this boundary value approach can be implemented as a benchmark solution for fields input into the wedge environment.

7.5: A Simple Connected Structure.

The propagation of the normal mode throughout the wedge environment by employing the Green's function approach was an attempt to approximate the propagation of the IM field. However, there was an ulterior motive to this calculation, as it is necessary for the evaluation of reflected fields from particular connected geometries. It is possible, in principle, to calculate exactly the field propagation throughout a simple structure by using the previously discussed Green's function method, the mechanism for which is demonstrated below. Consider the simple structure of a single mode guide attached to an expanding wedge region as depicted in Figure 7.5.1, with the upper boundary totally reflecting. This geometry is of significant importance in integrated optics as it forms part of a Y– junction structure [6].

Figure 7.5.1: A simple Connected Structure.

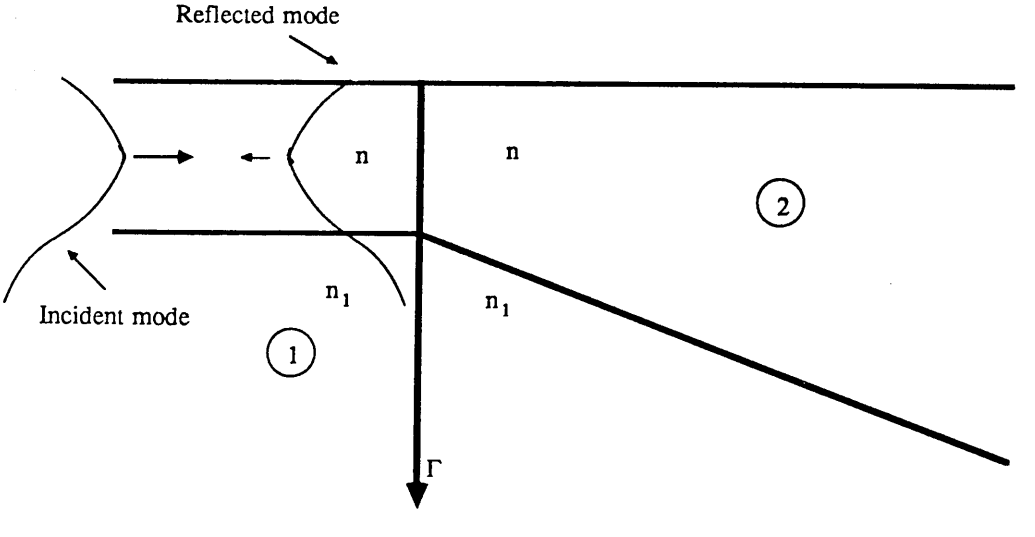

Assume that a single guided mode field of unit amplitude is incident from the left on the boundary Γ. It would be desirable to be able to calculate the total back reflected

field or the amount of power in the reflected guided mode, or both. The field in region 2 can be expressed by the boundary integral form of (7.1.5). The radiation condition at infinity allows the representation of the field to be,

$$U_2(\underline{x}) = \int_{\Gamma}\left[U(\underline{x}_s)\frac{dG(\underline{x},\underline{x}_s)}{dn} - G(\underline{x},\underline{x}_s)\frac{dU(\underline{x}_s)}{dn}\right]d\Gamma \qquad (7.5.1)$$

where $G(\underline{x},\underline{x}_s)$ is the appropriate WGF. The field in region 1 can be represented by the guided modes propagating to the left and right and the radiation field [44]. Thus the field in region 1 can be expressed mathematically as,

$$U_1(\underline{x}) = w_1^+(\underline{x}) + Rw_1^-(\underline{x}) + \int A_\mu w_\mu(\underline{x})dk_\mu \qquad (7.5.2)$$

where w_1 represents the guided mode field propagating to the left and right and R the amplitude of the reflected mode. The integral term is the radiation field with the A_μ the unknown amplitude of each individual radiation mode. The integration extends over all possible transverse wave numbers k_μ in the substrate. Let the boundary Γ be situated at $z = 0$, the variable of the observed field on Γ be x and the integration variable in (7.5.1) be x_s. In this expostion consideration is given only to the guided mode fields. The field and its derivative must be continuous across the boundary Γ, which gives rise to the two integral equations in (7.5.3).

$$(1+R)w_1(x) = -\int_{x_s}\left[U(x_s)\frac{dG(x,x_s)}{dz_s} - G(x,x_s)\frac{dU(x_s)}{dz_s}\right]dx_s \qquad (7.5.3a)$$

$$i\beta(1-R)w_1(x) = -\int_{x_s}\left[U(x_s)\frac{d^2G(x,x_s)}{dzdz_s} - \frac{dG(x,x_s)}{dz}\frac{dU(x_s)}{dz_s}\right]dx_s \qquad (7.5.3b)$$

with β the propagation constant of the guided mode. These equations require simplification which can be achieved by first assuming that the $U(x_s)$ in the diffraction integral is equivalent to the field in region one evaluated at the boundary. Thus multiplying equations (7.5.3) by $w_1(x)$, integrating over all x and applying the orthogonality relations gives,

$$(1+R) = -\int_x\int_{x_s}\left[(1+R)w_1(x_s)\frac{dG(x)}{dz_s} - G(x)i\beta(1-R)w_1(x_s)\right]w_1(x)dx_s dx \qquad (7.5.4a)$$

$$i\beta(1-R) = -\int_x\int_{x_s}\left[(1+R)w_1(x_s)\frac{d^2G(x)}{dzdz_s} - \frac{dG(x)}{dz}i\beta(1-R)w_1(x_s)\right]w_1(x)dx_s dx \qquad (7.5.4b)$$

with dependence on x_s omitted for clarity. The notation can be simplified further to give the simultaneous equations,

$$R = D$$
$$R = F \qquad (7.5.5a)$$

where,

$$D = \frac{-1 - C^-}{1 + C^+} \qquad F = \frac{-i\beta - \bar{C}_z}{C^+_z - i\beta} \qquad (7.5.5b)$$

with the z subscript denoting differentiation with respect to z and evaluated on Γ, and with,

$$C^{\pm} = \int_{x} \int_{x_s} \left[\left(\frac{dG(x,x_s)}{dz} \right)_s \pm i\beta G(x,x_s) \right] w_1(x_s) w_1(x) dx_s dx \qquad (7.5.5c)$$

Although these equations are over specified, due to the neglect of the radiation field and the known input mode amplitude, a good approximation to the reflected field is obtained from either of the equations (7.5.5a). The calculation of the exact field with radiation modes considered would require implementation of the orthogonality relation for radiation modes and the result would be two coupled integral equations. This more complicated approach would require large amounts of computer time, yet the result would not be significantly more accurate than the above approximate solution as numerical rounding error and an iterative method of solution would be important factors. Thus a simple approximation to the reflected field could be calculated from above where $C^{\pm}$ can be evaluated using the same method as in section 4.

Conclusions.

The exact WGF representation of chapter 2 can be exploited in an integral equation form obtained from work by Green [6f]. This method has distinct advantages over the WGF field when assessing the performance of other theories as the singularity present in the WGF (difficult to model in other theories) is integrated out analytically. Unfortunately the same difficulty in evaluating the initial fields near the source plane occurs in this formalism. The propagation of a Gaussian input field is demonstrated and compared with the BPM and PEM calculation of the same input field. The calculation of the modal part of the constructions in section 7.3 and 7.4 is accurate throughout the wedge geometry away from the apex. Also a method of

calculating the reflection coefficient of a mode in a parallel guide when striking an interface with a wedge environment is given. No numerical calculations of this quantity were carried out.

CONCLUSIONS AND FUTURE CONSIDERATIONS.

This work can be divided into two main areas. The first area is concerned with the numerical implementation of the spectral objects derived in chapter 2 and subsequent fields generated from the boundary approach of chapter 7. The second area of work was involved with the application, properties and usefulness of these spectral synthesised functions. As some of the applications of the spectral approach arise as a consequence of formulated numerical algorithms it is logical to examine firstly the numerical aspects of the work.

Previous calculations of the IM field in the J−K ocean have been carried out by several authors [4,5] , and Topuz and Felsen [3] have generated IM fields in optical wedge structures for both TE and TM propagation. In all these calculations a simple quadrature integration rule was applied along the real axis in the spectral domain to generate the fields. This method of calculation requires approximately .2 seconds of CPU time to generate one field point. In chapter 3 exploitation of the oscillatory spectrum with respect to four configuration space axes is demonstrated, which when used in the intrinsic direction enables calculation of an IM field point in approximately 10^{-3} seconds, provided at least 128 by 256 points are calculated. The employment of these highly efficient FFT routines has enabled the contour and isometric plots of the field throughout the wedge environment, highlighted in chapter 5, to be calculated in the order of minutes. This efficient evaluation of the IM field has allowed accurate examination of the conservation of power in this quantity as the observation point moves upslope, in minutes, which would previously have taken several hours. This facility has also made possible the introduction of an asymptotic form of the E−M remainder without dramatically increasing run times, and thus demonstrating conservation of power to within numerical capability. Another useful property of the IM field is that to calculate a point anywhere within the wedge does not require knowledge of any other field point. This fact combined with the z−directed FFT (along the interface) generates field points without the necessity of calculating redundant data field points. The field plots described above are shown in chapter 5. A marching algorithm method (which changes the boundary value problem into an initial value problem) used to evaluate this type of longitudinal field at specific transverse coordinates introduces a large amount of redundancy, and consequently increases run times. This advantage possessed by the IM over other marching algorithms has particular use in the field of acoustics. Practical measurements of acoustic fields are obtained by trailing a hydrophone behind a ship at a constant depth. The IM field generated using the ξ−directed FFT will produce comparable data field points with no redundancy in a very short period of time. The marching algorithm methods of the BPM and PEM will, by their nature, generate a large amount of redundant information, which will require some manipulation to

obtain the appropriate data field. It should be noted at this point that the inclusion of the end–point correction to the IM field did not increase run times perceptibly as this correction term was evaluated from previously calculated quantities.

The numerical evaluation of the WGF discussed in chapter 6 was split into two different problems; the evaluation of the modal and initial fields. The modal field proved simple enough to evaluate by the FFT method. Although the actual integrand was significantly more complicated to evaluate than the IM integrand, the actual FFT implementation was easier as the dominant spectral contribution was well confined to a small finite portion of the real axis and did not require any additional end–point corrections. To calculate the WGF three integrals needed to be evaluated; the phase integral, the source integral and the observation integral, with the latter being calculated by the FFT approach. However, with the kernel calculated for the desired wedge geometry (i.e. the integrand of the modal field, with source integral calculated, but independent of observation position) the field evaluation using FFTs is very fast. Thus the rate determining step in the calculations of the modal field is the evaluation of the kernel for the wedge geometry and source point, which takes typically 40 minutes. The evaluation of the initial fields was achieved using the FFT method, with additional end–point corrections caluclated by Laplace's method. However, as the distance between the source and observation points decreases, the large parameter essential for a good Laplace approximation also decreases and this method of end–point correction proved inaccurate. The asymptotic end–point correction was replaced by a Simpson's rule integration into the complex plane. Little improvement in accuracy was obtained by using the above method as the range of inhomogeneous plane waves which contribute significantly to the field increases as source and observation point converge. Indeed this inability to calculate accurately the initial terms when the source and observation point separation is small has hampered the calcualtion of the reflected field from the simply connected structure in chapter 7.

Having concluded as much as is possible of the numerical aspects of the work without reference to the properties of the spectral approach, it is appropriate to examine these, their utility and possible applications. The IM field has obvious disadvantages compared to marching algorithm methods and the numerically calculated coupled mode theory [21] discussed in chapter 1. The most glaring disadvantage in its present form is is its inflexibility in modelling other non–separable, weakly range dependent, environments. Also the generation of IM fields requires careful attention as the spectral integrands for different environments can vary significantly. This latter minor problem can be avoided by using a large number of integration points, but this will obviously reduce efficiency in computation. The other defect in the IM field approach is that it can only approximate different field inputs to the wedge environment by using the IM summation (equation (6.3.1.5) of chapter 6) and

employing the boundary value approach of chapter 7. While this method will produce stable numerical results they are only asymptotically accurate (i.e. provided source and observation point are well separated) and thus the exactness property of the IM becomes redundant.

The advantages of the IM formulation over contemporary theories are many and upon close inspection of the work in this thesis it becomes obvious that there are many possibilities for future work. In chapter 3 the IM was proved to be an exact solution of the source free wedge geometry (excluding the apex) which no other previous theory has achieved. This property implies that the IM can be used, in conjuntion with FFT algorithms, to generate efficient, accurate, benchmark solutions with which to compare approximate numerical and analytical methods. As all approximations used in the implementation of the IM field can be explicitly quantified, it allows quantitative comparisons, similar to those demonstrated in chapter 5, to be made. Indeed if the spectral integration range is large enough then the upper bound on error is the associated numerical rounding errors and the numerical solution can be considered exact. The construction of this spectral object furnishes a physical insight into the coupling processes as a mode propagates upslope. As a particular Intrinsic Mode propagates through the Adiabatic Mode critical transition region asymptotic analysis of the IM demonstrates how the field, asymptotically Adiabatic, couples to the multiply–reflected lateral ray field and the complex mode (i.e. AM representation with a complex propagation angle). It would be instructive to compare the IM field with other marching algorthims in this wedge environment as an assessment of their performance. Although the IM is limited in its versatility a further area of research could be concerned with the local intrinsic mode concept [31] in which local spectral patching techniques [62] are implemented. This type of approach will produce computable objects (by applying the FFT routines) which will be uniformly valid across caustic surfaces and other similar topologies, and as such will prove extremely useful in the modelling of focusing systems such as antennas and geodesic lenses.

The source induced global object derived in chapter 2 was demonstrated to possess all the properties of a Green's function in the wedge geometry excluding the apex. This demonstration was achieved by treating collectively the plane wave species in the wedge environment and tracking their consequent propagation. The asymptotic analysis of this WGF was shown to be equal to the asymptotic forms of the spectral function in [39], in which Arnold and Felsen construct an approximate solution. This as stated is equivalent at least asymptotically to work by Pierce [20] and Kamel and Felsen [19], although a different representation of the field after cut–off is used in the former.

There are distinct disadvantages in the application of the Wedge Green's Function to calculating fields in the wedge geometry. Two obvious disadvantages are

that the calculation of the initial fields proved significantly more difficult than expected and the evaluation time for the modal spectrum was approximately 40 minutes. Also, in a similar manner as for the IM, the WGF is only applicable to wedge shaped non–separable linear environments.

However, the advantages of this approach, its implications with respect to other theories, and possible applications are many. Before embarking upon applications, future attention must be placed on calculating the initial fields, so that it becomes possible to evaluate these quantities throughout the wedge structure (excluding the apex). When the initial fields can be correctly calculated arbitrarily close to the source point, the WGF will then produce a field due to that source point, in which the quantities neglected can be easily quantified. Thus the WGF in its pure form can be used as a tool for estimation of accuarcy of approximate numerical algorithms.

A more substantial use of the WGF occurs in the boundary value approach (Kirchhoff–Huygens diffraction integral) described in chapter 7. It is observed that with correctly calculated initial fields this method is a better comparitive tool than the WGF used on its own, because the occurrence of the singularity in the latter approach is integrated out in the former. The Kirchhoff diffraction integral method also allows any input to the wedge structure to be modelled, in principle exactly, and practically is at least able to account for all analytical approximations. Future investigations could be concerned with propagating the IM field by the above method to confirm its exact nature. To achieve this type of calculation further investigation of faster methods of integration are required.

At first sight the best area for future work is the calculations of reflected fields from connected structures. The method is demonstrated for a simple structure in chapter 7. On closer inspection it is clearly seen that this type of calculation will still require vast amounts of computer time. Generating solutions which account for the radiation fields in these geometries will obey the law of diminishing returns. Thus this approach, while interesting, is only worthwhile pursuing to the order of complexity demonstrated in chapter 7.

To conclude concisely, the work in this thesis has demonstrated conservation of power in this spectral treatment of Arnold and Felsen. Confirmation of the exactness of the IM and the WGF has been given. Also, asymptotic analysis has demonstrated applicability with other methods and different derivations of the same spectral object. This exact expression of the Green's function in the wedge environment has enabled integral approaches to be formulated for calculation of reflection coefficients of modes and propagation of fields throughout the taper. The numerical aspects of the work have derived efficient methods of calculating spectrally constructed fields. This work has enabled a practical assessment of future work. Firstly the boundary value approach for calculating reflected fields should not be applied in any greater depth than demonstrated in chapter 7. Work on the initial fields would be useful for

propagation of fields from a boundary and used as a comparative tool. Essentially the work on the IM field is complete and can now be used without hesitation as a benchmark solution of the 2–dimensional wedge geometry. The FFT methods are highly efficient in calculating spectrally synthesised fields and should be used in conjuntion with recently developed spectrally approximate field theories [63]. This type of approximate analysis is where the future of the techniques in this thesis can be best employed.

APPENDIX A Asymptotic Forms of the Euler–Maclaurin Remainder.

This appendix evalutates the asymptotic forms of $E_o(\theta)$, $F_1(\theta)$ and $F_2(\theta)$ with respect to the reciprocal of the smallness parameter α (the wedge angle). Examine firstly the function $E_o(\theta)$,

$$E_o(\theta) = E_p(\theta,\theta_q) + E_n(\theta,\theta_q) \tag{A1}$$

with $E_p(\theta,\theta_q)$ and $E_n(\theta,\theta_q)$ obtained from (2.3.3a). This can be evaluated straight forwardly by first letting $\delta \to 0$ and deforming the lower end points to $\theta \pm i\infty$ appropriately. If the substitution $s-\theta = t$ is made in $E_p(\theta,\theta_q)$ and $s-\theta = -t$ in $E_n(\theta,\theta_q)$ then the two integrals can be combined so that $E_o(\theta)$ becomes,

$$E_o(\theta) = \frac{1}{2\alpha}\int_{i\infty}^{0}\Big[\,\Phi(\theta+t) - \Phi(\theta-t)\,\Big]\frac{M(t)dt}{1-M(t)} \tag{A2}$$

As $\Phi(t)$ has only algebraic growth at infinity the convergence of the integral is dominated by the exponential term. The integrand rapidly decays away from the upper limit and exploiting this dominance the bracketed term is expanded in a Taylor series about this point to give,

$$\Phi(\theta+t)-\Phi(\theta-t) = 2t\Phi_\theta(\theta) + \frac{t^3}{3}\Phi_{\theta\theta\theta}(\theta) \tag{A3}$$

with $\Phi_\theta(\theta)$ denoting the derivatives with respect to θ. Substituting this into (A2) allows the asymptotic form of $E_o(\theta)$ to be,

$$E_o(\theta) \sim \frac{1}{\alpha}\,\Phi_\theta(\theta)\int_{i\infty}^{0}\frac{tM(t)dt}{1-M(t)} + O(t^3) \tag{A4}$$

Making the substitution,

$$v = \frac{-i\Pi t}{\alpha} \tag{A5}$$

$E_o(\theta)$ is thus transformed into the more managable form of,

$$E_o(\theta) \sim \frac{\alpha}{\Pi^2} \Phi_\theta(\theta) \int_0^\infty \frac{ve^{-v}dv}{1 - e^{-v}} + O(\alpha^3) \tag{A6}$$

The series representation,

$$\frac{e^{-v}}{1 - e^{-v}} = \sum_{n=-\infty}^{\infty} e^{-nv} \tag{A7}$$

can be exploited so that with a change of variables $nv = s$ the integral becomes,

$$\sum_n \frac{1}{n^2} \int_0^\infty e^{-s} sds \tag{A8}$$

Here the integral is the standard gamma function and the series sum is the zeta function [52]. This function can be calculated in this instance by Fourier series [53]. This then gives $E_o(\theta)$ as,

$$E_o(\theta) \sim \frac{\alpha}{6} \Phi_\theta(\theta) + O(t^3) \tag{A9}$$

To examine fully the asymptotic nature of $E_o(\theta)$ for $\alpha \to 0$ it is essential to look at the behaviour of $\Phi_\theta(\theta)$ throughout the complex $\theta-$plane. The branch cut integral $F_1(\theta)$ needs to be asymptotically evaluated.

$$F_1(\theta) = \frac{1}{2\alpha} \int_{P_a} \frac{\Phi(s)M(-s+\theta)ds}{1 - M(-s+\theta)} \tag{A10}$$

If θ is such that it has a very small positive imaginary part, then the integral can be approximated by,

$$F_1(\theta) \approx \frac{1}{2\alpha} \int_{P_a} \Phi(s) e^{\frac{i\Pi(\theta-s)}{\alpha}} ds \tag{A11}$$

Assume that the phase function can be expanded about its branch point such that,

$$\Phi(s) = \sum_m C_m (s-\theta_c)^{\frac{1}{2}+m} \tag{A12}$$

With the substitution

$$t^2 = (s-\theta_c) \tag{A13}$$

the branch cut integral can be approximated by,

$$F_1(\theta) \sim \sum_m \frac{C_m}{2\alpha} \int_{-\infty e^{i\Pi/4}}^{\infty e^{i\Pi/4}} 2t^{2+m} e^{-\frac{i\Pi t^2}{\alpha}} dt\, e^{\frac{i\Pi(\theta-\theta_c)}{\alpha}} \tag{A14}$$

Making the substitution

$$\zeta^2 = \frac{i\Pi}{\alpha} t^2$$

and considering the first term leads to

$$F_1(\theta) \sim -\frac{C_0}{\alpha} e^{\frac{i\Pi(\theta-\theta_c)}{\alpha}} \left[\frac{\alpha}{i\Pi}\right]^{3/2} \int_{-\infty}^{\infty} \zeta^2 e^{-\zeta^2} d\zeta \tag{A15}$$

recognising the gamma function and C_0 from appendix B the branch cut integral is,

$$F_1(\theta) \sim \frac{(2\alpha \cot\theta_c)^{\frac{1}{2}}}{2\Pi} e^{\frac{i\Pi(\theta-\theta_c)}{\alpha} - \frac{i\Pi}{4}} \tag{A16}$$

Indentical procedures gives rise to a similar branch cut integral for $F_2(\theta)$.

APPENDIX B Asymptotic Properties of Reflection Coefficients.

This appendix contains all the properties and asymptotic nature of the reflection coefficients and other functions necessary for the first order asymptotic evaluation of the Intrinsic Mode field. A generic reflection coefficient is,

$$e^{i\Phi(\theta)} = e^{i2\tan^{-1}\left[\frac{irn_1\sin\theta_1}{n\sin\theta}\right]} \tag{B1}$$

with $n\cos\theta = n_1\cos\theta_1$ and $r = d/d_1$ for ocean acoustics and $r = 1$ or n^2/n_1^2 for optical TE and TM propagation respectively. Expanding $\sin\theta_1$ about the critical angle requires,

$$\begin{aligned} \sin\theta &= \sin\theta_c + \delta\cos\theta_c + O(\delta^2) \\ \cos\theta &= \cos\theta_c - \delta\sin\theta_c + O(\delta^2) \qquad \delta = (\theta-\theta_c) \end{aligned} \tag{B2}$$

$$irn_1\sin\theta = ir\left[\, n_1^2 - n^2(\cos\theta_c - \delta\sin\theta_c + O(\delta^2))^2 \,\right]^{\frac{1}{2}}$$

$$= inr\left[2\delta\sin\theta_c\cos\theta_c + O(\delta^2)\right]^{\frac{1}{2}} \tag{B3}$$

As the expansion for $\tan^{-1}x$ is $x + O(x^3)$ then the phase of the reflection coefficient can be expressed as,

$$i\Phi(\theta) = \frac{nr(2\delta\sin\theta_c\cos\theta_c + O(\delta^2))}{n\sin\theta_c + n\delta\cos\theta_c + O(\delta^2)}$$

$$= r(2(\theta-\theta_c)\cot\theta_c)^{\frac{1}{2}} + O(\delta^{3/2}) \tag{B4}$$

Now require to expand $H^{\pm}(\theta,s)$ of chapter 6 to O(1)

$$\begin{aligned} \sin(s-a\alpha) &= \sin s + O(\alpha) \\ \cos(s-a\alpha) &= \cos s + a\alpha\sin s + O(\alpha^2) \end{aligned} \tag{B5}$$

where a is either 2 or 0. Using the quantities in equation (B5) gives the source plane waves as,

$$W_0^{\pm}(s-a\alpha) = e^{ikh_s\cos s/\alpha}e^{iks\sin s(ah_s \mp x_s)} + O(\alpha) \tag{B6}$$

The phase function shifted by $a\alpha$ is,

$$e^{i\Phi_j(s-a\alpha)} = \frac{n\sin(s-a\alpha) - (n_j^2 - (n\cos(s-a\alpha))^2)^{\frac{1}{2}}}{n\sin(s-a\alpha) - (n_j^2 - (n\cos(s-a\alpha))^2)^{\frac{1}{2}}} \tag{B7}$$

Substituting in equations (B5) gives,

$$e^{i\Phi_j(s-a\alpha)} = e^{i\Phi_j(s)} + O(\alpha) \qquad \text{(B8)}$$

Using (B6) and (B8) the appropriate asymptotic representation of the modal part of the WGF is demonstrated as in chapter 6.

APPENDIX C Proof of Exactness Property Of Intrinsic Mode.

This appendix demonstrates that the Intrinsic Mode field satisfies the boundary conditions of the wedge geometry. Before any proof of the boundary conditions it is essential to prove a specific result. From (2.2.8) of chapter 2,

$$S_q^-(\theta) = -\frac{\Phi^-(\theta)}{2} + \frac{1}{2\alpha}\int_{\theta_c}^{\theta} \Phi^-(s)ds - \frac{q\Pi\theta}{\alpha} + E_b^-(\theta,\theta_q) \qquad (C1)$$

When $S_q(\theta)$ is shifted by 2α to the right one obtains,

$$S_q^-(\theta+2\alpha) = -\frac{\Phi^-(\theta+2\alpha)}{2} + \frac{1}{2\alpha}\int_{\theta_c}^{\theta+2\alpha} \Phi^-(s)ds - \frac{q\Pi(\theta+2\alpha)}{\alpha} + E_b^-(\theta+2\alpha,\theta_q) \qquad (C2)$$

Adding and substracting $\Phi^-(\theta)/2$ to (C2) and applying the Euler–Maclaurin formula (equation (2.2.7) of chapter 2) leads to,

$$S_q^-(\theta+2\alpha) = \frac{\Phi^-(\theta)}{2} + \frac{1}{2\alpha}\int_{\theta_c}^{\theta} \Phi^-(s)ds - \frac{q\Pi\theta}{\alpha} + E_b^-(\theta,\theta_q) \qquad (C3)$$

In this form it becomes obvious that the shifted spectral amplitude function satisfies the relation

$$e^{iS_q^-(\theta+2\alpha)} = e^{iS_q^-(\theta)}e^{i\Phi^-(\theta)} \qquad (C4)$$

The uniqueness condition,

$$S_q^+(\theta) - S_q^-(\theta) = \Phi_1(\theta) \qquad (C5)$$

allows the identification of the shifted downward phase in terms of the upward phase as,

$$e^{iS_q^-(\theta+2\alpha)} = e^{iS_q^+(\theta)}e^{-i\Phi_1(\theta)}e^{i\Phi^-(\theta)} \qquad (C6)$$

Consider first the upper boundary condition where $x=-z\tan\alpha$. The total field at this upper boundary from inside the guide, from equation (2.2.11) of chapter 2, is

$$\sum_{-}^{+} \int_{C} e^{iS_q^{\pm}(\theta)} e^{\frac{inkzcos(\theta \pm \alpha)}{cos\alpha}} d\theta \qquad (C7)$$

If the downward field is then shifted to the right by the substitution $\theta \rightarrow \theta + 2\alpha$ and using Cauchy's theorem for infinite contours, so as to shift the contour by 2α to the left (to regain the C contour) leads to an Intrinsic Mode field, defined from inside the guide, on the boundary as,

$$W_q(\underline{x}) = \int_{C} \left[e^{iS_q^{+}(\theta)} + e^{iS_q^{-}(\theta+2\alpha)} \right] e^{\frac{inkzcos(\theta+\alpha)}{cos\alpha}} d\theta \qquad (C8)$$

Utilising the derived identity of equation (C6) gives,

$$W_q(\underline{x}) = \int_{C} \left[1 + e^{i\Phi_u(\theta+\alpha)} \right] e^{iS_q^{+}(\theta)} e^{\frac{inkzcos(\theta+\alpha)}{cos\alpha}} d\theta \qquad (C9)$$

This is exactly the derived form for the field on the boundary evaluated from the expression for the field above the upper interface as can be seen from equation 2.2.11 of chapter 2.

The lower boundary corresponds to $x = 0$ and so the field on the boundary calculated from inside the guide is

$$W_q(\underline{x}) = \int_{C} \left[e^{iS_q^{+}(\theta)} + e^{iS_q^{-}(\theta)} \right] e^{inkzcos\theta} d\theta \qquad (C10)$$

The uniqueness condition of equation (C5) leads to the expression for the field on the lower boundary, from inside the guide as,

$$W_q(\underline{x}) = \int_{C} \left[e^{i\Phi_l(\theta)} e^{iS_q^{-}(\theta)} + e^{iS_q^{-}(\theta)} \right] e^{inkzcos\theta} d\theta \qquad (C11)$$

This is exactly the same form as the field on the lower boundary from outside the guide as given in equation 2.2.11 of chapter 2. Hence the field is continuous across both boundaries of the wedge environment. To show continuity of the derivative of the field is a trivial extension of this approach.

APPENDIX D Stationary Phase Evaluation Of The Intrinsic Mode.

The equations of (4.3.2) are in a canonical form applicable for asymptotic evaluation by the method of steepest descents. The integrand has a rapidly oscillating phase except for a stationary phase point (θ_q) given by,

$$\frac{dZ_q(\theta_q)}{d\theta} = 0 \tag{D1}$$

The substitution,

$$Z_q(\theta) - Z_q(\theta_q) = \alpha S^2 \tag{D2}$$

can be made as the branch point θ_c in the phase function is not 'near' the stationary phase point θ_q. For the above change of variable the derivative,

$$\frac{d\theta}{dS} = \frac{2\alpha S}{\frac{-dZ_q(\theta)}{d\theta}} \tag{D3}$$

is indeterminate at the stationary phase point θ_q. However, application of L'Hopital's rule yields,

$$\lim_{\theta \to \theta_q} \frac{d\theta}{dS} = \left[\frac{2\alpha}{\frac{-d^2Z_q(\theta_q)}{d\theta^2}}\right]^{\frac{1}{2}} \tag{D4}$$

The positive square root been chosen. Using the substitutions of (D2) in (4.3.2) and considering only first order terms yields the asymptotic form for the field inside the guide to be,

$$W_q(\underline{x}) = \sum_{+-} \left[\frac{2\alpha}{\frac{-d^2Z_q(\theta_q)}{d\theta^2}}\right]^{\frac{1}{2}} e^{\frac{iZ_q(\theta_q)}{\alpha}} F^{\pm}(\theta_q) \int_{-\infty}^{\infty} e^{iS^2} dS \tag{D5}$$

Rotating the contour through $\Pi/4$ radians allows the recognition of the gamma function. The field inside the guide is then,

$$W_q(\underline{x}) = \sum_{+-} \left[\frac{2\Pi\alpha}{\frac{-d^2Z_q(\theta_q)}{d\theta^2}}\right]^{\frac{1}{2}} e^{\frac{iZ_q(\theta_q) - i\Pi}{\alpha} \frac{}{4}} F^{\pm}(\theta_q) \tag{D6}$$

From equation (4.3.2c) the addition of the upward and downward components in the guiding duct are,

$$\sum_{+-}^{\pm} F^{\pm}(\theta_q) = 2e^{-i\Pi/2}\sin\left[\frac{\Phi_1(\theta_q)}{2} + nkx\sin\theta_q\right] \qquad (D7)$$

Applying similar analysis to the field outside the guiding duct and using the stationary phase condition (D1) gives rise to the asymptotic form of the Intrinsic Mode field, when the adiabatic mode is well guided, as,

$$W_q(\underline{x}) = \begin{cases} \left[\frac{8\Pi\alpha}{-d^2Z_q(\theta_q)/d\theta^2}\right]^{\frac{1}{2}} e^{\frac{iZ_q(\theta_q)}{\alpha} - i\frac{\Pi}{4}} \sin\left[[h-x]nk\sin\theta_q\right], & \underline{x} \in X \\ \left[\frac{8\Pi\alpha}{-d^2Z_q(\theta_q)/d\theta^2}\right]^{\frac{1}{2}} e^{\frac{iZ_q(\theta_q)}{\alpha} - i\frac{\Pi}{4}} \sin\left[nkh\sin\theta_q\right]e^{-inkx\sin\theta_1}, & \underline{x} \in X_1 \end{cases} \qquad (D8)$$

where θ_1 is the refracted stationary phase point angle.

Demonstrating that the Approximation of the Intrinsic Mode to O(1) is equal to the Adiabatic Mode.

Noting from (4.3.2b) that,

$$\frac{d^2Z_q(\theta_q)}{d\theta^2} = \frac{d}{d\theta}\left[\Phi_1(\theta)/2 + nkh\sin\theta\right]_{\theta=\theta_q} \qquad (D9)$$

Using the reflection coefficient for acoustic fields with constant density and implementing the differentiation gives,

$$\frac{d^2Z_q(\theta_q)}{d\theta^2} = \frac{nk\cos\theta_q(1 + in_1kh\sin\theta_{q1})}{in_1k\sin\theta_{q1}} \qquad (D10)$$

Also it is observed that,

$$\frac{dZ_q(\theta_q)}{dz} \sim nk\cos\theta_q + \frac{d}{dz}\left[\frac{1}{2}(\Phi_1(\theta)+(\Pi-2q\Pi)) + nkh\sin\theta\right]_{\theta=\theta_q} \qquad (D11)$$

Using these equations together with the definitions of equation (1.1.7) of chapter 1 and the transverse resonance condition shows that the asymptotic form of the Intrinsic Mode is equal to the Adiabatic Mode field up to a constant multiplier.

Demonstrating the Smallness of the Field due to the Stationary Phase Point $\Pi - \theta_q$.

The stationary phase point at $\Pi - \theta_q$ is evaluated in the same way with θ_q replaced by $\Pi - \theta_q$ and with the identity,

$$Z_q(\Pi-\theta_q) = \frac{\Pi^2}{2}(1-2q) - Z_q(\theta_q) + \frac{1}{2\alpha}\sum_{n=-\infty}^{\infty}\int_{\theta_c}^{\Pi-\theta_c} \Phi_1(\delta)\, e^{\frac{in\Pi(\theta_q-\delta)}{\alpha}}\, d\delta \qquad (D12)$$

The integral in equation (D12) has a large positive imaginary part and consequently the field is small compared to the stationary phase point field at θ_q.

Approximation of the Endpoint Correction for the Intrinsic Mode.

Together with this staionary phase point there are other contributions to the field if the contour evaluation is finite and these endpoint fields can be calculated by using Laplaces Method. This situation arises for observation points inside the guiding structure. Assume,

$$W_q(\underline{x}) \approx \sum_{+-}\int_a^b F^{\pm}(\theta)\, e^{\frac{iZ_q(\theta)}{\alpha}}\, d\theta, \qquad \underline{x} \in X \qquad (D13)$$

The only contribution to consider is from $-i\infty$ to the lower endpoint a. Thus an approximation can be derived by integration by parts so that the contribution to the field from this contour is,

$$\left[\frac{\alpha F^{\pm}(\theta) e^{\frac{iZ_q(\theta)}{\alpha}}}{i\frac{dZ_q(\theta)}{d\theta}}\right]_{\sigma-i\infty}^{a} - \int_{\sigma-i\infty}^{a}\frac{\alpha F^{\pm\prime}(\theta) e^{\frac{iZ_q(\theta)}{\alpha}}}{i\frac{dZ_q(\theta)}{d\theta}}\, d\theta \qquad (D14)$$

Evaluating this integral then gives

$$-\left[\frac{\alpha^2 F^{\pm\prime}(\theta) e^{\frac{iZ_q(\theta)}{\alpha}}}{\left[i\frac{dZ_q(\theta)}{d\theta}\right]^2}\right]_{\sigma-i\infty}^{a} + O(\alpha^3) \qquad (D15)$$

Here σ is chosen such that the integrand decays exponentially as $\theta \to -i\infty$ and $'$ represents differentiation with respect to θ. Thus the lower endpoint of the finite integral can be approximated by,

$$\sum_{+-}\frac{\alpha e^{\frac{iZ_q(a)}{\alpha}}}{Z_q'(a)}\left\{ iF^{\pm}(a) - \frac{\alpha F^{\pm\prime}(a)}{Z_q'(a)}\right\} + O(\alpha^3) \qquad (D16)$$

APPENDIX E Asymptotic Evaluation of the IM throughout the Critical Transition Region.

This appendix calculates a uniform asymptotic field in the critical transition region when the Adiabatic Mode is close to cut-off using the method of Chester, Friedman and Ursell [32]. The Intrinsic Mode field inside the guiding structure is,

$$W_q(\underline{x}) = \sum_{+-} \int_C F^{\pm}(\theta)\, e^{\frac{iZ_q(\theta)}{\alpha}}\, d\theta \qquad \text{(E1)}$$

The method of Chester, Friedman and Ursell produces a uniform asymptotic expansion of an integral with two nearby saddle points. The branch point, at θ_c, in (E1) can be transformed into a saddle point using the substitution $t=(\theta-\theta_c)^{\frac{1}{2}}$, which gives the field inside the guide as,

$$W_q(\underline{x}) = \sum_{+-} \int_{C_t} tF^{\pm}(\theta)\, e^{\frac{iZ_q(\theta)}{\alpha}}\, dt \qquad \text{(E2)}$$

The stationary phase points of this integral are determined by,

$$\frac{dZ_q(\theta)}{dt} = \frac{dZ_q(\theta)}{d\theta}\frac{d\theta}{dt} = 0 \qquad \text{(E3)}$$

This has transformed the branch point in the θ plane into a saddle point at $t=0$ in the t plane. The transformation is such that,

$$|\arg t| < \frac{\Pi}{2} \qquad |\arg(\theta-\theta_c)| < \Pi \qquad \text{(E4)}$$

Applying the method of Chester, Friedman and Ursell requires the substitution,

$$\alpha^{-1}Z_q(\theta) = A - \frac{B}{2}S^2 + \frac{i}{3}S^3 \qquad \text{(E5)}$$

The right hand side of equation (E5) has stationary points at $S=0,+ib$ which will correspond to $\theta=\theta_c,\theta_q$ respectively. This gives A and B as,

$$A = \alpha^{-1}Z_q(\theta_c) \qquad B^3 = \frac{6}{\alpha}\left[Z_q(\theta_c) - Z_q(\theta_q)\right] \qquad \text{(E6)}$$

and thus the field inside the guide can be expressed as,

$$W_q(\underline{x}) = e^{\frac{iZ_q(\theta_c)}{\alpha}} \sum_{+-} \int_{C_s} tF^{\pm}(\theta)\frac{dt}{dS}\, e^{-iBS^2/2-S^3/3}dS \qquad (E7)$$

Expanding the remaining integrand about the maximum value of the exponent gives (S= 0) the field as,

$$W_q(\underline{x}) = e^{\frac{iZ_q(\theta_c)}{\alpha}} P\sum_{+-} \int_{C_s} Se^{-iBS^2/2-S^3/3}dS \qquad (E8)$$

where,

$$P = \frac{d}{dS}\left[tF^{\pm}(\theta)\frac{dt}{dS}\right] \Big|_{S=0,\ t=0,\ \theta=\theta_c} \qquad (E9)$$

carrying out the differentiation leads to,

$$P = F^{\pm}(\theta)\left[\frac{dt}{dS}\right]^2 \Big|_{S=0,\ t=0,\ \theta=\theta_c} \qquad (E10)$$

From equation (E5) it is possible to obtain,

$$\frac{dt}{dS} = \frac{(BS - iS^2)\alpha}{\frac{d\theta}{dt}\frac{dZ_q(\theta)}{d\theta}} \qquad (E11)$$

This is indeterminate at S= 0, but applying l'Hopital's rule gives,

$$\left[\frac{dt}{dS}\right]^2 = \frac{B\alpha}{2Z_q'(\theta_c)} \qquad (E12)$$

and using this gives the field inside the guide as,

$$W_q(\underline{x}) = \sum_{+-} \frac{F^{\pm}(\theta_c)\alpha B}{2Z_q'(\theta_c)}\, e^{\frac{iZ_q(\theta_c)}{\alpha}} \int_{C_s} Se^{-iBS^2/2-S^3/3}dS \qquad (E13)$$

From equation (4.3.2c) of chapter 4 it is obvious that,

$$F^{\pm}(\theta_c) = e^{\pm inkx\sin\theta_c} \qquad (E14)$$

and expanding B about the critical angle θ_c gives,

$$B = \left[6(\theta_q - \theta_c)\frac{dZ_q(\theta_c)}{d\theta}\right]^{1/3} \qquad (E15)$$

Expanding $Z_q(\theta_q)$, differentiated with respect to θ, about θ_c gives,

$$\frac{dZ_q(\theta_q)}{d\theta} = \frac{dZ_q(\theta_c)}{d\theta} + (2(\theta_q-\theta_c)\cot\theta_c)^{\frac{1}{2}} \qquad \text{(E16)}$$

which is known to be asymptotically small (i.e. equal to zero) and thus B is given as,

$$B = \frac{dZ_q(\theta_c)}{d\theta}\left[\frac{6}{\alpha(2\cot\theta_c)^{\frac{1}{2}}}\right]^{1/3} \qquad \text{(E17)}$$

and hence (E1) becomes

$$W_q(\underline{x}) \underset{+-}{=}\sum \frac{F^{\pm}(\theta_c)\alpha}{2Z_q'(\theta_c)}\, e^{\frac{iZ_q(\theta_c)}{\alpha}}\left[\frac{6}{\alpha(2\cot\theta_c)^{\frac{1}{2}}}\right]\int_{C_s} Se^{-iBS^2/2-S^3/3}dS \qquad \text{(E18)}$$

APPENDIX F Calculation of the Initial Fields for the Global WGF.

This appendix derives the initial, direct and reflected plane wave fields for WGFs which have source points outside the guiding medium.

Plane Wave Analysis of WGF for Source Points in Substrate.

Consider firstly the initial fields for the WGF with source points as depicted in Figure 6.1.1. It is possible to represent the transmission coefficient for an incident plane wave on B_1, at angle θ_1, as,

$$T_1 = 1 + e^{i\Psi_1(\theta_1)} \tag{F1}$$

using the same notation as in chapter 2. The reflection coefficient on the upper boundary can easily be identified in preceeding analysis. Consequently, using the source plane wave definition (6.1.1) and the spectral constructions of equations (6.1.2), (6.1.3), the upward and downward initial plane wave fields are,

$$\begin{aligned} &\int_{C_1} W_1^+(\theta_1)\left[1 + e^{i\Psi_1(\theta_1)}\right] V_\theta^+(\underline{x})\, d\theta_1 \\ &\int_{C_1} W_1^+(\theta_1)\left[1 + e^{i\Psi_1(\theta_1)}\right] e^{i\Phi_u(\theta+\alpha)} V^-_{\theta+2\alpha}(\underline{x})\, d\theta_1 \end{aligned} \tag{F2}$$

respectively. Here C_1 is the Sommerfeld contour which continues in the imaginary θ_1-plane making the integrand tend to zero. Using the relationship of (6.1.4) the substitution,

$$\theta = \cos^{-1}\left[\frac{n_1}{n}\cos\theta_1\right] \qquad \frac{d\theta_1}{d\theta} = \frac{n\sin\theta}{n_1\sin\theta_1} \tag{F3}$$

may be employed. The mathematical description of the transmission coefficient gives a relationship between the phase of the reflection coefficients from either side of the boundary and it is found to be,

$$\Psi_1(\theta_1) + \Pi = \Phi_1(\theta) \tag{F4}$$

Invoking the substitution (F3), applying (F4) and permissible deformations of the mapped contour C_1 to C, gives the upward and downward initial plane wave fields to be,

$$\int_C W_1^+(\theta_1)\left[1 + e^{i\Phi_1(\theta)}\right]V_\theta^+(\underline{x})\,d\theta$$

$$\int_C W_1^+(\theta_1')\left[1 + e^{i\Phi_1(\theta-2\alpha)}\right]e^{i\Phi_u(\theta-\alpha)}V_\theta^-(\underline{x})\,d\theta \qquad \text{(F5)}$$

respectively, with θ_1' given in (6.1.4). In the downward field a shift of 2α in the θ domain has occured, with allowable contour deformation. The same approach – i.e. substitution (F3) – can be adopted for the direct field, <4>, and the reflected field, <3>, to give the plane wave species over the θ variable as,

$$W_1^+(\theta_1)\frac{d\theta_1}{d\theta}\,V_{1\,\theta_1}^+(\underline{x})$$

$$W_1^+(\theta_1)\frac{d\theta_1}{d\theta}\,e^{i\Psi_1(\theta_1)}V_{1\,\theta_1}^-(\underline{x}) \qquad \text{(F6)}$$

Employing the phase relationship (F4) and contour shifts and deformations gives the direct and reflected plane wave fields as in (6.1.5).

Plane Wave Analysis of the WGF for Source Points in the Superstrate.

When the source point is in the upper medium as depicted in Figure 6.1.2 then it is clear that the transmission coefficient for a plane wave incident at an angle $\theta_2+\alpha$, on B_u, can be represented as,

$$T_2 = 1 + e^{i\Psi_u(\theta_2+\alpha)} \qquad \text{(F7)}$$

and with the corresponding phase reflection identity

$$\Psi_u(\theta_2+\alpha) + \Pi = \Phi_u(\theta+\alpha) \qquad \text{(F8)}$$

Thus the initial downward and upward plane wave fields are,

$$\int_C W_2^-(\theta_2+2\alpha)\left[1 + e^{i\Psi_u(\theta_2+\alpha)}\right]V_{\theta+2\alpha}^-(\underline{x})\,d\theta_2$$

$$\int_C W_2^-(\theta_2+2\alpha)\left[1 + e^{i\Psi_u(\theta_2+\alpha)}\right]e^{i\Phi_1(\theta+2\alpha)}V_{\theta+2\alpha}^+(\underline{x})\,d\theta_2 \qquad \text{(F9)}$$

respectively. Using Snell's law for the upper boundary, and permissible shifts of

contours and the the phase relationship (F8) gives the initial downward and upward reflected plane wave fields as,

$$\int_C W_2^-(\theta_2'+\alpha)\left[1 + e^{i\Phi_u(\theta-\alpha)}\right]V_\theta^-(\underline{x})d\theta$$

$$\int_C W_2^-(\theta_2'+\alpha)\left[1 + e^{i\Phi_u(\theta-\alpha)}\right]e^{i\Phi_l(\theta)}V_\theta^+(\underline{x})d\theta \qquad \text{(F10)}$$

$$n_2\cos(\theta_2') = n\cos(\theta-\alpha)$$

which provide the spectral amplitudes of equation (6.1.9). Again, as for the previously defined WGF the direct and reflected fields are required. Using permissible shifts of contours and appropriate substitutions gives the direct and reflected fields in the spectral domain as,

$$W_2^+(\theta_2)\frac{d\theta_2}{d\theta}\, V^+_{2\theta_2}(\underline{x})$$

$$-e^{i\Phi_l(\theta+\alpha)}\, W_2^-(\theta_2+2\alpha)\frac{d\theta_2}{d\theta}\, V^+_{2\theta_2}(\underline{x}) \qquad \text{(F11)}$$

respectively. This then gives direct and relected field as described in equations (6.1.10).

APPENDIX G Proof Of Satisfaction Of The Boundary Condtions By The WGF.

This appendix gives the manipulations of the spectral fields necessary for the proof of the upper and lower boundary conditions. The downward modal plane wave field inside the guiding medium is given by,

$$\int_C \left[\frac{1}{2\alpha} \sum_{q=-\infty}^{\infty} \int_{\theta_{q\infty}}^{\theta} U_j^-(s) F_q^-(\theta,s)\,ds \right] V_\theta^-(\underline{x})\,d\theta \qquad (G1)$$

making the substitutions $\theta = \theta + 2\alpha$ and $s = s + 2\alpha$ and a permissible shift of the contour C (see chapter 2) by 2α to the left gives,

$$\int_C \left[\frac{1}{2\alpha} \sum_{q=-\infty}^{\infty} \int_{\theta_{q\infty}}^{\theta} U_j^-(s+2\alpha) F_q^-(\theta+2\alpha, s+2\alpha)\,ds \right] V_{\theta+2\alpha}^-(\underline{x})\,d\theta \qquad (G2)$$

Using equations (6.2.1.3) and (H17), (H18) and (H19) of appendix H gives the modal downward plane wave field, at B_u, from inside the guide as,

$$\int_C \left[\frac{1}{2\alpha} \sum_{q=-\infty}^{\infty} \int_{\theta_{q\infty}}^{\theta} U_j^-(s+2\alpha) e^{-i\Phi_u(s+\alpha)} F_q^+(\theta,s)\,ds \right] e^{i\Phi_u(\theta+\alpha)} V_{2\,\theta_2}^+(\underline{x})\,d\theta \qquad (G3)$$

This leads to a generalised identity for the downward field at B_u.

$$U_j^-(s) F_q^-(\theta,s) = U_j^-(s+2\alpha) e^{-i\Phi_u(s+\alpha)} F_q^+(\theta,s) e^{i\Phi_u(\theta+\alpha)} \qquad (G4)$$

Continuity of Observed field at B_u for the WGF with the Source in the Substrate.

When the source point is in the lower medium it is obvious that the transmitted modal spectrum on B_u must equal the modal spectrum inside the guide evaluated on B_u. Using equations (6.1.11), (6.2.1.3) and the identity (G4), the proof of the continuity of the observed field requires that,

$$U_j^-(s+2\alpha) e^{-i\Phi_u(s+\alpha)} e^{i\Phi_u(\theta+\alpha)} = U_j^+(s) e^{i\Phi_u(\theta+\alpha)} \qquad (G5)$$

In a similar manner the initial transmitted field must equal the initial fields inside the guide evaluated at B_u. Shifting the downward field in this stated equality by 2α, then the satisfaction of the boundary conditions requires that,

$$U_j^-(\theta+2\alpha) = U_j^+(\theta)e^{i\Phi_u(\theta+\alpha)} \qquad (G6)$$

The initial fields for source points in the substrate are calculated in appendix F, and their spectral amplitude functions are given in equation (6.1.4). Substituting these spectral coefficients into (G5) and (G6) confirms the proof of the continuity of the observed field.

Continuity of Observed field at B_u for the WGF with the Source in the Guide.

In the text and from Figure 6.2.1.2(a) it was stated that category 1 plane wave species can be treated in an identical manner to that used above. From equation (2.4.3) of chapter 2 the category 1 terms are generated from the first term in the initial upward fields and the second term in the initial downward fields. These two spectral amplitude functions are seen to satisfy the relations (G5) and (G6). Hence continuity is demonstrated for category 1 fields at the upper boundary.

From the discussion in the text the difference between the modal fields and the transmitted modal field at B_u of category 2, must be equivalent to the difference between the initial transmitted fields and the initial fields of category 2. The difference in these modal fields is,

$$\int_C \frac{1}{2\alpha}\sum_{q=-\infty}^{\infty}\left[\int_{\theta_{q\infty}}^{\theta} U_j^-(s)F_q^-(\theta,s)V_\theta^-(\underline{x}) - \int_{\theta_{q\infty}}^{\theta} U_j^+(s)F_q^+(\theta,s)e^{i\Phi_u(\theta+\alpha)}V_{\theta_2}^+(\underline{x})\right]ds\,d\theta \qquad (G7)$$

If the substution of $\theta\rightarrow\theta+2\alpha$ is made in the first integral with an appropriate deformation of the contour C and taking account of the identities (6.2.1.3) and also the modal relationships (H17), (H18), then the difference in modal fields is,

$$\int_C \frac{1}{2\alpha}\sum_{q=-\infty}^{\infty}\left[\int_{\theta_{q\infty}+2\alpha}^{\theta+2\alpha} U_j^-(s)F_q^+(\theta,s)e^{i\Phi_1(s)} - \int_{\theta_{q\infty}}^{\theta} U_j^+(s)F_q^+(\theta,s)\right]e^{i\Phi_u(\theta+\alpha)}V_{\theta_2}^+(\underline{x})\,ds\,d\theta \qquad (G8)$$

From equations (2.4.3) of chapter 2 it is noticed that the fields of category 2 satisfy the relationship,

$$U_j^-(s)e^{i\Phi_1(s)} = U_j^+(s) \qquad (G9)$$

Acknowledging this property and allowing for deformation of the lower endpoint $\theta_{q\infty}$ gives the difference of the modal fields to be,

$$\int_C \frac{1}{2\alpha} \sum_{q=-\infty}^{\infty} \int_{\theta}^{\theta+2\alpha} U_j^+(s) F_q^+(\theta,s) e^{i\Phi_u(\theta+\alpha)} V_{2\theta_2}^+(\underline{x}) ds d\theta \qquad (G10)$$

Using the Euler Maclaurin formula of chapter 2 (equation (2.2.7)) and the identity phase relationship (H19) then the difference of modal terms becomes,

$$\int_C \frac{1}{2}\left[U_j^+(\theta+2\alpha) e^{-i\Phi^+(\theta+2\alpha)} + U_j^+(\theta) \right] e^{i\Phi_u(\theta+\alpha)} V_{2\theta_2}^+(\underline{x}) d\theta \qquad (G11)$$

Which is exactly the remainder of the initial and direct fields at the boundary and hence continuity is maintained.

Continuity of Observed field at B_u for the WGF with the Source in the Superstrate.

A similar approach as used for the category 2 plane wave species can be employed to demonstrate the continuity requirements of the field where the reflected and direct fields are given by (6.1.5).

Continuity of the Observed field at B_l for Source points in the Superstrate.

This case is simpler to examine due the plane wave identities (6.2.1.5). The difference in the modal fields, using the above identites, at this boundary can be shown to be,

$$\int_C \frac{1}{2\alpha} \sum_{q=-\infty}^{\infty} \int_{\theta_{q\infty}}^{\theta} \left[U_j^-(s) F_q^-(\theta,s) e^{i\Phi_l(\theta)} - U_j^+(s) F_q^+(\theta,s) \right] V_\theta^+(\underline{x}) ds d\theta \qquad (G12)$$

When the source point is in the upper medium the spectral amplitudes are given by (6.1.9) and are found to satisfy the relation,

$$U_j^+(\theta) = U_j^-(\theta) e^{i\Phi_l(\theta)} \qquad (G13)$$

Using the identity of (H17) the difference in modal fields is zero if,

$$U_j^+(s) F_q^+(\theta,s) = U_j^-(s) F_q^+(\theta,s) e^{i\Phi_l(s)} \qquad (G14)$$

It can be seen that the spectral amplitudes for this WGF defined in (6.1.9) satisfy relation (G14) and consequently the modal field is continuous across the lower boundary. It is observed that the difference between the initial transmitted field and the initial fields satisfies the relation (G13). Thus demonstrating that the continuity of the observed field is preserved across B_1.

Continuity of the Observed field across B_1 for a source point in the guide.

As stated in the text there are two cases to examine. The fields of category 2 defined in equation (2.4.3) of chapter 2 satisfy the equations (G13) and (G14) and consequently category 2 plane wave species are continuous across B_1. The difference in the category 1 modal species is,

$$\int_C \frac{1}{2\alpha} \sum_{q=-\infty}^{\infty} \int_{\theta_{q\infty}}^{\theta} \left[U_j^-(s) - U_j^+(s) e^{-i\Phi_1(s)} \right] F^-(\theta,s) e^{i\Phi_1(\theta)} V_\theta^-(\underline{x}) ds d\theta \qquad \text{(G15)}$$

shifting the first term by 2α to the right and employing identity (H19) and a permissible deformation of the lower endpoint gives the first term as,

$$\int_C \left[\frac{1}{2\alpha} \sum_{q=-\infty}^{\infty} \int_{\theta_{q\infty}}^{\theta-2\alpha} U_j^-(s+2\alpha) e^{-i\Phi^-(s)} F^-(\underset{q}{\theta},s) ds \right] e^{i\Phi_1(\theta)} V_\theta^-(\underline{x}) d\theta \qquad \text{(G16)}$$

Noting that the modal fields of this category have the relation,

$$U_j^-(s+2\alpha) e^{i\Phi^-(s)} = U_j^+(s) e^{-i\Phi_1(s)} \qquad \text{(G17)}$$

then the difference in the modal fields is,

$$-\int_C \left[\frac{1}{2\alpha} \sum_{q=-\infty}^{\infty} \int_{\theta-2\alpha}^{\theta} U_j^-(s+2\alpha) e^{-i\Phi^-(s)} F_q^-(\theta,s) ds \right] e^{i\Phi_1(\theta)} V_\theta^-(\underline{x}) d\theta \qquad \text{(G18)}$$

Employing the Euler Maclaurin formula with a shift of 2α it is found that the above is equivalent to minus the difference between the initial fields, so proving the continuity of the observation point for the source in the guiding layer.

Continuity of Observed field across B_1 for source points in the Substrate.

Applying identical analysis as that used to demonstrate the continuity of the category 1 species across B_1 will yield the desired confirmation of the continuity of the observed field, as the relation (G17) holds for all the plane wave species in this case.

Continuity of the Observed field as the source points cross B_1.

The difference between the modal terms of category 2 (the upward observed field) is,

$$\int_{C} \frac{1}{2\alpha} \sum_{q=-\infty}^{\infty} \int_{\theta_{q\infty}}^{\theta} \left[U_0^+(s) - U_1^+(s) \right] F^+(\theta,s) V_\theta^+(\underline{x}) ds d\theta \qquad \text{(G19)}$$

Shifting the second term by 2α and taking account of the identities (6.2.2.6), together with equations (2.4.3a) of chapter 2 and (6.1.4) leads to the difference in the modal field being expressed as,

$$\int_{C} \frac{1}{2\alpha} \sum_{q=-\infty}^{\infty} \int_{\theta}^{\theta+2\alpha} W_0^+(s) F^+(\theta,s) V_\theta^+(\underline{x}) ds d\theta \qquad \text{(G20)}$$

Applying the Euler–Maclaurin remainder with a shift of 2α gives this expression equal to minus the difference in the remaining plane wave species. This proves the desired continuity relation across B_1.

Continuity of the Observed field as the source point crosses B_0.

Here the difference in modal field for category 2 species (downward observed field) is,

$$\int_{C} \frac{1}{2\alpha} \sum_{q=-\infty}^{\infty} \int_{\theta_{q\infty}}^{\theta} \left[U_2^-(s) - U_0^-(s) \right] F^-(\theta,s) V_\theta^-(\underline{x}) ds d\theta \qquad \text{(G21)}$$

Taking the second term in this expression and shifting by 2α, together with the identities of equation (6.2.2.7) leads to the difference in the modal fields to be,

$$\int_{C} \frac{1}{2\alpha} \sum_{q=-\infty}^{\infty} \int_{\theta-2\alpha}^{\theta} W_{0}^{-}(s) F_{q}^{-}(\theta, s) V_{\theta}^{-}(\underline{x}) ds d\theta \qquad (G22)$$

Using the E– M remainder gives the above expression as equal to minus the difference between the remaining initial fields.

APPENDIX H Evaluates The Properties Of The Spectral Phase Function Of The WGF

This calculates the properties of the spectral phase function $F_q(\theta,s)$ given in equation (6.1.11) of chapter 6 as,

$$F_q^{\pm}(\theta,s) = \exp i\left[\frac{\Phi^{\pm}(s)}{2} - \frac{\Phi^{\pm}(\theta)}{2} + \frac{1}{2\alpha}\int_s^{\theta}\Phi^{\pm}(p)dp - \frac{q\Pi(\theta-s)}{\alpha} + E_b^{\pm}(\theta,s)\right] \qquad (H1)$$

This can be represented in a different manner by,

$$F_q^{\pm}(\theta,s) = e^{iS_q^{\pm}(\theta) - iS_q^{\pm}(s)} \qquad (H2)$$

and with the uniquenes condition of equation (2.2.10) chapter 2.

$$S_q^{+}(\theta) - S_q^{-}(\theta) = \Phi_1(\theta) \qquad (H3)$$

This gives rise to the uniqueness identity,

$$F_q^{+}(\theta,s) = F_q^{-}(\theta,s)e^{i\Phi_1(\theta)}e^{-i\Phi_1(s)} \qquad (H4)$$

Other identities also exist and they are essential for the proof of boundary conditions and of reciprocity of the Wedge Green's function. Consider the substitution $\theta = \theta + 2\alpha$ then,

$$F_q^{\pm}(\theta+2\alpha,s) = \exp i\left[\frac{\Phi^{\pm}(s)}{2} - \frac{\Phi^{\pm}(\theta+2\alpha)}{2} + \frac{1}{2\alpha}\int_s^{\theta+2\alpha}\Phi^{\pm}(p)dp - \frac{q\Pi(\theta-s)}{\alpha} + E_b^{\pm}(\theta+2\alpha,s)\right] \qquad (H5)$$

Adding and subtracting $\Phi^{\pm}(\theta)/2$ gives

$$F_q^{\pm}(\theta+2\alpha,s) = e^{i\left[\frac{\Phi^{\pm}(s)}{2} + \frac{\Phi^{\pm}(\theta)}{2} - \left[\frac{\Phi^{\pm}(\theta+2\alpha)}{2} + \frac{\Phi^{\pm}(\theta)}{2}\right] + \frac{1}{2\alpha}\int_s^{\theta+2\alpha}\Phi^{\pm}(p)dp - \frac{q\Pi(\theta-s)}{\alpha} + E_b^{\pm}(\theta+2\alpha,s)\right]}$$

Applying the Euler– Maclaurin formula to the square bracketed term leads to,

$$F_q^{\pm}(\theta+2\alpha,s) = \exp i\left[\frac{\Phi^{\pm}(s)}{2} + \frac{\Phi^{\pm}(\theta)}{2} + \frac{1}{2\alpha}\int_s^{\theta}\Phi^{\pm}(p)dp - \frac{q\Pi(\theta-s)}{\alpha} + E_b^{\pm}(\theta,s)\right] \qquad (H6)$$

and hence using (H1)

$$F_q^{\pm}(\theta+2\alpha,s) = F_q^{\pm}(\theta,s)e^{i\Phi^{\pm}(\theta)} \qquad (H7)$$

Invoking a similar method, substitute $s = s+2\alpha$ and adding and subtracting $\Phi^{\pm}(s)/2$ leads to,

$$F_q^{\pm}(\theta,s+2\alpha) = e^{i}\left[-\frac{\Phi^{\pm}(s)}{2}-\frac{\Phi^{\pm}(\theta)}{2}+\left[\frac{\Phi^{\pm}(s+2\alpha)}{2}+\frac{\Phi^{\pm}(s)}{2}\right]+\frac{1}{2\alpha}\int_{s+2\alpha}^{\theta}\Phi^{\pm}(p)dp-\frac{q\Pi(\theta-s)}{\alpha}+E(\theta,s+2\alpha)\right]$$

applying the E– M formula gives,

$$F_q^{\pm}(\theta,s+2\alpha) = \exp\left[-\frac{\Phi^{\pm}(s)}{2}-\frac{\Phi^{\pm}(\theta)}{2}+\frac{1}{2\alpha}\int_{s}^{\theta}\Phi^{\pm}(p)dp-\frac{q\Pi(\theta-s)}{\alpha}+E_b^{\pm}(\theta,s)\right] \qquad (H8)$$

and applying (H1) then produces the identity,

$$F_q^{\pm}(\theta,s+2\alpha) = F_q^{\pm}(\theta,s)e^{-i\Phi^{\pm}(s)} \qquad (H9)$$

The final useful identity is necessary for the proof of reciprocity. Firstly it is essential to define some quantities from chapter 2. The multiple reflection coefficient shifted by $\Pi-\theta$ can be represented by,

$$\Phi^{-}(\Pi-\theta) = \Phi^{-}(\theta) + D(\theta), \qquad D(\theta) = \Phi_u(\theta-\alpha) - \Phi_u(\theta+\alpha) \qquad (H10)$$

From this it is immediately obvious that

$$F_q^{-}(\Pi-\theta,\Pi-s) = e^{i}\left[\frac{D(s)}{2}-\frac{D(\theta)}{2}+\frac{\Phi^{-}(s)}{2}-\frac{\Phi^{-}(\theta)}{2}+\frac{1}{2\alpha}\int_{\Pi-s}^{\Pi-\theta}\Phi^{-}(p)dp+\frac{q\Pi(\theta-s)}{\alpha}+E_b^{-}(\Pi-\theta,\Pi-s)\right] \qquad (H11)$$

The integrals in this formalism can be expressed differently by using the substitution $\Pi-p=\delta$ and applying (H10) and are found to be,

$$\frac{1}{2\alpha}\sum_{-\infty}^{\infty}\int_{\theta}^{s}\Phi^{-}(\Pi-\delta)\,e^{\frac{iq\Pi(\theta-\delta)}{\alpha}}\,d\delta = \frac{1}{2\alpha}\sum_{-\infty}^{\infty}\int_{\theta}^{s}\left[\Phi^{-}(\delta)+\Phi_u(\delta-\alpha)-\Phi_u(\delta+\alpha)\right]e^{\frac{iq\Pi(\theta-\delta)}{\alpha}}\,d\delta$$

If the substitution $\delta-\alpha=p$ in the first term of the second integral and $\delta+\alpha=p$ in the second term and adding and subtracting the obvious integral then,

$$\frac{1}{2\alpha}\sum_{-\infty}^{\infty}\int_{\theta}^{s}\left[\Phi_u(\delta-\alpha)-\Phi_u(\delta+\alpha)\right]e^{\frac{iq\Pi(\theta-\delta)}{\alpha}}\,d\delta = \frac{1}{2\alpha}\sum_{-\infty}^{\infty}e^{iq\Pi}\left[\int_{s+\alpha}^{s-\alpha}+\int_{\theta-\alpha}^{\theta+\alpha}\Phi_u(p+\alpha)e^{\frac{iq\Pi(\theta-p)}{\alpha}}\,dp\right.$$

Using the Euler–Maclaurin formula of chapter 2 by appropriate shifts on the above equation gives the equation below.

$$\frac{1}{2\alpha}\int_{\Pi-s}^{\Pi-\theta}\Phi^{-}(p)dp + E_b^{-}(\Pi-\theta,\Pi-s) = \frac{1}{2\alpha}\int_{\theta}^{s}\Phi^{-}(p)dp + E_b^{-}(s,\theta) + N(\theta,s) \qquad (H12)$$

where

$$N(\theta,s) = \frac{1}{2}\left[\Phi_u(\theta+\alpha) + \Phi_u(\theta-\alpha) - \Phi_u(s-\alpha) - \Phi_u(s+\alpha)\right] \qquad (H13)$$

and as

$$\frac{1}{2}\left[D(s) - D(\theta)\right] + N(\theta,s) = \Phi_u(\theta+\alpha) - \Phi_u(s+\alpha) \qquad (H14)$$

Using (H12), (H14) in (H11) gives the following identity,

$$F_q^{-}(\Pi-\theta,\Pi-s) = F_q^{-}(s,\theta)e^{i\Phi_1(s)-i\Phi_1(\theta)} \qquad (H15)$$

Thus all the relations for this appendix are summarised below,

$$F_q^{-}(\Pi-\theta,\Pi-s) = F_q^{-}(s,\theta)e^{i\Phi_1(s)-i\Phi_1(\theta)} \qquad (H16)$$

$$F_q^{+}(\theta,s) = F_q^{-}(\theta,s)e^{i\Phi_1(\theta)}e^{-i\Phi_1(s)} \qquad (H17)$$

$$F_q^{\pm}(\theta+2\alpha,s) = F_q^{\pm}(\theta,s)e^{i\Phi^{\pm}(\theta)} \qquad (H18)$$

$$F_q^{\pm}(\theta,s+2\alpha) = F_q^{\pm}(\theta,s)e^{-i\Phi^{\pm}(s)} \qquad (H19)$$

APPENDIX I Demonstrating The Reciprocity Property Of The WGF.

This demonstrates mathematical the reciprocity of the WGF for the initial and modal fields. When the source points are in the guide the plane wave species are given by equations (2.4.3) in chapter 2.

Reciprocity for the Odd Reflected fields.

The initial odd reflected downward field <2> at the observation point with source and observation point interchanged is,

$$\int_C e^{inkrcos(\theta-2\alpha+\chi)} e^{i\Phi_u(\theta-\alpha)} e^{-inkr_s cos(\theta-\chi_s)} d\theta \qquad (I1)$$

Make the substitution $\theta\rightarrow\theta+2\alpha$ and the permissible shift of the infinite contour gives initial field as,

$$\int_C e^{inkrcos(\theta+\chi)} e^{i\Phi_u(\theta+\alpha)} e^{-inkr_s cos(\theta+2\alpha-\chi_s)} d\theta \qquad (I2)$$

If the substitution $\theta\rightarrow\Pi-\theta$ is made the contour C is mapped into itself and thus the field becomes,

$$\int_C e^{-inkrcos(\theta-\chi)} e^{i\Phi_u(\theta-\alpha)} e^{inkr_s cos(\theta-2\alpha+\chi_s)} d\theta \qquad (I3)$$

which is the identical to (6.2.3.9a). For the modal spectrum the same process is adopted. Interchanging source and observation point and making substitutions $s\rightarrow s+2\alpha$ and $\theta\rightarrow\theta+2\alpha$ and allowing legitimate deformations of the contour C and endpoint $\theta_{q\infty}$ gives this modal field as,

$$\int_C \frac{1}{2\alpha}\sum_{q=-\infty}^{\infty}\int_{\theta_{q\infty}}^{\theta} F_q^-(\theta+2\alpha, s+2\alpha) e^{inkrcos(s+\chi)} e^{i\Phi_u(s+\alpha)} ds\, e^{-inkr_s cos(\theta+2\alpha-\chi_s)} d\theta \qquad (I4)$$

Using the identities of appendix H for $F_q^{\pm}(\theta,s)$ gives this field as,

$$\int_C \frac{1}{2\alpha}\sum_{q=-\infty}^{\infty}\int_{\theta_{q\infty}}^{\theta} F_q^-(\theta, s) e^{inkrcos(s+\chi)} e^{i\Phi_u(s+\alpha)} e^{i\Phi^-(\theta)-i\Phi^-(s)} ds\, e^{-inkr_s cos(\theta+2\alpha-\chi_s)} d\theta \qquad (I5)$$

Making the substitutions $\theta \rightarrow \Pi - \theta$ and $s \rightarrow \Pi - s$ and making sure C is mapped into itself requires that the inner order of integration be reversed giving for each q,

$$\int_C \int_{\theta}^{\Pi-\theta_{q\infty}} F_q^-(\Pi-\theta,\Pi-s) e^{-ikr\cos(s-\chi)} e^{i\Phi_u(s-\alpha)} e^{i\Phi^-(\Pi-\theta)-i\bar{\Phi}(\Pi-s)} e^{ikr_s\cos(\theta-2\alpha+\chi_s)} ds d\theta \tag{16}$$

The orders of integration can now be interchanged as the contour C can legitimately be deformed into the region where $\Pi - \theta_{q\infty}$ may lie. The legitimacy of this interchange can be demonstrated easily by examination of diagram 2.5.1 of chapter 2.

$$\int_C \int_{s_{q\infty}}^{s} F_q^-(\Pi-\theta,\Pi-s) e^{-ikr\cos(s-\chi)} e^{i\Phi_u(s-\alpha)} e^{i\Phi^-(\Pi-\theta)-i\Phi^-(\Pi-s)} e^{ikr_s\cos(\theta-2\alpha+\chi_s)} ds d\theta \tag{17}$$

Using the identity (H16) of appendix H gives the relation,

$$F_q^-(\Pi-\theta,\Pi-s) e^{i\Phi_u(s-\alpha)} e^{i\Phi^-(\Pi-\theta)-i\Phi^-(\Pi-s)} = F_q^-(s,\theta) e^{i\Phi_u(\theta-\alpha)} \tag{18}$$

and so the modal odd downward reflected field becomes,

$$\int_C \frac{1}{2\alpha} \sum_{q=-\infty}^{\infty} \int_{s_{q\infty}}^{s} F_q^-(s,\theta) e^{-ikr\cos(s-\chi)} e^{i\Phi_u(\theta-\alpha)} e^{ikr_s\cos(\theta-2\alpha+\chi_s)} d\theta ds$$

This is exactly the same as (6.2.3.9b) and thus reciprocity is demonstrated for the odd reflected downward field at source. Due to the complexity of the contour shifting for the modal field, it will be assumed in all additional proofs that the desired contour deformations are allowable.

The next species to demonstrate reciprocity is the odd upward field <4> at the observation point. The initial field integrand is,

$$e^{ikr_s\cos(\theta-\chi_s)} e^{i\Phi_1(\theta)} e^{-ikr\cos(\theta+\chi)} \tag{19}$$

Interchanging source and observation points and applying the substitution $\theta \rightarrow \Pi - \theta$ with the knowledge that the single reflection process is symmetrical under this transformation leads to the identical integrand and thus this field is reciprocal. The modal field for this case is,

$$\int_{C} \frac{1}{2\alpha} \sum_{q=-\infty}^{\infty} \int_{\theta_{q\infty}}^{\theta} F_q^+(\theta,s) e^{ikr_s\cos(s-\chi_s)} e^{i\Phi_1(s)} e^{-ikr\cos(\theta+\chi)} ds d\theta \qquad (I10)$$

Interchanging source and observation point and applying the identities in appendix H gives the integrand as,

$$F_q^-(\theta,s) e^{i\Phi_1(\theta)-i\Phi_1(s)} e^{ikr\cos(s-\chi)} e^{i\Phi_1(s)} e^{-ikr_s\cos(\theta+\chi_s)} \qquad (I11)$$

making the substitutions $\theta \rightarrow \Pi - \theta$ and $s \rightarrow \Pi - s$ with the use of identity (H16) gives,

$$F_q^-(s,\theta) e^{-ikr\cos(s+\chi)} e^{i\Phi_1(s)} e^{ikr_s\cos(\theta-\chi_s)} \qquad (I12)$$

Using the identity (H17) with the corresponding variable change gives the integrand to be,

$$F_q^+(s,\theta) e^{-ikr\cos(s+\chi)} e^{i\Phi_1(\theta)} e^{ikr_s\cos(\theta-\chi_s)} \qquad (I13)$$

As all contour paths are shown to be equivalent after all substitutions and it is obvious that (I11) is equal to the integrand of (I10) and thus reciprocity for all the odd reflected fields is proved.

Reciprocity for the even reflected fields.

Here as in the previous case the shifts of contours are assumed to be legitimate so that only the integrands of the fields need to be examined. In this case the even reflected upward field must be shown to be equivalent evenly reflected downward field when the source and observation points are interchanged. This inverse of this must also be true. The integrand of the upward double reflected field <5> is

$$e^{ikr_s\cos(\theta-2\alpha+\chi_s)} e^{i\Phi^+(\theta-2\alpha)} e^{-ikr\cos(\theta+\chi)} \qquad (I14)$$

The double reflected initial downward field <3> must be equal to the above field when the source and observation points are interchanged. The downward initial field with source and observation point interchanged is,

$$e^{ikr\cos(\theta-2\alpha-\chi)} e^{i\Phi^-(\theta-2\alpha)} e^{-ikr_s\cos(\theta-\chi_s)} \qquad (I15)$$

With a simple shift of $\theta \rightarrow \theta + 2\alpha$ gives the above integrand as

$$e^{-ikr\cos(\theta-\chi)}e^{i\Phi^{-}(\theta)}e^{-ikr_s\cos(\theta+2\alpha-\chi_s)} \qquad (I16)$$

With the substitution $\theta\rightarrow\Pi-\theta$ the integrand becomes,

$$e^{ikr\cos(\theta+\chi)}e^{i\Phi^{-}(\Pi-\theta)}e^{ikr_s\cos(\theta-2\alpha+\chi_s)} \qquad (I17)$$

Using the standard formulae for the double reflection coefficient it is observed that the

$$\Phi^{-}(\Pi-\theta) = \Phi^{+}(\theta-2\alpha) \qquad (I18)$$

and hence the integrand of (I17) is equivalent to (I114). The integrand of the modal even upward field is

$$F_q^{+}(\theta,s)e^{ikr_s\cos(s-2\alpha+\chi_s)}e^{i\Phi^{+}(s-2\alpha)}e^{-ikr\cos(\theta+\chi)} \qquad (I19)$$

As for the initial field, the downward even reflected modal field integrand with source and observation point interchanged must be identical to the above integrand assuming that all contours are well behaved. The downward modal field integrand is,

$$F_q^{-}(\theta,s)e^{-ikr\cos(s-2\alpha-\chi)}e^{i\Phi^{-}(s-2\alpha)}e^{-ikr_s\cos(\theta-\chi_s)} \qquad (I20)$$

Making substitution $\theta\rightarrow\theta+2\alpha$ and $s\rightarrow s+2\alpha$ this integrand becomes with the aid of (H18) and (H19)

$$F_q^{-}(\theta,s)e^{i\Phi^{-}(\theta)-i\Phi^{-}(s)}e^{-ikr\cos(s-\chi)}e^{i\Phi^{-}(s)}e^{-ikr_s\cos(\theta+2\alpha-\chi_s)} \qquad (I21)$$

Then making the substitutions $\theta\rightarrow\Pi-\theta$ and $s\rightarrow\Pi-s$ gives the integrand as

$$F_q^{-}(\Pi-\theta,\Pi-s)e^{i\Phi^{-}(\Pi-\theta)}e^{ikr\cos(s+\chi)}e^{ikr_s\cos(\theta-2\alpha+\chi_s)} \qquad (I22)$$

Using the identity (H16) and (H17) with variable integrchange gives (I22) as,

$$F_q^{-}(s,\theta)e^{i\Phi^{-}(\Pi-\theta)}e^{ikr\cos(s+\chi)}e^{ikr_s\cos(\theta-2\alpha+\chi_s)} \qquad (I23)$$

The equality of (I18) implies that the integrand of (I19) is equal to the integrand of (I20). There is still one more case to consider. It has all ready been proved that interchanging source and observation point for the downward evenly reflected field <3> is equivalent to the part of the upslope WGF representing the upward evenly reflected field <5>. It now has to be demonstrated that the inverse is true. The

initial evenly reflected downward is

$$e^{ikr_s\cos(\theta-2\alpha-\chi_s)}e^{i\Phi^-(\theta-2\alpha)}e^{-ikr\cos(\theta-\chi)} \tag{I24}$$

The evenly reflected initial upward field integrand with source and observation interchanged is

$$e^{ikr\cos(\theta-2\alpha+\chi)}e^{i\Phi^+(\theta-2\alpha)}e^{-ikr_s\cos(\theta+\chi_s)} \tag{I25}$$

Shifting by 2α gives

$$e^{ikr\cos(\theta+\chi)}e^{i\Phi^+(\theta)}e^{-ikr_s\cos(\theta+2\alpha+\chi_s)} \tag{I26}$$

Again substitution of $\theta\rightarrow\Pi-\theta$ gives,

$$e^{-ikr\cos(\theta-\chi)}e^{i\Phi^+(\Pi-\theta)}e^{ikr_s\cos(\theta-2\alpha-\chi_s)} \tag{I27}$$

From chapter two and symmetry of phase reflection coefficient gives,

$$\Phi^+(\Pi-\theta) = \Phi^-(\theta-2\alpha) \tag{I28}$$

Using this identity it is obvious that the integrands of (I24) and (I25) are equal and thus reciprocity is proved for the initial ray fields. The even modal downward field is,

$$F_q^-(\theta,s)e^{ikr_s\cos(s-2\alpha-\chi_s)}e^{i\Phi^-(s-2\alpha)}e^{-ikr\cos(\theta-\chi)} \tag{I29}$$

As for the initial field the downward even reflected field integrand with source and observation point interchanged must be identical to the above integrand assuming that all contours are well behaved. The upward field with the source and observation point interchanged is,

$$F_q^+(\theta,s)e^{-ikr\cos(s-2\alpha+\chi)}e^{i\Phi^+(s-2\alpha)}e^{-ikr_s\cos(\theta+\chi_s)} \tag{I30}$$

Applying a shift of $s\rightarrow s+2\alpha$ and $\theta\rightarrow\theta+2\alpha$ and using (H17) (H18) and (H19) gives,

$$F_q^-(\theta,s)e^{i\Phi^+(\theta)+i\Phi_1(\theta)-i\Phi_1(s)}e^{-ikr\cos(s+\chi)}e^{-ikr_s\cos(\theta+2\alpha+\chi_s)} \tag{I31}$$

Shifting by $\Pi-\theta$ and $\Pi-s$ with (H16) and (I12) demonstrates that this is indeed equivalent to (I29). This final proof demonstrates that the WGF does possess the reciprocity property.

APPENDIX J Asymptotic Analysis Of The WGF.

Examining a single term in the summation of the modal part of the WGF gives,

$$M_q(\underline{x},\underline{x}_s) = \int_C \int_{\theta_{q\infty}}^{\theta} H(s,\theta) e^{\frac{iX_q(\theta,s)}{\alpha}} \, ds d\theta \tag{J1}$$

To evalute the integral aysmptotically the phase function must be expanded about its two dimensional saddle point at (θ_q, θ_{qs}). This is achieved by making the substitution,

$$\frac{1}{\alpha} X_q(\theta,s) = \frac{1}{\alpha} X_q(\theta_q,\theta_{qs}) + it^2 + it_s^2 \tag{J2}$$

From this equation it can be easily verified that,

$$it^2 = (\theta-\theta_q)^2 \frac{1}{2\alpha} \frac{\partial^2 X_q(\theta_q,s)}{\partial\theta^2} + O((\theta-\theta_q)^3) \tag{J3}$$

$$it_s^2 = (s-\theta_{qs})^2 \frac{1}{2\alpha} \frac{\partial^2 X_q(\theta,\theta_{qs})}{\partial s^2} + O((s-\theta_{qs})^3) \tag{J4}$$

This gives θ and s as asymptotic functions of t and t_s respectively.

$$(\theta-\theta_q) \sim \left[\frac{2\alpha}{\frac{\partial^2 X_q(\theta_q,s)}{\partial\theta^2}}\right]^{\frac{1}{2}} e^{i\Pi/4} t = \lambda t \tag{J5}$$

$$(s-\theta_{qs}) \sim \left[\frac{2\alpha}{\frac{\partial^2 X_q(\theta,\theta_{qs})}{\partial s^2}}\right]^{\frac{1}{2}} e^{i\Pi/4} t_s = \lambda_s t_s \tag{J6}$$

Using these equations into (J1) gives,

$$M_q(\underline{x},\underline{x}_s) \sim \sum^{\pm} (\lambda\lambda_s) \underset{\substack{\theta=\theta_q \\ s=\theta_{q\infty}}}{H^{\pm}(\theta_q,\theta_{qs})} e^{iX_q(\theta_q,\theta_{qs})/\alpha} \int_{-\infty}^{\infty} \int_a^b e^{-(t^2+t_s^2)} dt_s dt$$

where

$$b = \frac{1}{\lambda_s}\left[\lambda t + \theta_q - \theta_{qs}\right] \qquad a = \frac{\theta_{q\infty} - \theta_{qs}}{\lambda_s}$$

If these axes are then rotated so as to lie parallel to the upper end point. i.e. making the transformations

$$\left[t + \frac{\lambda}{\lambda_s} t_s\right]\left[1 + \frac{\lambda}{\lambda_s}\right] = p \tag{J7}$$

$$\left[t_s - \frac{\lambda}{\lambda_s} t\right]\left[1 + \frac{\lambda}{\lambda_s}\right] = p_s \tag{J8}$$

Using this transformation the q modal term becomes,

$$M_q(\underline{x},\underline{x}_s) \sim \sum_{\substack{\theta=\theta_q \\ s=\theta_{q\infty}}}^{\pm} (\lambda\lambda_s)\, H^{\pm}(\theta_q,\theta_{qs}) e^{iX_q(\theta_q,\theta_{qs})/\alpha} \int_{-\infty}^{\infty}\int_{X}^{\infty} e^{-(p^2+p_s^2)} dp_s dp$$

with

$$X = (\theta_{q\infty} - \theta_{qs})\left[\lambda_s^2 + \lambda^2\right]^{-\frac{1}{2}}$$

with all other limits being permissibly deformed to infinity, which gives integral as,

$$M_q(\underline{x},\underline{x}_s) \sim \sum_{\substack{\theta=\theta_q \\ s=\theta_{q\infty}}}^{\pm} (\lambda\lambda_s)\, H^{\pm}(\theta_q,\theta_{qs}) e^{iX_q(\theta_q,\theta_{qs})/\alpha} \Pi\left[1 - \Pi^{-\frac{1}{2}} \int_{-\infty}^{X} e^{-p_s^2} dp_s\right] \tag{J9}$$

which can be expressed in the form,

$$M_q(\underline{x},\underline{x}_s) \sim w_q^*(\underline{x}_s) w_q(\underline{x}) \left[1 - \Pi^{-\frac{1}{2}} \int_{-\infty}^{X} e^{-p_s^2} dp_s\right] \tag{J10}$$

where $w_q(\underline{x})$ is the asymptotic function defined in equation (4.3.1.3) chapter 4.

APPENDIX K Asymptotic Analysis Of The Initial Fields.

This calculates the asymptotic expansion of the ray integral terms when the stationary phase point is at a large distance away from the critical point of the reflection coefficient. The integral $I(R,\tau)$ can be represented exactly by,

$$I(R,\tau) = \int_{SDP} + \int_{P_b} A(\theta) e^{ikR\cos(\theta-\tau)} d\theta \qquad (K1)$$

The first contour corresponds to the normal ray field and is evaluated as follows;– Make the substitution,

$$ikR\cos(\theta-\tau) = ikR - S^2 \qquad (K2)$$

To invert asymptotic series assume,

$$\theta = a_1 S + a_2 S^2 + a_3 S^3 + O(S^4) \qquad (K3)$$

Substituting (K3) into (K2) and equating coefficients of S leads to

$$\theta = \frac{S 2^{\frac{1}{2}}}{\sqrt{(ikR)}} \left[1 + \frac{S^2}{12ikR} \right] + O(S^5) \qquad (K4)$$

This gives the derivative of S with respect to θ to be,

$$\frac{d\theta}{dS} = \frac{2^{\frac{1}{2}}}{\sqrt{(ikR)}} \left[1 + \frac{S^2}{4ikR} \right] + O(S^4) \qquad (K5)$$

The amplitude function $A(\theta)$ may also be expanded in terms of S to give,

$$A(\theta) = A(\tau) + \frac{A_\theta(\tau) 2^{\frac{1}{2}}}{\sqrt{(ikR)}} S + \frac{A_{\theta\theta}(\tau)}{ikR} S^2 + O(S^3) \qquad (K6)$$

Substituting (K2), (K5) and (K6) into (K1) gives the approximation to the ray integral as

$$I_r(R,\tau) \sim \int_{-\infty}^{\infty} \frac{2^{\frac{1}{2}}}{\sqrt{(ikR)}} \left[A(\tau) + \frac{A_\theta(\tau) 2^{\frac{1}{2}}}{\sqrt{(ikR)}} S + \left[A_{\theta\theta}(\tau) + \frac{A(\tau)}{4} \right] \frac{S^2}{ikR} \right] e^{-S^2} dS e^{ikR - i\Pi/4} \qquad (K7)$$

Using the integral expression for the gamma function the asymptotic expansion of the ray integral to second order is,

$$I_r(R,\tau) \sim \left[\frac{2\Pi}{ikR} \right]^{\frac{1}{2}} A(\tau) e^{ikR - i\Pi/4} \left[1 + \frac{e^{\frac{-i\Pi}{2}}}{8ikR} \left[\frac{8A_{\theta\theta}(\tau)}{A(\tau)} + 1 \right] \right] \quad (K8)$$

where $A_\theta(\tau)$ is the derivative of $A(\theta)$ with respect to θ evaluated at τ. The branch cut integral can be calculated asymptotically by using a similar procedure outlined below. The function $ikcos(\theta - \tau)$ can be expanded about the branch point of the function $A(\theta)$ denoted by θ_c and expanding the integral about this point, such that the substitution,

$$-S^2 = ikRcos(\theta_c - \tau) - (\theta - \theta_c) ikRsin(\theta_c - \tau) + O((\theta - \theta_c)^2) \quad (K9)$$

is made. As before for asymptotic inversion of series assume,

$$\theta - \theta_c = a_1 S^2 + a_2 S^3 + a_3 S^4 \quad (K10)$$

Inserting this into (K9) and equating coefficients of S gives the asymptotic form of the derivative of the change of variable to be,

$$\frac{d\theta}{dS} = \frac{2S}{ikrsin(\theta_c - \tau)} + O(S^3) \quad (K11)$$

The amplitude function $A(\theta)$ can be represented by an ascending power series of $(\theta - \theta_c)^{\frac{1}{2}}$ (see appendix B for calculated constants). i.e.

$$A(\theta) = C_0 + C_1 (\theta - \theta_c)^{\frac{1}{2}} + O((\theta - \theta_c)) \quad (K12)$$

With the substitution (K9) and the subsequent representations of the integrand, the branch cut integral can be represented in terms of the variable S. However, as the limits on the integral are $\pm\infty$ all odd powers of S will integrate out to zero. Hence the asymtotic value of the branch cut integral to first order is,

$$I_b(R,\tau) \sim \frac{C_1 \sqrt{\Pi} e^{ikrcos(\theta_c - \tau) - i\Pi/4}}{(nkRsin(\theta_c - \tau))^{3/2}} \quad (K13)$$

Provided that the branch point and the stationary phase point are isolated the integral can be asymptotically represented by (K13) and (K8).

REFERENCES.

[1]
ARNOLD J.M. and FELSEN L.B. 'Theory of Wave Propagation in a Wedge Shaped Layer', (submitted to wave motion).

[2]
OLVER F.W.J. 'Asymptotics and Special Functions', (Academic Press, New York. 1974).

[3]
TOPUZ E. and FELSEN L.B. 'Intrinsic Modes: Numerical implementation in a wedge–shaped ocean', J. Acoust. Soc. Am. 78(5), November (1985).

[4]
ARNOLD J.M., BELGHORAS A. and DENDANE A. 'intrinsic mode theory for tapers in integrated optics,' submitted to IEE Proc.

[5]
XIANG F., CADA M. and FELSEN L.B. 'Numerical Study Of Tapered Optical Waveguides By The Intrinsic Mode Approach', (IEEE Montech'86, Conference on Antennas and Communications. Sept 29– Oct 1, 1986).

[6]
ARNOLD J.M. and DENDANE A. 'Wave propagation with longitudinal variations,' SERC research grant GR/C/71804

[7]
OPPENHEIM A.V. and SCHAFER R.W. 'The discrete fourier transform,' Prentice–Hall, New Jersey, (1975).

[8]
LAGASSE P.E. and BAETS R. 'The beam propagation method in integrated optics,' NATO Advanced Research Workshop on Hybrid Formulation of Wave Propagation and Scattering, August 30 – Sept. 3, Rome (1983).

[9]
TAPPERT F.D. 'The parabolic approximation method,' in Chap. V, 'Wave Propagation and Underwater Acoustics,' edited by J.B. Keller and J.S. Papadakis, Springer Lecture Notes in Physics, No. 70 (Springer, Berlin, 1977)

[10]
MORSE P.M. and FESHBACH M. 'Methods of theoretical physics,' McGraw Hill (1953).

[11]
BREKHOVSKIKH L.M. 'Waves in Layered Media,' Academic Press, New York (1960).

[12]
PIERCE A.D. 'Extension of the method of mormal modes to sound propagation in an almost stratified medium,' J. Acoust. Soc. Am. **37**, 19–27 (1965).
[13]
SPORLEDER F. and UNGER H.G. 'Waveguide Tapers, Transitions and Couplers,' IEE Electromagnetic waves, series 6 Peter Pererinus, London (1979).
[14]
LAGASSE P.E. and BAETS R. 'Application of propagating beam methods to electromagnetic and acoustic wave propagation problems: a review,' Radio Science **22**(7), 1225–1233 (1986).
[15]
FIET M.D. and FLECK J.A. ' Light propagation in graded index optical fibres,' Appl. Opt. **17**(24), 3990–3998 Dec. (1978).
[16]
FIET M.D. and FLECK J.A. ' Calculation of dispersion in graded–index multimode fibers by the propagating beam method,' Appl. Opt. **18**(18), 2843–2851 (1979).
[17]
FINLAYSON N. 'Inhomogeneous lens structures for integrated optics,' PhD thesis, University of Glasgow (1985).
[18]
GRIBBLE J.J. and ARNOLD J.M. 'A ray optics analysis of the beam propagation method,' Proceedings of the fourth European Conference on integrated optics, Glasgow, ECIO edited by WILKINSON C.D.J. and LAMB J. (1987).
[19]
KAMEL A. and FELSEN L.B. 'Spectral theory of sound propagation in an ocean channel with a weakly sloping bottom,' J. Acoust. Soc. Am. **73**, 1120–1130 (1983).
[20]
PIERCE A.D. 'Guided mode disappearance during upslope propagation in variable depth shallow water overlying a fluid bottom,' J. Acoust. Soc. Am. **72**, 523–531 (1982).
[21]
EVANS R.B. 'A coupled mode solution for acoustic propagation: a waveguide with stepwise depth variation of penetrable bottom,' J. Acoust. Soc. Am. **74**, 188–195 (1983).
[22]
JENSEN F.B. and KUPERMAN W.A. 'Sound propagation in a wedge shaped ocean with a penetrable bottom,' J. Acoust. Soc. Am. **67**, 1564–1566 (1980).
[23]
NAYFEH A. 'Perturbation Methods,' Pure and Applied Mathematics. A Wiley Interscience series of Texts, Monographs and Transactions. (1973)

[24]
JONES D.S. 'The theory of electromagnetism,' Oxford (1964).
[25]
CLEMMOW P.C. 'The plane wave spectrum representation of electromagnetic fields,' Pergamon Press (1966).
[26]
CHOUDHARY S. and FELSEN L.B. 'Analysis of gaussian beam propagation and diffraction by inhomogeneous wave tracking,' IEEE Proc. 62(11), 1530–1541 Nov. (1974).
[27]
BOROVIKOV V.A. and KINBER B.Y. 'Some problems in the asymptotic theory of diffraction,' IEEE Proc. 62(11), 1416–1437 Nov. (1974).
[28]
KELLER J.B. 'Geometrical theory of diffraction,' J. Opt. Soc. Am. 52 116–130 (1962).
[29]
SOMMERFELD A. 'Optics,' Academic Press, New York (1964).
[30]
BAKER and COPSON 'Huygens Principle,' Oxford Uni. Press. (1939)
[31]
ARNOLD J.M. and FELSEN L.B. 'Local intrinsic modes: layer with nonplanar interface,' Wave Motion 8, 1–14 (1986).
[32]
BLEISTEIN N. and HANDELSMAN R.A. 'Asymptotic expansion of integrals,' Dover New York (1986).
[33]
ARNOLD J.M. 'A global geometrical theory of diffraction,' IMA J. Appl. Maths 35, 273–295 (1985).
[34]
ARNOLD J.M. 'Geometrical theories of wave propagation: a contemporary review,' IEE Proc. 133(2), Part J April (1986).
[35]
FELSEN L.B. 'Novel ways for tracking rays,' J. Opt. Soc Am. 2, 954–963 (1985).
[36]
FELSEN L.B. 'Real spectra, complex spectra, compact spectra,' J. Opt. Soc. Am. 3(4), 486–496 (1986).
[37]
FELSEN L.B. 'Longitudinally varying ducts with guiding to antiguiding transitions,' Radio Science 22(7), 1204–1210 Dec. (1987).
ARNOLD J.M. and FLESEN L.B. 'Ray invariants, plane wave spectra and adiabatic

modes for open waveguides,' Radio Science 19, 1256–1264 (1984).
[38]
CHEN C.H. 'Theory Of Electromagnetic Waves,' Fong and Sons, Singapore (1985)
[39]
ARNOLD J.M. and FELSEN L.B. 'Rays and local modes in a wedge shaped ocean,' J. Acost. Soc. Am. 73, 1105–1119 (1983).
[40]
ARNOLD J.M. and FELSEN L.B. 'Intrinsic modes in a non–separable ocean waveguide,' J. Acoust. Soc. Am. 76, 850–860 (1984).
[41]
TAMIR T. 'Integrated optics,' Springer–Verlag (1975).
[42]
ARNOLD J.M. and FELSEN L.B. 'Coupled mode theory of intrinsic modes,' J. Acoust. Soc. Am. 29, 31–40 (1986).
[43]
PIERCE A.D. 'Augmented adiabatic mode theory for upslope propagation from a source point in variable–depth shallow water overlying a fluid bottom,' J. Acoust. Soc. Am. 74, 1837–1847 (1983).
[44]
FELSEN L.B. and MARCUVITZ N. 'Radiation and Scattering of Waves', Prentice–Hall, New York. (1973).
[45]
VAN ROEY J., VAN DER DONK J. and LAGASSE P.E. 'Beam–propagation method: analysis and assessment,' J. Opt. Soc. Am. 71(7) 803–810 July (1981).
[46]
LUNEBURG R.K. 'Mathematical theory of optics,' Univ. Calif. Press (1964).
[47]
GRIBBLE J.J. and ARNOLD J.M. 'BPM ray equation,' Op. Soc. Am. Let. 13(8) (1988)
[48]
GRIBBLE J.J. and ARNOLD J.M. 'BPM and Geometrical Optics,' IEE Proc. 135 Pt. J No.5 (1988).
[49]
CHWIEROTH F.S., NAGL A., UBERALL R., GRAVES R.D. and ZARUR G.L. 'Mode coupling in sound channel with range dependent profile velocity,' J. Acoust. Soc. Am. 64, 1105–1112 (1978).
[50]
BORN M. and WOLF E. 'Principles of optics,' Pergamon New York (1959).

[51]
WHITTAKER E. and WATSON G.N. 'A course of modern analysis,' Cambridge (1927).
[52]
APOSTOL T.M 'Mathematical Analysis,' Addison– Wesley Publishing Company (1974).
[53]
SPENCER et Al 'Engineering Mathematics,' Volume 1. Van Nostrand (1983).
[54]
ABRAMOWITZ M. and STEGUN I. 'Handbook of mathematical functions and tables,' Dover (1964).
[55]
KAMEL A. and FELSEN L.B. 'Resolvent formulation of the Green's function for a wedge shaped ocean,' J. Acoust. Soc. Am. suppl. **70**, S3 (1981).
[56]
LORRAIN P. and CORSON D.R. 'Electromagnetic fields and waves,' W.H. Freeman and Company San Francisco (1970).
[57]
SWENSON G.W. 'Principles of modern acoustics,' Van Nostrand Company Inc. (1953).
[58]
JENSEN F. Private Communication.
[59]
SPENCER et Al 'Engineering Mathematics,' Volume 2. Van Nostrand (1983).
[60]
BLEISTEIN N. 'Uniform asymptotic expansions of integrals with stationary point near algebraic singulatrity,' Communications on Pure and Appl. Maths. **4**, 353–370 (1966).
[61]
SCREIBER M. 'Differential forms: A heuristic introduction,' Springer– Verlag (1977).
[62]
ARNOLD J.M 'Oscillatory integral theory for uniform representation of wavefunctions,' Radio Science **17**, 1181–1191 (1982).
[63]
ARNOLD J.M. 'Spectral synthesis of uniform wavefunctions,' Wave Motion **8**, 135–150 (1986)

GLASGOW